Delicate Topological Insulators: a New World of Phases between Trivial and Fragile

Dissertation

zur
Erlangung der naturwissenschaftlichen Doktorwürde
(Dr. sc. nat.)

vorgelegt der
Mathematisch-naturwissenschaftlichen Fakultät
der
Universität Zürich

von
Aleksandra Nelson
aus
Russland

Promotionskommission

Prof. Dr. Titus Neupert (Vorsitz)
Dr. Tomáš Bzdušek (Leitung der Dissertation)
Prof. Dr. Andreas Schilling
Prof. Dr. Oleg Yazyev

Zürich, 2022

To the memory of Alexey Soluyanov

ABSTRACT

Topological band theory studies the behavior of non-interacting electrons in solids that is protected by topological invariants and is therefore robust against system perturbations. Among many topics that are important for characterizing topological phases of matter, two are greatly relevant for the present work. The first is the stability of topological insulators against addition of trivial bands. Previous studies have identified fragile topological bands, which in contrast to stable topological bands, can be made trivial by adding a filled trivial band (in the language of fermionic band structures). In this thesis, we refine the notion of stability by defining delicate topological bands: they can be trivialized even by adding an empty trivial band above the Fermi level. Crucially, this weaker stability condition allows us to define new topological invariants that otherwise would not be recognized as topologically protected. The second important topic for topological insulators is the attempt to describe them in terms of Wannier orbitals. It is known that stable and fragile topology forms an obstruction to make these orbitals exponentially localized and locally symmetric. We show that delicate topology does not exhibit this 'strong' obstruction. Instead, its exponentially localized and symmetric Wannier orbitals can not be localized within one unit cell, which prevents the delicate topological insulator from being deformed to a trivial one. We call such Wannier orbitals multicellular.

In this thesis, we introduce the concepts of delicate and multicellular topology on the case of crystalline Hopf insulators: two-band three-dimensional insulators invariant under rotation symmetry. We identify the topological invariants characterizing this insulator, the Hopf and the returning Thouless pump (RTP) invariants, and show that they are delicate and multicellular. Moreover, the RTP invariant realizes symmetry-protected delicate topology: it can be trivialized only by addition of trivial bands of specific symmetry representations, while addition of other trivial bands preserves the invariant. This allows us to generalize delicate topological insulators characterized by RTP invariants to Hamiltonians with more than two bands, a step that is important for future materialization of delicate topology. For the specific delicate topological invariants, Hopf and RTP, we derive their bulk-boundary correspondence which realizes a novel way of separating non-trivial bands. For instance, the Hopf invariant induces bands carrying opposite Chern numbers on the opposite surfaces of a finite geometry. This corresponds to a spatial separation of bands with opposite Chern numbers, as opposed to energetic separation of such bands in a Chern insulator. The RTP invariant realizes the first example of 'conditionally robust' surface states which are present only at sharp boundaries. Furthermore, we prove that the Hopf and RTP invariants are not completely independent but are related modulo the order of protecting rotation symmetry. This property of delicate topological invariants resembles a similar relation between the Chern number and rotation eigenvalues of stable topological bands. Finally, we discuss an example of a mirror-protected delicate semimetal, showing that the concept of delicate topology can be generalized beyond insulating band structures. Our work on delicate topological phases introduces a new branch in topological band theory and paves the way for further investigation and materialization of delicate topology.

PUBLICATIONS

1. **A. Nelson**, T. Neupert, A. Alexandradinata, and T. Bzdušek, *Delicate Topology Protected by Rotation Symmetry: Crystalline Hopf Insulators and Beyond*. Phys. Rev. B **106**, 075124 (2022)

   Contribution of AN: performed most of the numerical computations and analytical derivatons under the supervision of other co-authors.

2. **A. Nelson**, T. Neupert, T. Bzdušek, and A. Alexandradinata, *Multicellularity of Delicate Topological Insulators*. Phys. Rev. Lett. **126**, 216404 (2021)

   Contribution of AN: performed most of the numerical computations and analytical derivations under the supervision of other co-authors.

3. A. Alexandradinata, **A. Nelson**, and A. A. Soluyanov, *Teleportation of Berry Curvature on the Surface of a Hopf Insulator*. Phys. Rev. B **103**, 045107 (2021)

   Contribution of AN: performed most of the numerical computations under the supervision of other co-authors.

ACKNOWLEDGMENTS

My journey through the world of topological phases of matter started under the guidance of Alexey Soluyanov. I am deeply grateful to Alexey for being so patient in explaining me all the important concepts and for the great sense of humor with which he helped me to overcome the difficulties. Alexey will always remain to me a model of passion for science; despite the serious health problems he continued doing great research. I hope that after Alexey's sudden and tragic death his memory continues living in the work of his colleagues and students, including this thesis.

For the possibility to continue my work after Alexey's demise I am indebted to Titus Neupert, who kindly adopted me in his group and made the transition period as smooth as possible. Throughout these years Titus was extremely encouraging and constantly inspired me with his enthusiasm and broad interests. I am also grateful to Titus for his support with my next career steps and the constructive advices that helped me to determine my path.

Tomáš Bzdušek just started his first senior position in Titus's group when I joined in, and I thank him greatly for becoming my supervisor. Every discussion with Tomáš gave me a huge boost in motivation and illuminating insights into my work. A good scientist must not only conduct research but also effectively disseminate it in the community. Tomáš acted for me as an excellent example of how to make clear and captivating presentations. I am also grateful to Tomáš for all the words of support that he gave me. After starting working with Tomáš I immediately realized how a simple "thank you" for an accomplished work increases the positivity and encourages you to keep going.

I thank Aris Alexandradinata for our joint work throughout my PhD. What started as a small common project, grew into the extensive work that constitutes the present thesis. For this work, Aris was essentially my second supervisor, second in order but not in importance. Aris taught me how to stay mathematically rigorous without forgetting about physics and explained me many mathematical subtleties behind the known physical concepts. I thank Aris for his tolerance to my naive questions when I was a fresh PhD student and for his trust in me when I grew more experienced.

The joy of a PhD journey is greatly determined by the people in the group, and with this I got extremely lucky. I thank all my PhD and postdoc peers for the great atmosphere and lively discussions about work and life. I greatly enjoyed our common trips to conferences and workshops as well as hikes in Swiss mountains. Thank you Arkadiy Davydov, Bartholomew Andrews, Djordje Pantic, Nikita Astrakhantsev, Xiaoxiong Liu, Michael Denner, Patrick Lenggenhager, Anastasiia Skurativska, Bastien Lapierre, Martina Soldini, Kenny Choo, Frank Schindler, Marta Brzezinska, Apoorv Tiwari, Glenn Wagner, Songbo Zhang, Stepan Tsirkin, Luka Trifunovic and Mark Fischer for the great time. At the beginning of my PhD I was lucky to share an office with a group of experimentalists. Thank you Gabriele de Luca, Umar Bashir, Jonathan Spring, Simon Jöhr and Marta Gibert for giving me some idea about real experiments and for the interesting chats over lunches and BBQs.

I thank the members of my PhD committee, Marta Gibert, Oleg Yazyev and Andreas Schilling, for discussing my work on the yearly meetings and asking

interesting questions from a different perspective. I express my thanks to all the administrative staff of our institute for making my stay at the institute so smooth and especially to Gaby Aeppli for processing all the paperwork so promptly. I am also grateful to Patrick Lenggenhager, Michael Denner and Nikita Astrakhantsev for proofreading parts of this thesis and for giving valuable comments.

Finally, I would not manage to complete this path if not all my friends: the wonderful time that I spent with them energized me to continue my work. And of course, the unconditional support and love of my family, my mom Katya, dad Dmitri, sister Natasha and my boyfriend Samuel, helped me to overcome ups and downs of these years and to remain in a good mood.

CONTENTS

Detailed tables of contents can be found at the beginning of each chapter.

1

INTRODUCTION

In mathematics, topology studies properties that are invariant under continuous transformations. Two objects, which can be continuously deformed into each other are thus called topologically equivalent, while if such continuous deformation does not exist, the objects are topologically distinct. To bring some intuition to this concept, let us consider a simple example from everyday life. Imagine looking at a map and trying to find two cities between which we can commute by a car. We can say that these cities must be located on the same island. On the other hand, traveling to a city on a different island requires entering another means of transport which we define as a discontinuous transformation. This construction gives a natural definition of an equivalence class as a set of all cities on the same island; more formally an equivalence class corresponding to a given object consists of all objects that are topologically equivalent to the first one. All elements of an equivalence class share the same topological property (e.g. the name of the hosting island for topologically equivalent cities). Topology has found numerous applications in diverse areas of applied and fundamental sciences. For instance, in robotics the equivalence classes of paths in a space with obstacles are used to efficiently plan the motion of robots [1, 2]. Knot theory, which studies topological equivalence of knots, found its applications in biochemistry in the study of DNA and protein structures [3, 4]. Topology is an important tool in condensed matter physics, where it is used to describe topological defects [5] or spin textures [6–8]. One direction of research which has flourished in the past twenty years is topological band theory [9].

Band theory [10, 11] describes the behavior of electrons in solids, assuming a single-particle picture of weakly-interacting electrons. It predicts the allowed energies of electrons which are called energy bands; these bands are separated by forbidden regions, the gaps, and together they form a band structure. If the Fermi level, indicating the level to which the band structure is filled with electrons, lies inside of a gap, this band structure describes an insulator. Otherwise, if the Fermi level intersects an energy band, it is a metal. In the framework of topological band theory, two insulating band structures are said to belong to the same equivalence class, if the corresponding single-particle Hamiltonians can be continuously deformed into each other without the band gap being closed, in other words without an insulator turning into a metal. This means that topologically distinct insulators are separated by a phase transition across a metallic phase. Every equivalence class of insulating Hamiltonians is characterized by topological invariants, that are computed over the occupied eigenstates and take integer values. A hallmark of a topological insulator is the presence of conducting states localized on its surface [12, 13]; the number of these surface states corresponds to the value of a topological invariant. This relation is known under the name of the bulk-boundary correspondence.

The history of topological band structures dates back to the discovery of the quantum Hall effect [14], which showed plateaus of quantized Hall conductivity as a function of applied magnetic field. A theoretical explanation of this effect was proposed by Halperin [15]. Namely, the bulk electrons in the presence of a magnetic field form flat bands called Landau levels [16]. Assuming that the Fermi level lies between two Landau levels, the bulk of the sample is insulating. At the boundary, the Landau levels asymptotically approach infinite energy and therefore cross the Fermi level. These conducting surface states lead to a quantized Hall conductivity. In agreement with the bulk-boundary correspondence, the bulk Landau levels form a topological band structure and carry a topological invariant, called the Chern number [17]. The concept of topological insulators was finally established (although not yet named so at that time) when Haldane showed that an insulating band structure can carry a non-zero Chern number and host conducting surface states in the absence of an external magnetic field but due to the intrinsic magnetic structure [18].

For a long time, the quantum Hall effect was the only experimental realization of a topological band structure, until a time-reversal symmetric topological insulator was theoretically predicted [13, 19] and then realized in a real material [20, 21]. Crucially, this introduced the notion of symmetry protected topological insulators, which is based on a more relaxed definition of topologically distinct phases. Specifically, two insulators are topologically distinct if any deformation from one to another either closes the band gap or breaks the protecting symmetry, for instance time-reversal symmetry. Within this relaxed definition, topological phases protected by internal symmetries, such as time-reversal, particle-hole or chiral, were studied in different spacial dimensions and their classification was summarized under the so-called periodic table of topological insulators and superconductors [22, 23]. A further relaxation of the definition allowed to study topological insulators protected by crystalline symmetries, such as spatial inversion [24], mirror [25, 26], rotation [27] or non-symmorphic [28] symmetries. The general framework of symmetry indicators and topological quantum chemistry allows to diagnose a topological insulator based on the symmetry representations in its band structure [29–34]. On the one hand, the crystalline topological insulators present more difficulties in observing the bulk-boundary correspondence, as it is only valid at the surfaces that respect the protecting symmetry [24, 25]. On the other hand, their discovery greatly enhanced material realizations of topological insulators [35–40] as crystalline symmetries are widespread in natural materials.

Another important outcome of the symmetry indicators framework was a further refinement of the definition of topological band structures. It was shown [41–43] that topological insulators can be of two types. They are called stable if they remain topological after a set of topological bands is enlarged by adding a trivial electronic band (that carries a zero topological invariant). Otherwise, when insulators become trivial after such enlargement they are called fragile. Many known topological insulators, such as Chern insulators, are stable, while a more relaxed condition on stability of topological bands resulted in novel topological phases [44–46] as well as a reevaluation of the already known models [47, 48]. Examples of fragile topological insulators were found in various meta-materials [49–51] as well as real materials [52]. Although fragile topology does not manifest the same bulk-boundary correspondence as stable topology [47], there are approaches to determine its boundary signatures. For example, in some cases fragile

topological insulators possess fractional corner charges due to the filling anomaly [53]. Alternatively, gapless states appear on their boundary in the presence of twisted boundary conditions [51, 54].

In this thesis, we proceed even further in relaxing the definition of topological band structures and introduce the notion of delicate topology. In order to compare it with fragile topology, we note that a set of topological bands (which are assumed to be occupied in electronic systems) is complemented by a set of empty bands above the Fermi level; together these bands span the entire Hilbert space. The fragile topology, while being trivialized after enlarging the set of occupied bands, is insensitive to the enlargement of the empty bands. Delicate topology, on the contrary, can be trivialized by adding trivial bands to either the set of occupied bands, or to the empty bands. Thus, it manifests an even more relaxed way of defining topological insulators. Although delicate topological insulators are more difficult to realize in experiments, we show that they introduce so far unknown topological invariants and boundary signatures.

The discussion in this thesis is structured as follows. First, in Chapter 2 we review important concepts of the topological band theory that are necessary to understand the new results presented in the following chapters. These results are split into two parts. In Part I, we study a specific example of delicate topological insulators, named crystalline Hopf insulator, which is described by a two-band Hamiltonian over a three-dimensional space and is invariant under rotation symmetry. We assume that all stable topological invariants vanish. We start by considering a continuous momentum model in Chapter 3 and showing that a delicate topological phase can be obtained by gapping a semimetallic phase which acts as a dipole source of Berry curvature. After regularizing the continuous model on a lattice in Chapter 4, we investigate its topological classification and show that the rotation symmetry protects new topological invariants, equal to the differences in electric polarization along rotation-invariant lines. These invariants complement the Hopf invariant which is known to characterize topology of two-band 3D Hamiltonians in the absence of point group symmetries [55]. Viewing momentum components perpendicular to the rotation axis as adiabatic parameters, we see that the polarization difference invariant corresponds to a Thouless pump over half of the adiabatic cycle. In the absence of stable topology, this pump is reverted back on the second half of the cycle, and therefore we name the polarization difference invariant 'returning Thouless pump' (RTP).

For both topological invariants, Hopf and RTP, we derive the bulk-boundary correspondence in Chapter 5. We show that the Hopf invariant manifests in the equal in value Chern number assigned to states localized on the top boundary of a finite sample, while the bottom boundary carries an opposite Chern number. Thus, the Hopf insulator establishes a new way of separating bands with opposite Chern number: in real space. In contrast, in Chern insulators bands with opposite Chern numbers are separated along the energy axis. The RTP invariants induce a similar spatial separation of anomalous symmetry eigenvalues, the so-called angular momentum anomaly. We indicate two consequences of this anomalous behavior. First, the existence of conducting surface states at sharp symmetric boundaries of the crystalline Hopf insulator. Importantly, in the absence of rotation symmetry even the sharp boundaries are generally gapped. Second, anomalous symmetry eigenvalues on the surface result in anomalous Berry-Zak phases computed along specific symmetric paths that take different values from analogous Berry-Zak phases computed for the bulk bands. In Chapter 6,

we further prove that the RTP and the Hopf invariants are not completely independent, namely a specific linear combination of these invariants vanishes modulo the order of the rotation symmetry. This property can be viewed as a delicate topology analog of a similar relation in rotation symmetric Chern insulators; there, the Chern number is related modulo the rotation order to the symmetry eigenvalues of the occupied bands [56].

In Part II we discuss the delicacy of the crystalline Hopf insulators. In Chapter 7, we show that both invariants are destroyed by addition of trivial bands, while the RTP invariants are destroyed only by addition of bands with specific symmetry eigenvalues. This is a manifestation of symmetry-protected delicate topology, which provides a way to generalize this delicate invariant to Hamiltonians with more than two bands. It is known that stable and fragile topology introduce an obstruction to describe an insulator in terms of exponentially localized and locally symmetric Wannier orbitals. We show in Chapter 8, that the studied delicate topological insulators realize a milder obstruction: their Wannier orbitals can be made exponentially localized, but necessarily spread over several unit cells. We call this property multicellularity. Finally, in Chapter 9 we summarize the main results of the thesis and give an outlook on potential future developments in the field.

2

BASICS OF TOPOLOGICAL BAND THEORY

Before presenting the original results of this thesis, we review some concepts of the topological band theory which are important for the following chapters. First, in Sec. 2.1, after specifying the tight-binding notations that are used throughout the thesis, we briefly explain the notions of topologically equivalent and inequivalent insulating Hamiltonians. We illustrate these ideas on the widely known Chern insulator. We also present several methods to distinguish topologically inequivalent Chern insulators, namely by computing their topological invariants called Chern numbers, by studying their Wilson loop spectra or by observing a phase transition across a semimetallic phase. We introduce a real space description of insulators in terms of Wannier orbitals and show that a non-zero Chern number introduces an obstruction to exponentially localize these orbitals in the Chern insulator. Using the same example of the Chern insulator we describe how the bulk topological invariant leads to conducting states localized on the boundary – the bulk-boundary correspondence. Additionally we introduce another topological insulator, the Hopf insulator, which forms the basis for this thesis.

In Sec. 2.2 of this chapter, we overview the role of symmetries in topological phases. On the one hand, symmetry constraints introduce symmetry protected topological invariants. We review the classification of symmetry protected topological phases in 10 classes of internal symmetries and discuss crystalline topological insulators, whose invariants are protected by crystalline symmetries. On the other hand, symmetry eigenvalues of the occupied bands can be used as indicators of existing topological invariants. Topological quantum chemistry provides a tool to determine topological Hamiltonians based on symmetry representations of their valence eigenstates. We briefly overview this method. Topological invariants protected by crystalline symmetry can have different stability under addition of trivial bands; in this sense previous works distinguish between stable and fragile topology, which we introduce in this chapter. Finally, we give a very short outlook on the results of this thesis by discussing delicate topology, which realizes a different level of stability than fragile topology.

CHAPTER CONTENTS

2.1 TOPOLOGICAL INSULATORS

In this thesis, we focus our attention (with a sole exception discussed in Sec. 7.4) on topological properties of insulating Hamiltonians; Fermi level in their band structures lies within a band gap. We define two Hamiltonians with gapped band structures as *topologically equivalent* if they can be deformed into each other without closing the band gap throughout the deformation. If in every possible deformation the band gap necessarily closes, the Hamiltonians are said to be *topologically distinct*.

2.1.1 *Tight-binding formalism*

To formalize this definition we use the *tight-binding formalism* [57–59] in which a solid is described by a set of orbitals $\varphi_{\boldsymbol{R},\alpha} \equiv |\boldsymbol{R},\alpha\rangle\rangle$, labeled by a Bravais lattice vector $\boldsymbol{R} = \sum_{i=1}^{d} n_i \boldsymbol{a}_i$, with d denoting the number of space dimensions, $n_i \in \mathbb{Z}$ and $\boldsymbol{a}_i$ denoting linearly independent primitive translation vectors, and by an index $\alpha = 1, \dots N$ distinguishing N linearly-independent orbitals within a primitive unit cell [cf. Fig. 2.1(a) for an illustration]; $\mathscr{H}$ is the *tight-binding Hilbert space* spanned by $\varphi_{\boldsymbol{R},\alpha}$. The tight-binding Hamiltonian is written in a basis of these orbitals: its diagonal matrix elements describe onsite energies of the corresponding orbitals, while the off-diagonal terms describe the probability that an electron hops from one orbital to another.

According to the Bloch theorem [10, 11], discrete translational symmetry makes the crystal momentum $\boldsymbol{k}$ a good quantum number that is used to index the Bloch states (in this thesis we use the units where $\hbar = e = c = 1$ and identify the wave vector $\boldsymbol{k}$ with the crystal momentum $\hbar\boldsymbol{k}$). Momenta $\boldsymbol{k}$ are defined up to a reciprocal lattice vector $\boldsymbol{G}_i$, determined from the primitive translation vectors as $\boldsymbol{a}_i \cdot \boldsymbol{G}_j = 2\pi\delta_{ij}$, such that all unique momenta form the *Brillouin zone (BZ)* [illustrated in Fig. 2.1(b)]. It is convenient to write the tight-binding Hamiltonian in the $\boldsymbol{k}$-dependent basis that spans the same tight-binding Hilbert space $\mathscr{H}$:

$$|\boldsymbol{k},\alpha\rangle\rangle = \sum_{\boldsymbol{R}} e^{i\boldsymbol{k}\cdot(\boldsymbol{R}+\boldsymbol{r}_\alpha)} |\boldsymbol{R},\alpha\rangle\rangle, \tag{2.1}$$

with the choice of gauge that explicitly includes the spatial information about the basis orbitals in terms of their positions $\boldsymbol{r}_\alpha$ within a representative unit cell [60]. This choice of gauge allows assigning a physical meaning to geometric quantities computed for Hamiltonian eigenstates over momentum space; more precisely, the 2π-normalized Berry-Zak phase defined in the further discussion in Eq. (2.30) can be interpreted as an electric polarization, as we elaborate in Sec. 2.1.4.2. In the introduced $\boldsymbol{k}$-dependent basis we can define the *Bloch eigenstates* to be

$$|\psi_{j,\boldsymbol{k}}\rangle\rangle = \sum_{\alpha} u_j^\alpha(\boldsymbol{k}) |\boldsymbol{k},\alpha\rangle\rangle, \tag{2.2}$$

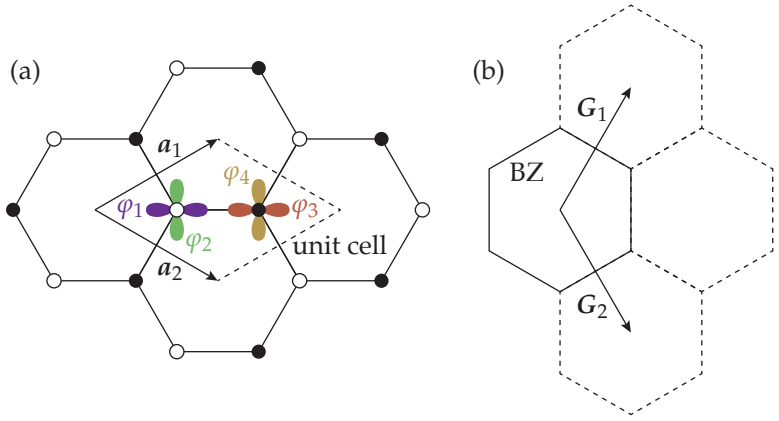

Figure 2.1: (a) Bravais lattice in 2-dimensional space given by the primitive translation vectors $\boldsymbol{a}_1$, $\boldsymbol{a}_2$. Linearly independent orbitals φ_i, $i = 1, \dots 4$ are illustrated within the primitive unit cell. (b) Crystal momentum $\boldsymbol{k}$ is defined over the BZ and is invariant under translation by reciprocal lattice vectors $\boldsymbol{G}_1$, $\boldsymbol{G}_2$.

where the coefficients in front of the basis states form the eigenvectors of the Hamiltonian matrix $h(\boldsymbol{k})$:

$$h(\boldsymbol{k}) \left|u_j(\boldsymbol{k})\right\rangle = E_j(\boldsymbol{k}) \left|u_j(\boldsymbol{k})\right\rangle . \tag{2.3}$$

Note that both the tight-binding Hamiltonian $h(\boldsymbol{k})$ and its eigenvectors $\left|u_j(\boldsymbol{k})\right\rangle$ are defined in the *intra-cell Hilbert space* $\mathscr{H}_{\text{cell}}$, which is spanned by basis orbitals lying within one primitive unit cell $\varphi_\alpha \equiv |\alpha\rangle$ for $\alpha = 1, \dots N$. To distinguish the states living in the larger vs. the smaller Hilbert space, we denote them with different bra/ket symbols, i.e.,

$$|A\rangle\rangle \in \mathscr{H} \qquad \text{vs.} \qquad |A\rangle \in \mathscr{H}_{\text{cell}}. \tag{2.4}$$

The corresponding inner products are similarly denoted as $\langle\langle A|B\rangle\rangle$ vs. $\langle A|B\rangle$.

Because of the gauge convention in Eq. (2.1), the tight-binding Hamiltonian and its eigenvectors $\left|u_j(\boldsymbol{k})\right\rangle$ are $\boldsymbol{k}$-aperiodic for generic values of $\boldsymbol{r}_\alpha$ [60]. In particular, the Hamiltonian transforms under translation by a reciprocal lattice vector $\boldsymbol{G}$ as

$$h(\boldsymbol{k} + \boldsymbol{G}) = V(\boldsymbol{G})^{-1} h(\boldsymbol{k}) V(\boldsymbol{G}), \tag{2.5}$$

$$[V(\boldsymbol{G})]_{\alpha\beta} = \exp(i\boldsymbol{G} \cdot \boldsymbol{r}_\alpha)\delta_{\alpha\beta}. \tag{2.6}$$

At the same time the Bloch function

$$\psi_{j,k}(\boldsymbol{R}, \alpha) = \left\langle\left\langle \boldsymbol{R}, \alpha \middle| \psi_{j,k} \right\rangle\right\rangle = e^{i\boldsymbol{k}\cdot(\boldsymbol{R}+\boldsymbol{r}_\alpha)} u_j^\alpha(\boldsymbol{k}), \tag{2.7}$$

can be chosen to be $\boldsymbol{k}$-periodic, as the non-periodicity of the intra-cell component of the Bloch function $u_j^\alpha(\boldsymbol{k})$ and the plane wave cancel each other. Assuming a periodic gauge of the Bloch functions $\psi_{j,k}$, aperiodicity of the intra-cell component can be expressed as

$$u_j^\alpha(\boldsymbol{k} + \boldsymbol{G}) = e^{-i\boldsymbol{G}\cdot\boldsymbol{r}_\alpha} u_j^\alpha(\boldsymbol{k}). \tag{2.8}$$

An alternative gauge convention deals with strictly $\boldsymbol{k}$-periodic Hamiltonians and intra-cell wave functions by choosing the $\boldsymbol{k}$-dependent basis to be

$$|\widetilde{\boldsymbol{k}, \alpha}\rangle\rangle = \sum_{\boldsymbol{R}} e^{i\boldsymbol{k}\cdot\boldsymbol{R}} \left|\boldsymbol{R}, \alpha\right\rangle\rangle. \tag{2.9}$$

In this case the Hamiltonian and the intra-cell wave functions are periodic in $\boldsymbol{k}$ (assuming that the full Bloch function is periodic in $\boldsymbol{k}$):

$$\begin{aligned}&\tilde{h}(\boldsymbol{k})\left|\tilde{u}_j(\boldsymbol{k})\right\rangle = E_j(\boldsymbol{k})\left|\tilde{u}_j(\boldsymbol{k})\right\rangle,\\ &\tilde{h}(\boldsymbol{k}+\boldsymbol{G}) = \tilde{h}(\boldsymbol{k}), \quad \left|\tilde{u}_j(\boldsymbol{k}+\boldsymbol{G})\right\rangle = \left|\tilde{u}_j(\boldsymbol{k})\right\rangle.\end{aligned} \tag{2.10}$$

The Hamiltonians and the intra-cell wave functions in the two conventions are related by

$$h(\boldsymbol{k}) = V(\boldsymbol{k})^{-1}\tilde{h}(\boldsymbol{k})V(\boldsymbol{k}), \tag{2.11a}$$

$$\left|u_j(\boldsymbol{k})\right\rangle = V(\boldsymbol{k})^{-1}\left|\tilde{u}_j(\boldsymbol{k})\right\rangle, \tag{2.11b}$$

where in Eq. (2.11b) we assumed a periodic gauge of the Bloch functions $\psi_{j,\boldsymbol{k}}$. Although this convention does not allow to interpret the Berry-Zak phase in terms of electric polarization, we will use it in some parts of the thesis to provide a geometrical meaning to the discussed topological invariants. As the relation between the two conventions is known, we will be able to show for the studied topological insulators that the topological invariants coincide in both conventions, and hence, the corresponding Hamiltonians are topologically equivalent.

2.1.2 *Topological equivalence*

In the just introduced tight-binding formalism, the band structures are given by tight-binding eigenenergies $\{E_j(\boldsymbol{k})\}_{j=1,\dots N}$ that are functions of momentum $\boldsymbol{k} \in \mathrm{BZ}$. We assume N_v valence bands to be filled with electrons and the rest $N_c = N - N_v$ conduction bands to be empty. The studied band structure describes an insulator if the gap between the top-most valence band $E_{N_v}(\boldsymbol{k})$ and the lower-most conduction band $E_{N_v+1}(\boldsymbol{k})$ is non-zero for all $\boldsymbol{k} \in \mathrm{BZ}$, $\Delta(\boldsymbol{k}) = E_{N_v+1}(\boldsymbol{k}) - E_{N_v}(\boldsymbol{k}) \neq 0$. An example of an insulating band structure is shown in Fig. 2.2(a). All gapped Hamiltonians $h(\boldsymbol{k}) = \sum_{j=1}^{N}\left|u_j(\boldsymbol{k})\right\rangle E_j(\boldsymbol{k})\left\langle u_j(\boldsymbol{k})\right|$, with $E_{N_v+1}(\boldsymbol{k}) - E_{N_v}(\boldsymbol{k}) \neq 0$, that can be deformed into each other in such a way that their gap never closes throughout the deformation are said to be *topologically equivalent* [9]. All gapped Hamiltonians are characterized by a topological invariant – an integer-valued quantity computed using the valence eigenvectors $\left|u_j(\boldsymbol{k})\right\rangle$, $j = 1, \dots N_v$. The topological invariant takes the same value for all Hamiltonians belonging to the same topological equivalence class and takes different values for Hamiltonians that are *topologically inequivalent*. In the following we present two examples of topological insulators, the Chern insulator in Sec. 2.1.3 and the Hopf insulator in Sec. 2.1.6, and define the corresponding topological invariants.

Before we do this, let us remark that in some situations, discussion of topological properties and invariants can be simplified if a given model Hamiltonian $h(\boldsymbol{k})$ is replaced by a topologically equivalent to it Hamiltonian $h_{\mathrm{flat}}(\boldsymbol{k})$ with a *flattened spectrum*. All valence eigenenergies of the flattened Hamiltonian are equal to -1, while all conduction eigenenergies are $+1$ [cf. Fig. 2.2(b) for illustration]. To see that for every gapped Hamiltonian there exists a topologically equivalent flattened Hamiltonian, consider a deformation, in which all eigenvectors $\left|u_j(\boldsymbol{k})\right\rangle$ remain unchanged, while all valence eigenenergies are continuously deformed to -1 and all conduction eigenenergies to $+1$. Clearly, the gap never closes throughout this deforma-

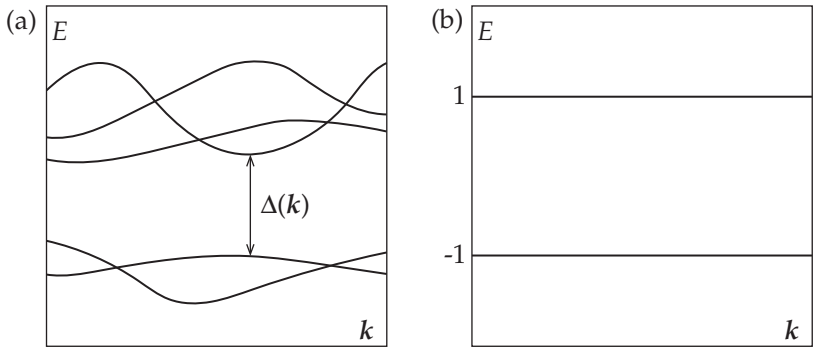

Figure 2.2: (a) Example of an insulating band structure with a non-zero band gap $\Delta(\boldsymbol{k})$ at all $\boldsymbol{k} \in$ BZ. (b) Band structure of a flattened Hamiltonian with all valence (conduction) eigenenergies being -1 ($+1$). If the eigenstates corresponding to the bands in panels (a) and (b) are the same, the corresponding Hamiltonians are topologically equivalent.

tion, and hence the Hamiltonians are topologically equivalent. The original and flattened Hamiltonians can be expressed as

$$h(\boldsymbol{k}) = \sum_{j=1}^{N} \left|u_j(\boldsymbol{k})\right\rangle E_j(\boldsymbol{k}) \left\langle u_j(\boldsymbol{k})\right|,$$
$$h_{\text{flat}}(\boldsymbol{k}) = \mathbb{1} - 2\sum_{j=1}^{N_v} \left|u_j(\boldsymbol{k})\right\rangle \left\langle u_j(\boldsymbol{k})\right|, \tag{2.12}$$

where $\mathbb{1}$ is a $N \times N$ unit matrix.

2.1.3 *Chern insulators*

2.1.3.1 *Lattice model*

To illustrate the notions of a topological insulator and a characterizing it topological invariant, we consider an example of a *Chern insulator* which can be defined in 2D space. At the beginning, we focus on the simplest two-band model at half filling defined on a square lattice with a lattice constant $a = 1$ [61]. In a $\boldsymbol{k}$-dependent basis the Hamiltonian is given by

$$h(\boldsymbol{k}) = \sin k_x\, \sigma_x + \sin k_y\, \sigma_y + (M + \cos k_x + \cos k_y)\sigma_z, \tag{2.13}$$

where $k_x \in [-\pi, \pi]$ and $k_y \in [-\pi, \pi]$ cover the 2D BZ, σ_i for $i = x, y, z$ are Pauli matrices and M is a continuous tuning parameter. We may ask, which parameter intervals define topologically equivalent Hamiltonians? First, we obtain the band structure by computing the eigenenergies of the model

$$E_\pm = \pm\sqrt{\sin^2 k_x + \sin^2 k_y + (M + \cos k_x + \cos k_y)^2}. \tag{2.14}$$

At half filling the lower band is filled with electrons, and the upper is empty [in the following we denote the valence (resp. conduction) band with the subscript v (resp. c)]. The gap between these two bands closes at critical parameter values $M = -2, 0, 2$, meaning that for M between two neighboring critical values, the corresponding Hamiltonians are deformable into each other without closing the band gap and are therefore topologically equivalent. This means that the characterizing topological invariant takes the

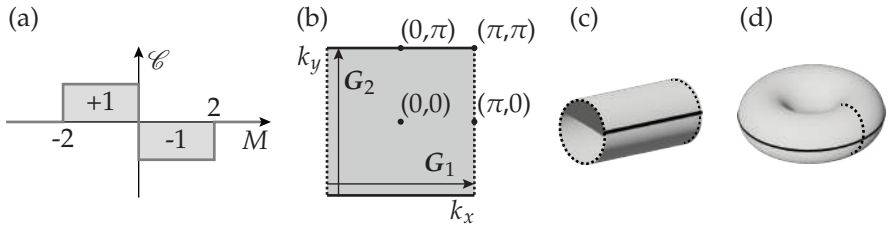

Figure 2.3: (a) Phase diagram of the Chern insulator given by the Hamiltonian in Eq. (2.13). The model describes two topological phases with Chern number $\mathscr{C} = +1$ for parameters in the interval $M \in (-2, 0)$ and $\mathscr{C} = -1$ for $M \in (0, 2)$. (b) Brillouin zone of a 2D Chern insulator (2.13); the edges of the BZ that are separated by a reciprocal lattice vector $\boldsymbol{G}_i$ are pairwise identified (denoted by solid black lines resp. dashed black lines). (c) When the BZ is folded to glue two edges denoted by solid lines it forms a cylinder. (d) After the second folding and glueing the dashed edges the BZ forms a 2D torus.

same value for these Hamiltonians. This invariant is called the *Chern number* and is defined as an integral over the entire BZ of a geometrical quantity $\mathcal{F}_{xy}(\boldsymbol{k})$ called the *Berry curvature*

$$\mathscr{C} = \int_{\mathrm{BZ}} \frac{d^2\boldsymbol{k}}{2\pi}\, \mathcal{F}_{xy}(\boldsymbol{k}). \tag{2.15}$$

The Berry curvature in its turn is defined via the *Berry connection* $\boldsymbol{\mathcal{A}}(\boldsymbol{k})$ computed for a given valence eigenvector $|u_v(\boldsymbol{k})\rangle$ as:

$$\mathcal{F}_{xy}(\boldsymbol{k}) = \partial_x \mathcal{A}_y(\boldsymbol{k}) - \partial_y \mathcal{A}_x(\boldsymbol{k}), \tag{2.16a}$$
$$\mathcal{A}_\mu(\boldsymbol{k}) = i \left\langle u_v(\boldsymbol{k}) \middle| \partial_\mu u_v(\boldsymbol{k}) \right\rangle. \tag{2.16b}$$

Importantly, Berry curvature is a gauge invariant quantity, meaning that it does not change if the eigenvector undergoes a gauge transformation $|u_v(\boldsymbol{k})\rangle \to e^{i\beta(\boldsymbol{k})} |u_v(\boldsymbol{k})\rangle$, and therefore the Chern number is also gauge invariant. Computing the Chern number for the given model (2.13) as a function of the tuning parameter M we get a phase diagram presented in Fig. 2.3(a). We see that indeed the Chern number is constant within every interval bounded by the critical parameter values and it changes its value when the Hamiltonian is tuned across a gapless phase. We call an insulator *topological* if it carries a non-zero value of the characterizing topological invariant, the Chern number in the considered example, and call an insulator *trivial* if all characterizing topological invariants are zero.

Before we discuss how the Chern number can be defined in a more general case not limited to two energy bands, let us show how a two-band model provides an intuitive geometrical meaning for the Chern number. For this, it is convenient to use the convention for the $\boldsymbol{k}$-dependent basis, in which the Hamiltonian is periodic (2.9); recall that the Hamiltonians in periodic and non-periodic conventions are related by Eq. (2.11). We note that the Berry curvature (2.16a) is generally different in the two conventions [62]. Nevertheless, the difference integrated over the BZ vanishes, leading to the same Chern number in both conventions. This means that the two Hamiltonians in different conventions are topologically equivalent.

Every two-band gapped periodic-in-$\boldsymbol{k}$ Hamiltonian can be written in the form

$$\tilde{h}(\boldsymbol{k}) = E_v(\boldsymbol{k}) \left|\tilde{u}_v(\boldsymbol{k})\right\rangle \left\langle\tilde{u}_v(\boldsymbol{k})\right| + E_c(\boldsymbol{k}) \left|\tilde{u}_c(\boldsymbol{k})\right\rangle \left\langle\tilde{u}_c(\boldsymbol{k})\right|. \tag{2.17}$$

To recognize a geometrical meaning of the Chern number, it is convenient to flatten the energy spectrum and get a topologically equivalent Hamiltonian

$$\tilde{h}_{\text{flat}}(\boldsymbol{k}) = \mathbb{1} - 2\,|\tilde{u}_v(\boldsymbol{k})\rangle\,\langle\tilde{u}_v(\boldsymbol{k})|\,. \tag{2.18}$$

We see that a two-band Hamiltonian is defined by $|\tilde{u}_v(\boldsymbol{k})\rangle$, a spinor living on the Bloch sphere S^2. At the same time, the BZ is topologically equivalent to a 2D torus [63]. This follows from the periodicity of the Hamiltonian in the reciprocal space, which allows us to identify a momentum shifted by a reciprocal lattice vector with itself, $\boldsymbol{k} + \boldsymbol{G}_1 \equiv \boldsymbol{k}$ and $\boldsymbol{k} + \boldsymbol{G}_2 \equiv \boldsymbol{k}$. In Fig. 2.3(b-d) we illustrate how the BZ, whose edges are pairwise identified, folds into a torus. With these geometrical observations, the Hamiltonian $\tilde{h}_{\text{flat}}(\boldsymbol{k})$ can be viewed as a map from the 2D torus to the Bloch sphere. Since the torus does not have a boundary, its image on the Bloch sphere does not have a boundary too. Therefore, the torus wraps around the sphere integer number of times; no deformation of the Hamiltonian map that does not close the band gap can change the wrapping number. We conclude, that this wrapping number defines the topological invariant for the map $\tilde{h}_{\text{flat}}(\boldsymbol{k})$, which is nothing else but the Chern number [17]. The geometrical meaning of the Chern number suggests an intuitive explanation of its quantization.

The Chern number is not limited to two-band models and can be defined for N_v valence bands separated by a gap from the conduction bands. For this we need to introduce a *non-Abelian Berry connection* computed between different eigenstates in the valence subspace [64, 65]

$$\mathcal{A}_\mu^{jj'}(\boldsymbol{k}) = i\left\langle u_j(\boldsymbol{k})\middle|\partial_\mu u_{j'}(\boldsymbol{k})\right\rangle. \tag{2.19}$$

Corresponding *non-Abelian Berry curvature* is defined as

$$\mathcal{F}_{\mu\nu}^{jj'} = \partial_\mu \mathcal{A}_\nu^{jj'} - \partial_\nu \mathcal{A}_\mu^{jj'} - i[\mathcal{A}_\mu^{jj'}, \mathcal{A}_\nu^{jj'}], \tag{2.20}$$

where we implicitly assume the dependence on $\boldsymbol{k}$. The Chern number of all valence bands is defined as

$$\mathscr{C} = \int_{\text{BZ}} \frac{d^2\boldsymbol{k}}{2\pi}\ \text{Tr}\,\mathcal{F}_{xy}(\boldsymbol{k}), \tag{2.21}$$

where Tr denotes the trace over the valence band indices $j, j' \in 1, \ldots N_v$. After some manipulations with the Berry curvature trace, the Chern number can be rewritten as a sum of individual contributions from all valence bands

$$\mathscr{C} = \sum_{j=1}^{N_v} \int_{\text{BZ}} \frac{d^2\boldsymbol{k}}{2\pi}\left[\partial_x \mathcal{A}_y^{jj} - \partial_y \mathcal{A}_x^{jj}\right]. \tag{2.22}$$

Importantly, each single contribution from an eigenvector with index j is not quantized to an integer. Nevertheless, the sum over all valence bands results in an integer-valued invariant. The necessary condition for the Chern number of a set of bands to be well-defined and quantized is the energetic separation of these bands from other bands in the spectrum. The multi-band Chern number also has a geometrical meaning. It says how many times the BZ wraps around the manifold formed by all multi-band flattened Hamiltonians [66]. Due to the larger number of bands this manifold is more complicated than the simple Bloch sphere and is described by a mathematical object called Grassmannian [67]. The maps from the BZ torus to the Grassmannian are characterized by homotopy groups [63].

2.1.3.2 *Continuous momentum expansion*

In this section we discuss in more details what happens at the topological phase transition when the band gap closes and the Chern number changes its value. For this we focus on the phase transition that happens at $M = -2$, during which the band gap closes at $\boldsymbol{k} = (0, 0)$ [cf. Fig. 2.3(b) for the BZ]. It turns out that to determine the change in the Chern number it is enough to consider the behavior of the model at momenta $\boldsymbol{k}$ in the vicinity of the band touching point. We can claim that this single band touching point is responsible for the entire change in the Chern number computed over the entire BZ, as at other momenta far from $\boldsymbol{k} = (0, 0)$ the gap remains open throughout the entire deformation [61].

Expanding the lattice Hamiltonian at small momenta $\boldsymbol{k} = (0, 0) + \boldsymbol{\kappa}$ and parameter value $M = -2 + m$ we get the $\boldsymbol{k} \cdot \boldsymbol{p}$ *Hamiltonian*

$$h(\boldsymbol{\kappa}) = \kappa_x \sigma_x + \kappa_y \sigma_y + m\sigma_z, \tag{2.23}$$

which takes the form of a Dirac Hamiltonian with a mass term m and a continuous momentum $\boldsymbol{\kappa} \in \mathbb{R}^2$. As expected, the $\boldsymbol{k} \cdot \boldsymbol{p}$ Hamiltonian is gapless at $m = 0$ and has a band gap for $m < 0$ and $m > 0$.

Contribution to the Chern number from the vicinity of the band touching point can be quantified by a *continuous Chern number* defined as

$$\mathscr{C}^{\text{cont.}} = \int_{\mathbb{R}^2} \frac{d^2\boldsymbol{\kappa}}{2\pi} \mathcal{F}_{xy}(\boldsymbol{\kappa}), \tag{2.24}$$

with the Berry curvature calculated for the valence eigenvector of the $\boldsymbol{k} \cdot \boldsymbol{p}$ Hamiltonian (2.23). After diagonalizing Eq. (2.23) and computing the Berry curvature using Eq. (2.16) we get

$$\mathcal{F}_{xy}(\boldsymbol{\kappa}) = \frac{m}{2(m^2 + \boldsymbol{\kappa}^2)^{3/2}}, \tag{2.25}$$

which integrated over $\mathbb{R}^2$ gives the continuous Chern number

$$\mathscr{C}^{\text{cont.}} = \frac{\operatorname{sgn} m}{2}. \tag{2.26}$$

We note that the value of the continuous Chern number is not quantized, which is the consequence of integration over part of the BZ. Contributions from the Berry curvature at momenta far away from the band touching point comprise the missing values. Adding these values to the continuous Chern number results in an integer. Despite a non-quantized value, Eq. (2.26) immediately shows that the band touching at $\boldsymbol{k} = (0, 0)$ at parameter value $M = -2$ changes the Chern number by $\mathscr{C}^{\text{cont.}}[m > 0] - \mathscr{C}^{\text{cont.}}[m < 0] = 1$ and therefore intermediates a trivial phase at $M < -2$ and a topological phase at $M > -2$.

Following the tuning parameter M we perform the same analysis at $M = 0$, where the bands touch at two momenta $\boldsymbol{k} = (0, \pi)$ and $(\pi, 0)$. Expanding the Hamiltonian in the vicinity of each of them we see that each contributes a change in the Chern number by -1 resulting in the total change by -2. Finally, at $M = 2$ the band touching point at $\boldsymbol{k} = (\pi, \pi)$ changes the Chern number by 1 resulting in a topologically trivial phase with Chern number $\mathscr{C} = 0$.

The introduced method of determining the change in the topological invariant by expanding the lattice Hamiltonian at small momenta is universal. In this thesis, we use it to determine the change in delicate topological invariants, as presented in details in Chapter 3.

2.1.3.3 *Berry-Zak phase*

In this section we reformulate the Chern number in terms of *Berry-Zak phases* which is an important concept for this thesis. Additionally, this will allow us to determine a physical meaning of the Chern number as a a quantized charge pump over an adiabatic cycle, called the Thouless pump, as we discuss in the later Sec. 2.1.4.3.

We start by rewriting the Chern number given in Eq. (2.15) as an integral over the BZ of a curl of the Berry connection

$$\mathscr{C} = \int_{\mathrm{BZ}} \frac{d^2\boldsymbol{k}}{2\pi} \left[\nabla_{\boldsymbol{k}} \times \boldsymbol{\mathcal{A}}(\boldsymbol{k})\right]_z . \tag{2.27}$$

Applying the Stokes' theorem [68] we can express it as an integral of the Berry connection over the BZ border

$$\mathscr{C} = \frac{1}{2\pi} \int_{\partial \mathrm{BZ}} d\boldsymbol{k} \cdot \boldsymbol{\mathcal{A}}(\boldsymbol{k}) = \frac{1}{2\pi} \left[\int_{\gamma_1} + \int_{\gamma_2+\boldsymbol{G}_1} - \int_{\gamma_1+\boldsymbol{G}_2} - \int_{\gamma_2} \right] d\boldsymbol{k} \cdot \boldsymbol{\mathcal{A}}(\boldsymbol{k}), \tag{2.28}$$

where $\gamma_{1(2)}$ denote a path along the reciprocal vector $\boldsymbol{G}_{1(2)}$ as specified in Fig. 2.4(a). At this moment we need to make a remark that the Berry connection itself is not gauge-invariant, and to compute the Chern number using Eq. (2.28) we need to fix the gauge to be smooth over the BZ. Moreover, the gauge of the valence eigenvector can be chosen smooth over the BZ and also periodic with respect to one reciprocal lattice vector [69], let us choose it to be $\boldsymbol{G}_2$. Then the integral of the Berry connection over paths γ_1 and $\gamma_1 + \boldsymbol{G}_2$ cancel each other and we arrive at the Chern number

$$\mathscr{C} = \frac{1}{2\pi} \int_{\gamma_2} d\boldsymbol{k} \cdot \boldsymbol{\mathcal{A}}(\boldsymbol{k} + \boldsymbol{G}_1) - \frac{1}{2\pi} \int_{\gamma_2} d\boldsymbol{k} \cdot \boldsymbol{\mathcal{A}}(\boldsymbol{k}), \tag{2.29}$$

expressed as a difference between two quantities called Berry-Zak phases. Importantly, a Berry-Zak phase, defined as an integral of the Berry connection over a closed loop γ in the BZ [70, 71]

$$\mathscr{Z}_\gamma = \int_{\gamma} d\boldsymbol{k} \cdot \boldsymbol{\mathcal{A}}(\boldsymbol{k}), \tag{2.30}$$

is a gauge invariant quantity, defined modulo 2π. Periodicity of gauge-invariant quantities over the BZ ensures that two Berry-Zak phases computed along the opposite edges of the BZ may differ by an integer multiple of 2π. This agrees with the fact that the Chern number is quantized to integers. Note that ambiguity of the Berry-Zak phase by 2π does not contradict the fact that the difference in Eq. (2.29) is well defined without any ambiguity. Indeed, this difference is fixed given that the valence eigenvector has a smooth gauge over the entire BZ. In other words, the Chern number measures how the Berry-Zak phase computed along a line parallel to the reciprocal vector $\boldsymbol{G}_2$ changes when this line advances in the direction of $\boldsymbol{G}_1$ while keeping the gauge smooth [cf. Fig. 2.4(b) for illustration]. Note, that if one can find a gauge that is smooth and periodic over the BZ (with periodicity in both directions), the Berry-Zak phases computed along related by a reciprocal vector paths are equal to each other, and hence the Chern number computed using Eq. (2.29) vanishes. This shows that a non-zero Chern number introduces an *obstruction to find a smooth and periodic gauge* [72]. This leads to an obstruction to describe

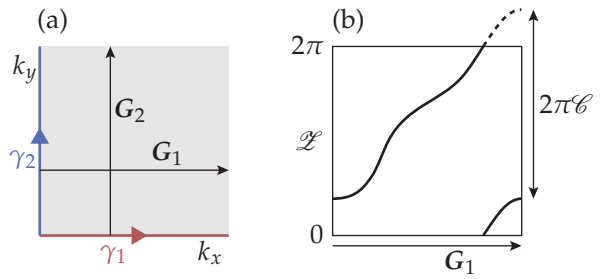

Figure 2.4: (a) Two closed paths in the BZ parallel to reciprocal lattice vectors $\boldsymbol{G}_1$ and $\boldsymbol{G}_2$ are denoted by red (γ_1) and blue (γ_2) oriented lines, respectively. (b) Berry-Zak phase $\mathscr{Y}$ computed along a path parallel to $\boldsymbol{G}_2$ as a function of momentum k_x along $\boldsymbol{G}_1$. The winding number of the Berry-Zak phase normalized by 2π gives the Chern number.

a Chern insulator in terms of exponentially localized orbitals in real space as will be discussed in Sec. 2.1.4.1.

Berry-Zak phases can as well be defined for a set of N_v valence bands. For this, one defines a *Wilson loop* as a path ordered exponent of the Berry connection integral along a closed loop in the BZ [73]

$$\mathcal{W}_\gamma = \hat{\mathrm{T}} \exp\left[i \int_\gamma d\boldsymbol{k} \cdot \boldsymbol{\mathcal{A}} \right], \tag{2.31}$$

where $\hat{\mathrm{T}}$ is the path-ordering operator and $\boldsymbol{\mathcal{A}}$ is the non-Abelian Berry connection defined for N_v valence bands in Eq. (2.19). Berry-Zak phases of the valence bands are defined as phases of the Wilson loop eigenvalues. The Chern number of these bands can be computed in analogy with Eq. (2.29) by summing up the contribution from all Berry-Zak phases. It can be equivalently expressed in terms of Wilson loops as

$$\mathscr{C} = \frac{1}{2\pi} \left[\mathrm{Im} \log \det \mathcal{W}_{\gamma_2 + \boldsymbol{G}_1} - \mathrm{Im} \log \det \mathcal{W}_{\gamma_2} \right]. \tag{2.32}$$

2.1.4 *Real space picture*

2.1.4.1 *Wannier orbitals*

So far we described topological insulators in momentum space in terms of Bloch functions. However, solids allow for an alternative description in terms of *Wannier orbitals* – linear combinations of the Bloch functions localized in real space [60, 74]. As we will see by the end of this section, the Wannier description of topological insulators differs from that of trivial insulators. To construct a Wannier orbital we gather Bloch functions at all momenta in the BZ and take the Fourier transform

$$\begin{aligned} W_{j,\bar{\boldsymbol{R}}}(\boldsymbol{R}, \alpha) &= \int \frac{d^d \boldsymbol{k}}{|\mathrm{BZ}|} e^{-i\boldsymbol{k}\cdot\bar{\boldsymbol{R}}} \psi_{j,\boldsymbol{k}}(\boldsymbol{R}, \alpha) \\ &= \int \frac{d^d \boldsymbol{k}}{|\mathrm{BZ}|} e^{-i\boldsymbol{k}\cdot(\bar{\boldsymbol{R}} - \boldsymbol{R} - \boldsymbol{r}_\alpha)} u_j^\alpha(\boldsymbol{k}), \end{aligned} \tag{2.33}$$

where d denotes the number of spatial dimensions and $|\mathrm{BZ}|$ denotes the volume of the Brillouin zone. The Wannier orbitals in the tight-binding formalism are defined over a set of discrete sites (specified by a Bravais

vector $\boldsymbol{R}$ and a position of the basis orbital $\boldsymbol{r}_\alpha$) rather than over continuous space. Wannier orbitals with different indices $\bar{\boldsymbol{R}}$ are related to each other by a lattice translation. With the normalization $\left\langle u_j(\boldsymbol{k}) \middle| u_{j'}(\boldsymbol{k}) \right\rangle = \delta_{jj'}$ it follows that the Wannier orbitals are orthonormal $\langle\langle W_{j,\bar{\boldsymbol{R}}} | W_{j',\bar{\boldsymbol{R}}'} \rangle\rangle = \delta_{jj'}\delta_{\bar{\boldsymbol{R}},\bar{\boldsymbol{R}}'}$.

The Wannier orbitals are not uniquely defined and depend on the gauge choice of the Bloch functions. The allowed gauge transformations are $u_j^\alpha(\boldsymbol{k}) \to e^{i\beta_j(\boldsymbol{k})} u_j^\alpha(\boldsymbol{k})$, where $\beta_j(\boldsymbol{k})$ are real analytic functions that transform under reciprocal lattice translations as $\beta_j(\boldsymbol{k}+\boldsymbol{G}) = \beta_j(\boldsymbol{k}) + 2\pi l$ with $l \in \mathbb{Z}$. When $\beta(\boldsymbol{k})$ does not wind around the BZ, meaning $l = 0$, the spread of the Wannier orbital may change, but its positional center remains fixed. If, on contrary, $\beta(\boldsymbol{k})$ winds in the direction of $\boldsymbol{G}_1$ with $l \neq 0$ (so-called large gauge transformation), the center of the Wannier orbital will shift in the direction of the corresponding lattice vector $\boldsymbol{R}_1$ (with $\boldsymbol{G}_1 \cdot \boldsymbol{R}_1 = 1$) by l unit cells.

One may ask for a Wannier orbital computed using Eq. (2.33), how well is it localized. If the gauge of the Bloch function $\psi_{j,\boldsymbol{k}}(\boldsymbol{R},\alpha)$ can be chosen to be smooth and periodic over the entire BZ, the Wannier orbital, as a Fourier transform of a smooth and periodic function is necessarily exponentially localized. In this case, Marzari and Vanderbilt proposed a method to find a gauge in which the Wannier orbitals are maximally localized [75, 76]. As was discussed in Sec. 2.1.3.3, a non-zero Chern number imposes an obstruction to find a smooth and periodic gauge for the valence Bloch function. Therefore, the Wannier orbitals of the Chern insulator decay at most polynomially from their charge center [72, 77]. As we will outline in Sec. 2.2.3, the obstruction to construct exponentially localized Wannier orbitals is also present for symmetry protected topological insulators (defined in Sec. 2.2) if the sought Wannier orbitals are required to respect the protecting symmetry [31, 78, 79]. However, delicate topological insulators, which are the topic of this thesis, manifest a milder form of obstruction. Their Wannier orbitals are exponentially localized but can not be compressed within one unit cell. A more detailed discussion is presented in Sec. 2.2.5 and Chapter 8.

Independent of the value of a topological invariant, it is always possible to find a gauge that is smooth and periodic in one direction, for example along k_x, while it can exhibit gauge discontinuities in other directions, generally denoted as $\boldsymbol{k}_\perp$ and called a *reduced momentum*. [We call the BZ projection which is spanned by reduced momenta $\boldsymbol{k}_\perp$ the *reduced Brillouin zone (rBZ)*.] We utilize this gauge and construct a *hybrid Bloch-Wannier function* [80, 81] that is exponentially localized as a Wannier orbital in x direction and remains delocalized as a Bloch function in $\boldsymbol{k}_\perp$ direction. For this the Bloch functions are Fourier transformed only in k_x direction:

$$\begin{aligned}\mathcal{V}_{j,\bar{R}_x,\boldsymbol{k}_\perp}(R_x,\boldsymbol{k}_\perp,\alpha) &= \frac{a_x}{2\pi}\int_{-\pi/a_x}^{\pi/a_x} dk_x e^{-ik_x\bar{R}_x}\psi_{j,\boldsymbol{k}}(R_x,\boldsymbol{k}_\perp,\alpha) \\ &= \frac{a_x}{2\pi}\int_{-\pi/a_x}^{\pi/a_x} dk_x e^{-ik_x(\bar{R}_x-R_x-x^\alpha)} u_j^\alpha(\boldsymbol{k}), \end{aligned} \tag{2.34}$$

where a_x is the lattice constant in x direction. In this expression, we for simplicity assumed a lattice, whose primitive translation vectors are orthogonal to each other. Equation (2.34) can be generalized to the case of non-orthogonal translation vectors [60] but this generalization is not relevant for this thesis.

2.1.4.2 *Electric polarization*

The momentum space quantities discussed in Sec. 2.1.3.3 have a direct relation to real-space properties of the Wannier orbitals. This introduces additional physical meaning to the Berry-Zak phases and the Chern number. To simplify the discussion in this section, we assume a topological insulator to be defined on a lattice given by d orthogonal primitive translation vectors and with lattice constants a_i, $i = 1, \dots d$ in these directions. The BZ in this case is spanned by d momentum components, taking values in intervals $[-\pi/a_i, \pi/a_i]$.

The main result of the geometric theory of polarization [82–85] says that the normalized BZ integral of the Berry connection is related, modulo a Bravais-lattice vector, to the position of the *charge center* of the corresponding Wannier orbital, with the charge center given by the expectation value of the discrete position operator:

$$\int \frac{d^d\boldsymbol{k}}{|\mathrm{BZ}|} \langle u(\boldsymbol{k})|i\nabla_{\boldsymbol{k}} u(\boldsymbol{k})\rangle =_{\boldsymbol{R}} \langle\langle W_{\boldsymbol{0}}|\, \boldsymbol{\mathcal{R}}\, |W_{\boldsymbol{0}}\rangle\rangle, \tag{2.35}$$

where '$=_{\boldsymbol{R}}$' means 'equal modulo Bravais lattice vector'. In the tight-binding basis, the discrete position operator can be decomposed as:

$$\boldsymbol{\mathcal{R}} = \sum_{\boldsymbol{R},\alpha} |\boldsymbol{R},\alpha\rangle\rangle(\boldsymbol{R}+\boldsymbol{r}_\alpha)\langle\langle \boldsymbol{R},\alpha|, \tag{2.36}$$

with $\boldsymbol{r}_\alpha$ being an intra-cell position coordinate of the orbital α. To simplify the notation, we dropped the band index j from both the Bloch and the Wannier state. Equation (2.35) is a tight-binding analog of the expression derived in Refs. [83, 86] for Bloch/Wannier functions defined over continuous real space. Importantly, Eq. (2.35) only holds with $u^\alpha(\boldsymbol{k})$ satisfying the transformation relation given by (2.8), which implies that $u(\boldsymbol{k})$ is aperiodic in reciprocal-lattice translations for generic values of $\boldsymbol{r}_\alpha$.

Details 2.1 To prove Eq. (2.35), we use the definition of the Wannier function [Eq. (2.33)] and explicitly allow for a gauge transformation $u^\alpha(\boldsymbol{k}) \to e^{i\beta(\boldsymbol{k})}u^\alpha(\boldsymbol{k})$. Then

$$\begin{aligned}
\langle\langle W_{\boldsymbol{0}}|\boldsymbol{\mathcal{R}}|W_{\boldsymbol{0}}\rangle\rangle &= \sum_{\boldsymbol{R},\alpha} \overline{W_{\boldsymbol{0}}(\boldsymbol{R},\alpha)}(\boldsymbol{R}+\boldsymbol{r}_\alpha)W_{\boldsymbol{0}}(\boldsymbol{R},\alpha) = \\
&= \int \frac{d^3\boldsymbol{k}d^3\boldsymbol{k}'}{|\mathrm{BZ}|^2} \sum_{\boldsymbol{R},\alpha} \overline{u^\alpha(\boldsymbol{k})} e^{-i\beta(\boldsymbol{k})-i\boldsymbol{k}(\boldsymbol{R}+\boldsymbol{r}_\alpha)}(\boldsymbol{R}+\boldsymbol{r}_\alpha) \\
&\qquad \times e^{i\boldsymbol{k}'(\boldsymbol{R}+\boldsymbol{r}_\alpha)+i\beta(\boldsymbol{k}')}u^\alpha(\boldsymbol{k}') \\
&= \int \frac{d^3\boldsymbol{k}d^3\boldsymbol{k}'}{|\mathrm{BZ}|^2} \sum_{\boldsymbol{R},\alpha} \overline{u^\alpha(\boldsymbol{k})} e^{-i\beta(\boldsymbol{k})-i\boldsymbol{k}\cdot(\boldsymbol{R}+\boldsymbol{r}_\alpha)}[-i\nabla_{\boldsymbol{k}'}e^{i\boldsymbol{k}'\cdot(\boldsymbol{R}+\boldsymbol{r}_\alpha)}] \\
&\qquad \times e^{i\beta(\boldsymbol{k}')}u^\alpha(\boldsymbol{k}').
\end{aligned} \tag{2.37}$$

Because $\psi_{\boldsymbol{k}'}$ and any gauge function $e^{i\beta(\boldsymbol{k}')}$ are periodic-in-$\boldsymbol{k}'$ by construction, one may integrate by parts without acquiring a boundary term:

$$\begin{aligned}
(2.37) = \int \frac{d^3\boldsymbol{k}d^3\boldsymbol{k}'}{|\mathrm{BZ}|^2} \sum_{\boldsymbol{R},\alpha} \overline{u^\alpha(\boldsymbol{k})} e^{-i\boldsymbol{k}(\boldsymbol{R}+\boldsymbol{r}_\alpha)-i\beta(\boldsymbol{k})}e^{i\boldsymbol{k}'(\boldsymbol{R}+\boldsymbol{r}_\alpha)+i\beta(\boldsymbol{k}')} \\
\times \left[i\nabla_{\boldsymbol{k}'}u^\alpha(\boldsymbol{k}') - u^\alpha(\boldsymbol{k}')\nabla_{\boldsymbol{k}'}\beta(\boldsymbol{k}')\right].
\end{aligned} \tag{2.38}$$

After carrying out the sum over $\boldsymbol{R}$ with the Dirac-delta-function identity:

$$\sum_{\boldsymbol{R}} e^{i\boldsymbol{k}\cdot\boldsymbol{R}} = |\mathrm{BZ}|\, \delta(\boldsymbol{k}), \tag{2.39}$$

we get

$$(2.38) = \int \frac{d^3\boldsymbol{k}}{|\mathrm{BZ}|} \left[\langle u(\boldsymbol{k})|i\nabla_{\boldsymbol{k}}u(\boldsymbol{k})\rangle - \nabla_{\boldsymbol{k}}\beta(\boldsymbol{k})\right], \tag{2.40}$$

where the first term gives the desired relation (2.35) and the second term introduces a modulo-$\boldsymbol{R}$ ambiguity, as the gauge phase $\beta(\boldsymbol{k})$ can (in principle) wind nontrivially over the Brillouin torus.

The sum over charge centers of all valence bands can be interpreted (in the units with $e = 1$) as the *electric polarization* of the solid, which in the geometric theory of polarization takes the form:

$$\mathscr{P} =_{\boldsymbol{R}} \sum_{j=1}^{N_v} \left\langle \left\langle W_{j,\boldsymbol{0}} \right| \boldsymbol{\mathcal{R}} \left| W_{j,\boldsymbol{0}} \right\rangle \right\rangle \overset{\text{Eq. (2.35)}}{=_{\boldsymbol{R}}} \sum_{j=1}^{N_v} \int \frac{d^d\boldsymbol{k}}{|\mathrm{BZ}|} \left\langle u_j(\boldsymbol{k}) \middle| i\nabla_{\boldsymbol{k}} u_j(\boldsymbol{k}) \right\rangle . \quad (2.41)$$

An analogous to Eq. (2.35) relation connects the Berry-Zak phase with the charge center of a hybrid Bloch-Wannier function

$$\frac{a_x}{2\pi} \int dk_x \left\langle u_j(\boldsymbol{k}) \middle| i\partial_x u_j(\boldsymbol{k}) \right\rangle =_{a_x} \left\langle \left\langle \mathcal{V}_{j,0,\boldsymbol{k}_\perp} \right| P_{\boldsymbol{k}_\perp} \hat{x} P_{\boldsymbol{k}_\perp} \left| \mathcal{V}_{j,0,\boldsymbol{k}_\perp} \right\rangle \right\rangle, \quad (2.42)$$

$$P_{\boldsymbol{k}_\perp} = \sum_{R_x,\alpha} |R_x, \boldsymbol{k}_\perp, \alpha\rangle\rangle \langle\langle R_x, \boldsymbol{k}_\perp, \alpha| ,$$

where $\hat{x}$ is a component of the discrete position operator $\boldsymbol{\mathcal{R}} = (\hat{x}, \hat{y}, \dots)$ and $P_{\boldsymbol{k}_\perp}$ is the projector onto the Hilbert space sector with momentum $\boldsymbol{k}_\perp \in \mathrm{rBZ}$. Note that the charge center of a hybrid Bloch-Wannier function depends on the reduced momentum $\boldsymbol{k}_\perp$, along which the function is delocalized. If we view $\boldsymbol{k}_\perp$ as external parameters and the Hamiltonian $h(k_x, \boldsymbol{k}_\perp)$ as an effectively 1D Hamiltonian, the Berry-Zak phase computed for a valence eigenvector of this Hamiltonian (along the only momentum k_x) is equal modulo the lattice constant to the charge center of the corresponding 1D Wannier orbital. The sum over charge centers of all valence Bloch-Wannier functions can be interpreted as an electric polarization of the 1D Hamiltonian and we get

$$\mathscr{P}_x(\boldsymbol{k}_\perp) =_{a_x} \frac{a_x}{2\pi} \sum_{j=1}^{N_v} \int dk_x \mathcal{A}_x(\boldsymbol{k}). \quad (2.43)$$

2.1.4.3 *Thouless pump*

The relation (2.43) introduced in the previous section provides additional physical interpretation to the Chern number. As we showed in Sec. 2.1.3.3, the Chern number can be expressed as a difference in Berry-Zak phases computed along opposite edges of the BZ and summed over all valence eigenvectors [cf. Eq. (2.32)]. Again, we interprete the Chern Hamiltonian (defined on a rectangular lattice) as a 1D Hamiltonian that depends on momentum k_y, while k_x is viewed as a cyclic adiabatic parameter. Then the Chern number is expressed as a change in 1D polarization while the adiabatic parameter goes over the full cycle from $-\pi/a_x$ to π/a_x

$$\mathscr{C} = \frac{1}{a_y} \left[\mathscr{P}_y(\pi/a_x) - \mathscr{P}_y(-\pi/a_x) \right] . \quad (2.44)$$

In other words there is a *charge pump* from one unit cell to the neighboring unit cell equal in magnitude to the Chern number, when the adiabatic parameter k_x translates over the full cycle. This charge pump was first studied by Thouless in Ref. [87] and therefore got the name of the *Thouless pump*.

2.1.5 *Bulk-boundary correspondence*

One of the most important observations of the topological band theory is the *bulk-boundary correspondence*, which relates topological invariants computed in the bulk with the topological states on the surface [9, 88, 89]. In the case of

the Chern insulator, this correspondence manifests in *chiral surface states* [15] whose number is equal to the Chern number. These states are dissipationless and robust under surface deformations, and their presence explains the quantum Hall conductivity [14], which is proportional to the Chern number $\sigma_{xy} = \mathscr{C}e^2/h$ [17]. One way to derive the bulk-boundary correspondence is by employing the relation (2.32), which expresses the Chern number via the Berry-Zak phases of the valence bands, and applying the argument presented in Ref. [88]. In this section, we outline this derivation for the Chern insulator, while the argument goes through for other topological insulators as well.

As we already showed in Sec. 2.1.4.2, the Berry-Zak phase computed along the k_x direction is given by the expectation value of the position operator projected onto $\boldsymbol{k}_\perp$ sector of the Hilbert space $P_{\boldsymbol{k}_\perp}\hat{x}P_{\boldsymbol{k}_\perp}$ [cf. Eq. (2.42)]. A stronger statement is true, namely the Berry-Zak phases of all valence eigenvectors define the spectrum of the position operator projected onto the valence subspace with momentum $\boldsymbol{k}_\perp$ [90, 91]

$$P_{v,\boldsymbol{k}_\perp}\hat{x}P_{v,\boldsymbol{k}_\perp}, \tag{2.45}$$

with the corresponding projector expressed in terms of Bloch or hybrid Bloch-Wannier functions as

$$P_{v,\boldsymbol{k}_\perp} = \sum_{j=1}^{N_v}\sum_{R_x} |\mathcal{V}_{j,R_x,\boldsymbol{k}_\perp}\rangle\rangle\langle\langle \mathcal{V}_{j,R_x,\boldsymbol{k}_\perp}| = \sum_{j=1}^{N_v}\int dk_x \frac{a_x}{2\pi} |\psi_{j,\boldsymbol{k}}\rangle\rangle\langle\langle\psi_{j,\boldsymbol{k}}|. \tag{2.46}$$

The eigenvectors of the projected position operator are the hybrid Bloch-Wannier states defined in Eq. (2.34)

$$P_{v,\boldsymbol{k}_\perp}\hat{x}P_{v,\boldsymbol{k}_\perp}|\mathcal{V}_{j,R_x,\boldsymbol{k}_\perp}\rangle\rangle = [\bar{x}_j(\boldsymbol{k}_\perp) + R_x]|\mathcal{V}_{j,R_x,\boldsymbol{k}_\perp}\rangle\rangle, \quad \text{for } j = 1,\dots N_v, \tag{2.47}$$

and the eigenvalues are related modulo the lattice constant to the Berry-Zak phase of the corresponding Bloch function $\bar{x}_j(\boldsymbol{k}_\perp) =_{a_x} \frac{a_x}{2\pi}\int dk_x \mathcal{A}^j_x(\boldsymbol{k})$. The projected position operator is symmetric under discrete translations by a lattice constant a_x in x direction. Therefore, if $\bar{x}(\boldsymbol{k}_\perp)$ is its eigenvalue then $\bar{x}(\boldsymbol{k}_\perp) + R_x$ for $R_x = na_x$, $n \in \mathbb{Z}$ is also its eigenvalue. The eigenvalues of the projected position operator form a ladder-like structure illustrated in Fig. 2.5(a).

A non-zero value of the Chern number ensures a protected spectral flow in each unit cell of this ladder structure, namely that $\mathscr{C}$ equals to the net number of eigenvalues that shift by one unit cell while momentum k_y changes by minus a reciprocal vector [an illustration for $\mathscr{C} = 1$ is shown in Fig. 2.5(a)]. Note, that the minus sign in the change in k_y appears as we flipped the role of momentum components k_x and k_y comparing to Eq. (2.44) for the Chern number. It was shown in Ref. [88] that the spectrum of the projected position operator can be continuously deformed to the energy spectrum of a flattened Hamiltonian with a single boundary; this semi-infinite geometry is illustrated in Fig. 2.5(b). After such deformation, the eigenvalues $\bar{x}_j(k_y) + R_x$ that are positioned in unit cells within the Chern insulator or outside of it (labeled by $|R_x| \geq 1$) are mapped onto the bulk energy eigenvalues of the flattened spectrum ± 1, while the eigenvalues $\bar{x}_j(k_y)$ at the boundary unit cell (labeled by $R_x = 0$) are mapped onto the boundary spectrum. Therefore, the protected spectral flow in the projected position operator spectrum corresponds to protected chiral surface states that interpolate between the valence and the conduction band. The energy spectrum obtained after the deformation is illustrated in Fig. 2.5(c). The number of the surface bands equals to the Chern number.

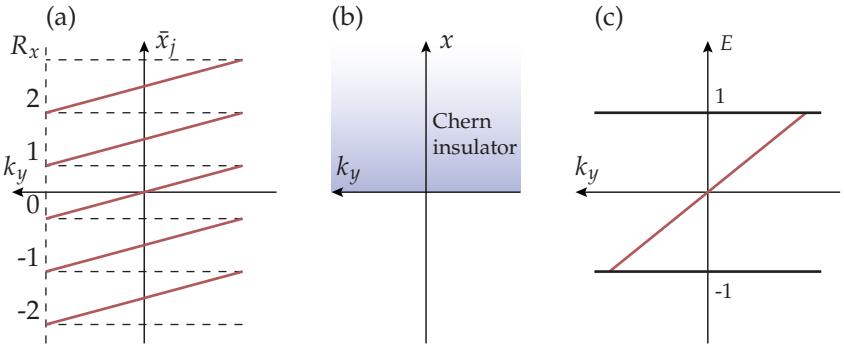

Figure 2.5: (a) Spectrum of the projected position operator $P_{v,k_y}\hat{x}P_{v,k_y}$ of a Chern insulator with Chern number $\mathscr{C} = 1$. In every unit cell (labeled by R_x) the eigenvalues exhibit a spectral flow when momentum k_y moves over the BZ. (b) Semi-infinite geometry of a Chern insulator with a boundary at $x = 0$. (c) Spectrum of a flattened semi-infinite Chern Hamiltonian. Number of chiral surface states (red line) equals to the Chern number. According to Ref. [88], projected position operator spectrum (a) can be continuously deformed to a semi-infinite Chern insulator energy spectrum (c). This proves the bulk-boundary correspondence for the Chern insulator.

2.1.6 *Hopf insulators*

In this section we present another example of a topological insulator that is particularly important for this thesis: the *Hopf insulator*, defined over a 3D space [55, 92, 93]. Contrary to the Chern insulators, that are defined for an arbitrary number of bands, the Hopf insulators are restricted to two-band Hamiltonians, with a single valence and a single conduction bands separated by a gap. This impossibility to enlarge the Hilbert space by adding another valence or conduction band while keeping the topological invariant well-defined is a defining property of *delicate topology*, a crucial concept of this thesis. The differences between delicate topology and the established notions of stable and fragile topology are briefly discussed in Sec. 2.2.5, while Chapter 7 in Part II of this thesis presents our results on delicate topology in details.

2.1.6.1 *Topological classification*

To see why a two band 3D Hamiltonian is topological, recall from the discussion in Sec. 2.1.3.1 that a two-band Hamiltonian with a flattened spectrum can be viewed as a map from the BZ to the Bloch sphere spanned by the valence eigenvector $|\tilde{u}_v(\boldsymbol{k})\rangle$. Here, we again chose the convention for the $\boldsymbol{k}$-dependent basis in which the Hamiltonian is periodic over the BZ; we prove that the Hamiltonians in both conventions are equivalent in the next Sec. 2.1.6.2. In 3D the BZ forms a 3-torus T^3. Is a map from T^3 to S^2 characterized by a topological invariant?

We first answer this question in the case when the Hamiltonian belongs to the trivial first Chern class, meaning that the Chern numbers computed on all 2D subtori of the 3D BZ are zero. In this case, the Hamiltonian can be continuously deformed to have the same value on the boundary of the BZ. In algebraic topology, this allows to identify all points on the boundary of the BZ [94] meaning that the boundary is given by a single point and the BZ forms a sphere S^3. This suggests that a 3D two-band Hamiltonian with a trivial first Chern class is topologically equivalent to a seminal *Hopf map* from S^3 to S^2 studied in mathematics long time ago

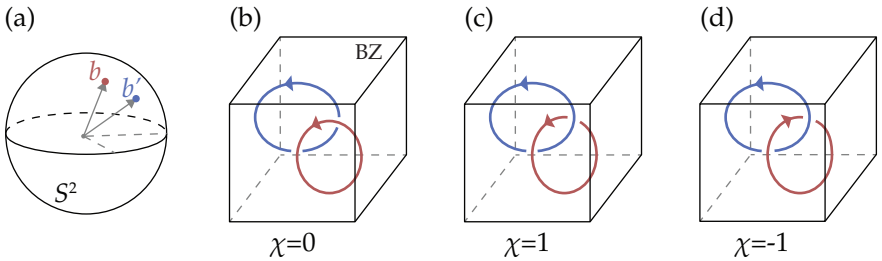

Figure 2.6: Relation between the Hopf invariant and the linking of preimages. (a) The Bloch sphere (S^2) represents the space of (spectrally flattened) gapped two-band Hamiltonians. (b) For a Hamiltonian with trivial Hopf invariant, and for two arbitrarily chosen points on the Bloch sphere: $b, b' \in S^2$ [indicated by red and blue dots on panel (a)], we plot their respective preimages inside the Brillouin zone (black frame), i.e., the collection of momenta $\boldsymbol{k}$ where $h_{\text{flat}}(\boldsymbol{k}) \sim b$ and $h_{\text{flat}}(\boldsymbol{k}) \sim b'$ respectively. We see that the linking number is zero. Panel (c) shows the linked preimages with co-aligned orientations corresponding to a Hamiltonian with the Hopf invariant $\chi = 1$. On panel (d) the linked preimages have counter-aligned orientation and the Hopf invariant is $\chi = -1$. The definition of the preimage orientation is given in Sec. 6.5.2.

[95]. To formulate the geometric invariant which characterizes topology of this map, we notice that a set of points that is mapped onto a single point on the Bloch sphere generically forms a 1D loop; this follows from the difference between dimensions of the two manifolds S^3 and S^2. Therefore, preimages of two distinct points on the Bloch sphere form two loops, which can link with each other [cf. Fig. 2.6]. At the same time this link can not be removed by a continuous deformation, since the two loops are mapped onto different points on the sphere and hence can not cross. Thus, we conclude that the *linking number* of two preimage loops is a topological invariant which characterizes the Hopf map [93, 95, 96]; it is called the *Hopf invariant* and is denoted by χ. The sign of the linking number depends on the relative orientations of the preimages [cf. Fig. 2.6(c,d)]. The procedure to define these orientations is described in details in Sec. 6.5.2.

The linking number gives a geometric intuition for the Hopf invariant, however, it is not very useful for numerical computations. Wilczek and Zee showed that the Hopf invariant can be computed as an integral of the *Chern-Simons form* over the map domain, which is the BZ for the Hopf Hamiltonian:

$$\chi = \frac{1}{4\pi} \int_{\text{BZ}} d^3k \, \boldsymbol{\mathcal{F}} \cdot \boldsymbol{\mathcal{A}}, \tag{2.48}$$

where the Berry connection vector is computed for the valence band $|\tilde{u}_v(\boldsymbol{k})\rangle$ using Eq. (2.16b) and the Berry curvature pseudovector is defined as

$$\mathcal{F}_\mu = \epsilon_{\mu\nu\lambda} \partial_\nu \mathcal{A}_\lambda, \tag{2.49}$$

where ϵ is the fully antisymmetric Levi-Civita symbol.[1] Importantly, although the Chern-Simons form $\boldsymbol{\mathcal{F}} \cdot \boldsymbol{\mathcal{A}} \, d^3k$ is not gauge-invariant, the Hopf invariant of a two-band Hamiltonian (2.48) is gauge invariant. The same integral computed for a more-than-two-band Hamiltonian loses its gauge-invariance which renders the Hopf invariant ill-defined. From this follows, that discrete translational symmetry is necessary to protect topology of the Hopf insulator. Indeed, translational symmetry forbids enlargement of the unit cell that

1 Berry curvature $\mathcal{F}_{xy}$ defined in Eq. (2.16a) conicides with the z component of the pseudovector in Eq. (2.49). This relation is discussed in more details in Dets. 2.2.

would lead to an increased number of basis orbitals and hence more than two bands in the Hamiltonian. This is in sharp contrast with the Chern insulator, which is robust under breaking the translational symmetry. This symmetry only acts as a helping tool that allows computing the Chern number over the momentum space (as discussed in Sec. 2.1.3).

How does the topological classification of the Hopf insulator changes if the assumption of the trivial first Chern class is relaxed? This question was answered by Pontrjagin in Ref. [97], where he showed that the topological classification of a map from T^3 to S^2 is given by four invariants. Three of these invariants are the Chern numbers computed on the three 2D subtori of the BZ. The fourth invariant is an integer number defined modulo twice the greater common divisor of the three Chern numbers [98, 99]. In the case when all the three Chern numbers are zero, the fourth invariant coincides with the Hopf invariant (2.48) defined modulo nothing. In this thesis, we restrict ourselves to Hamiltonians with a trivial first Chern class and will only discuss the Hopf invariant (2.48).

2.1.6.2 *Equivalence of the Hopf invariant in periodic and non-periodic tight-binding Hamiltonian*

So far, we assumed the $\boldsymbol{k}$-dependent basis convention in which the Hopf Hamiltonian is periodic over the BZ. Finally, let us show that the Hopf invariant, defined using Eq. (2.48) is quantized also in the non-periodic tight-binding Hamiltonian convention, and that it takes the same value in both conventions: $\chi[u(\boldsymbol{k})] = \chi[\tilde{u}(\boldsymbol{k})]$.

In order to appreciate this, we consider a continuous interpolation between Hamiltonians in the periodic and non-periodic conventions and show that the Hopf invariant is quantized throughout the interpolation, and therefore does not change. The desired interpolation parametrized by a real variable $t \in [0,1]$ is given by

$$h(\boldsymbol{k},t) = V(t\boldsymbol{k})^{-1}\tilde{h}(\boldsymbol{k})V(t\boldsymbol{k}), \tag{2.50}$$

which satisfies $h(\boldsymbol{k},0) = \tilde{h}(\boldsymbol{k})$ (periodic) and $h(\boldsymbol{k},1) = h(\boldsymbol{k})$ (non-periodic) with $[V(t\boldsymbol{k})]_{\alpha\beta} = \exp(it\boldsymbol{k}\cdot\boldsymbol{r}_\alpha)\delta_{\alpha\beta}$. One can view this interpolation as a continuous shift of the basis orbitals from the spatial origin within the unit cell to their actual positions $\boldsymbol{r}_\alpha$. Throughout this interpolation, both the energy spectrum and the translational symmetry are invariant; the spectral invariance implies that the assumed gap does not close.

Crucially, the Chern-Simons form $\boldsymbol{\mathcal{F}}\cdot\boldsymbol{\mathcal{A}}\,d^3k$ remains $\boldsymbol{k}$-periodic for any $t \in [0,1]$. To see this, take into account the relation between intra-cell wave functions throughout the interpolation

$$u(\boldsymbol{k},t) = V(t\boldsymbol{k})^{-1}\tilde{u}(\boldsymbol{k}). \tag{2.51}$$

This implies that the Berry connections are related as

$$\begin{aligned}\boldsymbol{\mathcal{A}}[u(\boldsymbol{k},t)] &= \langle u(\boldsymbol{k},t)|i\nabla_{\boldsymbol{k}}u(\boldsymbol{k},t)\rangle \\ &= \boldsymbol{\mathcal{A}}[\tilde{u}(\boldsymbol{k})] + t\,\langle\tilde{u}(\boldsymbol{k})|\,\hat{\boldsymbol{r}}\,|\tilde{u}(\boldsymbol{k})\rangle\,,\end{aligned} \tag{2.52}$$

where $[\hat{\boldsymbol{r}}]_{\alpha\beta} = \boldsymbol{r}_\alpha\delta_{\alpha\beta}$ is the matrix with positions of the basis orbitals on the diagonal. The periodicity of $|\tilde{u}(\boldsymbol{k})\rangle$ implies that $\boldsymbol{\mathcal{A}}[u(\boldsymbol{k},t)]$ is periodic-in-$\boldsymbol{k}$ for all $t \in [0,1]$, and hence also its curl $\boldsymbol{\mathcal{F}}$ (the Berry curvature). Therefore the Chern-Simons form is periodic throughout the interpolation.

To derive the difference in the Hopf invariant (computed as an integral of the Chern-Simons form) between the two conventions, we adopt the notation

of differential forms [100]: we take $\mathcal{A} = \boldsymbol{\mathcal{A}} \cdot d\boldsymbol{k}$ to be the Berry connection one-form, and its exterior derivative $\mathcal{F} = d\mathcal{A}$ to be the Berry curvature two-form. The Chern-Simons three-form in these notations can be simply written as $\mathcal{F}\wedge\mathcal{A}$ [see Dets. 2.2 for a componentwise definition of the wedge product]. Now we can write the difference in the Hopf invariants as

$$\begin{aligned}
&\chi[u(\boldsymbol{k})] - \chi[\tilde{u}(\boldsymbol{k})] \\
&\propto \int_{\mathrm{BZ}} \mathcal{F}(\boldsymbol{k},1)\wedge\mathcal{A}(\boldsymbol{k},1) - \int_{\mathrm{BZ}} \mathcal{F}(\boldsymbol{k},0)\wedge\mathcal{A}(\boldsymbol{k},0) \\
&= \int_{\partial(\mathrm{BZ}\times[0,1])} \mathcal{F}(\boldsymbol{k},t)\wedge\mathcal{A}(\boldsymbol{k},t) \\
&= \int_{\mathrm{BZ}\times[0,1]} \mathcal{F}(\boldsymbol{k},t)\wedge\mathcal{F}(\boldsymbol{k},t),
\end{aligned} \tag{2.53}$$

where in the second row we used the just-proven fact that the Chern-Simons form is periodic-in-$\boldsymbol{k}$, and hence its integration over two BZs at $t = 0$ and $t = 1$ taken with opposite orientations can be enlarged to integration over the boundary of $\mathrm{BZ} \times [0, 1]$. In the third row we applied the Stokes' theorem and expressed the external derivative of the Chern-Simons form $d(\mathcal{F} \wedge \mathcal{A}) = \mathcal{F} \wedge \mathcal{F}$, which is proportional to the *second Chern character* $\mathrm{ch}_2(\mathcal{F}) = (1/2!)(i/2\pi)^2\mathcal{F} \wedge \mathcal{F}$ [68]. Importantly, for two-band Hamiltonians the second Chern character vanishes (the proof of this statement is given in Appendix A.2.4), which allows us to conclude that the Hopf invariant does not change and hence remains quantized throughout the interpolation. We conclude that Eq. (2.48) can be used to compute the Hopf invariant in both Bloch conventions.

Details 2.2 Componentwise definition of the wedge product is the following:

$$\mathcal{F} \wedge \mathcal{A} = \frac{3!}{2!\,1!}\mathcal{F}_{[\alpha\beta}\,\mathcal{A}_{\gamma]}\,dx_\alpha\,dx_\beta\,dx_\gamma, \tag{2.54}$$

where $\{x_\alpha\}_{\alpha=1}^3$ are right-handed coordinates on the 3-sphere.

In this definition, our convention to denote objects related to the Berry curvature is as follows: the components of the Berry curvature 2-form are $\mathcal{F}_{\alpha\beta} = \partial_\alpha\mathcal{A}_\beta - \partial_\beta\mathcal{A}_\alpha$ (with two indices), from which one obtains components of the Berry pseudovector (2.49) in 3D as $\mathcal{F}_\alpha = \frac{1}{2}\epsilon_{\alpha\beta\gamma}\mathcal{F}_{\beta\gamma}$ (with a single index). We further use the plain calligraphic symbol $\mathcal{F}$ to indicate the complete Berry curvature 2-form, and the bold version $\boldsymbol{\mathcal{F}}$ to denote the complete Berry curvature pseudovector. Components of the exterior product of a p-form a and q-form b are given by [100]

$$(a \wedge b)_{\alpha\ldots\beta\gamma\ldots\delta} = \frac{(p+q)!}{p!\,q!}a_{[\alpha\ldots\beta}b_{\gamma\ldots\delta]} \tag{2.55}$$

Square brackets around indices indicate the fully antisymmetric component; in particular, we have

$$\mathcal{F}_{[\alpha\beta}\mathcal{A}_{\gamma]} = \frac{1}{3!}\left(\mathcal{F}_{\alpha\beta}\mathcal{A}_\gamma - \mathcal{F}_{\alpha\gamma}\mathcal{A}_\beta + \mathcal{F}_{\beta\gamma}\mathcal{A}_\alpha - \mathcal{F}_{\beta\alpha}\mathcal{A}_\gamma + \mathcal{F}_{\gamma\alpha}\mathcal{A}_\beta - \mathcal{F}_{\gamma\beta}\mathcal{A}_\alpha\right) \tag{2.56}$$

in the case of Eq. (2.54). Note that we do not distinguish between covariant and contravariant indices, and place both in the subscript.

2.2 SYMMETRIES IN TOPOLOGICAL INSULATORS

So far, we considered topological insulators in the absence of any symmetry with a sole exception of the lattice translation symmetry, which is necessary for defining the reciprocal space and the expressions for topological invariants (2.21) and (2.48). We note, that even the translational symmetry is not necessary for defining the Chern insulator and the Chern Hamiltonian with small enough disorder is topologically equivalent to the translationally symmetric Chern Hamiltonian. Nevertheless, symmetries are ubiquitous in

solids and play an important role in topological insulators, as we show in this section.

2.2.1 *Symmetry-protected topological insulators*

Let us consider a set of Hamiltonians that are invariant under some symmetry operation. The symmetry condition restricts this set comparing to the set of all Hamiltonians. Consequently, two Hamiltonians that are equivalent in the absence of symmetries can become topologically inequivalent when the symmetry is present. This happens if the gap-preserving deformation connecting the Hamiltonians passes through a non-symmetric 'sector' of the Hamiltonian set. We define *symmetry-protected topological insulators* that can not be deformed to a trivial insulator without closing the band gap and without breaking the protecting symmetry throughout the deformation. One can distinguish two types of protecting symmetries. The first is *internal symmetries* that are local in space and impose particular constraints on the energy spectrum. The second type is *crystalline symmetries* that act nontrivially in space; they are represented by a unitary matrix and therefore allow to decompose the Hamiltonian into a block structure with each block describing states with specific symmetry eigenvalues. We discuss separately how the two types of symmetries modify the topological classification.

2.2.1.1 *Internal symmetries and the 10-fold way*

Time-reversal symmetry (Θ) is the first example of internal symmetries and it is given by an antiunitary operator. In momentum space it imposes the following constraint on the Hamiltonian

$$\Theta h(\boldsymbol{k})\Theta^{-1} = h(-\boldsymbol{k}), \quad \Theta^2 = \pm 1. \tag{2.57}$$

The time-reversal symmetry squares to $+1$ (resp. -1) for particles with integer (resp. half-integer) spin. When $\Theta^2 = -1$ the eigenstates of the time-reversal symmetric Hamiltonian obey the Kramers theorem [101] and form the Kramers pairs of states with the same energy, related to each other by the reversal of time. In momentum space the states forming a Kramers pair have opposite momenta. Therefore, at time-reversal invariant momenta each energy is doubly degenerate.

So far, when considering gapped single particle Hamiltonians we were referring to them as insulators. At the same time, Bogoliubov-de Gennes (BdG) Hamiltonians of superconductors also form a gapped single-particle spectrum, and therefore, one can study topological classification of BdG Hamiltonians in the same way as of insulators [102]. Due to the redundancy of the BdG basis, BdG Hamiltonians are invariant under the *particle-hole symmetry* ($\mathfrak{P}$), which is another internal symmetry and is given by an antiunitary operator which anticommutes with the Hamiltonian. In momentum space the particle-hole symmetry imposes the following constraint

$$\mathfrak{P} h(\boldsymbol{k})\mathfrak{P}^{-1} = -h(-\boldsymbol{k}), \quad \mathfrak{P}^2 = \pm 1. \tag{2.58}$$

Different sign of the squared particle-hole operator corresponds to different pairing in the superconductor. Particle-hole symmetry guarantees that for every state with energy E and momentum $\boldsymbol{k}$ in the spectrum, there exists a state with opposite energy $-E$ and momentum $-\boldsymbol{k}$.

Finally, the combination of the time-reversal and the particle-hole symmetry called *chiral symmetry* ($\mathfrak{C} = \Theta\mathfrak{P}$) is also an internal symmetry. As a

Table 2.1: Topological classification of insulators and superconductors in 10 Altland-Zirnbauer (AZ) symmetry classes

AZ	symmetry			topological classification for $d =$							
class	Θ^2	$\mathfrak{P}^2$	$\mathfrak{C}^2$	0	1	2	3	4	5	6	7
A	$\times$	$\times$	$\times$	$\mathbb{Z}$	0	$\mathbb{Z}$	0	$\mathbb{Z}$	0	$\mathbb{Z}$	0
AIII	$\times$	$\times$	1	0	$\mathbb{Z}$	0	$\mathbb{Z}$	0	$\mathbb{Z}$	0	$\mathbb{Z}$
AI	$+1$	$\times$	$\times$	$\mathbb{Z}$	0	0	0	$\mathbb{Z}$	0	$\mathbb{Z}_2$	$\mathbb{Z}_2$
BDI	$+1$	$+1$	1	$\mathbb{Z}_2$	$\mathbb{Z}$	0	0	0	$\mathbb{Z}$	0	$\mathbb{Z}_2$
D	$\times$	$+1$	$\times$	$\mathbb{Z}_2$	$\mathbb{Z}_2$	$\mathbb{Z}$	0	0	0	$\mathbb{Z}$	0
DIII	-1	$+1$	1	0	$\mathbb{Z}_2$	$\mathbb{Z}_2$	$\mathbb{Z}$	0	0	0	$\mathbb{Z}$
AII	-1	$\times$	$\times$	$\mathbb{Z}$	0	$\mathbb{Z}_2$	$\mathbb{Z}_2$	$\mathbb{Z}$	0	0	0
CII	-1	-1	1	0	$\mathbb{Z}$	0	$\mathbb{Z}_2$	$\mathbb{Z}_2$	$\mathbb{Z}$	0	0
C	$\times$	-1	$\times$	0	0	$\mathbb{Z}$	0	$\mathbb{Z}_2$	$\mathbb{Z}_2$	$\mathbb{Z}$	0
CI	$+1$	-1	1	0	0	0	$\mathbb{Z}$	0	$\mathbb{Z}_2$	$\mathbb{Z}_2$	$\mathbb{Z}$

product of two antiunitary operators, it is unitary itself and anticommutes with the Hamiltonian. In momentum space it imposes the following constraint

$$\mathfrak{C}h(\boldsymbol{k})\mathfrak{C}^{-1} = -h(\boldsymbol{k}). \tag{2.59}$$

Note, that as a unitary operator the chiral symmetry always squares to $\mathfrak{C}^2 = +1$. A given Hamiltonian can be invariant under chiral symmetry even if both time-reversal and particle-hole symmetries are not obeyed. The spectrum of a chiral symmetric Hamiltonian is symmetric with respect to zero energy.

All possible internal symmetries form 10 *Altland-Zirnbauer symmetry classes* [103, 104]: 9 of them are formed by all possible configurations of the time-reversal and particle-hole symmetries, while an additional class corresponds to chiral symmetry in the absence of time-reversal and particle-hole symmetries. All 10 classes are listed in the first four columns of Table 2.1. A stepping stone in the theory of topological insulators and superconductors was the derivation of a topological classification for gapped single-particle Hamiltonians in all 10 symmetry classes [22, 23], also called the *10-fold way*. This classification was obtained in all d-dimensional spaces. For each symmetry class and space dimension d, the classification predicts the group that is formed by all possible topological invariants. We present this classification in Table 2.1; the classification $\mathbb{Z}$ is given by an integer-valued topological invariant, $\mathbb{Z}_2$ is given by an invariant which takes only two values 0 and 1 (one agrees to call a Hamiltonian carrying a zero invariant trivial and a unit invariant topological), the classification given by 0 implies that no topological invariant can be defined and all Hamiltonians in the corresponding symmetry class and space dimension are topologically equivalent to each other. We can notice that the table has a periodic structure: topological classification of a d-dimensional Hamiltonian in one symmetry class coincides with the topological classification of a $d-1$-dimensional Hamiltonian in a symmetry class specified by the upper row. For this reason, the table was named the *periodic table of topological insulators and superconductors*.

The presented classification includes the Chern insulator, introduced in Sec. 2.1.3. The Chern insulator is defined in a 2-dimensional space in the

absence of any symmetry which corresponds to the Altland-Zirnbauer class A. According to the Table 2.1, the topological classification of this insulator is given by an integer-valued invariant, which is precisely the Chern number defined in Eq. (2.21).

Let us look at the entry in the table that corresponds to a 3D Hamiltonian in the symmetry class A (with no internal symmetry) discussed in Sec. 2.1.6. We see that the topological classification is trivial and no topological invariant can be defined. Does this contradict to the discussion of the Hopf insulators characterized by the Hopf invariant? The answer is no, as the periodic table assumes the freedom to extend the Hilbert space by additional trivial bands (the topological invariants carried by these bands is zero). In this sense, all 3D Hamiltonians in the symmetry class A are topologically equivalent to each other. However, if we restrict the Hamiltonians to have only two bands and do not allow enlarging the Hilbert space, these Hamiltonians are characterized by the Hopf invariant. Therefore, the Hopf insulators are not captured by the 10-fold way classification.

The periodic table 2.1 lists only so-called *strong topological invariants*, the invariants that are intrinsic in the corresponding dimension d and can not be defined in a $< d$-dimensional Hamiltonian of the same symmetry class. As was shown in Ref. [22], in addition to strong topological invariants, a d-dimensional Hamiltonian possesses *weak topological invariants* inherited from all $< d$-dimensional Hamiltonians. For instance, a 3D Hamiltonian in class A is characterized by Chern numbers that are computed on 2-dimensional subtori of its 3-dimensional BZ, these Chern numbers are weak topological invariants. As we discussed in Sec. 2.1.6.1, the presence of these weak Chern numbers alter the topological classification of two-band Hamiltonians; in this thesis we assume all weak Chern numbers of 3D Hamiltonians in class A to be zero.

2.2.1.2 *Crystalline topological insulators*

In addition to the internal symmetries defined in the previous section, a solid may possess crystalline symmetries such as spatial inversion, mirrors and rotations. These symmetries are represented by unitary operators and additionally act nontrivially on the spatial coordinates. In momentum space a crystalline symmetry C constraints the Hamiltonian as

$$R_C h(\boldsymbol{k}) R_C^{-1} = h(C\boldsymbol{k}), \tag{2.60}$$

where R_C denotes the unitary representation of the symmetry C.

Crystalline symmetries can also protect topological invariants giving rise to *crystalline topological insulators* [24–28, 105]. One mechanism for defining such a topological invariant [106] stems from the fact that at C-invariant submanifold of the BZ, i.e. $\{\boldsymbol{k}|C\boldsymbol{k} = \boldsymbol{k} + \boldsymbol{G}\}$, the Hamiltonian commutes with a unitary operator R_C. Therefore it decomposes into a block-diagonal structure with each block describing bands of the same symmetry representation. For valence bands that have a specific symmetry representation on the symmetry-invariant manifold, one can define a topological invariant from Table 2.1, which corresponds to the dimension d of this manifold and the internal symmetry class of the relevant block of the Hamiltonian $h(\boldsymbol{k})$.

To see more clearly how this works, let us present an example of a mirror protected topological invariant, called *mirror Chern number*. This invariant was first introduced in Ref. [25] and later was predicted to protect conducting surface states in SnTe [107]. These predictions were experimentally confirmed

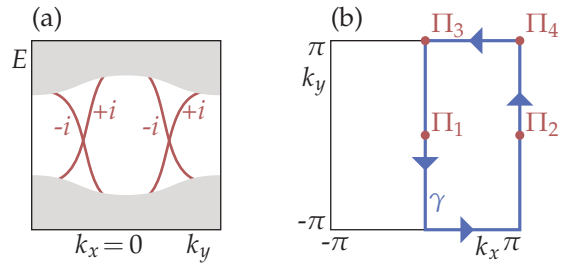

Figure 2.7: (a) Energy spectrum of a 3D mirror Chern insulator finite in z-direction restricted to $k_x = 0$ line. The mirror Chern number is $\mathscr{C}_M = 2$. Gray areas denote the bulk spectrum, while red lines denote the topological surface states protected by mirror symmetry. Mirror eigenvalue of each surface band is shown next to it. (b) BZ of a 2D time-reversal invariant topological insulator. Blue oriented line γ shows the integration path for the $\mathbb{Z}_2$ topological invariant (2.63). The simpler way to compute the invariant in the presence of inversion symmetry is to take a product of inversion eigenvalues at time-reversal invariant momenta Π_i denoted with red points.

in Refs. [35, 108]. To define a mirror Chern number we consider a 3D Hamiltonian that is symmetric under the mirror symmetry with respect to the $(x = 0)$ plane, denoted by M_x. One of the mirror-invariant submanifolds of the BZ forms a 2D plane at $k_x = 0$. At this plane the Hamiltonian is split into two blocks corresponding to mirror eigenvalues $\pm i$, assuming the particles to be spinful. For valence bands in each block we can define a Chern number, which is a suitable topological invariant for 2D Hamiltonians in the symmetry class A

$$\mathscr{C}_M^{\pm} = \int \frac{dk_y dk_z}{2\pi} \operatorname{Tr}\left[\mathcal{F}_v^{\pm}(0, k_y, k_z)\right], \tag{2.61}$$

where the Berry curvature matrix $\mathcal{F}_v^{\pm}$ is computed for all valence bands with mirror eigenvalue $\pm i$. Assuming that the model is additionally symmetric under time-reversal symmetry, all Chern numbers on the 2D cuts of the BZ vanish. Nevertheless, we can still define a topological invariant protected by the mirror symmetry – the mirror Chern number

$$\mathscr{C}_M = (\mathscr{C}_M^{+} - \mathscr{C}_M^{-})/2. \tag{2.62}$$

In Sec. 2.1.5 we saw that a topological invariant computed in the bulk of a topological insulator is reflected in conducting states on the boundary. Crystalline-symmetry-protected topological invariants also feature conducting surface states given that the surface is invariant under the protecting symmetry [106]. In this way, the mirror Chern number fixes the number of counter-propagating chiral modes with different mirror eigenvalues along the $k_x = 0$ line on the boundaries orthogonal to the y and z axes [as illustrated in Fig. 2.7(a) for $\mathscr{C}_M = 2$]. The Dirac crossing of two surface modes is protected by the mirror symmetry and can not be gapped if the symmetry is preserved and the bulk gap remains open. Away from the $k_x = 0$ line the surface is generally gapped, meaning that any boundary that is mapped onto itself by the mirror hosts $|\mathscr{C}_M|$ Dirac points located at a mirror-invariant $\boldsymbol{k}$-line.

2.2.2 *Symmetry indicators*

In the previous section we saw how symmetries, internal and crystalline, can protect topological phases. Crystalline symmetries have another impor-

tant role in topological insulators. Namely, for some topological invariants defined in one of the Altland-Zirnbauer classes of internal symmetries, if the corresponding Hamiltonian is also invariant under particular crystalline symmetry, the symmetry eigenvalues of the valence bands can be used to (partially) determine the topological invariant [24, 56, 109, 110]. First, this simplifies the computation of topological invariants. Second, the idea that information about symmetry eigenvalues can indicate a topological insulator lies in the foundation of the topological quantum chemistry (TQC) (reviewed in Sec. 2.2.3), which massively expanded the amount of known topological materials and led to the discovery of new concepts, such as fragile topology (reviewed in Sec. 2.2.4). We illustrate the idea of *symmetry indicators* on two examples in different symmetry classes.

2.2.2.1 *Inversion symmetry indicates time-reversal protected topological invariant*

First, we consider an example of a topological invariant, that is completely defined by crystalline symmetry eigenvalues. The relevant Hamiltonians are defined in the 2D space and belong to the AII symmetry class with only time-reversal symmetry that squares to $\Theta^2 = -1$. The topological classification of such Hamiltonians is given by a $\mathbb{Z}_2$ invariant. The first model that realizes a *time-reversal symmetric topological insulator* was proposed in Refs. [13, 19] and was subsequently realized in HgTe/CdTe quantum wells [20, 21]. The $\mathbb{Z}_2$ topological invariant is defined as

$$I = \frac{1}{2\pi i} \oint_\gamma d\boldsymbol{k} \cdot \nabla_k \log\left[P(\boldsymbol{k}) + i\delta\right] \mod 2, \tag{2.63}$$

where $P(\boldsymbol{k}) = \mathrm{Pf}[\langle u_i(\boldsymbol{k})|\,\Theta|u_j(\boldsymbol{k})\rangle]$, Pf denotes a Pfaffian, infinitesimally small real number δ is introduced for convergence of the integral and closed loop γ surrounds half of the BZ such that if $\boldsymbol{k}$ is inside of the loop, $-\boldsymbol{k}$ lies outside of it [see blue line in Fig. 2.7(b) illustrating such loop in a square lattice]. Computing the invariant using this formula is not very practical. Although, later Fu and Kane [111] introduced a simpler expression for the time-reversal protected $\mathbb{Z}_2$ invariant in terms of Berry-Zak phases, the simplest way to compute this invariant exists in the presence of the inversion symmetry. As was shown in Ref. [109], the sought invariant can be computed from the inversion eigenvalues of the valence bands at all time-reversal invariant momenta (TRIM) in the BZ

$$\begin{aligned}(-1)^I &= \prod_{i\in\mathrm{TRIM}} \delta_i, \\ \delta_i &= \prod_{j=1}^{N_v/2} \xi_{2j}(\Pi_i),\end{aligned} \tag{2.64}$$

where $\xi_j(\Pi_i)$ is the inversion eigenvalue of a band with index j at a TRIM point $\Pi_i \in$ BZ [red points in Fig. 2.7(b)] and bands with indices $2j-1$ and $2j$ are Kramers partners of each other. We see that the topological invariant is simply the product of the symmetry eigenvalues at specific points in the BZ.

2.2.2.2 *Rotation symmetry indicates Chern number modulo the order of rotation*

Let us consider another example when rotation eigenvalues indicate a nonzero value of the Chern number. In this case, the eigenvalues do not give the full information about the topological invariant and define it only

modulo the order of the rotation symmetry. The discussion in this section closely follows Ref. [56], which derived this result for the first time.

We assume that a single particle 2D Hamiltonian is invariant under the n-fold rotation symmetry C_n, where n can take values $2, 3, 4, 6$ that are compatible with a commensurate lattice. Together with translation symmetries, the rotation symmetry generate the plane group pn, $n = 2, 3, 4, 6$. Rotation symmetry puts the following constraint on the Hamiltonian

$$R_{C_n} h(\boldsymbol{k}) R_{C_n}^{-1} = h(C_n \boldsymbol{k}), \tag{2.65}$$

where R_{C_n} denotes the representation of the rotation symmetry in the space of single-particle Hamiltonians. Within the 2D BZ we can define the high-symmetry momenta, which remain invariant under a symmetry operation from the point group generated by C_n. These are all C_m-invariant momenta, for $1 < m \leq n$ dividing n. For the plane groups pn $= 2, 3, 4, 6$ all high-symmetry momenta are illustrated in Fig. 2.8. At a C_m-invariant momentum, the Hamiltonian obeys the following commutation relation

$$[V(\boldsymbol{G}_{\boldsymbol{k}}) R_{C_m}, h(\boldsymbol{k})] = 0, \tag{2.66}$$

where matrix $V(\boldsymbol{G}_{\boldsymbol{k}})$, $\boldsymbol{G}_{\boldsymbol{k}} = C_m \boldsymbol{k} - \boldsymbol{k}$ defined in Eq. (2.6) accounts for possible non-periodicity of the Hamiltonian under reciprocal lattice translations. This means that the eigenvectors of the Hamiltonian at the C_m-invariant momenta are also the eigenvectors of the *itinerant rotation operator* $V(\boldsymbol{G}_{\boldsymbol{k}}) R_{C_m}$ with eigenvalues

$$\widetilde{\rho}_{m,j}(\boldsymbol{k}) = \left\langle u_j(C_m \boldsymbol{k}) \right| R_{C_m} \left| u_j(\boldsymbol{k}) \right\rangle . \tag{2.67}$$

Fang et. al. in Ref. [56] derived the following expressions for the Chern numbers in terms of these rotation eigenvalues

$$\text{for } C_2\text{:} \quad e^{i\pi \mathscr{C}} = \prod_{j=1}^{N_v} \widetilde{\rho}_{2,j}(\Gamma) \widetilde{\rho}_{2,j}(\mathrm{X}) \widetilde{\rho}_{2,j}(\mathrm{Y}) \widetilde{\rho}_{2,j}(\mathrm{M}), \tag{2.68a}$$

$$\text{for } C_4\text{:} \quad e^{i\pi \mathscr{C}/2} = \prod_{j=1}^{N_v} (-1)^F \widetilde{\rho}_{4,j}(\Gamma) \widetilde{\rho}_{2,j}(\mathrm{X}) \widetilde{\rho}_{4,j}(\mathrm{M}), \tag{2.68b}$$

$$\text{for } C_3\text{:} \quad e^{i2\pi \mathscr{C}/3} = \prod_{j=1}^{N_v} (-1)^F \widetilde{\rho}_{3,j}(\Gamma) \widetilde{\rho}_{3,j}(\mathrm{K}) \widetilde{\rho}_{3,j}(\mathrm{K}'), \tag{2.68c}$$

$$\text{for } C_6\text{:} \quad e^{i\pi \mathscr{C}/3} = \prod_{j=1}^{N_v} (-1)^F \widetilde{\rho}_{6,j}(\Gamma) \widetilde{\rho}_{3,j}(\mathrm{K}) \widetilde{\rho}_{2,j}(\mathrm{M}), \tag{2.68d}$$

where F is equal to twice the spin of the particle. Relation (2.68a) was initially derived in Ref. [24] for inversion as protecting symmetry; in genuinely 2D systems inversion acts in the same way as the two-fold rotation. In Dets. 2.3 for the representative case of C_3 symmetry we outline the derivation of Eq. 2.68 presented in Ref. [56].

Details 2.3 We start proving Eq. (2.68c) by noticing that the trace of the Berry curvature computed for valence states of a C_3 invariant Hamiltonian is itself invariant under C_3 operation:

$$\mathrm{Tr}\left[\mathcal{F}_{xy}(\boldsymbol{k})\right] = \mathrm{Tr}\left[\mathcal{F}_{xy}(C_3 \boldsymbol{k})\right]. \tag{2.69}$$

This means that one third of the Chern number can be computed as the integral of the Berry curvature over one third of the BZ [blue region in Fig. 2.8(c)], which after a series of rotations by $2\pi/3$ reconstructs the entire BZ. Applying the Stokes' theorem to this integral we can re-express it as a line-integral of the Berry connection [the integration path is shown in Fig. 2.8(c) with an oriented blue line]. In the mutli-band case this integral is replaced by the phase of the Wilson loop determinant [cf. Eq. (2.31) for the definition of the Wilson loop]. Then the Chern number is given by

$$e^{i2\pi \mathscr{C}/3} = \det \mathcal{W}_{\Gamma \leftarrow \mathrm{K}'' \leftarrow \mathrm{K}' \leftarrow \mathrm{K} \leftarrow \Gamma}. \tag{2.70}$$

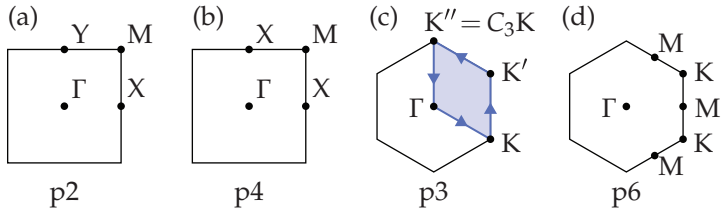

Figure 2.8: Rotation-invariant momenta in the BZ of a Hamiltonian symmetric under (a) p2, (b) p4, (c) p3, or (d) p6 plane group. (c) Blue area denotes one third of the BZ which reconstructs the full BZ after a series of rotations by $2\pi/3$; Berry curvature integrated over this area gives one third of the Chern number. Blue oriented line denotes the path for the Wilson loop operator used in the derivation of Eq. (2.68c).

The path ΓKK′K″Γ consists of four pieces, along each of them one can compute a Wilson line as

$$\mathcal{W}_{\Pi_1\Pi_2} = \hat{\mathrm{T}}\exp\left[i\int_{\Pi_1}^{\Pi_2} d\boldsymbol{k}\cdot\boldsymbol{\mathcal{A}}\right], \tag{2.71}$$

with $\Pi_1, \Pi_2 \in \{\Gamma, \mathrm{K}, \mathrm{K}', \mathrm{K}''\}$. The Wilson loop is given by the product of all sequential Wilson lines

$$e^{i2\pi\mathscr{C}/3} = \det\left[\mathcal{W}_{\Gamma\leftarrow\mathrm{K}''}\mathcal{W}_{\mathrm{K}''\leftarrow\mathrm{K}'}\mathcal{W}_{\mathrm{K}'\leftarrow\mathrm{K}}\mathcal{W}_{\mathrm{K}\leftarrow\Gamma}\right] \tag{2.72}$$

Next, we use how the Wilson line transforms under rotation

$$\mathcal{W}_{C_m\Pi_2\leftarrow C_m\Pi_1} = \hat{\rho}_m(\Pi_2)\mathcal{W}_{\Pi_2\leftarrow\Pi_1}\hat{\rho}_m^{-1}(\Pi_1), \tag{2.73}$$

where by $\hat{\rho}_m(\Pi)$ we denote the diagonal matrix consisting of m-fold rotation eigenvalues at C_m-invariant momentum Π [given by Eq. (2.67)] of all bands included in the Wilson loop; here these are all valence eigenstates of the Hamiltonian. Then

$$\begin{aligned}(2.72) = \det\big[&\hat{\rho}_3(\Gamma)\mathcal{W}_{\Gamma\leftarrow\mathrm{K}}\hat{\rho}_3^{-1}(\mathrm{K})\mathcal{W}_{\mathrm{K}''\leftarrow\mathrm{K}'}\\ &\times\hat{\rho}_3(\mathrm{K}')\mathcal{W}_{\mathrm{K}'\leftarrow\mathrm{K}''}\hat{\rho}_3^{-1}(\mathrm{K}'')\mathcal{W}_{\mathrm{K}\leftarrow\Gamma}\big].\end{aligned} \tag{2.74}$$

Using that determinant of a matrix product is a product of determinants we rewrite

$$(2.74) = \det\left[\hat{\rho}_3(\Gamma)\hat{\rho}_3(\mathrm{K}')\hat{\rho}_3^{-2}(\mathrm{K})\right]\det\left[\mathcal{W}_{\Gamma\leftarrow\mathrm{K}}\mathcal{W}_{\mathrm{K}''\leftarrow\mathrm{K}'}\mathcal{W}_{\mathrm{K}'\leftarrow\mathrm{K}''}\mathcal{W}_{\mathrm{K}\leftarrow\Gamma}\right], \tag{2.75}$$

where we took into account that points K and K″ are equivalent modulo a reciprocal lattice vector and therefore rotation eigenvalues at these points are equal. Expression under the second determinant equals the unity matrix as the Wilson loops computed along the same path in opposite directions cancel each other. In the expression under the first determinant we use that the eigenvalue of the rotation by 2π amounts to the phase factor $(-1)^F$ with $F = 0$ ($F = 1$) for spinless (spinful) particles. Then $\hat{\rho}_3^{-2}(\mathrm{K}) = (-1)^F\hat{\rho}_3(\mathrm{K})$. Explicitly writing the determinant of the diagonal matrices $\hat{\rho}$ as the product of the diagonal elements we get Eq. (2.68c).

2.2.3 *Topological quantum chemistry*

We saw in Secs. 2.2.1.2 and 2.2.2 that crystalline symmetries play a two-fold role in the theory of topological insulators. On the one hand, they can protect new topological invariants, on the other hand they can indicate non-trivial values of existing topological invariants. Looking at the presented case studies, one may ask: given a tight-binding model of a specific material, can we say whether this material is topological by knowing its symmetry space group and how its eigenstates transform under the elements of this group. The answer to this question was given in the framework of the *topological quantum chemistry* (TQC) [29–31] which we overview in this section following Ref. [34].

The main idea behind the TQC is to define a set of all possible band structures (together with the corresponding symmetry representations) that correspond to an *atomic limit* in which the electrons are tightly localized to atomic or molecular orbitals in real space. A given material is topological if

its valence bands can not be decomposed into a direct sum of atomic limits. Next, we formally introduce this method using the mathematical language of *band representations* (BRs) [112, 113]. Before we start, let us emphasize that TQC does not give a complete classification of crystalline topological insulators. It may happen that a non-trivial band structure is compatible with an atomic limit and therefore will be missed by the TQC classification scheme. However, despite being incomplete, TQC has proved its effectiveness in predicting topological materials [37–40] and led to a discovery of such important concepts as higher order topology [114, 115] and fragile topology [41, 43]. The later is important for this thesis and is reviewed in Sec. 2.2.4.

2.2.3.1 *Symmetry groups*

We start by reviewing the most important notions of the group theory. Assume that a studied Hamiltonian is symmetric under operations that form a *space group* $\mathcal{G}$. Each element of this group can be decomposed into a point group operation p (inversion, rotation or mirror) and a translation by a vector $\mathbf{v}$; we use the following notations $g = \{p|\mathbf{v}\} \in \mathcal{G}$. For each point in the real space $\boldsymbol{r}$ we define a *site-symmetry* or *site stabilizer group* $\mathcal{G}_{\boldsymbol{r}} \subset \mathcal{G}$ that consists of symmetry opertations that leave the site $\boldsymbol{r}$ invariant

$$\mathcal{G}_{\boldsymbol{r}} = \{g|g\boldsymbol{r} = \boldsymbol{r}\}. \tag{2.76}$$

We define a *Wyckoff position* to be a set of sites whose stabilizer groups are conjugate to each other. In other words, $\boldsymbol{r}_1$ and $\boldsymbol{r}_2$ belong to the same Wyckoff position if $\exists g \in \mathcal{G}$ such that $g\mathcal{G}_{\boldsymbol{r}_1}g^{-1} = \mathcal{G}_{\boldsymbol{r}_2}$. Site stabilizer groups of all sites in the same Wyckoff position are isomorphic to each other and also to some point group. We call a Wyckoff position *maximal* if its site-symmetry group is not a subgroup of any other site-symmetry group. We also define an *orbit* of $\boldsymbol{r}$ as a set of sites obtained from $\boldsymbol{r}$ by acting with the elements of the space group $\{g\boldsymbol{r}|g \in \mathcal{G}\}$.

In momentum space a symmetry operation $g \in \mathcal{G}$ acts as $g\boldsymbol{k} = p\boldsymbol{k}$, meaning that the translation part of the operation is dropped. For each momentum in the BZ we define a *little group* $\mathcal{G}_{\boldsymbol{k}} \subset \mathcal{G}$ that consists of symmetry operations that leave this momentum invariant up to translations by reciprocal lattice vectors

$$\mathcal{G}_{\boldsymbol{k}} = \{g|g\boldsymbol{k} = \boldsymbol{k} + n_i\boldsymbol{G}_i\}. \tag{2.77}$$

2.2.3.2 *Band representations*

Now we are ready to construct a *band representation* (BR) – a representation of the space group induced from a site stabilizer group representation. A band representation carries the information about how a band that corresponds to a localized orbital in the real space transforms under symmetry operations. As we see in the next section, band representations act as a reference to determine whether a given band structure is topological.

We start with a site-stabilizer group for an arbitrarily chosen site $\mathcal{G}_{\boldsymbol{r}}$ and find its representation in the basis of Wannier orbitals localized at $\boldsymbol{r}$. A symmetry operation $g \in \mathcal{G}_{\boldsymbol{r}}$ acts on these orbitals according to the representation $\rho(g)$:

$$g\,|W_{i\mathbf{1},\mathbf{0}}\rangle\rangle = \sum_{j=1}^{\dim(\rho)} [\rho(g)]_{ji}\,|W_{j\mathbf{1},\mathbf{0}}\rangle\rangle, \tag{2.78}$$

where subscripts i, j index the basis Wannier orbitals, 1 indicates that the orbitals are localized at the site $\boldsymbol{r}_1 = \boldsymbol{r}$ (sites with other than 1 indices

will be defined shortly) and $\mathbf{0}$ indicates localization of the orbitals in the primitive unit cell. Note that these Wannier orbitals are different from the Wannier orbitals of a given Hamiltonian defined in Eq. (2.33); here, the Wannier orbitals are exponentially localized functions that form a basis for the symmetry representation.

To derive representation of the full symmetry group $\mathcal{G}$ induced from the representation of $\mathcal{G}_{\boldsymbol{r}}$ we use that the full group can be generated from the stabilizer group through a coset decomposition

$$\mathcal{G} = \bigcup_{a=1}^{A} g_a(\mathcal{G}_{\boldsymbol{r}} \ltimes T), \tag{2.79}$$

where T is the subgroup of translations, $\ltimes$ denotes the semidirect product of subgroups and $g_a \in \mathcal{G}$, $g_1 = \mathbb{1}$. Action of g_a on the site $\boldsymbol{r}$ generates all sites in the orbit of $\boldsymbol{r}$ within the primitive unit cell $\{\boldsymbol{r}_1 = \boldsymbol{r}, \boldsymbol{r}_2 = g_2\boldsymbol{r}, \ldots, \boldsymbol{r}_A = g_A\boldsymbol{r}\}$. Action of the symmetry operations g_a and lattice translations on the basis Wannier orbitals $|W_{j1,\mathbf{0}}\rangle\rangle$ generate Wannier orbitals localized at all sites belonging to the orbit of $\boldsymbol{r}$

$$|W_{ia,\bar{\boldsymbol{R}}}\rangle\rangle = \{g_a|\bar{\boldsymbol{R}}\}\,|W_{i1,\mathbf{0}}\rangle\rangle, \tag{2.80}$$

where index a denotes the site from the set $\{\boldsymbol{r}_a = g_a\boldsymbol{r}\}_{a=1}^{A}$ and $\bar{\boldsymbol{R}}$ denotes the unit cell at which the Wannier orbital is localized. These Wannier orbitals form a basis for the representation of $\mathcal{G}$ induced from $\mathcal{G}_{\boldsymbol{r}}$. Performing the induction procedure (cf. Ref. [34] for details) we get the representation of a symmetry $h = \{p|\mathbf{v}\} \in \mathcal{G}$

$$[\rho_{\mathcal{G}}(h)]_{(ia\bar{\boldsymbol{R}})(jb\bar{\boldsymbol{R}}')} = [\tilde{\rho}(g_a^{-1}\{\mathbb{1}|\bar{\boldsymbol{R}}\}h\{\mathbb{1}|\bar{\boldsymbol{R}}'^{-1}\}g_b)]_{ij}, \tag{2.81}$$

$$[\tilde{\rho}(g)]_{ij} = \begin{cases} [\rho(g)]_{ij} & \text{if } g \in \mathcal{G}_{\boldsymbol{r}} \\ 0 & \text{else} \end{cases}$$

which acts on the Wannier orbitals as

$$\rho_{\mathcal{G}}(h)\,|W_{ia,\bar{\boldsymbol{R}}}\rangle\rangle = \sum_{j=1}^{\dim(\rho)} [\rho(g)]_{ji}\,|W_{jb,p\bar{\boldsymbol{R}}+\boldsymbol{\Delta}_{ab}}\rangle\rangle, \tag{2.82}$$

where $\boldsymbol{\Delta}_{ab} = h\boldsymbol{r}_1 - \boldsymbol{r}_b$, while the index b and $g \in \mathcal{G}_{\boldsymbol{r}}$ are uniquely defined from the coset decomposition $hg_a = \{\mathbb{1}|\boldsymbol{\Delta}_{ab}\}g_b g$.

How does the band representation act in momentum space? To answer this question, we construct basis functions in momentum space as a Fourier transform of the basis Wannier orbitals

$$|\psi_{ia,\boldsymbol{k}}\rangle\rangle = \sum_{\bar{\boldsymbol{R}}} e^{i\boldsymbol{k}\cdot\bar{\boldsymbol{R}}}\,|W_{ia,\bar{\boldsymbol{R}}}\rangle\rangle \tag{2.83}$$

The band representation of the symmetry $h \in \mathcal{G}$ acts on these functions as

$$\rho_{\mathcal{G}}(h)\,|\psi_{ia,\boldsymbol{k}}\rangle\rangle = e^{-i(p\boldsymbol{k})\cdot\boldsymbol{\Delta}_{ab}} \sum_{j=1}^{\dim(\rho)} [\rho(g)]_{ji}\,|\psi_{jb,p\boldsymbol{k}}\rangle\rangle, \tag{2.84}$$

where again b and g are defined from the coset decomposition. In momentum space representation $\rho_{\mathcal{G}}$ forms non-zero blocks of size $A\dim(\rho) \times A\dim(\rho)$ between momenta $\boldsymbol{k}$ and $h\boldsymbol{k}$, we denote these blocks as $\rho_{\mathcal{G}}^{\boldsymbol{k}}(h)$. If $\boldsymbol{k}$ is left invariant under h, which happens when h is in the little group of $\boldsymbol{k}$, $h \in \mathcal{G}_{\boldsymbol{k}}$,

then the $\rho^{\boldsymbol{k}}_{\mathcal{G}}(h)$ block is on the diagonal of $\rho_{\mathcal{G}}$; it defines a representation of $\mathcal{G}_{\boldsymbol{k}}$ denoted as $\rho_{\mathcal{G}} \downarrow \mathcal{G}_{\boldsymbol{k}}$. The set of little group representations $\rho_{\mathcal{G}} \downarrow \mathcal{G}_{\boldsymbol{k}}$ at each $\boldsymbol{k}$ carries an important information about the band representation $\rho_{\mathcal{G}}$ and it is often enough to distinguish a topological insulator from a trivial one, despite that it looses information about connectivity of representations at different $\boldsymbol{k}$.

As the last step before we introduce the method to distinguish a topological insulator, we define the building blocks of band representations – *elementary band representations* (EBRs). We say that two band representations $\rho_{\mathcal{G}}$ and $\sigma_{\mathcal{G}}$ are *symmetry equivalent* if and only if there exist a unitary matrix-valued function $S(\boldsymbol{k}, t, g)$ for all $g \in \mathcal{G}$, such that

$$\begin{aligned} &S(\boldsymbol{k}, 0, g) = \rho_{\mathcal{G}}(g), \\ &S(\boldsymbol{k}, 1, g) = \sigma_{\mathcal{G}}(g), \\ &S(\boldsymbol{k}, t, g) \text{ is a BR } \forall t \in [0, 1]. \end{aligned} \tag{2.85}$$

A band representation is said to be composite if it is symmetry equivalent to a direct sum of other band representations. The elementary band representations are those that are not composite. It was shown [31] that all EBRs can be induced from irreducible representations of the site stabilizer groups of the maximal Wyckoff positions and that there is a finite amount of EBRs. An arbitrary band representation can be expressed as a direct sum of EBRs.

2.2.3.3 *Non-band-representations are topological*

In the theory of TQC a trivial tight-binding model is said to have valence bands that admit a description in terms of exponentially localized Wannier orbitals that are consistent with the symmetries of the model. In momentum space these orbitals form a direct sum of band representations. Therefore, any set of bands that can not be expressed as a sum of elementary band representations is topological. In this sense, the Wannier orbitals computed for topological bands according to Eq. (2.33) can not be continuously deformed to exponentially localized Wannier orbitals (2.80) that form a basis of band representations.

A sufficient condition for a set of bands to be topological is when its little group representations can not be expressed as a direct sum of little group representations of EBRs. Such bands are called symmetry-indicated topological bands; the specific examples were discussed in Sec. 2.2.2. To formulate the statement more formally, we define a vector space with the basis given by all irreducible representations of little groups at all symmetry-equivalent classes of momenta in the BZ $[\boldsymbol{k}]$; we denote the elements of this basis as $\rho_{i[\boldsymbol{k}]}$, where i enumerates the irreducible representation of a little group $\mathcal{G}_{[\boldsymbol{k}]}$. Every set of bands can be mapped to a vector in this vector space

$$\boldsymbol{v} = \sum_{i,[\boldsymbol{k}]} v_{i[\boldsymbol{k}]} \rho_{i[\boldsymbol{k}]}, \tag{2.86}$$

with non-negative integers $v_{i[\boldsymbol{k}]}$ indicating the number of bands that transform under irreducible representation $\rho_{i[\boldsymbol{k}]}$ at momenta within the equivalence class $[\boldsymbol{k}]$. EBRs are mapped onto a set of vectors $\boldsymbol{e}_\alpha$, where α runs over all EBRs. We construct a non-negative-integer-valued matrix $E = (\boldsymbol{e}_1, \boldsymbol{e}_2, \dots)$ by stacking all EBR vectors in the horizontal direction. To find whether the bands mapped onto vector $\boldsymbol{v}$ are topological we search for a non-negative-integer-valued vector $\boldsymbol{n}$, such that:

$$E\boldsymbol{n} = \boldsymbol{v}. \tag{2.87}$$

Vector $\boldsymbol{n}$ gives the multiplicities with which the EBRs must be summed in order to result in bands $\boldsymbol{v}$. If such non-negative-integer vector can not be found, the bands are topological. We note that since irreducible representations of little groups do not carry complete informations about a band representation, it is possible that Eq. (2.87) admits a non-negative-integer-valued solution, but the studied set of bands is topological. In this case to identify topological bands one needs to use the complete information about the symmetry group representation. The details about this procedure can be found in Refs. [31, 34].

2.2.4 *Stable and fragile topology*

When trying to solve Eq. (2.87) to find whether the set of bands is topological, there can be different reasons for the absence of a non-negative integer solution. First, there can be no integer-valued solution and second, as was realized in Ref. [41], there can exist an integer-valued solution with some of the integers in the vector $\boldsymbol{n}$ being negative. In both cases the bands are topological, but they have different level of stability. If no integer-valued solution exists, the topology of the bands is *stable*: a direct sum of the studied bands with any trivial band that forms a band representation remains topological. On the other hand, if an integer-valued $\boldsymbol{n}$ is found, the vector $\boldsymbol{v}$ corresponding to the studied bands can be expressed as

$$\boldsymbol{v} = \sum_{\alpha_+} n_{\alpha_+} \boldsymbol{e}_{\alpha_+} - \sum_{\alpha_-} n_{\alpha_-} \boldsymbol{e}_{\alpha_-}, \tag{2.88}$$

where $n_{\alpha_+}, n_{\alpha_-} \in \mathbb{Z}^{\geq 0}$. The bands are topological as they do not admit description in terms of exponentially localized symmetric Wannier orbitals. However, their topology is *fragile* in a sense that a direct sum of these bands with EBRs $\boldsymbol{e}_{\alpha_-}$ can be expressed as a sum of EBRs with positive integer coefficients and therefore can be made trivial [41–43].

Fragile topological bands have found their realization in real materials [52]. However, the signatures of fragile bands in crystalline solids may be hindered by the presence of trivial low energy modes, which may trivialize topology of the valence bands. Other platforms which do not have this problem are metamaterials, such as photonic crystals or acoustic metamaterials. They were also shown to host fragile topological bands [49–51]. Finally, fragile topology was shown to appear in flat bands of the magic angle twisted bilayer graphene [44, 116, 117].

2.2.5 *Delicate topology*

In the theory of topological quantum chemistry band representations are taken as a definition of a trivial band. The main result of this thesis is that even among band representations there are topological bands. To see this we introduce a different definition of a trivial band: a band representation induced from a Wannier orbital that is localized within a single unit cell, i.e. a *tightly-bound band representation*. In the tight binding formalism this can be any orbital that forms the tight-binding basis of the studied Hilbert space. We call such band representations *basis band representations* (BBRs). Contrary to the band representations, which are equipped with the equivalency relation (2.85) and therefore form equivalence classes of band representations, basis band representations are strictly defined by the basis Wannier orbitals that are specified by their localization centers and the representation of the site

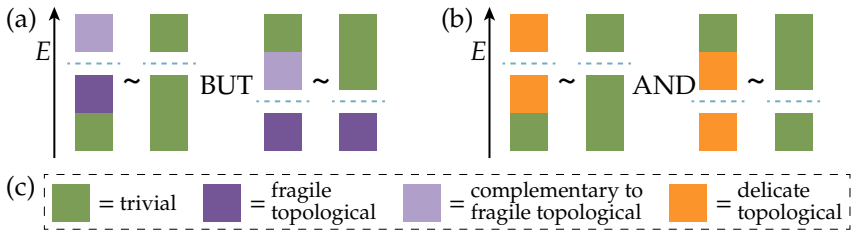

Figure 2.9: Topological stability of (a) fragile vs. (b) delicate topology. The blocks [colored according to legend in (c)] below/above the Fermi energy (dashed blue lines) are valence/conduction bands, with addition indicated by stacking and topological equivalence by '$\sim$'. In panel (a) the complement to fragile topological bands could be fragile topological, obstructed atomic limit, or fully trivial.

stabilizer group. The formal definition of the BBR for specific symmetry groups Pn for $n = 2, 3, 4, 6$ is given in Chapter 4 of Part I.

A band representation is topological if it can not be continuously deformed to a basis band representation. In this case, the defining Wannier orbital is exponentially localized but can not be localized within one unit cell, instead it spreads over several unit cells, and therefore is called *multicellular*. We discuss in details what can lead to such multicellular obstruction of the Wannier representation in Part II, Chapter 8 of this thesis.

We may also ask how stable are these topological band representations under a direct sum with trivial bands. The answer is that they are *delicate*, which is a new level of stability that complements stable and fragile topology. To define this we need to distinguish between valence band representations that are assumed to be topological and the complementary conduction band representations that are separated from the valence bands by a gap. Delicate topological bands lose their topology in two situations: if the trivial bands are added to the valence bands or if they are added to the conduction bands [cf. Fig. 2.9(b) for an illustration]. This distinguishes delicate topology from fragile, for which topological bands retain their topology if the conduction subspace is enlarged with additional trivial bands [cf. Fig. 2.9(a)]. An extensive discussion of delicate topology is presented in Part II, Chapter 7 of the thesis.

Part I

CRYSTALLINE HOPF INSULATORS

In this part, we investigate the Hopf insulator in the presence of crystalline symmetry. As we discussed in Sec. 2.1.6 the Hopf insulators are described by two-band insulating Hamiltonians defined over the 3D momentum space [55, 92, 93]. Their topological classification was derived by Pontrjagin [97] and is given by four quantized invariants [98, 99], three of which are Chern invariants defined on two-dimensional sub-tori of the BZ, while the fourth can be identified as the integer ($\mathbb{Z}$) valued Hopf invariant (2.48) if the Chern class is trivial. However, Pontrjagin's classification has never been generalized to include crystallographic point-group symmetries, i.e., crystalline symmetries beyond discrete translations.

As we partially saw in Sec. 2.2, crystallographic point-group symmetries have had a transformative role in the topological classification of band structures, rendering some topological invariants to vanish [56], as well as introducing new topological invariants [56, 91, 107, 114, 115, 118, 119]. One approach to characterize band topology is based on the analysis of crystalline symmetry representations of one-particle Bloch states [29–31, 41] as was introduced in Sec. 2.2.3. This approach led to a successful prediction of numerous new topological materials [37–39]; however, by design, these symmetry-representation-based filtering schemes do not identify topologically nontrivial band structures that are *band representations* [112, 113], i.e., band structures admitting a description by a set of exponentially-localized, locally-symmetric crystalline (Wannier) orbitals [43, 47, 120], of which the Hopf insulator [55] is an example.

In this part of the thesis, we show that the presence of crystalline symmetry also extends the characterization of two-band, insulating Hamiltonians with trivial first Chern class beyond the $\mathbb{Z}$-valued Hopf invariant. In particular, if the valence and the conduction bands transform differently under rotation, additional $\mathbb{Z}$-valued topological invariants can be defined: each of them is given by a 2π-quantized difference in Berry-Zak phase between two rotation-invariant lines (in the Brillouin zone) separated by half a reciprocal-lattice vector, with the Zak phase reverting to its original value over a full reciprocal vector. By viewing two of three independent momentum coordinates as adiabatic parameters, this Zak-phase reversion can be interpreted as an adiabatic evolution of the electric polarization defined for a single-momentum Hamiltonian: a unit charge is pumped across one (or more) real-space lattice periods within half an adiabatic cycle, and is then pumped back in the next half of the cycle. In analogy with the quantized charge pumping first investigated by Thouless [87] and reviewed in Sec. 2.1.4.3, we call this Zak-phase reversion a returning Thouless pump (RTP). We refer to the corresponding rotation-symmetry-enriched topological two-band Hamiltonians as *crystalline Hopf insulators*.

We classify two-band, insulating Hamiltonians (with trivial Chern class) by the Hopf and the rotation-protected RTP invariants, for all crystallographically allowed orders of rotation: $n = 2, 3, 4, 6$. We discover that these invariants are not independent: the RTP invariants determine the Hopf invariant modulo n, resembling in spirit a known relation between rotation-symmetry representations and the Chern number [56], discussed in Sec. 2.2.2.2. At the same time, the RTP invariants characterize qualitatively distinct phases beyond the Pontrjagin classification; as proof of principle we demonstrate a model that carries vanishing Chern and Hopf invariants but nonvanishing RTP invariants.

Both the Hopf and RTP invariants lead to potentially measurable surface signatures which are qualitatively unique among the known topological

insulators. The Hopf invariant results in teleportation of Berry curvature on the surface of the Hopf insulator. The paradigm of topological insulators asserts that an energy gap separates conduction and valence bands with opposite topological invariants. Here, we propose that *equal*-energy bands with opposite Chern invariants can be *spatially* separated – onto opposite facets of a finite crystalline Hopf insulator. On a single facet, the Chern number computed for all surface states is in one-to-one correspondence with the bulk Hopf invariant. By 'facet', we mean a crystalline surface retaining two of three independent translational symmetries of the bulk space group; by 'all surface states', we mean all surface-localized states irrespective of whether they are occupied or unoccupied by fermions. At the same time the Hopf invariant does not guarantee a conducting boundary and the boundary spectrum can be gapped by some boundary deformation.

In its turn the RTP leads to *anomalous* values for the angular momentum of *all* surface states that are localized to a single, rotation-invariant crystalline *facet*. By 'anomalous', we mean that these angular-momentum values are non-identical to the angular momentum of bulk valence states, and also non-identical to the angular momentum of bulk conduction states. Such an *angular-momentum anomaly* is physically manifested in two ways.

(*i*) For open boundaries with sharply-terminated hoppings, the anomaly implies the existence of facet-localized states along any line in the surface Brillouin zone connecting a certain pair of rotation-invariant reduced momenta. These states energetically connect the bulk valence and bulk conduction bands in a manner that is robust against continuous, gap-preserving deformations of the *bulk* Hamiltonian; however, the energetic connection crucially relies on the *sharpness* of the boundary condition, namely that Hamiltonian matrix elements are everywhere identical as in the bulk, except for those hopping matrix elements crossing a facet; these exceptions are set to zero. Such *conditionally robust* surface states have no analog in stable [17, 19, 119] and fragile [41, 43, 45, 47, 120] topological insulators, and are unique to delicate topological insulators (a notion introduced in Sec. 2.2.5). In Chapter 7 of Part II we argue that the crystalline Hopf insulators are delicate.

(*ii*) For a general choice of the Hamiltonian termination, facet-localized states are characterized by Berry-Zak phases that are quantized to a rational multiple of 2π, which is distinct from the Berry-Zak phases of bulk states in both the bulk conduction and the bulk valence bands. How surface states can be topologically distinct from bulk states may be rationalized in a slab geometry with two facets: the Zak phase of top-facet-localized states are 'conjugate' to the Zak phase of the bottom-facet-localized states, such that the totality of states localized to both facets are topologically equivalent to the bulk states. Colloquially, in analogy with the Berry curvature teleportation in Hopf insulators, one may say that topologically 'interesting' bands have arisen from being *physically* separated across the bulk of the slab; such a hallmark of delicate topological insulators stands in stark contrast to the conventional wisdom of *energetically* separating topologically-interesting bands across a bulk energy gap.

We structure the discussion in this part as follows. We start by showing that the crystalline Hopf insulator originates from a unique semi-metallic phase – characterized by a band-touching point that acts as a rotation-symmetric, dipolar source of Berry curvature. This result is formulated in the first chapter in terms of $\boldsymbol{k} \cdot \boldsymbol{p}$ Hamiltonians and is consequently regularized on a lattice in the second chapter. In the same chapter we formalize the notion of the

returning Thouless pump (RTP), explain why it is quantized and present several models illustrating crystalline Hopf insulators. In the next chapter we establish the boundary signatures of the bulk Hopf and RTP invariants. Finally, in the last chapter we show that the Hopf and RTP invariants are not independent but are related modulo n for all Pn space groups.

PART CONTENTS

3

BERRY-DIPOLE BAND DEGENERACY

One convenient strategy to realize known topological insulators has been to perturb topological semi-metallic phases so as to develop an energy gap (cf. discussion in Sec. 2.1.3.2 as well as Refs. [13, 121] and chapter 8 of Ref. [61]). We show here that crystalline Hopf insulators can be realized by perturbing a rotation-symmetric semi-metallic phase with a band touching (at an isolated $\boldsymbol{k}$-point) that acts as a dipolar source of Berry curvature. We present a $\boldsymbol{k} \cdot \boldsymbol{p}$ Hamiltonian for such a *Berry dipole* in Sec. 3.1, then argue in Sec. 3.2 that a Berry-dipole band degeneracy mediates a topological phase transition. In the following Chapter 4, we move from $\boldsymbol{k} \cdot \boldsymbol{p}$ Hamiltonians to tight-binding lattice models showing that a Berry dipole mediates a quantized change of the integer-valued Hopf and RTP invariants.

The Berry dipole Hamiltonian offers several advantages for studying crystalline Hopf insulators, namely (*a*) it affords a clean, analytic derivation of the simultaneous change in Hopf and RTP invariants across a Berry-dipole phase-transition point, and (*b*) it gives a practical strategy to construct tight-binding-model Hamiltonians of crystalline Hopf insulators [presented in Sec. 4.4 of the next Chapter]. The price to pay for these advantages is that a Berry-dipole phase transition lies in a region of the phase diagram that is 'hard to reach', i.e., per codimension counting [122, 123], a generic band degeneracy in a 4-dimensional momentum-parameter space for Wigner-Dyson class A extends over 1-dimensional nodal lines. Therefore, the Berry dipole, which constitutes a single gapless *point* in the 4-dimensional space, requires certain amount of fine-tuned parameters as we discuss in Sec. 3.3. If one is interested in realizing delicate topology for realistic Hamiltonians, it pays to explore the phase diagram in the vicinity of the fine-tuned Berry-dipolar form of the Hamiltonian. It turns out the vicinity contains a variety of topological (semi)metallic phases, discussed in Sec. 3.4.

CHAPTER CONTENTS

3.1 ROTATION-SYMMETRIC $\boldsymbol{k}\cdot\boldsymbol{p}$ MODEL OF A BERRY DIPOLE

In contrast to a Weyl point [Fig. 3.1(a)], the Berry curvature integrated over a sphere enclosing the Berry dipole necessarily vanishes. We define the Berry

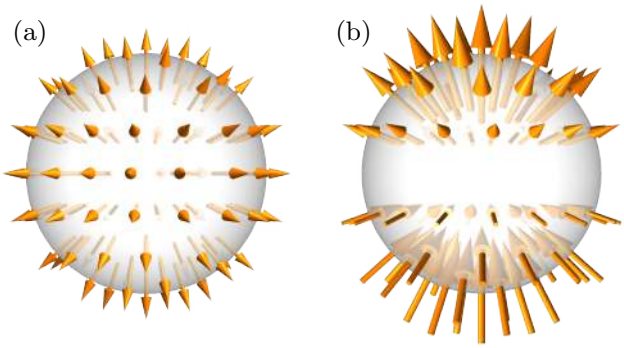

Figure 3.1: Berry-curvature vector fields of (a) an isotropic Weyl point with positive chirality, and of (b) a rotation-symmetric Berry dipole in Eq. (3.3) with spin $\Delta\ell = -1$. Both vector fields are plotted over a sphere centered at the band-touching point.

dipole such that the Berry flux through a hemisphere oriented parallel to the dipole axis is quantized to integer multiplies of 2π [Fig. 3.1(b)],

$$\Psi = \int_{\text{hemisphere}} \boldsymbol{\mathcal{F}} \cdot d\boldsymbol{S} \quad \in 2\pi\mathbb{Z}, \tag{3.1}$$

where $\boldsymbol{\mathcal{F}}$ is the Berry curvature of the valence band and $d\boldsymbol{S}$ is an infinitesimal surface element normal to the hemisphere. We say that the Berry dipole is of the $\mathbb{d}$-th order if the absolute value of the flux $|\Psi|$ through a hemisphere equals $2\pi\mathbb{d}$.

We further restrict our attention to *rotation-symmetric* Berry-dipoles, for which the dipole axis coincides with a rotation axis of symmetry. We assume that a two-band Hamiltonian is symmetric under continuous rotations with respect to the z-axis:

$$\begin{aligned} &R_\theta\, h(\boldsymbol{k})\, R_\theta^{-1} = h(\theta\boldsymbol{k}), \\ &R_\theta = e^{-i\theta\Delta\ell/2\cdot\sigma_z}, \end{aligned} \tag{3.2}$$

with $\theta\boldsymbol{k}$ being the momentum vector obtained from $\boldsymbol{k}$ by a counterclockwise rotation of (k_x, k_y) by an arbitrary angle θ, R_θ being the matrix representation of a rotation by angle θ, and $\Delta\ell$ (assumed $\neq 0$) is the integer-valued *Berry-dipole spin*, in units where $\hbar = 1$.

To study the prospective gapped phases obtained by lifting the Berry-dipole band degeneracy, we construct a two-band $\boldsymbol{k}\cdot\boldsymbol{p}$ Hamiltonian that depends on a tuning parameter ϕ. At $\phi \neq 0$ the two energy bands are separated by a finite gap, which closes for $\phi = 0$ when the bands form a Berry dipole. A simple realization of a rotation-symmetric Berry-dipole Hamiltonian is encoded with a spinor

$$\zeta(\boldsymbol{k}) = \begin{pmatrix} \zeta_1(\boldsymbol{k}) \\ \zeta_2(\boldsymbol{k}) \end{pmatrix} = \begin{pmatrix} \left(k_{-\,\mathrm{sgn}(\Delta\ell)}\right)^{|\Delta\ell|} \\ v\,k_z + i\phi \end{pmatrix} \in \mathbb{C}^2, \tag{3.3}$$

with $k_\pm = k_x \pm ik_y$ and helicity $v \in \{-1, +1\}$ (cf. Dets. 3.3 for a geometric interpretation of v). The spinor serves as an input for the

$$\textit{spinor-form Hamiltonian:} \quad h(\boldsymbol{k}) = [\zeta^\dagger(\boldsymbol{k})\sigma\zeta(\boldsymbol{k})]\cdot\boldsymbol{\sigma}, \tag{3.4}$$

with $\boldsymbol{\sigma} = (\sigma_x, \sigma_y, \sigma_z)$ being the vector of Pauli matrices. We have obtained Eq. (3.3) by first assuming that ζ has a multi-variable Taylor expansion in all

momentum components and in the tuning parameter ϕ, then deriving [in Appendix A.1] the lowest-order form for ζ such that the $\boldsymbol{k}\cdot\boldsymbol{p}$-Hamiltonian in Eq. (3.4) fulfills the symmetry condition in Eq. (3.2). If one further allows for continuous deformations of the Hamiltonian that preserve its 'topology' (as formulated more precise in Appendix A.1.3), ζ can be simplified to the form shown in Eq. (3.3).

We note that a Hamiltonian with rotation symmetry given by Eq. (3.2) can as well be constructed with the spinor

$$\zeta(\boldsymbol{k}) = \begin{pmatrix} v\,k_z + i\phi \\ \left(k_{\mathrm{sgn}(\Delta\ell)}\right)^{|\Delta\ell|} \end{pmatrix}, \tag{3.5}$$

as shown in Appendix A.1. Spinor-form Hamiltonians [Eq. (3.4)] constructed with spinors given by Eqs. (3.3) resp. (3.5) differ by symmetry eigenvalues of their eigenstates. Namely, define an angular momentum ℓ_v (ℓ_c) of the valence (conduction) eigenstate as

$$R_\theta \left| u_{v(c)}(0,0,k_z) \right\rangle = e^{i\theta\ell_{v(c)}} \left| u_{v(c)}(0,0,k_z) \right\rangle. \tag{3.6}$$

Then for the Hamiltonian defined through spinor (3.3) the difference $\ell_c - \ell_v$ coincides with the Berry-dipole spin $\Delta\ell$. This corresponds to a valence (conduction) state at rotation axis being induced from the first (second) basis orbital, where these orbitals define a basis of the Hamiltonian and the rotation matrix. For the Hamiltonian defined though spinor (3.5), one instead finds that the difference $\ell_c - \ell_v = -\Delta\ell$, meaning that the valence (conduction) state is induced by the second (first) basis orbital. The two classes of models are related by flipping the sign of their energy bands. Throughout Chapter 3 we will present results for the Hamiltonian given by the spinor (3.3) and comment on their applicability to the spinor (3.5).

The energy-momentum dispersion of each band of the spinor-form Hamiltonian (indexed by $\pm$) is simply the squared norm of the spinor multiplied by ± 1 [cf. Dets. 3.1 for the derivation]:

$$E_\pm(\boldsymbol{k}) = \pm\|\zeta(\boldsymbol{k})\|^2. \tag{3.7}$$

The particular form of the Hamiltonian defined by Eqs. (3.3) and (3.4) implies that the energy gap grows quadratically with the k_z-component of momentum and with the parameter ϕ. Furthermore, the Berry-dipole spin $\Delta\ell$ determines the exponent of $k_\pm$ to be $|\Delta\ell|$, and therefore the energy gap grows with $2|\Delta\ell|$-th power of the momentum distance from the rotation axis. In certain parts of our discussion, it will be convenient to consider the *spectrally flattened*[1] spinor-form Hamiltonian,

$$h_{\mathrm{flat}}(\boldsymbol{k}) = \frac{1}{\|\zeta(\boldsymbol{k})\|^2} h(\boldsymbol{k}), \tag{3.9}$$

which is defined for all $(\boldsymbol{k},\phi) \neq (\boldsymbol{0},0)$, and for which the spectrum is simply $E_{\mathrm{flat}}(\boldsymbol{k}) = \pm 1$.

We derive in Appendix A.2.1 that for Hamiltonians given by Eqs. (3.3) and (3.4) the Berry-dipole spin $\Delta\ell$ determines the Berry flux through the upper hemisphere as

$$\Psi\left(\begin{smallmatrix}\text{Berry dipole}\\ \text{spinor (3.3)}\end{smallmatrix}\right) = -2\pi\Delta\ell; \tag{3.10}$$

1 For traceless, two-band Hamiltonians that are *not* of the spinor form, the spectral flattening is instead defined as

$$h_{\mathrm{flat}}(\boldsymbol{k}) = \frac{h(\boldsymbol{k})}{\sqrt{-\det[h(\boldsymbol{k})]}}. \tag{3.8}$$

implying that the absolute value of the Berry-dipole spin equals the order of the Berry dipole $|\Delta\ell| = \mathbb{d}$.[2] To derive the Berry flux for the Hamiltonian defined through the spinor (3.5), observe that this spinor can be brought to the form (3.3) by first flipping the order of the basis orbitals (i.e., rotating the Hilbert space with Pauli matrix σ_x) and by subsequently changing the sign of the Berry-dipole spin. The order of the basis orbitals (i.e., the rotation of the Hilbert space) does not affect the Berry flux, and therefore

$$\Psi\begin{pmatrix}\text{Berry dipole}\\ \text{spinor (3.5)}\end{pmatrix} = 2\pi\Delta\ell. \tag{3.11}$$

Recalling the expression for the valence and conduction angular momenta (3.6), we conclude that the Berry flux through the upper hemisphere of both spinor-form Hamiltonians is given by

$$\Psi\begin{pmatrix}\text{rotation-sym.}\\ \text{Berry dipole}\end{pmatrix} = -2\pi(\ell_c - \ell_v). \tag{3.12}$$

Details 3.1 To prove Eq. (3.7), first recall the completeness relation for the Pauli matrices: $\frac{1}{2}\sum_{i\in\{0,x,y,z\}} \sigma^i_{\alpha\beta}\sigma^i_{\gamma\delta} = \delta_{\alpha\delta}\delta_{\beta\gamma}$ [124], where δ is the Kronecker symbol and σ^0 is the identity matrix. This is equivalent to

$$\sum_{i\in\{x,y,z\}} \sigma^i_{\alpha\beta}\sigma^i_{\gamma\delta} = 2\delta_{\alpha\delta}\delta_{\beta\gamma} - \delta_{\alpha\beta}\delta_{\gamma\delta}. \tag{3.13a}$$

Since the two-band Hamiltonian in Eq. (3.4) is traceless, the two eigenvalues have the same magnitude but opposite sign: $\pm E$. The determinant (being the product of eigenvalues) is then found as $\det h = -E^2$. Simultaneously, for a Pauli-matrix Hamiltonian $h = \sum_{i\in\{x,y,z\}} h_i\sigma^i$, the determinant is also expressed as $\det h = -\sum_{i\in\{x,y,z\}} h_i^2$. For the spinor-form Hamiltonian, $h_i = \zeta^*_\alpha\sigma^i_{\alpha\beta}\zeta_\beta$; therefore, matching the two expressions for $\det h$ results in

$$E^2 = \sum_{i\in\{x,y,z\}} \zeta^*_\alpha\sigma^i_{\alpha\beta}\zeta_\beta\zeta^*_\gamma\sigma^i_{\gamma\delta}\zeta_\delta \overset{(3.13a)}{=} \zeta^*_\alpha\zeta^*_\gamma\left(2\delta_{\alpha\delta}\delta_{\beta\gamma} - \delta_{\alpha\beta}\delta_{\gamma\delta}\right)\zeta_\beta\zeta_\delta, \tag{3.13b}$$

where summation over repeated indices $\alpha, \beta, \gamma, \delta$ is implied. From the last expression, $E^2 = (\zeta^*_\alpha\zeta_\alpha)^2$ follows easily, which is equivalent to Eq. (3.7).

3.2 BERRY DIPOLE AS A TOPOLOGICAL PHASE TRANSITION

While the Hamiltonian given in Eqs. (3.3) and (3.4) has been defined for $\boldsymbol{k} \in \mathbb{R}^3$, the fact that each Hamiltonian matrix element is a low-order polynomial in $\boldsymbol{k}$ allows us to interpret the same Hamiltonian as a small-momentum, truncated Taylor expansion of a tight-binding Hamiltonian defined over the Brillouin zone. Tuning ϕ through zero makes the energy gap close at an isolated point $\boldsymbol{k} = \boldsymbol{0}$, then subsequently reopens the gap; throughout this tuning, the rotation-symmetry representations at $\boldsymbol{k} = \boldsymbol{0}$ are *not* inverted. We will find that the parameter $\phi = 0$ marks a critical point between two gapped phases that are distinguished by the Hopf and Returning-Thouless-pump topological invariants, both of which are integers defined for the tight-binding Hamiltonian.

To demonstrate why the Berry dipole intermediates a change in the Hopf invariant, we utilize the linking-number interpretation of the Hopf invariant, introduced in Sec. 2.1.6 and illustrated in Fig. 2.6. This interpretation applies to two-band Hamiltonians with trivial Chern class, which is assumed throughout this thesis. In the $\boldsymbol{k}\cdot\boldsymbol{p}$ model, the linking number is not well-defined since the preimage manifolds are noncompact, forming a family of

2 We note that the hemisphere Berry flux quantization holds for the Hamiltonian (3.3, 3.4) due to the accidental z-mirror symmetry at the critical parameter $\phi = 0$, that is discussed in Sec. 3.3. We expect that this symmetry is broken in the higher-order in $\boldsymbol{k}$ expansion of the spinor (3.3). Therefore, quantization (3.10) holds only for small spheres surrounding the Berry dipole, for which the lowest-in-$\boldsymbol{k}$ expansion of the spinor gives a good approximation of the Hamiltonian.

infinite (and for $\phi \neq 0$ non-intersecting) straight lines in $\mathbb{R}^3$, as proven in Dets. 3.2 and illustrated representatively by two lines in Fig. 3.2(a) for the case $\Delta\ell = 1$ and $v = 1$. The geometric constellation of the preimages motivates the adopted name *helicity* for the parameter $v \in \{-1, +1\}$ as discussed in Dets. 3.3. [The red line is the preimage of $\boldsymbol{h} \propto (1, 0, 0)$, and the cyan line a preimage of $\boldsymbol{h} \propto (-1, 0, 0)$, where $h = \boldsymbol{h} \cdot \boldsymbol{\sigma}$ is the Berry-dipole Hamiltonian.] Given any two distinct points on the two-sphere, a *change* in their associated linking number (as attributed to the Berry-dipole band touching) remains well-defined. For instance, comparing Figs. 3.2(a) and (c) (for $\phi < 0$ and $\phi > 0$, respectively) shows that the red and cyan lines 'pass through' each other as ϕ is tuned through zero, which can be interpreted as a unit change in the linking number. The sense of this interpretation is that no matter how we 'close off' the cyan and red lines at $\boldsymbol{k}$-infinity, their linking number must change by unity under the 'passing through'.

Details 3.2 According to the correspondence $S^2 \approx \mathbb{C}P^1$ (the complex projective plane), points on the Bloch sphere are in one-to-one correspondence with rays in the Hilbert space $\mathbb{C}^2$ [68]. Therefore, for any two $\boldsymbol{k}$-points ($\boldsymbol{k}_1$ and $\boldsymbol{k}_2$) in the preimage of a single Bloch-sphere point, the corresponding spinors $\zeta(\boldsymbol{k}_1)$ and $\zeta(\boldsymbol{k}_2)$, as given by the Hamiltonian in Eq. (3.4), are related to each other by rescaling with a non-zero complex number. Such rescaling keeps the ratio of the two spinor components invariant; specifying the preimage is equivalent to fixing a constant $c \in \mathbb{C}$ in $\zeta_1(\boldsymbol{k}) = c\zeta_2(\boldsymbol{k})$. Plugging in the spinor components of a first-order Berry dipole from Eq. (3.3) for the case $|\Delta\ell| = 1$, one obtains $k_x \pm i\,k_y = c(vk_z + i\phi)$, where the sign on the left-hand side equals $-\operatorname{sgn}(\Delta\ell)$. This may be viewed as a straight $\boldsymbol{k}$-line (parametrized by k_z) which intersects the $k_z = 0$ plane at point $k_x \pm ik_y = ic\phi$. Note that the inclination of the straight line, as captured by $d(k_x \pm ik_y)/dk_z = cv$, is independent of the tuning parameter ϕ.

Details 3.3 Let us comment on the meaning of the name *helicity* for the parameter $v \in \{-1, +1\}$ in the spinor function (3.3). If we extract the polar coordinate of any particular preimage line, $\theta(k_z) = \arg[k_x(k_z) + ik_y(k_z)]$ (where polar coordinate θ and the radial coordinate k are defined via $k_x = k\cos\theta$ and $k_y = k\sin\theta$), as a function of k_z [the dependence being emphasized by the round brackets: '(k_z)'], then

$$\operatorname{sgn}\left[\frac{d\theta(k_z)}{dk_z}\right] = \operatorname{sgn}[\phi v]. \tag{3.14}$$

Pictorially, as one moves along the positive k_z direction, we observe all preimage lines to wind in the positive direction around the k_z axis when $\operatorname{sgn}[\phi v] = +1$ (resp. in the negative direction when $\operatorname{sgn}[\phi v] = -1$), indicating a notion of handedness. [Note that these conclusions are derived for a Hamiltonian given by Eqs. (3.3) and (3.4) with the Berry-dipole spin fixed to $\Delta\ell = 1$; the sign of Eq. (3.14) is flipped for $\Delta\ell = -1$.]

To diagnose a change in the Hopf invariant of the tight-binding Hamiltonian, we look at changes in the *continuum Hopf number* (of the $\boldsymbol{k} \cdot \boldsymbol{p}$ Hamiltonian), defined as an integral of the Chern-Simons three-form:

$$\chi^{\text{cont.}} = -\frac{1}{4\pi^2}\int_{\mathbb{R}^3} d^3k\, \boldsymbol{\mathcal{F}} \cdot \boldsymbol{\mathcal{A}}, \quad \boldsymbol{\mathcal{F}} = \boldsymbol{\nabla}_{\boldsymbol{k}} \times \boldsymbol{\mathcal{A}}(\boldsymbol{k}) \tag{3.15}$$

with $\boldsymbol{\mathcal{A}}(\boldsymbol{k}) = \langle u_v(\boldsymbol{k}) | i\nabla_{\boldsymbol{k}} u_v(\boldsymbol{k})\rangle$ the Berry connection of the intra-cell wave function $|u_v(\boldsymbol{k})\rangle$ (the subscript 'v' stands for 'valence band'), and $\boldsymbol{\mathcal{F}}(\boldsymbol{k})$ the corresponding Berry curvature.

The continuum analog of the RTP invariant is given by the Berry-Zak phase computed along the rotation axis:

$$\mathscr{Z}^{\text{cont.}} = \int_{-\infty}^{\infty} \mathcal{A}_z(0, 0, k_z) dk_z, \tag{3.16}$$

where $\mathcal{A}_z$ is the z component of the Berry connection. We refer to Eq. (3.16) as the *continuum Zak phase*. Let us clarify that the quantity is indeed a phase, meaning it is well-defined modulo integer multiples of 2π. This holds under the conditions that the wave function is differentiable everywhere on the

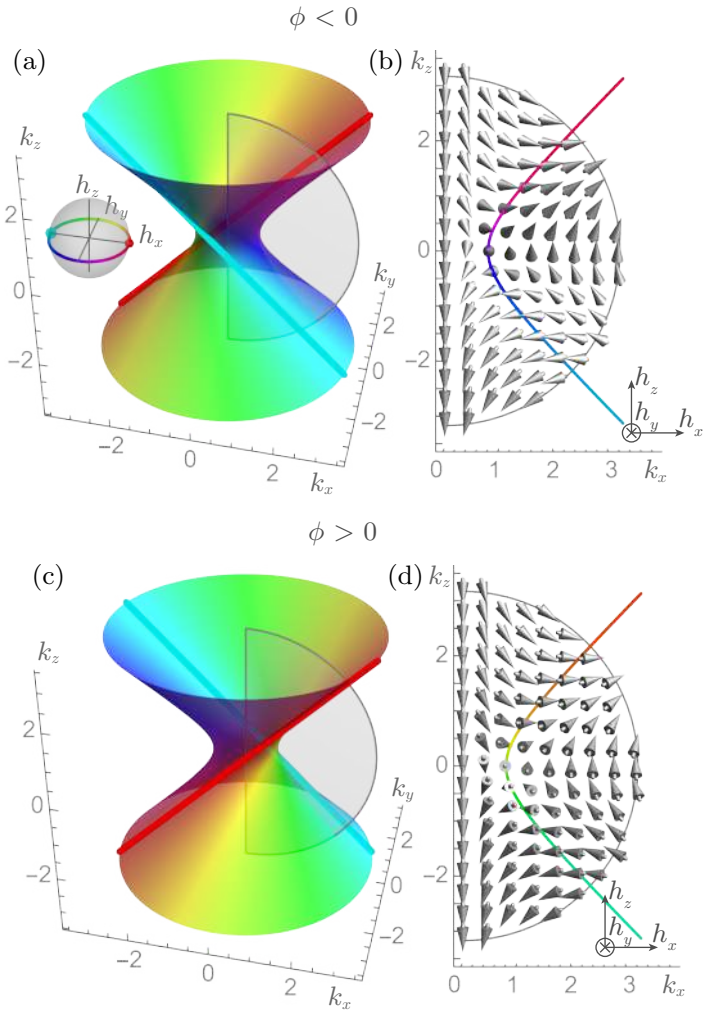

Figure 3.2: Panels (a–b) characterize the Hamiltonian of Eqs. (3.3–3.4) with $\Delta\ell = v = +1$ and $\phi = -0.8$; for panels (c–d), we maintain $\Delta\ell = v = +1$ but change $\phi = +0.8$. For both Hamiltonians, the corresponding momentum surfaces where the z-component of $\boldsymbol{h}_{\text{flat}}(\boldsymbol{k})$ vanishes [$h_{\text{flat},z}(\boldsymbol{k}) = 0$] form hyperboloids illustrated in panels (a) and (c) respectively. The coloring of the surfaces indicates the values of $h_{\text{flat},x}$ and $h_{\text{flat},y}$ according to an inset in panel (a). The cyan and red lines indicate the momenta where the Hamiltonian $\boldsymbol{h}_{\text{flat}} \propto (1,0,0)$ and $\boldsymbol{h}_{\text{flat}} \propto (-1,0,0)$, respectively. The gray semicircle represents a 2D radial cut given by $\varphi_{\boldsymbol{k}} = 0$, $\theta_{\boldsymbol{k}} \in [0,\pi]$ and $|\boldsymbol{k}| \in [0,R]$, with spherical coordinates $(|\boldsymbol{k}|,\theta_{\boldsymbol{k}},\varphi_{\boldsymbol{k}})$ specified in the main text. The vector field of $\boldsymbol{h}_{\text{flat}}(\boldsymbol{k})$ is illustrated over the gray semicircle in panels (b) and (d), for $\phi = -0.8$ and $+0.8$ respectively. The colored line in panel (b) [and also (d)] denotes momenta where the radial cut is intersected by the hyperboloid; the color scheme follows again the legend in panel (a).

k_z-line, and moreover coincides at $k_z \to \pm\infty$, allowing to 'compactify' the k_z-line by identifying the points at infinity. Under these conditions, as we show in Dets. 3.4, gauge transformations can at most change the value of $\mathscr{Z}^{\text{cont.}}$ by an integer multiple of 2π. A stronger statement, namely that $\mathscr{Z}^{\text{cont.}}/2\pi$ is integer-valued, follows from the Hamiltonian matrix being diagonal along the rotation-invariant $\boldsymbol{k}$-line, according to the rotation constraint in Eq. (3.2). Indeed, the diagonal constraint ensures the existence of a gauge where the wave function is constant along the rotation-invariant $\boldsymbol{k}$-line, and hence the Berry connection vanishes at each point on said line.

Details 3.4 Under a gauge transformation $|u(\boldsymbol{k})\rangle \to e^{-i\beta(\boldsymbol{k})}|u(\boldsymbol{k})\rangle$, the Berry connection transforms as $\mathcal{A}_z \to \mathcal{A}_z + \partial_{k_z}\beta$. If the resultant wave function is to remain differentiable with respect to k_z and periodic over the compactified k_z axis, then $\beta/2\pi$ must be a differentiable function of k_z with $\int(\partial_{k_z}\beta)\,dk_z/2\pi$ being an integer-valued winding number.

Changes in the continuum Hopf number $\chi^{\text{cont.}}$ and Zak phase $\mathscr{Z}^{\text{cont.}}/2\pi$ across a gapless point are quantized to integer values, assuming that the $\boldsymbol{k}\cdot\boldsymbol{p}$ Hamiltonian is a small-momentum expansion of a tight-binding Hamiltonian. In the next section, we will identify $\delta\chi^{\text{cont.}} \in \mathbb{Z}$ as the change in the Hopf invariant of the tight-binding model, and $\delta\mathscr{Z}^{\text{cont.}}/2\pi \in \mathbb{Z}$ as the corresponding change in the RTP invariant. Assuming the gapless point is described by the Berry-dipole Hamiltonian [Eqs. (3.3),(3.4)], $\chi^{\text{cont.}}$ and $\mathscr{Z}^{\text{cont.}}$ are modified by

$$\delta\chi^{\text{cont.}} = -v\Delta\ell, \tag{3.17}$$
$$\delta\mathscr{Z}^{\text{cont.}} = -2\pi v, \tag{3.18}$$

as ϕ is tuned from negative to positive values. Note that although the continuum Zak phase is defined only modulo 2π, the change in the Zak phase across a Berry dipole (3.18) is well defined modulo nothing if we require a wave function to be smooth for all $(\boldsymbol{k},\phi) \neq (0,0)$.

In analogy with the derivation of Eq. (3.11), we argue that the change in the continuum Hopf number over a Berry dipole given by the spinor (3.5) has an opposite sign than for the spinor (3.3), $\delta\chi^{\text{cont.}} = v\Delta\ell$. Therefore, more generally for both spinors (3.3) and (3.5) this change is determined by the difference in angular momenta between the conduction and the valence band, defined in Eq. (3.6):

$$\delta\chi^{\text{cont.}} = -v(\ell_c - \ell_v). \tag{3.19}$$

The change in the continuum Zak phase given by Eq. (3.18) is valid for Hamiltonians defined through both spinors (3.3) and (3.5).

Equation (3.18) can be directly derived after noticing that the valence intra-cell wave function of the Hamiltonian in Eq. (3.4) can be analytically expressed as

$$|u_v(\boldsymbol{k})\rangle = e^{i\beta(k_z)} i\sigma_y \zeta^*(\boldsymbol{k})/\|\zeta(\boldsymbol{k})\|, \tag{3.20}$$

with ζ given in Eq. (3.3) and a phase $\beta(k_z)$ chosen to ensure a smooth wave function along the compactified k_z-axis.[3] Plugging this wave function in the definition of the continuum Zak phase in Eq. (3.16) gives the change in the Zak phase according to Eq. (3.18).

Details 3.5 The Berry connection computed in the gauge specified in Eq. (3.20) is $\mathcal{A}_z(0,0,k_z) = -v\phi/(k_z^2+\phi^2) - \partial_{k_z}\beta(k_z)$, which plugged into the definition of the continuum Zak phase in Eq. (3.16) gives $\mathscr{Z}^{\text{cont.}} = -\pi\,[1 + v\,\text{sgn}(\phi)]$. Hence, when ϕ changes sign from negative to positive, the continuum Zak phase changes according to Eq. (3.18).

3 To guarantee this, we choose the phase $\beta(k_z)$, which depends smoothly on k_z, such that $\beta(-\infty) = 0$ and $\beta(\infty) = \pi$.

The quantized jump of the Hopf number expressed in Eq. (3.17) is derived generally in Appendix A.2.3. For the particular case of $\Delta\ell = 1$ and $v = 1$, we present here a pictorial argument for $\chi^{\text{cont.}} = \pm 1/2$, with the sign changing across $\phi = 0$. We utilize Wilczek and Zee's [68, 96] correspondence of the unit Hopf invariant with a 'self-eating, rotating' skyrmion texture for the *pseudospin vector* $\boldsymbol{h}$ associated with the Hamiltonian $h(\boldsymbol{k}) = \boldsymbol{h}(\boldsymbol{k}) \cdot \boldsymbol{\sigma}$. By 'self-eating' and 'rotating', we mean that the skyrmion's 'worldline' forms a loop in $\boldsymbol{k}$-space, with the skyrmion pseudospin texture (in a plane orthogonal to the loop) rotating by 2π as $\boldsymbol{k}$ is advanced along the loop, as illustrated in Fig. 1 of Ref. [96]. Analogously, we now argue that $\chi^{\text{cont.}} = \pm 1/2$ for the Berry-dipole transition is associated with 'half' a self-eating, rotating skyrmion: consider a 2-dimensional radial cut given by $\varphi_{\boldsymbol{k}} = 0$, $\theta_{\boldsymbol{k}} \in [0, \pi]$ and $|\boldsymbol{k}| \in [0, R]$, where $(|\boldsymbol{k}|, \theta_{\boldsymbol{k}}, \varphi_{\boldsymbol{k}})$ are spherical coordinates in the $\boldsymbol{k}$-space[4] and R is a large radius. The pseudospin texture on this cut forms half of a skyrmion, as $\boldsymbol{h}(\boldsymbol{k})$ covers half of the Bloch two-sphere when $\boldsymbol{k}$ is swept over the cut [cf. Fig. 3.2(b)]. Indeed the vectors on the edge of the cut are mapped to the great circle of the two-sphere with $h_y = 0$, while all vectors within the cut cover the hemisphere given by $h_y < 0$ for $\phi < 0$, and the hemisphere given by $h_y > 0$ for $\phi > 0$ [cf. Fig. 3.2(d)]. Whether it is the hemisphere with $h_y < 0$ or with $h_y > 0$, determines the sign of $\chi^{cont.} = \pm 1/2$. The sense in which this half-skyrmion is 'rotating' is illustrated in Fig. 3.2(a,c), where the hyperboloid is the preimage of the Bloch-sphere equator ($h_z = 0$): each point on the hyperboloid is colored according to the angle θ_{xy} between the (h_x, h_y)-vector and the h_x-axis ($h_x = \sqrt{h_x^2 + h_y^2}\cos\theta_{xy}$), following a color-coding scheme in the inset of Fig. 3.2(a). For any point on the hyperboloid, we see that θ_{xy} changes by 2π as we encircle the rotation axis while circumnavigating the hyperboloid sheet at a fixed 'elevation' k_z.

The presented results demonstrate that the Berry-dipole transition alters the value of the topological numbers in Eqs. (3.15) and (3.16). In the following Chapter 4, we show how the $\boldsymbol{k} \cdot \boldsymbol{p}$ model of the Berry dipole arises as the small-momentum expansion of a tight-binding Hamiltonian on a lattice. Such a lattice regularization makes precise the notion of 'closing off' the infinite preimage lines.

3.3 THE BERRY DIPOLE IS 'HARD TO REACH'

To interpolate from an insulating, rotation-symmetric Hamiltonian to a Berry-dipole Hamiltonian requires fine-tuning more Hamiltonian parameters than would otherwise be needed to interpolate to a generic, non-insulating, rotation-symmetric Hamiltonian. How many more parameters exactly? We address this question in this section, wherein we also attribute the additional fine-tuning to an 'emergent' mirror symmetry of the Berry-dipole $\boldsymbol{k} \cdot \boldsymbol{p}$ Hamiltonian (that is absent in the tight-binding Hamiltonian).

Let us construct a rotation-symmetric $\boldsymbol{k} \cdot \boldsymbol{p}$ Hamiltonian exhibiting a Berry dipole. For concreteness, we choose the Berry dipole spin to be $\Delta\ell = 1$ (which corresponds to the unit difference between angular momenta of the

4 We specify the spherical coordinates to be $k_x = |\boldsymbol{k}|\sin\theta_{\boldsymbol{k}}\cos\varphi_{\boldsymbol{k}}$, $k_y = |\boldsymbol{k}|\sin\theta_{\boldsymbol{k}}\sin\varphi_{\boldsymbol{k}}$ and $k_z = |\boldsymbol{k}|\cos\theta_{\boldsymbol{k}}$.

basis orbitals), and then a general rotation-symmetric Hamiltonian has the form

$$\begin{aligned} h(\boldsymbol{k}) &= f(\boldsymbol{k})\sigma_+ + f(\boldsymbol{k})^*\sigma_- + g(\boldsymbol{k})\sigma_z, \quad \sigma_\pm = \frac{\sigma_x \pm i\sigma_y}{2}, \\ f(\boldsymbol{k}) &= \alpha k_- + \beta k_-(k_z - b) \ \in \mathbb{C}; \quad k_\pm = k_x \pm i k_y, \\ g(\boldsymbol{k}) &= a(k_z - b)^2 + c k_+ k_- + d \ \in \mathbb{R}, \end{aligned} \tag{3.21}$$

with α, β being complex constants, and a, b, c, d real constants. Equation (3.21) reduces to the Hamiltonian of a Berry dipole centered at the momentum origin [Eqs. (3.3,3.4) with $\phi = 0$] if the above $\boldsymbol{k}\cdot\boldsymbol{p}$ parameters take the particular values:

$$\text{Berry dipole:} \quad b = d = \alpha = 0, \quad c = -a = \beta/2 = 1. \tag{3.22}$$

Even after allowing for simple generalizations of the Berry-dipole Hamiltonian, we find it necessary to tune at least three real parameters to attain a Berry-dipole Hamiltonian from Eq. (3.21).

Details 3.6 The said generalizations are the following. First, the sign of the Hamiltonian is of little significance; second, the momenta can be rescaled while preserving rotation symmetry; third, the bands are allowed to touch at an arbitrary point along the k_z-axis. The resulting more general Berry-dipole Hamiltonian has the form

$$\begin{aligned} h(\boldsymbol{k}) &= \pm\zeta^\dagger(\boldsymbol{k})\sigma\zeta(\boldsymbol{k})\cdot\boldsymbol{\sigma}, \\ \zeta(\boldsymbol{k}) &= \begin{pmatrix} Zk_- \\ A(k_z - b) \end{pmatrix}, \end{aligned} \tag{3.23}$$

with parameters $Z, A \in \mathbb{C}$ and $b \in \mathbb{R}$.

To tune the Hamiltonian given by Eq. (3.21) to the Berry-dipole Hamiltonian (3.23), one needs to tune two real parameters to $d = \alpha = 0$. Parameters β and c, related to the free parameters of the Berry-dipole Hamiltonian as $\beta = \pm 2ZA^* \in \mathbb{C}$ and $c = \pm|Z|^2 \in \mathbb{R}$, are kept free. However, the real parameter a must be tuned to the value fixed by the free parameters β and c, namely $a = -|\beta/2|^2/c$. Thus, in total, we require fine tuning of three real parameters.

The necessity of fine-tuning can be partially justified by certain symmetries of the Berry-dipole $\boldsymbol{k}\cdot\boldsymbol{p}$ Hamiltonian that are generically absent in the tight-binding Hamiltonian. Since the $\boldsymbol{k}\cdot\boldsymbol{p}$ Hamiltonian is obtained by truncating a Taylor expansion of the tight-binding Hamiltonian, these 'certain symmetries' apply to low-order terms in the expansion but are generically broken at higher order. To the extent that the low-energy physics of insulators is determined by Bloch states in a small $\boldsymbol{k}$-region containing the band-touching point, one may refer to these 'symmetries' as *emergent*.

One of these emergent symmetries constrains the Berry-dipolar Hamiltonian [Eqs. (3.3–3.4)] as

$$\sigma_z h(\boldsymbol{k}_\perp, k_z; \phi)\sigma_z = h(\boldsymbol{k}_\perp, -k_z; -\phi), \tag{3.24}$$

which might be viewed as a π-rotation symmetry in the 4D $(\boldsymbol{k}, \phi)$-space. [Cf. Dets. 3.7 for the proof of Eq. (3.24).] At the phase-transition point ($\phi = 0$), the π-rotation reduces to a mirror symmetry that inverts k_z in $\boldsymbol{k}$-space, and correspondingly inverts the rotational axis in real space.[5] (In short, we call this symmetry over the 3D $\boldsymbol{k}$-space a *z-mirror symmetry*.) An alternative view of Eq. (3.24) is that ϕ parametrizes a Hamiltonian perturbation that breaks the z-mirror symmetry. One may further verify that the z-mirror symmetry fixes the complex $\boldsymbol{k}\cdot\boldsymbol{p}$ parameter α in Eq. (3.21) to zero, as is true for the Berry-dipole Hamiltonian.

5 For rotation-symmetric $\boldsymbol{k}\cdot\boldsymbol{p}$ Hamiltonians, composing a z-mirror reflection with a two-fold rotation (about z) gives a spatial-inversion operation.

Details 3.7 To see that the Berry-dipole Hamiltonian obeys the constraint (3.24), note that the spinor-form Hamiltonian (3.4) can be written in terms of spinor components as

$$h(\boldsymbol{k};\phi) = \begin{pmatrix} |\zeta_1(\boldsymbol{k};\phi)|^2 - |\zeta_2(\boldsymbol{k};\phi)|^2 & 2\zeta_1(\boldsymbol{k};\phi)\zeta_2^*(\boldsymbol{k};\phi) \\ 2\zeta_1^*(\boldsymbol{k};\phi)\zeta_2(\boldsymbol{k};\phi) & -|\zeta_1(\boldsymbol{k};\phi)|^2 + |\zeta_2(\boldsymbol{k};\phi)|^2 \end{pmatrix}, \tag{3.25}$$

where $\zeta(\boldsymbol{k};\phi) = (\zeta_1(\boldsymbol{k};\phi), \zeta_2(\boldsymbol{k};\phi))^\top$. Components of the spinor (3.3) satisfy the relations $\zeta_{1(2)}(\boldsymbol{k}_\perp, -k_z; -\phi) = (-)\zeta_{1(2)}(\boldsymbol{k}_\perp, k_z; \phi)$. Plugging the spinor components evaluated at $(\boldsymbol{k}_\perp, -k_z; -\phi)$ into Eq. (3.25), we see that Eq. (3.24) holds.

Identifying the 4D π-rotation symmetry confers two other advantages: the first is that it inspires a strategy to realize crystalline Hopf insulators that is alluded to in Sec. 3.4.1; the second is that it explains why the continuum Hopf number [Eq. (3.15)] and continuum Zak phase [Eq. (3.16)] attain the half-integer values for the spinor-form Hamiltonians [Eqs. (3.3–3.4)]:

$$\chi^{\text{cont.}}[h(\boldsymbol{k};\phi)] = -\frac{1}{2} v \Delta\ell \, \text{sgn}[\phi], \tag{3.26a}$$

$$\frac{\mathscr{Z}^{\text{cont.}}}{2\pi}[h(\boldsymbol{k};\phi)] = -\frac{1}{2} v \, \text{sgn}[\phi]. \tag{3.26b}$$

Equation (3.26a) was argued pictorially in Sec. 3.2 and is proven in Appendix A.2.3, while Eq. (3.26b) can be proven in analogy with the argument in Sec. 3.2 and Dets. 3.5, with the modified assumption that the intra-cell function is symmetric under the π-rotation. The 4D π-rotation symmetry constrains the continuum topological numbers as:

$$\chi^{\text{cont.}}[h(\boldsymbol{k};\phi)] = -\chi^{\text{cont.}}[h(\boldsymbol{k};-\phi)], \tag{3.27a}$$

$$\frac{\mathscr{Z}^{\text{cont.}}}{2\pi}[h(\boldsymbol{k};\phi)] = -\frac{\mathscr{Z}^{\text{cont.}}}{2\pi}[h(\boldsymbol{k};-\phi)], \tag{3.27b}$$

where the square brackets indicate arguments of $\chi^{\text{cont.}}$ and of $\mathscr{Z}^{\text{cont.}}/2\pi$, here treated as functionals. To rationalize Eqs. (3.27), we equate the Hopf number and the Zak phase of two equal Hamiltonians $h(\boldsymbol{k};\phi)$ and $\sigma_z h(\boldsymbol{k}_\perp, -k_z; -\phi)\sigma_z$ [related by Eq. (3.24)]. Interpreting the conjugation of the Hamiltonian with σ_z matrices (and the associated reversal of sign of k_z) as the z-mirror crystallographic operation, we obtain Eqs. (3.27) by (a) the interpretation of the Zak phase as a positional z-polarization which is odd under z-mirror operation, and by (b) the fact (proven in Sec. 4.5) that the Hopf invariant is odd under improper crystallographic spacetime operations – of which z-mirror is a case in point.[6] Coupling Eq. (3.27) with the guaranteed integer-quantization of *changes* to the continuum topological numbers across the phase-transition point ($\phi = 0$) (which were discussed in Sec. 3.2), one derives that the continuum topological numbers are indeed quantized to half-integer values as ϕ approaches zero from both positive and negative directions.

3.4 SEMIMETALS INTERMEDIATING CRYSTALLINE HOPF INSULATORS

In this section we explore semi-metallic phases in the vicinity of the Berry dipole that are 'easier-to-reach' as they do not require fine tuning. In Sec. 3.4.1 we show that a rotation-symmetric interpolation[7] from trivial to crystalline

6 Any crystallographic spacetime operation has a four-dimensional matrix action on the four-vector of spacetime, with the matrix M a direct sum $O(3) \oplus O(1)$; $O(1) = \{1, -1\}$ simply distinguishes if the operation reverses time or not. We say the spacetime operation is proper if $\det[M] = 1$, and improper if $\det[M] = -1$.

7 If $h(\boldsymbol{k};t)$ interpolates between a trivial insulator $h(\boldsymbol{k};0)$ to a crystalline Hopf insulator $h(\boldsymbol{k};1)$, we say the interpolation is rotation-symmetric if the Hamiltonian is rotation-symmetric for all $t \in [0,1]$.

Hopf insulator is typically intermediated by a topological-semimetallic phase that involves either Weyl-point or nodal-line degeneracies. The basic properties of these intermediate topological-semimetallic phases are illustrated by a model $\boldsymbol{k}\cdot\boldsymbol{p}$ Hamiltonian in Sec. 3.4.2, which is a first step toward more naturalistic/material-realistic models of delicate topology.

The emergent mirror symmetry discussed in the previous section offers a symmetrically-distinct route to a crystalline Hopf insulator. This stems from the observation that the mirror-symmetric Berry-dipole band-touching *point* can be continuously expanded (in $\boldsymbol{k}$-space) to a mirror-symmetric topological nodal-*loop*. Thus, an alternative strategy to realize a crystalline Hopf insulator is to begin from a mirror-symmetric topological-nodal-line semimetal and break the mirror symmetry in a manner to be ascertained.

3.4.1 *Topological semimetals are 'easier to reach'*

To understand the generic phase transition between distinct crystalline Hopf insulators, note that the considered symmetry setting (Wigner-Dyson class A with rotation symmetry) imposes no local-in-$\boldsymbol{k}$ constraint on the $\boldsymbol{k}\cdot\boldsymbol{p}$/tight-binding Hamiltonian $h(\boldsymbol{k})$ at generic $\boldsymbol{k}$. This implies [122, 123] that the generic number of real parameters needed to tune to an energy degeneracy (or two-band touching) is three; the number $\mathfrak{D}=3$ is sometimes referred to as the *codimension of an eigenvalue degeneracy*. One implication is that the generic band degeneracy in three momentum dimensions is a Weyl point [125], i.e., a band-touching point in $\boldsymbol{k}$-space acting as a monopole source of Berry curvature [70].

If the three-dimensional $\boldsymbol{k}$-space is supplemented with a tuning parameter ϕ, the generic band-degeneracy in the four-dimensional $(\boldsymbol{k},\phi)$-space is a one-dimensional line. Without additional symmetries and without fine-tuning, such a line generically forms a contractible loop with a nonzero projection $[\phi_1,\phi_2]$ on the ϕ-axis; such loop can be interpreted as the concatenation of world-lines of at-least-two Weyl $\boldsymbol{k}$-points (of opposite monopole charge) which are created at an earlier 'time' ϕ_1 and annihilated at a later ϕ_2. In other words, for any ϕ in the (open) interval (ϕ_1,ϕ_2), the $\boldsymbol{k}$-space Hamiltonian corresponds to a Weyl semimetal (WSM). We will refer to the union of these world-lines as a *Weyl-point trajectory* (WPT). By enclosing the trajectory with a momentum 3-sphere S^3, the WPT can be ascribed a topological charge given by an element of the third homotopy group of the classifying space of two-band Hamiltonians: $\pi_3(S^2)=\mathbb{Z}$, i.e., the Hopf invariant on the enclosing sphere. If this invariant is nontrivial, then the two insulating phases for $\phi<\phi_1$ resp. $\phi>\phi_2$ exhibit a different value of the Hopf invariant.

Reading the above argument 'backwards', one finds that two rotation-symmetric Hamiltonians with distinct Hopf invariants are generically intermediated by an extended WSM region. The exceptions require to either:

(*i*) continuously shrink the WPT to a single point (a Berry dipole!) on a rotation-invariant $\boldsymbol{k}$-line, or

(*ii*) continuously deform the WPT such that it lies entirely within the $\boldsymbol{k}$-space at fixed 'time' $\phi=\phi_0$.

Observe that a WPT occurring 'instantaneously' is simply a topological nodal-line degeneracy. While both options generically require to fine-tune the rotation-symmetric Hamiltonian in Wigner-Dyson symmetry class A, option (*ii*) can also arise in a non-generic/higher-symmetry scenario where the Hamiltonian is z-mirror-symmetric at $\phi=\phi_0$ but z-mirror-asymmetric

at $\phi \neq \phi_0$; this is consistent with a previous observation that a non-trivial Hopf invariant requires breaking all improper crystallographic symmetries, including all mirror symmetries.

3.4.2 *Case study of intermediate topological semimetals*

We illustrate options (*i–ii*) with a model $\boldsymbol{k} \cdot \boldsymbol{p}$ Hamiltonian:

$$\begin{aligned} h(\boldsymbol{k}; \mathbb{m}) = 2\alpha k_z \left(k_x \sigma_x - k_y \sigma_y\right) - 2\beta k_z \left(k_x \sigma_y + k_y \sigma_x\right) \\ + \left[\gamma(k_x^2 + k_y^2) - \delta k_z^2 - \mathbb{m}\right] \sigma_z, \end{aligned} \tag{3.28}$$

where $\mathbb{m}$ is a real-valued tuning parameter which we will shortly relate to the parameter ϕ in the Berry-dipole Hamiltonian. The Hamiltonian in Eq. (3.28) is invariant under mirror symmetry $M_z : (k_x, k_y, k_z) \mapsto (k_x, k_y, -k_z)$ represented by σ_z, and rotation symmetry $C_\theta : (k_+, k_-, k_z) \mapsto (e^{i\theta} k_+, e^{-i\theta} k_-, k_z)$ represented by $R_{C_\theta} = \exp(i\theta\sigma_z/2)$. The mirror symmetry implies that the $\sigma_{x,y}$ (σ_z) term is odd (even) in k_z, and the C_θ-symmetry then guarantees that (up to unimportant terms proportional to the identity matrix) the expression in Eq. (3.28) with free coefficients α, β, γ, δ and $\mathbb{m}$ is the most general symmetry-compatible Hamiltonian up to quadratic order in the momentum components.

By employing a rotation of the in-plane coordinates (k_x, k_y), and after rescaling k_z relative to the in-plane coordinates, we can generally achieve $\alpha = |\gamma| = |\delta| = 1$ and $\beta = 0$. We further assume $\gamma, \delta > 0$, leading to

$$h_0(\boldsymbol{k}; \mathbb{m}) = 2k_z \left(k_x \sigma_x - k_y \sigma_y\right) + \left(k_x^2 + k_y^2 - k_z^2 - \mathbb{m}\right) \sigma_z, \tag{3.29}$$

in which case the model is a Weyl semimtal (WSM) with a pair of Weyl points located at $\boldsymbol{k} = (0, 0, \pm\sqrt{|\mathbb{m}|})$ for $\mathbb{m} < 0$,and a nodal-line semimetal (NLSM) with a nodal ring of radius $\sqrt{\mathbb{m}}$ located at the $k_z = 0$ plane for $\mathbb{m} > 0$ [126]. Notably, the critical point $\mathbb{m} = 0$ is a Berry dipole, described by the spinor $\zeta(\boldsymbol{k})^\top = (k_x + ik_y\,,\, k_z)$, suggesting that the outlined model is close to the Hopf-insulating phase.

We now consider breaking of the M_z and C_θ symmetry, and study the fate of the semi-metallic phases and of the Berry dipole. Multiple additional terms can be added to the Hamiltonian; for simplicity, we consider only two,

$$h_{\text{perp.}}(\boldsymbol{k}; A, B) = +2A \left(k_x \sigma_y + k_y \sigma_x\right) + 2B\sigma_x, \tag{3.30}$$

which illustrate the generic behavior of the Berry dipole under perturbations. The B term breaks both mirror and rotation symmetries, while the A term breaks only the mirror symmetry. As a function of parameters $(\mathbb{m}, A, B)$, the combined Hamiltonian $h_0(\boldsymbol{k}; \mathbb{m}) + h_{\text{perp.}}(\boldsymbol{k}; A, B)$ has a rich phase diagram illustrated in Fig. 3.3, which we now discuss in detail.

First, for $B = 0$ (when rotation symmetry is preserved) there is a WSM phase at $\mathbb{m} < 0$, and a NLSM phase at $A = 0, \mathbb{m} > 0$. The union of both gapless phases separates two gapped regions, which we now argue to be topologically distinct. Observe that the trajectory marked by '2' (dashed green line), parametrized as $A = \phi$ and $\mathbb{m} = \phi^2$, corresponds *exactly* to the Hamiltonian in Eq. (3.4) with spinor $\zeta(\boldsymbol{k})^\top = (k_x + ik_y\,,\, k_z + i\phi)$, which exhibits a single gapless point: a Berry dipole. It is stated in Eq. (3.17) (and derived in Appendix A.2.3) that the Berry dipole carries a non-trivial Hopf charge; therefore, the two insulating phases are characterized by a different value of the Hopf invariant, which changes by -1 along the trajectory '2'.

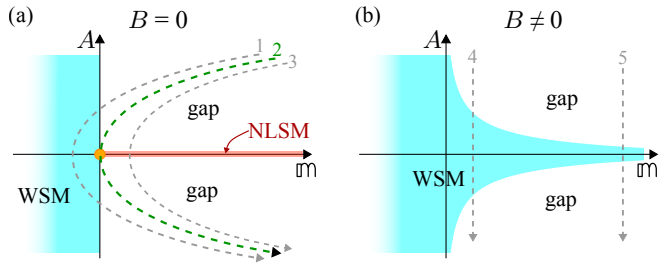

Figure 3.3: Phase diagram of the Hamiltonian in Eq. (3.29) with the perturbations in Eq. (3.30) that break both M_z and C_{4z} symmetry. (a) For $B = 0$ (rotation symmetry preserved) there is a Weyl semimetal (WSM, cyan) phase at $\mathbb{m} < 0$, and a nodal-line semimetal (NLSM, red) phase at $A = 0, \mathbb{m} > 0$. The gapless phases separate two gapped regions (white) that have different values of the Hopf invariant. The trajectory '2' (dashed green line), described by $A = \phi$ and $\mathbb{m} = \phi^2$, reproduces the spinor-form Hamiltonian in Eqs. (3.4) and (3.3). However, a more generic trajectory connecting the two gapped regions either exhibits an extended WSM phase (path '1') or passes through the NLSM phase (path '3'). (b) For $B \neq 0$, the NLSM phase expands into a Weyl semimetal. In this case, arbitrary trajectory connecting the two gapped regions passes through an extended WSM phase. Paths '4' and '5' are discussed in the text of Sec. 3.4.2. The change in the Hopf invariant along the trajectories '1'–'5' amounts to $\delta\chi = -1$.

However, the Berry-dipole transition is fine-tuned: small deviations (indicated by path '1' resp. '3') result in an intermediate semi-metallic phase that is either a WSM or NLSM. In these cases, the change of the Hopf invariant is facilitated by the non-trivial Hopf charge carried by the WPT in the four-dimensional $(\boldsymbol{k}, \phi)$-space, representing an "expanded" analog of the Berry dipole.

The inclusion of finite $B \neq 0$ transforms the NLSM phase into a WSM region, bounded by lines $|A| < |B|/\sqrt{\mathbb{m}}$. Therefore, when moving from the gapped phase at $A > 0$ to the gapped phase at $A < 0$, one always needs to pass through an extended WSM phase where a pair of Weyl points are first created and later annihilated. [One rationalization is that the mirror symmetry needed to protect the NLSM is broken throughout the phase diagram in Fig. 3.3(b).] The corresponding WPT is nearly vertical (i.e, along the k_z-axis) in the $\boldsymbol{k}$-space for small $\mathbb{m}/B$ (path '4') and nearly horizontal [i.e., inside the (k_x, k_y)-plane] for large $\mathbb{m}/B$ (path '5'). Setting $\mathbb{m} = \cos t$ and $B = \sin t$ with $t \in [0, \frac{\pi}{2}]$ allows us to 'rotate' the WPT trajectory in the $(\boldsymbol{k}, A)$ space from lying in (k_x, k_y)-plane (phase transition via NLSM) to lying in (k_z, A)-plane (phase transition via extended WSM region with Weyl points along the rotation axis). We have thus shown on a concrete model how the Berry-dipole transition is generically altered into a NLSM or an extended WSM phase.

4

RTP AND HOPF INVARIANTS

In this chapter we extend the notion of the Berry dipole from $\boldsymbol{k} \cdot \boldsymbol{p}$ models to Pn-symmetric tight-binding Hamiltonians ($n \in \{2, 3, 4, 6\}$), with Pn being the space group whose order-n point group is generated by an n-fold rotation. These tight-binding Hamiltonians will be formulated in Sec. 4.1. In Sec. 4.2 we define the lattice analogs of the continuum Hopf number and Zak phase. The lattice analog of a nontrivial continuum Zak phase will be interpreted as a 'returning' Thouless pump (RTP), by analogy with charge pumping in one-momentum-parameter Hamiltonians. In Sec. 4.3, we discuss the changes in the Hopf and in the RTP invariants across the possible Berry-dipole band touching points. In particular, we show how the individual contributions from each touching point add up for a resulting change in a lattice invariant. We proceed with Sec. 4.4 by presenting representative models of crystalline Hopf insulators for all Pn space groups (as summarized in Table 4.2). These models illustrate how crystallographic symmetry enriches the topological classification of two-band Hamiltonians. Are crystallographic symmetries always compatible with a non-trivial Hopf invariant? We conclude this chapter with Sec. 4.5, where we determine the symmetries that set the Hopf invariant to zero.

CHAPTER CONTENTS

4.1 Pn-SYMMETRIC TIGHT-BINDING HAMILTONIANS

We consider a class of Pn-symmetric tight-binding Hamiltonian whose Hilbert space is specified by two *representative tight-binding-basis orbitals*: φ_1 and φ_2, with φ_1 unrelated to φ_2 by any space-group operation.[1] Modulo Bravais-lattice translations, φ_α is defined to have a positional center (or *Wyckoff position*) $\boldsymbol{r}_\alpha = (\boldsymbol{r}_{\alpha,\perp}, z_\alpha)$.

We assume the site-stabilizer group of $\boldsymbol{r}_\alpha$ ($\mathcal{G}_{\boldsymbol{r}_\alpha}$) to be isomorphic to the order-n-rotational point group C_n; in short, we say that $\boldsymbol{r}_\alpha$ is a C_n-*invariant*

1 Our considerations can be generalized to any $\mathcal{G}$-symmetric tight-binding Hamiltonian, with $\mathcal{G}$ any space group (double or not, magnetic or not) that contains Pn as a subgroup, such that φ_1 is unrelated to φ_2 by elements in $\mathcal{G}$.

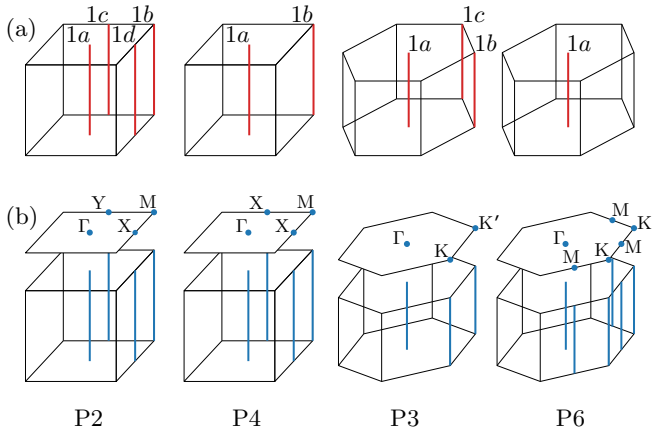

Figure 4.1: For each of the space groups Pn ($n \in \{2,4,3,6\}$), we show (a) all C_n-invariant Wyckoff positions in the primitive unit cell, and (b) all C_m-invariant momentum-lines in the Brillouin zone (BZ), with m a nontrivial divisor of n, as well as all C_m-invariant momentum-points in the reduced Brillouin zone (rBZ); rBZ is obtained from BZ by projection in the direction of the rotation axis.

Wyckoff position. All C_n-invariant Wyckoff positions for space groups Pn, $n \in \{2,3,4,6\}$ are presented in Fig. 4.1(a) as red lines, indicating that $\boldsymbol{r}_{\alpha,\perp}$ are symmetry-fixed but z_α are not.

We further assume φ_α transforms under a one-dimensional representation $e^{i2\pi\mathcal{L}_\alpha/n}$ of C_n, for both $\alpha = 1,2$. We refer to $\mathcal{L}_\alpha \in \{0,1,\ldots,n-1\}$ as the *on-site angular momenta*.[2] Mod-n integer-valued angular momenta most directly apply to bosonic particles, with the caveat that 'insulating Hamiltonians' should be interpreted more generally as single-boson Hamiltonians with a spectral gap separating the two bands. The ultra-cold atomic realization of the Hopf invariant in Ref. [127] is a case in point.

Mod-n integer-valued angular momenta also apply to three categories of single-*fermion* Hamiltonians:

(*i*) In the absence of spin-orbit-coupling, the wave function at each $\boldsymbol{k}$ factorizes into a tensor product of orbital and spin wave functions. Assuming the spin $SU(2)$ symmetry is not spontaneously broken by magnetism, the spin wave function plays a trivial 'spectator role' and is removed from the Hilbert space under consideration. A 'two-band Hamiltonian' is then implicitly the restriction of a spin-dependent Hamiltonian to its action on the orbital wave function; a conduction band (given by a single linearly-independent Bloch-type orbital wave function) is implicitly a shorthand for an energy-degenerate conduction band (given by two linearly-independent, spin-dependent Bloch functions), and likewise for the valence band.

(*ii*) If the spin $SU(2)$ symmetry is spontaneously broken down to a subgroup $H \subset SU(2)$, with H containing $U(1)$ as a subgroup (meaning one component of spin is conserved, say, S_z), then the Hilbert space decomposes into two

2 For the purpose of introducing notation used throughout the text, $\mathcal{L}_\alpha$ is an example of a *mod-p quantity*, $p \in \mathbb{Z}$:

$$\text{integer mod } p \in \{0,1,\ldots,p-1\}, \tag{4.1a}$$

and we will denote a mod-p equivalence between two integer-valued quantities by '$=_p$':

$$a =_p b \quad \text{meaning} \quad a \bmod p = b \bmod p. \tag{4.1b}$$

S_z-labeled sectors, and our 'two-band Hamiltonian' should be interpreted as a mean-field Hamiltonian applying to either of these sectors. In each sector, one can remove the spectator spin quantum number, such that all angular momenta are integer-valued. For instance, the Hopf insulator could be realized in a spin-$U(1)$-symmetric ferromagnetic insulator.

(*iii*) If the spin $SU(2)$ symmetry is spontaneously broken down to H with no $U(1)$ subgroup, then the mean-field Hamiltonian essentially has a interaction-induced spin-orbit coupling, which can be addressed in essentially the same manner as a single-particle, non-symmetry-breaking Hamiltonian whose spin-orbit coupling has a relativistic origin. In both cases, the spin quantum number is not a spectator variable, and one should begin by considering *half-integer-spin representations* of the site stabilizer. However, our restriction to one-dimensional representations of the site stabilizer allow to redefine the n-fold rotation operator by an overall multiplicative phase factor, such that all eigenvalues of the redefined rotation operator are shifted toward mod-n integer-valued angular momenta. A 'two-band Hamiltonian' is then unambiguously 'two-band', with the spin-orbit coupling needing to be sufficiently strong that the bands closest to the Fermi level are spin-split.

By applying all Bravais-lattice translations to the representative basis orbital φ_α, one generates an infinite set of Wannier orbitals that forms a representation space of Pn [compare with the basis defined in Eq. (2.80)]. The band representation induced from φ_α [see Sec. 2.2.3.2 for the definition of the band representation] is equipped with the equivalence relation as specified in Eq. (2.85). Under this equivalence, the center of the representative orbital z_α can be continuously deformed along the rotation axis, and the support of the representative Wannier orbital can be continuously deformed from one-site-localized to exponentially-localized. Then the equivalence class is fully specified by the data $(\mathcal{L}, \boldsymbol{r}_\perp)$ with $\mathcal{L}$ an on-site angular momentum and $\boldsymbol{r}_\perp$ position in the plane perpendicular to the rotation axis. Henceforth, we will often apply the figure-of-speech of a *band representation induced from an $(\mathcal{L}, \boldsymbol{r}_\perp)$-orbital*, and denote the corresponding equivalence class by $\mathrm{BR}(\mathcal{L}, \boldsymbol{r}_\perp)$.

In the particular case that the representative Wannier orbital is a tight-binding-basis orbital φ_α with on-site angular momentum $\mathcal{L}_\alpha$ and Wyckoff position $\boldsymbol{r}_\alpha$, the induced representation will be referred to as a *basis band representation* and denoted by $\mathrm{BBR}[\varphi_\alpha]$. Importantly, contrary to a band representation, a basis band representation comes without equivalence relation (2.85), and therefore it is a refined notion of a band representation carrying two pieces of additional data: (a) the z_α coordinate of the Wyckoff position, and (b) the fact that the representative Wannier orbital φ_α is not just exponentially-localized but also compactly supported on a single 'site'. $\mathrm{BBR}[\varphi_\alpha]$ is a member of the equivalence class $\mathrm{BR}(\mathcal{L}_\alpha, \boldsymbol{r}_{\alpha,\perp})$. Data (a), despite being irrelevant to the symmetry representation, are of paramount relevance to the returning Thouless pump – a topological invariant that we define in the next section.

The sum of basis band representations induced from φ_1 and φ_2 defines the Hilbert space of our tight-binding Hamiltonian. The two Bloch states attained from the Wannier basis as specified by Eq. (2.1) may be viewed as basis vectors for a two-by-two $\boldsymbol{k}$-dependent tight-binding Hamiltonian $h(\boldsymbol{k})$. Because the Wyckoff positions of φ_1 and φ_2 are not necessarily equal (modulo lattice translations), the tight-binding Hamiltonian is not necessarily periodic, but transforms under reciprocal lattice translations as given by Eq. (2.5).

The Pn symmetry constrains the Hamiltonian as

$$R_{C_n} h(\boldsymbol{k}) R_{C_n}^{-1} = h(C_n \boldsymbol{k}), \tag{4.2}$$

with R_{C_n} a *rotation matrix* that is more generally defined as

$$R_{C_m} = \begin{pmatrix} e^{i2\pi\mathcal{L}_1/m} & 0 \\ 0 & e^{i2\pi\mathcal{L}_2/m} \end{pmatrix} \tag{4.3}$$

for $1 < m \leq n$ being any non-unit, positive divisor of n; the diagonal elements of the rotation matrix specified by the on-site angular momenta of the two representative basis orbitals.

An important concept that underlies the returning Thouless pump (to be formally defined in the next section) is that individual Bloch states can carry an angular momentum. To elaborate, we focus on Bloch states with momenta on any of the vertical C_m-invariant $\boldsymbol{k}$-lines in the BZ. Each such line is denoted γ_Π, where the *reduced momentum* Π is the projection of γ_Π onto the 2D plane perpendicular to the rotation axis. Analogously, the projection of the 3D BZ will be referred to as the *reduced BZ* (rBZ). For each of the space groups Pn, $n \in \{2,3,4,6\}$, all rotation-invariant $\boldsymbol{k}$-lines are presented in Fig. 4.1(b). Note that when $m < n$, the C_m-invariant $\boldsymbol{k}$-lines form an n/m-fold multiplet (n/m-*plet*, in short) of C_n-related $\boldsymbol{k}$-lines. Therefore, we will sometimes speak of the *set of rotation-inequivalent rotation-invariant* $\boldsymbol{k}$*-lines*, which includes only one $\boldsymbol{k}$-line per each n/m-plet.

For any $\boldsymbol{k} \in \gamma_\Pi$, the Hamiltonian satisfies the commutation relation [note the similarity with the rotation-symmetric Chern insulator discussed in Sec. 2.2.2.2]:

$$\begin{aligned} C_m\text{-invariant } \boldsymbol{k}\text{-line } \gamma_\Pi: \quad & [h(\Pi, k_z), V_{\boldsymbol{G}_\Pi} R_{C_m}] = 0, \\ & \boldsymbol{G}_\Pi = C_m \Pi - \Pi. \end{aligned} \tag{4.4}$$

Hence, for a Hamiltonian restricted to a rotation-invariant line, we can define an *itinerant rotation matrix*

$$\widetilde{R}_{C_m}(\Pi) = V_{\boldsymbol{G}_\Pi} R_{C_m}, \tag{4.5}$$

whose two eigenvalues

$$\widetilde{\rho}_{m,\alpha}(\Pi) = \exp\left[i \left(\frac{2\pi\mathcal{L}_\alpha}{m} + \boldsymbol{r}_{\alpha,\perp} \cdot \boldsymbol{G}_\Pi \right) \right] := \exp\left(i \frac{2\pi\widetilde{\mathcal{L}}_\alpha(\Pi)}{m} \right) \tag{4.6}$$

determine the symmetry of extended/itinerant basis Bloch states. The eigenvalues of $\widetilde{R}_{C_m}$ are a function of the on-site angular momenta and Wyckoff positions, because $V_{\boldsymbol{G}_\Pi}$ and R_{C_m} are both diagonal matrices with eigenvalues $e^{i\boldsymbol{r}_{\alpha,\perp}\cdot\boldsymbol{G}_\Pi}$ and $e^{i2\pi\mathcal{L}_\alpha/m}$, respectively. The logarithm of $\widetilde{\rho}_{m,\alpha}(\Pi)$ defines a mod-m *itinerant angular momentum*

$$\widetilde{\mathcal{L}}_\alpha(\Pi) = \mathcal{L}_\alpha + m \frac{\boldsymbol{r}_{\alpha,\perp} \cdot \boldsymbol{G}_\Pi}{2\pi} \mod m, \tag{4.7}$$

which sums two contributions: the first from rotating the representative basis orbital φ_α about its positional center, and the second from rotating the plane-wave phase factor $e^{i\boldsymbol{k}\cdot(\boldsymbol{R}+\boldsymbol{r}_\alpha)}$ in the definition of the Bloch state.

The commutation relation Eq. (4.4) guarantees that the Hamiltonian matrix and the itinerant rotation matrix have common eigenstates at C_m-invariant $\boldsymbol{k}$-lines. The eigenvalue of the itinerant rotation matrix corresponding to the

valence state of the Hamiltonian defines the itinerant angular momentum of the valence band $\widetilde{\mathcal{L}}_v(\Pi)$, which at a fixed reduced momentum Π coincides either with $\widetilde{\mathcal{L}}_1(\Pi)$ or with $\widetilde{\mathcal{L}}_2(\Pi)$, with a possibly different choice at different Π. Defined in a similar way is the itinerant angular momentum of the conduction band $\widetilde{\mathcal{L}}_c(\Pi)$, which coincides with $\widetilde{\mathcal{L}}_2(\Pi)$ or $\widetilde{\mathcal{L}}_1(\Pi)$, respectively.

In this thesis, we restrict ourselves to tight-binding insulating Hamiltonians with trivial Chern class. A theorem proven in Ref. [120] ensures that the bulk valence band, being nondegenerate at each $\boldsymbol{k}$ and with trivial Chern class, is a band representation; this also holds for the bulk conduction band. It follows that our models would be missed under classification schemes in which band representations are deemed trivial, such as the methods of band structure combinatorics [30], topological quantum chemistry [31], and symmetry indicators [29].

To remind ourselves that the valence band is a band representation, we sometimes refer to the valence band as a *valence band representation* (VBR). Note however that the valence band is generically *not* a basis band representation, even if the two are symmetry-equivalent. The inter-orbital matrix elements of the tight-binding Hamiltonian prevent the valence band from being *continuously deformable* to a basis band representation.

4.2 RTP AND HOPF INVARIANTS FOR TIGHT-BINDING HAMILTONIANS

We are ready to discuss the lattice analogs of the continuum Hopf number and Zak phase discussed in Sec. 3.2 of the previous chapter. The Hopf invariant was already defined in Sec. 2.1.6 as

$$\chi = -\frac{1}{4\pi^2}\int_{\mathrm{BZ}} d^3k\, \boldsymbol{\mathcal{F}}\cdot\boldsymbol{\mathcal{A}}. \tag{4.8}$$

As a reminder, it differs from its continuum analog (3.15) in two aspects: (*i*) the integration domain is changed from the 3-dimensional real space to the BZ, and (*ii*) the intra-cell wave function $|u_v(\boldsymbol{k})\rangle$, used to compute the Berry connection and curvature, is now an eigenstate of the lattice tight-binding Hamiltonian.

According to the geometric theory of polarization [71, 83] and similar to the discussion presented in Sec. 2.1.4.2, the Zak phase of the valence-band wave function [computed over a $\boldsymbol{k}$-line with a fixed reduced momentum $\boldsymbol{k}_\perp = (k_x, k_y)$] is equal (up to a factor 2π) to the 1D electric polarization for a one-momentum-parameter Hamiltonian, obtained by restricting $h(\boldsymbol{k})$ to the same $\boldsymbol{k}$-line:

$$\mathscr{P}(\boldsymbol{k}_\perp) = \frac{1}{2\pi}\int_{-\pi}^{\pi} \mathcal{A}_z(\boldsymbol{k}_\perp, k_z)dk_z. \tag{4.9}$$

Unlike the Hopf invariant, this direct analog of the continuum Zak phase is not quantized, and therefore does not constitute a topological invariant. Instead, we define a topological invariant as a difference in polarization between two inequivalent rotation invariant lines. To guarantee the quantization of the polarization difference, we additionally assume two conditions introduced in details below. The first condition [Eq. (4.10)] ensures that the polarization along a chosen line is fixed modulo integer to the z position of one of the basis orbitals, while the second condition [Eq. (4.16)] fixes the orbitals to be the same at both rotation invariant lines. This is enough for the difference in polarization to be integer-valued [Eq. (4.18)].

Suppose that at a C_m-invariant reduced momentum Π, the itinerant angular momenta of the valence band $\widetilde{\mathcal{L}}_v(\Pi)$ and of the conduction band $\widetilde{\mathcal{L}}_c(\Pi)$ are distinct. In the sense that $\{\widetilde{\mathcal{L}}_v(\Pi)\} \cap \{\widetilde{\mathcal{L}}_c(\Pi)\} = \varnothing$, we call this a

$$\begin{aligned} &\textit{mutually-disjoint condition at } \Pi: \quad \Delta\widetilde{\mathcal{L}}(\Pi) \neq 0. \\ &\text{where } \Delta\widetilde{\mathcal{L}}(\Pi) = \widetilde{\mathcal{L}}_c(\Pi) - \widetilde{\mathcal{L}}_v(\Pi) \mod m. \end{aligned} \tag{4.10}$$

It follows from this condition that the tight-binding Hamiltonian $h(\boldsymbol{k})$ *is diagonal along the line* γ_Π *in a basis that simultaneously diagonalizes the rotation matrix* [cf. Eq. (4.2)].

Let us not forget that $h(\boldsymbol{k})_{\alpha\beta}$ is a two-by-two matrix with row index α corresponding to a basis Bloch state that linearly combines the representative tight-binding-basis orbital φ_α with all its Bravais-lattice translations [cf. Eq. (2.1)]. Each of the two basis Bloch states may be said to be purely of one *orbital character*; clearly, there are only two orbital characters in a two-band Hamiltonian. The above-positioned, italicized statement may then be equivalently stated as: any Bloch energy eigenstate (with momentum $\boldsymbol{k} \in \gamma_\Pi$) is (up to a trivial $U(1)$ phase) a basis Bloch state with momentum $\boldsymbol{k}$, and is thus purely of one orbital character. Because the Hamiltonian is assumed to be insulating, the orbital character is constant along any rotation-invariant $\boldsymbol{k}$-line γ_Π. If the valence-band wave function along γ_Π is of the φ_α-character, then the polarization at Π is fixed, up to an integer, to the z-coordinate of φ_α's Wyckoff position:

$$\gamma_\Pi \text{ of } \varphi_\alpha\text{-character} \quad \Rightarrow \quad \mathscr{P}(\Pi) =_1^{\mathrm{P}n} z_\alpha. \tag{4.11}$$

We have added a superscript to $=_1^{\mathrm{P}n}$ to remind ourselves that the equivalence modulo integers is robust under continuous deformations of the Hamiltonian that preserves both the bulk energy gap and the Pn symmetry. For a derivation of the intuitive result in Eq. (4.11), see Dets. 4.1.

Details 4.1 As was shown in Sec. 2.1.4.2, the geometric theory of polarization gives the following relation

$$\begin{aligned} &\int \frac{dk_z}{2\pi} \left\langle u_j(\boldsymbol{k}_\perp, k_z) \middle| i\partial_{k_z} u_j(\boldsymbol{k}_\perp, k_z) \right\rangle \\ &\qquad =_1 \left\langle\!\left\langle \mathcal{V}_{j,\boldsymbol{k}_\perp,0} \right| P_{\boldsymbol{k}_\perp} \hat{z} P_{\boldsymbol{k}_\perp} \left| \mathcal{V}_{j,\boldsymbol{k}_\perp,0} \right\rangle\!\right\rangle, \end{aligned} \tag{4.12}$$

where the lattice constant in z-direction assumed to be unit, $|\mathcal{V}_{j,\boldsymbol{k}_\perp,0}\rangle\rangle$ are the hybrid Bloch-Wannier states localized in z-direction, defined as in Eq. (2.34), $P_{\boldsymbol{k}_\perp}$ is the projector onto states with reduced momentum $\boldsymbol{k}_\perp$, and the position operator in the z-direction can be decomposed as

$$\hat{z} = \sum_{\boldsymbol{R},\alpha'} |\boldsymbol{R},\alpha'\rangle\rangle (R_z + z_{\alpha'}) \langle\langle \boldsymbol{R},\alpha' \big|. \tag{4.13}$$

Along the rotation-invariant lines γ_Π with distinct itinerant angular momenta, the two basis orbitals do not hybridize, and hence, the valence hybrid state is simply the basis state $|\mathcal{V}_{v,\Pi,R_z}\rangle\rangle = |\Pi, R_z, \alpha\rangle\rangle$. Plugging this state at $R_z = 0$ into Eq. (4.12) we can straightforwardly compute that the right-side of the equation is equal to the z position of the basis orbital φ_α and we get

$$\mathscr{P}(\Pi) = \frac{1}{2\pi} \int dk_z \, \langle u_v(\Pi, k_z) | i\partial_{k_z} u_v(\Pi, k_z) \rangle =_1 z_\alpha. \tag{4.14}$$

If on the contrary we choose to work in the periodic convention for the tight-binding Hamiltonian (introduced in Eq. (2.9)), the position operator in z-direction will lose the information about the spacial positions of the basis orbitals:

$$\hat{z} = \sum_{\boldsymbol{R},\alpha'} |\boldsymbol{R},\alpha'\rangle\rangle R_z \langle\langle \boldsymbol{R},\alpha' \big|. \tag{4.15}$$

In this case the geometric phase defined by Eq. (4.9) is not equal to the position of the basis orbital z_α, but instead acquires an integer value.

Let us assume that the mutually-disjoint condition is satisfied at a pair of rotation-invariant reduced momenta Π_1 and Π_2. Two possibilities emerge:

either (a) the valence-band wave functions along γ_{Π_1} and γ_{Π_2} are of the same orbital character, or (b) they are not. Utilizing the Greek word '*isos*' meaning 'equal to', we say in case (a) that the *iso-orbital condition* holds at Π_1 and Π_2. An instructive restatement of the iso-orbital condition is that there exists a single basis band representation $\mathrm{BBR}[\varphi_\alpha]$ induced from a tight-binding-basis orbital φ_α ($\alpha \in \{1,2\}$), such that the restriction of the valence band representation VBR to γ_{Π_1} equals[3] the restriction of $\mathrm{BBR}[\varphi_\alpha]$ to γ_{Π_1}, and likewise for $\gamma_{\Pi_1} \to \gamma_{\Pi_2}$:[4]

$$\begin{aligned} &\textit{iso-orbital condition at } \Pi_1 \text{ and } \Pi_2: \quad \exists\, \alpha \in \{1,2\} \text{ s.t.} \\ &\mathrm{VBR}\Big|_{\gamma_{\Pi_1}} = \mathrm{BBR}[\varphi_\alpha]\Big|_{\gamma_{\Pi_1}} \text{ and } \mathrm{VBR}\Big|_{\gamma_{\Pi_2}} = \mathrm{BBR}[\varphi_\alpha]\Big|_{\gamma_{\Pi_2}}. \end{aligned} \tag{4.16}$$

It follows from Eq. (4.11) that the polarizations at both Π_1 and Π_2 are symmetry-fixed to z_α, modulo integers. This contrasts with case (b), where one of the two polarizations is symmetry-fixed to z_1, and the other to z_2. In the absence of fine-tuning, one expects that $z_1 \neq_1 z_2$, because by assumption no space-group symmetry relates the two tight-binding-basis orbitals.[5]

Since our interest is to formulate an invariant difference in polarizations, let us assume that both mutually-disjoint and iso-orbital conditions hold:

$$\textit{RTP invariant}: \quad \Delta\mathscr{P}_{\Pi_1\Pi_2} = \mathscr{P}(\Pi_2) - \mathscr{P}(\Pi_1), \tag{4.17}$$

$$\Delta\mathscr{P}_{\Pi_1\Pi_2} \in \mathbb{Z} \Leftarrow \begin{cases} \textit{mutually-disjoint condition}\text{: Eq. (4.10)} \\ \textit{iso-orbital condition}\text{: Eq. (4.16)} \end{cases} \tag{4.18}$$

It is worth emphasizing that the integer-valued polarization difference is uniquely defined, because the triviality of the first Chern class allows to find a global smooth gauge for the intra-cell wave function $|u_v(\boldsymbol{k})\rangle$ (cf. Refs. [128–130] and footnote 12 in Ref. [120]), so that the polarization $\mathscr{P}(\boldsymbol{k}_\perp)$ is a continuous and periodic function over the rBZ.

A nonzero value of this polarization difference can be interpreted as a *returning Thouless pump* (RTP) in a 2D sub-torus of the BZ containing the lines γ_{Π_1} and γ_{Π_2}. For this interpretation, we view the Hamiltonian as having only one momentum component k_z and view the perpendicular momentum component $\boldsymbol{k}_\perp$ as an external adiabatic parameter. $\Delta\mathscr{P}_{\Pi_1\Pi_2} \neq 0$ then means that a charge is pumped across $\Delta\mathscr{P}_{\Pi_1\Pi_2}$-number of lattice periods in the z-direction, when $\boldsymbol{k}_\perp$ is advanced from Π_1 to Π_2. The assumption of a trivial first Chern class ensures that the pumped charge is reverted back in the second half of the adiabatic cycle. Henceforth, we refer to the quantized polarization difference as the *RTP invariant*.

The RTP invariant is well-defined for any pair of 'mutually-disjoint' reduced momenta that also satisfies the iso-orbital condition (4.16). It turns out that a combination of symmetry (Pn), topology (triviality of Chern class) and

3 To formalize being 'equal', one may say that the projector to all Bloch states (on the BZ-line γ_Π at fixed reduced momentum Π) are equal for VBR and for $\mathrm{BBR}[\varphi_\alpha]$. Note that equality of the sum of projectors over a $\boldsymbol{k}$-line γ_Π implies equality of projectors at each point $\boldsymbol{k} \in \gamma_\Pi$ individually.

4 If this equality holds at *all* rotation-invariant lines γ_Π, we say that the valence band representation VBR is *symmetry-equivalent* to the basis band representation $\mathrm{BBR}[\varphi_\alpha]$. In other words, both band representations belong to the equivalent class $\mathrm{BR}(\mathcal{L}_\alpha, \boldsymbol{r}_{\alpha,\perp})$, cf. Sec. 4.1.

5 Depending on the context, there may exist chemical principles (beyond symmetry principles) that approximately enforce $z_1 =_1 z_2$. For instance, this is true of crystals containing a single atom within each primitive unit cell, with both tight-binding-basis orbitals chosen to be atomic orbitals.

Hilbert-space constraint (two-band Hamiltonian) imposes that the iso-orbital condition holds for any 'mutually-disjoint' pair in space groups Pn with $n = 3, 4, 6$, as is proven in Appendix B.3. This has implications – for the mod-n relation between the Hopf and RTP invariants – that are discussed in Sec. 6.3.2, wherein we also discuss the exceptional case of P2.

For any Pn-symmetric two-band tight-binding Hilbert space induced by any pair of basis orbitals on C_n-symmetric Wyckoff positions, we have exhaustively identified all possible pairs of reduced momenta which satisfy the mutually-disjoint condition [the first line in Eq. (4.18)]. We summarize in Table 4.1 the itinerant angular momentum difference $\widetilde{\mathcal{L}}_2(\Pi) - \widetilde{\mathcal{L}}_1(\Pi)$ $(\mathrm{mod}\ m)$ between two basis Bloch states for (*i*) all rotation-invariant lines at (*ii*) all space groups Pn, $n \in \{2, 3, 4, 6\}$, given (*iii*) any difference of the on-site angular momenta, $\Delta\mathcal{L} = \mathcal{L}_2 - \mathcal{L}_1$, and (*iv*) any positional difference: $\Delta\boldsymbol{r}_\perp = \boldsymbol{r}_{2,\perp} - \boldsymbol{r}_{1,\perp}$ [projected to the (x, y)-plane] of the two tight-binding-basis orbitals. All these options [with the sole exception of $\Delta\mathcal{L} = 0, \Delta\boldsymbol{r}_\perp = (0, 0)$, which is not listed in the table] exhibit at least two rotation-invariant reduced momenta with non-zero values of $\widetilde{\mathcal{L}}_2(\Pi) - \widetilde{\mathcal{L}}_1(\Pi)$ $(\mathrm{mod}\ m)$. These momenta thus have non-zero itinerant angular momentum differences between conduction and valence states $\Delta\widetilde{\mathcal{L}}(\Pi) = \widetilde{\mathcal{L}}_c(\Pi) - \widetilde{\mathcal{L}}_v(\Pi)$ $(\mathrm{mod}\ m)$ and therefore satisfy the mutually-disjoint condition.

To recapitulate, Table 4.1 tells us where (in the BZ) one might in principle find a nontrivial RTP, given a certain tight-binding Hilbert space. To derive the tight-binding Hamiltonian that realizes an RTP, our strategy (elucidated in Sec. 4.4) is to design Berry-dipole band-touching points along any rotation-invariant $\boldsymbol{k}$-line specified in Table 4.1.

Table 4.1: Itinerant angular momenta differences $\widetilde{\mathcal{L}}_2(\Pi) - \widetilde{\mathcal{L}}_1(\Pi)$ $\mathrm{mod}\ m$ at all C_m-invariant reduced momenta Π (value of m given in brackets) [cf. Fig. 4.1(b)] for space groups Pn, $n \in \{2, 3, 4, 6\}$, and for basis orbitals with all possible differences in angular momentum $\Delta\mathcal{L} = \mathcal{L}_2 - \mathcal{L}_1$ and with relative displacement $\Delta\boldsymbol{r}_\perp = \boldsymbol{r}_{2,\perp} - \boldsymbol{r}_{1,\perp} = \sum_i \Delta r_{\perp,i}\boldsymbol{a}_i$ where $\boldsymbol{a}_i$, $i = 1, 2$ are primitive lattice translation vectors. For P2 and P4 symmetries we choose $\boldsymbol{a}_1 = (1, 0)$ and $\boldsymbol{a}_2 = (0, 1)$, while for P3 and P6 symmetries $\boldsymbol{a}_1 = \frac{\sqrt{3}}{2}(\sqrt{3}, 1)$ and $\boldsymbol{a}_2 = \frac{\sqrt{3}}{2}(\sqrt{3}, -1)$. We omit the cases $\Delta\mathcal{L} = 0$ with $\Delta\boldsymbol{r}_\perp = (0, 0)$, when the itinerant angular momenta of the two bands coincide at all Π.

Group	$\Delta\mathcal{L}$	$\Delta\boldsymbol{r}_\perp = (\Delta r_{\perp,1}, \Delta r_{\perp,2})$	$\widetilde{\mathcal{L}}_2(\Pi) - \widetilde{\mathcal{L}}_1(\Pi)$ $\mathrm{mod}\ m$ for C_m-invariant Π			
			$\Gamma(C_2)$	$\mathrm{X}(C_2)$	$\mathrm{Y}(C_2)$	$\mathrm{M}(C_2)$
P2	0	$(0, 1/2)$	0	0	1	1
		$(1/2, 0)$	0	1	0	1
		$(1/2, 1/2)$	0	1	1	0
	1	$(0, 0)$	1	1	1	1
		$(0, 1/2)$	1	1	0	0
		$(1/2, 0)$	1	0	1	0
		$(1/2, 1/2)$	1	0	0	1
			$\Gamma(C_3)$	$\mathrm{K}(C_3)$	$\mathrm{K}'(C_3)$	
P3	0	$(1/3, 1/3)$	0	1	2	
		$(2/3, -1/3)$	0	2	1	
	1	$(0, 0)$	1	1	1	

		$(1/3, 1/3)$	1	2	0
		$(2/3, -1/3)$	1	0	2
	-1	$(0,0)$	2	2	2
		$(1/3, 1/3)$	2	0	1
		$(2/3, -1/3)$	2	1	0
			$\Gamma(C_4)$	$X(C_2)$	$M(C_4)$
P4	0	$(1/2, 1/2)$	0	1	2
	1	$(0,0)$	1	1	1
		$(1/2, 1/2)$	1	0	3
	2	$(0,0)$	2	0	2
		$(1/2, 1/2)$	2	1	0
	-1	$(0,0)$	3	1	3
		$(1/2, 1/2)$	3	0	1
			$\Gamma(C_6)$	$K(C_3)$	$M(C_2)$
P6	1	$(0,0)$	1	1	1
	2	$(0,0)$	2	2	0
	3	$(0,0)$	3	0	1
	-2	$(0,0)$	4	1	0
	-1	$(0,0)$	5	2	1

4.3 CHANGE IN RTP AND HOPF INVARIANTS ACROSS BERRY DIPOLE

Both the Hopf and the RTP invariants of a lattice tight-binding Hamiltonian can be altered across critical phase-transition points where the conduction and valence bands touch (as a Berry dipole) along one (or more) rotation-invariant $\boldsymbol{k}$-line(s).

For any Berry-dipole band touching at C_m-invariant momentum $\boldsymbol{k}^{\mathrm{t}}$, we assume that the tight-binding Hamiltonian $h(\boldsymbol{k})$ has a convergent, multivariable Taylor expansion in $(\boldsymbol{k} - \boldsymbol{k}^{\mathrm{t}})$, such that the truncated Taylor expansion is a $\boldsymbol{k} \cdot \boldsymbol{p}$ Hamiltonian of the spinor-form [cf. Eq. (3.4)], with spinor given by Eq. (3.3) for a certain Berry-dipole spin $[\Delta\ell(\boldsymbol{k}^{\mathrm{t}}) \in \mathbb{Z}]$ and a certain Berry-dipole helicity $[v(\boldsymbol{k}^{\mathrm{t}}) = \pm 1]$ that both depend on the particular band touching $\boldsymbol{k}^{\mathrm{t}}$. For this to be possible, we additionally assume that the valence band is of a φ_1 character at $\boldsymbol{k}^t$ – this guarantees that the valence band in the $\boldsymbol{k} \cdot \boldsymbol{p}$ expansion is also of the first orbital character, as required for the Hamiltonian defined through the spinor (3.3). In this expression, the Berry-dipole helicity depends on details of the Hamiltonian hopping matrix elements. At the same time, comparison of the symmetry constraints Eq. (3.2) and Eqs. (4.4–4.6) allows to equate (modulo m) the Berry-dipole spin with the difference in itinerant angular momenta of the basis Bloch states:

$$\Delta\ell(\boldsymbol{k}^{\mathrm{t}}) =_m \widetilde{\mathcal{L}}_2(\Pi^{\mathrm{t}}) - \widetilde{\mathcal{L}}_1(\Pi^{\mathrm{t}}) =_m \Delta\widetilde{\mathcal{L}}(\Pi^{\mathrm{t}}), \tag{4.19}$$

with Π^{t} the projection of $\boldsymbol{k}^{\mathrm{t}}$ onto the (k_x, k_y)-plane; as we show in Appendix A.1.5, to the lowest-in-$\boldsymbol{k}$ order, $\Delta\ell(\boldsymbol{k}^{\mathrm{t}})$ of corresponding continuum expansion is chosen to be the smallest (in absolute value) integer that obeys this constraint. The second equality in Eq. (4.19) follows from the assumption

that the valence band is of φ_1 character, and hence conduction band is of φ_2 character, at $\boldsymbol{k}^{\mathrm{t}}$.

Recall from Sec. 3.2 that the Berry dipole results in an integer-valued change of the continuum Hopf number $\delta\chi^{\text{cont.}} = -\Delta\ell\, v$ according to Eq. (3.17). Recall that $\chi^{\text{cont.}}$ can be viewed as a momentum-local contribution to the Hopf invariant – a BZ-integral of the Chern-Simons three-form. Suppose our tight-binding Hamiltonian depends on a non-momentum variable $\Phi \in \mathbb{R}$, and that for an isolated value of $\Phi = \Phi_c$, the conduction and valence bands touch as Berry dipoles at T momenta, $\{\boldsymbol{k}^{\mathrm{t}}\}_{\mathrm{t}=1,\ldots,T}$. The net change in the Hopf invariant is then obtained by summing over all $\boldsymbol{k}^{\mathrm{t}}$:

$$\delta\chi = \sum_{\mathrm{t}=1}^{T} \delta\chi^{\text{cont.}}(\boldsymbol{k}^{\mathrm{t}}), \quad \delta\chi^{\text{cont.}}(\boldsymbol{k}^{\mathrm{t}}) = -v(\boldsymbol{k}^{\mathrm{t}})\Delta\ell(\boldsymbol{k}^{\mathrm{t}}) \in \mathbb{Z}. \tag{4.20}$$

If $\boldsymbol{k}^{\mathrm{t}}$ is a C_m-invariant momentum in a Pn-symmetric BZ with $m < n$, then $\boldsymbol{k}^{\mathrm{t}}$ belongs to an n/m-plet of dipole-band-touching momenta which are mutually related by C_n symmetry, and $\delta\chi^{\text{cont.}}$ is identical for each member of this n/m-plet. This follows from the fact that the Berry-connection vector $\boldsymbol{\mathcal{A}}$ transforms as a vector under spatial operations, Berry-curvature vector $\boldsymbol{\mathcal{F}} = \boldsymbol{\nabla} \times \boldsymbol{\mathcal{A}}$ transforms as a pseudo-vector, and hence the Chern-Simons three-form $\boldsymbol{\mathcal{F}} \cdot \boldsymbol{\mathcal{A}}$ transforms as a pseudo-scalar.

Details 4.2 If the valence band is instead of a φ_2 character, the $\boldsymbol{k} \cdot \boldsymbol{p}$ expansion in the spinor-form Hamiltonian will be defined via the spinor given in Eq. (3.5). In this case, the local contributions to the Hopf invariant will instead be given by

$$\delta\chi^{\text{cont.}}(\boldsymbol{k}^{\mathrm{t}}) = v(\boldsymbol{k}^{\mathrm{t}})\Delta\ell(\boldsymbol{k}^{\mathrm{t}}). \tag{4.21}$$

Both Eqs. (4.20) and (4.21) can be formulated with the *same* sign on the right-hand side if we employ the difference $\ell_c - \ell_v$ (instead of $\Delta\ell = \ell_2 - \ell_1$) at $\boldsymbol{k}^{\mathrm{t}}$, as in Eq. (3.19).

Recall that a Berry-dipole band touching at $\boldsymbol{k}^{\mathrm{t}}$ changes also the continuum Zak phase by $\delta\mathscr{Z}^{\text{cont.}} = -2\pi v$ according to Eq. (3.18). $\delta\mathscr{Z}^{\text{cont.}}$ can be viewed as a momentum-local contribution to the RTP invariant $\Delta\mathscr{P}_{\Pi_1\Pi_2}$ if $\boldsymbol{k}^{\mathrm{t}}$ is a point on either of the rotation-invariant lines: γ_{Π_1} and γ_{Π_2}. The net change in the RTP invariant across the critical parameter value Φ_c is contributed by all dipole-band-touching points within either line:

$$\delta\Delta\mathscr{P}_{\Pi_1\Pi_2} = \sum_{\boldsymbol{k}^{\mathrm{t}}\in\gamma_{\Pi_1}} v(\boldsymbol{k}^{\mathrm{t}}) - \sum_{\boldsymbol{k}^{\mathrm{t}}\in\gamma_{\Pi_2}} v(\boldsymbol{k}^{\mathrm{t}}). \tag{4.22}$$

If $\boldsymbol{k}^{\mathrm{t}}$ belongs to a n/m-plet, then v is identical for each member of this multiplet. This is because $\boldsymbol{\mathcal{A}}$ transforms as a vector under spatial operations, and in particular $\mathcal{A}_z$ transforms as a scalar under rotations with axes parallel to z.

Let us begin from a canonical trivial phase with only on-site energies and zero 'hopping' matrix elements of the real-space tight-binding Hamiltonian. In such a phase, both valence and conduction bands are basis band representations, and the Hopf and RTP invariants vanish. By tuning the Hamiltonian, we then transit to a different gapped phase via a Berry-dipole critical point, with both Hopf and RTP invariants simultaneously modified through Eqs. (4.20) and (4.22). One can eliminate the Berry-dipole helicity $v(\boldsymbol{k}^{\mathrm{t}})$ from both equations, thus expressing the Hopf invariant in terms of the RTP invariants – this is done in Chapter 6. A phase transition involving multiple Berry dipoles can in principle leave the Hopf invariant unchanged, while altering the RTP invariant. This happens when the individual band-touching contributions in Eq. (4.20) cancel each other.

We name insulators that are classified by both Hopf and RTP invariants as *crystalline Hopf insulators*. In the next section we illustrate the richness of their classification by means of explicit tight-binding models. The RTP invariant, in contrast to the Hopf invariant, admits generalization to more than two bands as will be discussed in details in Sec. 7.3 of Chapter 7. Therefore, we adopt the name of *RTP insulator* to define a two-or-more band insulator characterized by at least one non-zero RTP invariant.

4.4 MODELS OF CRYSTALLINE HOPF INSULATORS

In this section we illustrate the concept of crystalline Hopf insulators on several explicit tight-binding models. In Secs. 4.4.1, we present an example model for which the Hopf invariant remains zero although the RTP invariants are nontrivial. In Sec. 4.4.2, we introduce a model that exhibits two phases with the same non-vanishing value of the Hopf invariant but which are topologically distinguished by the RTP invariant. Based on these examples, we claim that rotational symmetry enriches the topological classification of Hopf insulators through the introduction of the RTP invariants. We also note a relation between the Hopf and the RTP invariants that holds in both models. This relation is formally generalized and proven in Chapter 6. Finally, in Sec. 4.4.3 we present several representative tight-binding models, that possess quantized values of the Hopf and RTP invariants, in all space groups Pn. All the presented models are summarized in Table 4.2 and their phase diagrams are presented in Table 5.1.

4.4.1 *Hopf-less RTP insulator*

We present a model that has a trivial Hopf invariant but non-trivial RTP invariants. The existence of such a model demonstrates that in the presence of crystalline symmetries the topological classification of two-band Hamiltonians (with trivial first Chern class) is not exhausted by the Hopf invariant.

One way to realize a tight-binding model with the above-mentioned property is to start with a trivial insulator and induce a phase transition via a pair of Berry dipoles at two rotation-invariant points $\boldsymbol{k}^1 \in \gamma_{\Pi_1}$, $\boldsymbol{k}^2 \in \gamma_{\Pi_2}$, that lie on two rotation-invariant lines in the BZ. For simplicity, we assume that both γ_{Π_j} ($j = 1, 2$) are invariant (modulo lattice translations) under n-fold rotation, with n the order of the maximal point group of Pn. The changes in the Hopf invariant attributed to the two Berry dipoles are chosen to cancel each other: $\delta\chi(\boldsymbol{k}^1) = -\delta\chi(\boldsymbol{k}^2)$. The model can nonetheless acquire a nonzero RTP invariant $\Delta\mathscr{P}_{\Pi_1\Pi_2}$, if the corresponding changes in polarization at these points have opposite signs, $\delta\mathscr{P}(\Pi_1) = -\delta\mathscr{P}(\Pi_2)$.

With the RTP-protecting symmetry chosen to be a 4-fold rotation C_{4z}, represented by $R_{C_{4z}} = \mathrm{diag}(1, i)$, a model with the required characteristics is achieved by the Hamiltonian

$$\begin{aligned} h(\boldsymbol{k}) &= [\zeta^\dagger(\boldsymbol{k})\sigma\zeta(\boldsymbol{k})]\cdot\sigma, \quad \zeta(\boldsymbol{k}) = (\zeta_1, \zeta_2)^\top \\ \zeta_1(\boldsymbol{k}) &= \sin k_x - i \sin k_y, \\ \zeta_2(\boldsymbol{k}) &= \sin k_z + i\,\Phi\left[\Phi + \cos k_z(\cos k_x + \cos k_y)\right], \end{aligned} \tag{4.23}$$

with $\sigma = (\sigma_x, \sigma_y, \sigma_z)$ a vector of the Pauli matrices and $\Phi \in \mathbb{R}$ a tuning parameter. The model is defined on a tetragonal lattice in $\boldsymbol{r} = (x, y, z)$ space, and we rescale the dimensionless lattice constants/periods in both the vertical

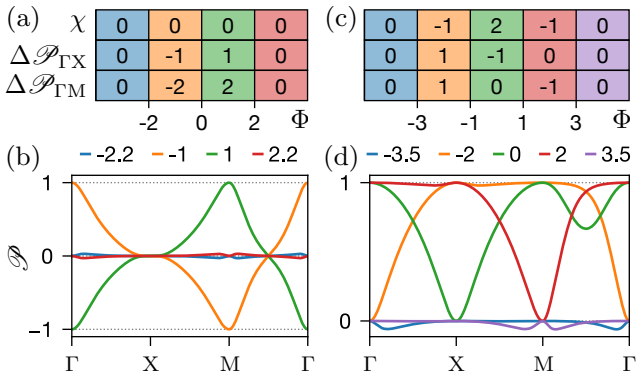

Figure 4.2: Phase diagram (a) of the model with zero Hopf invariant [defined in Eq. (4.23)], and (c) of the Moore-Ran-Wen (MRW) model [described by Eq. (4.24)]. Both models belong to space group P4, with $\mathcal{L}_1 = 0$ and $\mathcal{L}_2 = 1$ orbitals set along the same C_4 rotation axis. The three rows corresponds to the values of the Hopf invariant (χ) and of two quantized polarization differences between points Γ and X ($\Delta\mathscr{P}_{\Gamma X}$) resp. between Γ and M ($\Delta\mathscr{P}_{\Gamma M}$) in the reduced Brillouin zone. (b,d) For each phase in the phase diagram (a) resp. (c), the z-component of the polarization as a function of momentum along path ΓXMΓ is shown for a representative value of the parameter Φ.

and the in-plane direction to 1, such that the first Brillouin zone is given by $|k_{x,y,z}| \leq \pi$. The presented model has a pair of basis orbitals $\{\varphi_j\}_{j=1,2}$ placed along a rotational axis passing through the center of the unit cell, which transform under rotations like a spinless s and $p_+ = p_x + ip_y$ orbital (i.e., they carry angular momenta $\mathcal{L}_1 = 0$ and $\mathcal{L}_2 = 1$, respectively).

Owing to the trivial value of the Chern number on all subplanes of the BZ, the eigenstates of the Hamiltonian (4.23) can be expressed as periodic and analytic functions of $\boldsymbol{k}$ over the Brillouin torus. We adopt the gauge in which the valence (conduction) eigenstates are given by $|u_v\rangle = i\sigma_y\zeta^*/\|\zeta\|$ ($|u_c\rangle = \zeta/\|\zeta\|$), with $\zeta(\boldsymbol{k})$ an analytic and periodic function specified in Eq. (4.23). One easily verifies that the valence and conduction wave functions along each rotation-invariant line transform under rotation with itinerant angular momenta $\widetilde{\mathcal{L}}_v = 0$ resp. $\widetilde{\mathcal{L}}_c = 1$, implying that the mutually-disjoint condition is fulfilled. The RTP invariants are the polarization differences between pairs of C_{4z}-invariant reduced momenta $\Gamma = (0,0)$ and $\mathrm{M} = (\pi,\pi)$ and C_{2z}-invariant reduced momentum $\mathrm{X} = (\pi,0),(0,\pi)$. All possible pairwise differences in polarization can be expressed as a linear combination of two independent ones: $\Delta\mathscr{P}_{\Gamma X}$ and $\Delta\mathscr{P}_{\Gamma M}$.

To verify that the Hamiltonian indeed enters the phase with zero Hopf invariant but non-trivial RTP, we analyze in detail the phase transition at $\Phi_c = -2$. For large negative parameter values $\Phi \to -\infty$, the valence band is $\boldsymbol{k}$-independent and the Hopf invariant and the differences in polarization are all zero. Increasing Φ to -2, the gap closes simultaneously at two BZ points $(\Gamma,0)$ and (M,π). Expanding the Hamiltonian in Eq. (4.23) around $(\Gamma,0)$ [resp. (M,π)], to quadratic order in $\phi = \Phi - \Phi_c$ and in $\boldsymbol{\kappa} = \boldsymbol{k} - (\Gamma,0)$ [resp. $\boldsymbol{\kappa} = \boldsymbol{k} - (\mathrm{M},\pi)$], we get $\zeta(\boldsymbol{\kappa}) = (\kappa_-, \kappa_z - 2i\phi)^\top$ [resp. $\zeta(\boldsymbol{\kappa}) = (-\kappa_-, -\kappa_z - 2i\phi)^\top$]. These spinor functions are topologically equivalent to the form in Eq. (3.3) with $\Delta\ell = 1$ and $v = -1$ [resp. $v = +1$]. According to Eqs. (3.17) and (4.20) the Hopf invariant does not change through this phase transition while from Eq. (3.18) the polarization exhibits a positive (resp. negative) unit jump at Γ (resp. M). This produces two

nonzero topological invariants $\Delta\mathscr{P}_{\Gamma X} = -1$ and $\Delta\mathscr{P}_{\Gamma M} = -2$, as governed by Eq. (4.22).

Upon further increasing Φ, the model defined by Eq. (4.23) exhibits two more phase transitions (namely at parameter values $\Phi \in \{0, +2\}$), and eventually returns to the trivial phase, as summarized by the phase diagram in Fig. 4.2(a). To illustrate the quantization of the RTP invariants we plot in Fig. 4.2(b) the electric polarization of the valence band [Eq. (4.9)] as a function of rBZ momentum on a path connecting rotation-invariant momenta Γ, M and X for a representative parameter value in each topological phase.

4.4.2 *RTP invariant distinguishes between insulators with the same Hopf invariant*

We now consider the possibility that the RTP invariant distinguishes two topological insulators with the same and *nontrivial* value of the Hopf invariant. For this purpose we re-examine the role of symmetries of the canonical Moore-Ran-Wen (MRW) model of the Hopf insulator [55],

$$\begin{aligned} h(\boldsymbol{k}) &= \left[\zeta^\dagger(\boldsymbol{k})\sigma\zeta(\boldsymbol{k})\right]\cdot\boldsymbol{\sigma}, \quad \zeta(\boldsymbol{k}) = (\zeta_1,\zeta_2)^\top \\ \zeta_1(\boldsymbol{k}) &= \sin k_x - i\sin k_y, \\ \zeta_2(\boldsymbol{k}) &= \sin k_z + i\left(\sum_{i=x,y,z}\cos k_i + \Phi\right). \end{aligned} \tag{4.24}$$

The tight-binding basis vectors coincide with those of the previous model in Sec. 4.4.1, hence the MRW model is classified by the same topological invariants $\Delta\mathscr{P}_{\Gamma X}$ and $\Delta\mathscr{P}_{\Gamma M}$ in addition to the Hopf invariant χ.

By applying Eqs. (3.17) and (4.20) to the phase transitions exhibited by the MRW model at $\Phi \in \{-3, -1, 1, 3\}$, we get the phase diagram given in Fig. 4.2(c); the polarization as a function of rBZ momentum for all representative parameter values is numerically plotted in Fig. 4.2(d). We observe that two phases with $-3 < \Phi < -1$, resp. $1 < \Phi < 3$, have the same value of the Hopf invariant $\chi = -1$. However, the two phases are distinguished by the RTP invariants, i.e., it is impossible to deform one phase into the other without closing the energy gap or breaking P4 symmetry.

In addition to refining the topological classification, the RTP invariant also explains the existence of mid-gap surface states at open boundaries with sharply terminated hoppings, as elaborated in Sec. 5.3. Such surface states were first numerically observed in Ref. [55]; however, since the crystalline symmetries and the RTP invariants of the model have previously not been analyzed, the appearance of these surface states lacked explanation. We are proposing in Sec. 5.3, that the RTP invariants not only guarantee that surface states interpolate across the bulk gap for sharply-terminated boundaries, but also put some restrictions on the shape-topology of the Fermi surface (of surface states) over the rBZ.

From the colored panels in Fig. 4.2(a) and (c), one can deduce a pattern among the Hopf and RTP invariants that holds for both Hopfless and MRW models [cf. Eqs. (4.23) resp. (4.24)]:

$$\chi =_4 2\Delta\mathscr{P}_{\Gamma X} + \Delta\mathscr{P}_{\Gamma M}. \tag{4.25}$$

This *Hopf-RTP relation* can be rationalized by noticing that all phase transitions in both models occur via Berry dipoles at rotation-invariant momenta; each Berry dipole is responsible for an increment to the Hopf and RTP

invariants given by Eqs. (3.17) and (3.18). This suggests a more general Hopf-RTP relation that depends on the itinerant-angular-momentum difference between the valence and conduction bands, which reduces to Eq. (4.25) in the case when the itinerant-angular-momentum difference is unity. This general relation is derived in Chapter 6 for all space groups Pn and all possible combinations of tight-binding-basis orbitals. We will further reveal in that chapter that the Hopf-RTP relation holds whether or not the band-topology-altering band touchings are of the Berry-dipolar form.

4.4.3 *Representative models of crystalline Hopf insulators in all* Pn *space groups*

Adopting the tight-binding Hilbert spaces described in Sec. 4.1, we will construct tight-binding Hamiltonians in the spinor form given by Eq. (3.4) with different choices of the spinor functions $\zeta(\boldsymbol{k}, \Phi)$. All the constructed Hamiltonians below have a trivial first Chern class and a valence band representation which is symmetry-equivalent to[6] a basis band representation, i.e., a band representation induced from either of the tight-binding-basis orbitals.

As shown in Appendix A.1.1, the rotation-symmetry condition in Eq. (4.2) is equivalent to the following condition on the spinor function:

$$R_{C_n}(\boldsymbol{k})\zeta(\boldsymbol{k}) = e^{i\beta(\boldsymbol{k})}\zeta(C_n\boldsymbol{k}), \tag{4.26}$$

with $\beta(\boldsymbol{k})$ being an arbitrary phase factor. To construct a Hamiltonian that transforms under reciprocal lattice translations according to Eq. (2.5), we choose each spinor component to transform as

$$\zeta_j(\boldsymbol{k} + \boldsymbol{G}) = e^{-i\boldsymbol{G}\cdot\boldsymbol{r}_j}\zeta_j(\boldsymbol{k}) \tag{4.27}$$

for both $j = 1, 2$.[7]

To find model Hamiltonians that realize non-trivial RTP and Hopf invariants, we look for spinor functions that vanish $[\zeta(\boldsymbol{k}^0, \Phi^0) = (0,0)^\top]$ at a rotation-invariant point $\boldsymbol{k}^0$ at an isolated parameter value Φ^0; in the vicinity of $\boldsymbol{k}^0$, we want the effective $\boldsymbol{k}\cdot\boldsymbol{p}$ Hamiltonian to have the Berry-dipolar form given by Eq. (3.3). We can then claim with certainty that after reopening the gap the values of the Hopf and the RTP invariants will change according to Eqs. (3.17, 3.18).

In Table 4.2, we list representative spinors for several choices of the space group symmetry Pn and of the basis orbitals, the latter specified by the difference in on-site angular momenta $\Delta\mathcal{L} = \mathcal{L}_2 - \mathcal{L}_1$ and in the positional centers $\Delta\boldsymbol{r}_\perp = \boldsymbol{r}_{2,\perp} - \boldsymbol{r}_{1,\perp}$. The phase diagrams showing the values of the Hopf and RTP invariants as a function of parameter Φ in the constructed models are listed in Table 5.1.

A few comments are in order:

(*i*) A tight-binding Hamiltonian with a fixed value for $\Delta\mathcal{L}$ and $\Delta\boldsymbol{r}_\perp$ is compatible with multiple choices of the basis orbitals whose on-site angular momenta and Wyckoff positions differ by $\Delta\mathcal{L}$ and $\Delta\boldsymbol{r}_\perp$ respectively, as long as both Wyckoff positions are C_n-invariant. However, in deriving the specific forms for the spinor ζ in Table 4.2, we have assumed that the tight-binding-basis

6 Symmetry-equivalent to, but *not continuously deformable to*; cf. end of Sec. 4.1 for the definition of these two distinct notions.

7 To see this, we use completeness of the Pauli matrices (3.13a) to rewrite the spinor form Hamiltonian (3.4) as $h_{\alpha\beta}(\boldsymbol{k}) = 2\zeta_\alpha(\boldsymbol{k})^*\zeta_\beta(\boldsymbol{k}) - \delta_{\alpha\beta}|\zeta|^2$. Taking into account Eq. (4.27) we see that this Hamiltonian transforms under reciprocal lattice translation according to Eq. (2.5).

Table 4.2: Glossary of representative Hamiltonians of crystalline Hopf insulators. The model Hamiltonians, with the indicated space group symmetry Pn and basis orbitals $\varphi_{1,2}$ characterized by their angular momentum difference $\Delta\mathcal{L} = \mathcal{L}_2 - \mathcal{L}_1$ and real-space position difference $\Delta\boldsymbol{r} = (\Delta\boldsymbol{r}_\perp, 0)$, $\Delta\boldsymbol{r}_\perp = \boldsymbol{r}_{1,\perp} - \boldsymbol{r}_{2,\perp}$, are of the form $h(\boldsymbol{k}) = [\zeta^\dagger(\boldsymbol{k})\sigma\zeta(\boldsymbol{k})]\cdot\boldsymbol{\sigma}$ with the spinor components $\zeta(\boldsymbol{k}) = [\zeta_1(\boldsymbol{k}), \zeta_2(\boldsymbol{k})]^\top$ listed in the table. Notations in the table: $\boldsymbol{t}(a) = \sqrt{3}\,(\sin(\pi a/3), -\cos(\pi a/3))^\top$, $\boldsymbol{k}_\perp = (k_x, k_y)^\top$. The 'Hopf-less model' of Sec. 4.4.1 is not included in the table, while the 'MRW model' of Sec. 4.4.2 corresponds to the second listed model. In the presented models the reciprocal lattice vectors in (k_x, k_y) plane are $\boldsymbol{G}_{1,\perp} = (1,0)$, $\boldsymbol{G}_{2,\perp} = (0,1)$ in the case of P2 and P4 space groups and $\boldsymbol{G}_{1,\perp} = \frac{2\pi}{3}(1,\sqrt{3})$, $\boldsymbol{G}_{2,\perp} = \frac{2\pi}{3}(1,-\sqrt{3})$ in the case of P3 and P6 space groups.

SG	$\Delta\mathcal{L}$	$\Delta\boldsymbol{r}_\perp$	$\zeta(\boldsymbol{k})$
P4	0	$\left(\frac{1}{2},\frac{1}{2}\right)$	$e^{i\frac{k_x+k_y}{2}}\begin{bmatrix}\cos\frac{k_x}{2}\cos\frac{k_y}{2} + i\sin\frac{k_x}{2}\sin\frac{k_y}{2}\sin\frac{k_x+k_y}{2}\sin\frac{k_x-k_y}{2}\\ \sin k_z + i\left(\sum_{i=x,y,z}\cos k_i + \Phi\right)\end{bmatrix}$
	1	$(0,0)$	$\begin{bmatrix}\sin k_x - i\sin k_y\\ \sin k_z + i\left(\sum_{i=x,y,z}\cos k_i + \Phi\right)\end{bmatrix}$
		$\left(\frac{1}{2},\frac{1}{2}\right)$	$e^{i\frac{k_x+k_y}{2}}\begin{bmatrix}\sin\frac{k_x+k_y}{2} + i\sin\frac{k_x-k_y}{2}\\ \sin k_z + i\left(\sum_{i=x,y,z}\cos k_i + \Phi\right)\end{bmatrix}$
	2	$(0,0)$	$\begin{bmatrix}\sin\frac{k_x+k_y}{2}\sin\frac{k_x-k_y}{2} + i\sin k_x\sin k_y\\ \sin k_z + i\left(\sum_{i=x,y,z}\cos k_i + \Phi\right)\end{bmatrix}$
P3	0	$\left(\frac{1}{3},\frac{1}{3}\right)$	$\begin{bmatrix}1 + 2\exp\left\{-i\frac{3}{2}k_x\right\}\cos\left\{\frac{\sqrt{3}}{2}k_y\right\}\\ e^{-ik_x}\left[\sin k_z + i\left(\sum_{a=1}^3\sqrt{3}\sin\{\boldsymbol{t}(2a)\cdot\boldsymbol{k}_\perp\} + \frac{9}{2}\cos k_z + \Phi\right)\right]\end{bmatrix}$
	1	$(0,0)$	$\begin{bmatrix}\sum_{a=1}^3 e^{-ia\frac{2\pi}{3}}\exp\{i\boldsymbol{t}(2a)\cdot\boldsymbol{k}_\perp\}\\ \sin k_z + i\left(\sum_{a=1}^3\sqrt{3}\sin\{\boldsymbol{t}(2a)\cdot\boldsymbol{k}_\perp\} + \frac{9}{4}\cos k_z + \Phi\right)\end{bmatrix}$
P6	1 or 2	$(0,0)$	$\begin{bmatrix}\sum_{a=1}^6 e^{-i\Delta\mathcal{L}a\frac{\pi}{3}}\exp\{i\boldsymbol{t}(a)\cdot\boldsymbol{k}_\perp\}\\ \sin k_z + i\left(\sum_{a=1}^6\cos\{\boldsymbol{t}(a)\cdot\boldsymbol{k}_\perp\} + 4\cos k_z + \Phi\right)\end{bmatrix}$
	3	$(0,0)$	$\begin{bmatrix}\sum_{a=1}^6 e^{i\pi a}\left[\exp\{i\boldsymbol{t}(a)\cdot\boldsymbol{k}_\perp\} - i\exp\left\{i\sqrt{3}\boldsymbol{t}\left(a+\frac{1}{2}\right)\cdot\boldsymbol{k}_\perp\right\}\right]\\ \text{as for } \Delta\mathcal{L} = 1,2\end{bmatrix}$

orbital φ_1 has trivial on-site angular momentum $\mathcal{L}_1 = 0$ and a C_n-invariant Wyckoff position with reduced coordinate $\boldsymbol{r}_{1,\perp} = (0,0)$.[8]

(*ii*) Table 4.2 does not explicitly present P2-symmetric models. However, a representative P2-symmetric model can be obtained simply by perturbatively lowering the symmetry of the explicitly-given P4-symmetric models, e.g., by applying a small uniaxial compression in one of the directions perpendicular to the rotation axis, while maintaining the bulk energy gap.

(*iii*) In Table 4.2, we have listed only models with positive values for the difference in on-site angular momenta: $\Delta\mathcal{L} \geq 0$ for a given difference in Wyckoff position $\Delta\boldsymbol{r}_\perp$. Model Hamiltonians with the same $\Delta\boldsymbol{r}_\perp$ but with negative $\Delta\mathcal{L}$ can be obtained from the tabulated model Hamiltonians by applying complex conjugation composed with the inversion $\boldsymbol{k} \to -\boldsymbol{k}$:

$$h_{-\Delta\mathcal{L}}(\boldsymbol{k}) = h^*_{\Delta\mathcal{L}}(-\boldsymbol{k}). \tag{4.28}$$

$h_{-\Delta\mathcal{L}}$ and $h_{\Delta\mathcal{L}}$ can be viewed as two Hamiltonians related by time reversal, which inverts angular momenta while preserving real-spatial positions, as argued in Dets. 4.3. Because time reversal also inverts the Berry-curvature vector, the polarization and the Hopf invariant of a pair of time-reversal-related Hamiltonians are related as

$$\mathscr{P}(\Pi; h_{\Delta\mathcal{L}}) = \mathscr{P}(-\Pi; h_{-\Delta\mathcal{L}}), \quad \chi[h_{\Delta\mathcal{L}}] = -\chi[h_{-\Delta\mathcal{L}}]. \tag{4.29}$$

Details 4.3 To see that $h_{-\Delta\mathcal{L}}$ and $h_{\Delta\mathcal{L}}$ are related by time reversal, recall that a two-band Hamiltonian $h_{\Delta\mathcal{L}}(\boldsymbol{k})$ is expressed in the basis of orbitals $\varphi_{1,2}$. Adopting the complex-conjugate orbitals $\varphi^*_{1,2}$, the time-reversal operator [understood as a linear map from the Hilbert space spanned by orbitals (φ_1, φ_2) to the Hilbert space spanned by $(\varphi^*_1, \varphi^*_2)$] is represented as complex conjugation; therefore, the time-reversal-related Hamiltonian is $h^\Theta_{\Delta\mathcal{L}}(\boldsymbol{k}) = h^*_{\Delta\mathcal{L}}(-\boldsymbol{k})$. Additionally, time-reversal flips the on-site angular momenta, but preserves the real-space coordinates: if the basis vectors $\varphi_{1,2}$ are characterized by the onsite angular momenta difference $\Delta\mathcal{L}$ and position difference $\Delta\boldsymbol{r}$, then $\varphi^*_{1,2}$ are characterized by $-\Delta\mathcal{L}$ and $\Delta\boldsymbol{r}$. In other words, it must be that $h^\Theta_{\Delta\mathcal{L}}(\boldsymbol{k}) = h_{-\Delta\mathcal{L}}(\boldsymbol{k})$. The sought Eq. (4.28) follows by combining the previous two.

4.5 INCOMPATIBILITY CRITERION FOR THE HOPF INVARIANT

In the last section of this chapter we show that a nontrivial Hopf invariant is *incompatible* with certain crystallographic spacetime symmetries, as summarized by the following criterion:

Hopf incompatibility criterion: Let $|u(\boldsymbol{k})\rangle$ be a nondegenerate energy band of a tight-binding Hamiltonian with the symmetry of a symmorphic magnetic space group $\mathcal{G}$ in three spatial dimensions. Assuming $|u(\boldsymbol{k})\rangle$ has trivial first Chern class on all planes, the Hopf invariant [cf. Eq. (4.8)] of band $|u(\boldsymbol{k})\rangle$ vanishes if $\mathcal{G}$ contains either of these elements: (*i*) an element that inverts the arrow of time but preserves the orientation of space, or (*ii*) an element that preserves the arrow of time but inverts the orientation of space.

In the following we first provide an intuitive understanding of this criterion in Sec. 4.5.1. After that we proceed to formally prove the criterion in Sec. 4.5.2.

4.5.1 *Intuitive understanding of the criterion*

The incompatibility criterion for a nontrivial Hopf invariant can intuitively be understood in the following way. Since the Berry connection $\boldsymbol{\mathcal{A}}(\boldsymbol{k})$ forms

8 $\boldsymbol{r}_{1,\perp} = (0,0)$ implies that ζ_1 is periodic in reciprocal-vector translations orthogonal to the k_z-axis, according to Eq. (4.27).

part of the matrix elements of the position operator in the basis of Bloch functions [131], $\boldsymbol{\mathcal{A}}$ transforms under spatial symmetries like a vector, and is moreover even under time reversal. (There is a separate gauge-dependent component of $\boldsymbol{\mathcal{A}}$ that does not transform as a vector, but this component vanishes when integrated over the Brillouin zone, owing to the triviality of the first Chern class.) Likewise, the curvature $\boldsymbol{\mathcal{F}}(\boldsymbol{k}) = \nabla_{\boldsymbol{k}} \times \boldsymbol{\mathcal{A}}$ transforms like a pseudovector that is odd under time reversal [132]. In combination, $\boldsymbol{\mathcal{F}} \cdot \boldsymbol{\mathcal{A}}$ transforms as a pseudoscalar that is odd under time reversal, and therefore its integral over the BZ vanishes. The Hopf incompatibility criterion is a straightforward consequence of these transformation properties.

In the following we provide some clarifying remarks:

(*a*) We restrict the above criterion to *symmorphic* magnetic space groups $\mathcal{G}$, because to our knowledge there exists no unit-rank band in a nonsymmorphic space group. (For a band whose projector is periodic and analytic in $\boldsymbol{k}$ throughout the BZ, the rank of a band is the number of linearly independent Bloch functions at every $\boldsymbol{k}$, e.g., the Hopf-insulating conduction and valence bands each has unit rank.) For nonsymmorphic space groups with a nonsymmorphic symmetry element (screw or glide), the non-existence of unit-rank bands has been proven.[9] For nonsymmorphic space groups without a nonsymmorphic element, the non-existence of unit-rank bands has not been generally proven, though this seems empirically to be true for a wide variety of space groups [135–137].

(*b*) Possible magnetic space groups $\mathcal{G}$ which are not ruled out by the Hopf incompatibility criterion are restricted to Type I (colorless groups) derived from chiral non-magnetic space groups, and to Type III (black-and-white groups with ordinary Bravais lattice) with symmetry elements that include space inversion and time reversal only in combination.

(*c*) The criterion is valid for both integer-spin and half-integer-spin energy bands. This suggests that a Hopf insulator can be sought in electronic systems with and without spin-orbit coupling as well as in bosonic metamaterials.

(*d*) Finally, let us note that the presented proof of the incompatibility criterion explicitly assumes vanishing Cher numbers, and does not generalize to the case of Hopf-Chern insulators with non-vanishing Chern numbers.

4.5.2 *Formal proof of the Hopf incompatibility criterion*

In order to prove the incompatibility criterion formulated at the beginning of this Appendix we assume that the tight-binding Hamiltonian has exponentially-decaying matrix elements in real space, and therefore the Fourier transform of the Hamiltonian is an analytic function of $\boldsymbol{k}$ throughout the Brillouin zone (BZ).

To prove the criterion, we need to address the transformation of $\boldsymbol{\mathcal{A}}(\boldsymbol{k})$ under a symmetry $g \in \mathcal{G}$:

$$\boldsymbol{\mathcal{A}}(s_g \check{g} \boldsymbol{k}) = \check{g} \boldsymbol{\mathcal{A}}(\boldsymbol{k}) + s_g \check{g} \nabla_{\boldsymbol{k}} \beta_g, \tag{4.30}$$

where $s_g = \pm 1$ indicates the reversal of time, and $\check{g} \in O(3)$ is the matrix representation of $g \in \mathcal{G}$ acting on spatial coordinates. The second term on the

9 For band representations, this has been proven by Michel and Zak [133]; more generally, this has been proven in the Supplementary Material of Ref. [134].

right-hand side of Eq. (4.30) is derived from the symmetry constraint between tight-binding wave functions at symmetry-related momenta $\boldsymbol{k} \leftrightarrow s_g \check{g}\boldsymbol{k}$,

$$R_g \left|u(\boldsymbol{k})\right\rangle = e^{i\beta_g(\boldsymbol{k})} \left|u(s_g \check{g}\boldsymbol{k})\right\rangle, \tag{4.31}$$

where R_g is a matrix representation of g that is antiunitary if g inverts time, and unitary otherwise. Crucially, the $U(1)$ phase $\beta_g(\boldsymbol{k})$ in Eq. (4.31) encodes the change of the Wannier-center position due to g [120] and cannot generally be made $\boldsymbol{k}$-independent [24, 56]. On the other hand, the transformation of the curvature does not involve β_g and is exactly as claimed in the intuitive argument from Sec. 4.5.1,

$$\boldsymbol{\mathcal{F}}(s_g \check{g}\boldsymbol{k}) = s_g \det[\check{g}]\, \check{g}\boldsymbol{\mathcal{F}}(\boldsymbol{k}). \tag{4.32}$$

Combining Eq. (4.30) with Eq. (4.32) we derive that the Hopf invariant is proportional to

$$\begin{aligned} \int d\boldsymbol{k}\boldsymbol{\mathcal{F}} \cdot \boldsymbol{\mathcal{A}}\big|_{\boldsymbol{k}} &= \int d\boldsymbol{k}\boldsymbol{\mathcal{F}} \cdot \boldsymbol{\mathcal{A}}\big|_{s_g \check{g}\boldsymbol{k}} \\ = s_g \det[\check{g}] \int d\boldsymbol{k}\boldsymbol{\mathcal{F}} \cdot \boldsymbol{\mathcal{A}}\big|_{\boldsymbol{k}} &+ \det[\check{g}] \int d\boldsymbol{k}\boldsymbol{\mathcal{F}} \cdot \nabla_{\boldsymbol{k}} \beta_g, \end{aligned} \tag{4.33}$$

where the first step corresponds to a change of coordinates, and in the second step we used the invariance of the dot product under rotations.

Next we would like to prove that the last term in this expression vanishes. Having trivial first Chern class means that $|u(\boldsymbol{k})\rangle$ can be made an analytic and periodic function of $\boldsymbol{k}$ throughout the BZ [128]. Applying these properties to Eq. (4.31), we deduce that the phase factor $e^{i\beta_g(\boldsymbol{k})}$ can also be made analytic and periodic. The phase β_g is then also analytic, but can in principle wind by integer multiples of 2π if $\boldsymbol{k}$ is advanced by a reciprocal vector $\boldsymbol{G}$. Without loss of generality, we may separate $\beta_g(\boldsymbol{k}) = \tilde{\beta}_g(\boldsymbol{k}) + \boldsymbol{k} \cdot \boldsymbol{R}_g$ into a periodic component $[\tilde{\beta}_g(\boldsymbol{k}) = \tilde{\beta}_g(\boldsymbol{k} + \boldsymbol{G})]$ and a winding component, with $\boldsymbol{R}_g$ a $\boldsymbol{k}$-independent Bravais-lattice vector.

The term in Eq. (4.33) that is proportional to $\tilde{\beta}_g$ may be expressed via Leibniz rule as

$$\int d\boldsymbol{k}\boldsymbol{\mathcal{F}} \cdot \nabla_{\boldsymbol{k}} \tilde{\beta}_g = \int d\boldsymbol{k} \nabla_{\boldsymbol{k}} \cdot (\tilde{\beta}_g \boldsymbol{\mathcal{F}}) - \int d\boldsymbol{k} \beta_g \nabla_{\boldsymbol{k}} \cdot \boldsymbol{\mathcal{F}}; \tag{4.34}$$

the first term on the right-hand side is seen to vanish by applying Stoke's theorem and the periodicity of both $\tilde{\beta}_g$ and $\boldsymbol{\mathcal{F}}$; the second term on the right-hand side vanishes because the curvature is generally divergence-free for a nondegenerate energy band of a tight-binding Hamiltonian (assumed to be analytic in $\boldsymbol{k}$). Similarly, the winding component of β_g leads to a term in Eq. (4.33) that is proportional to $\int d\boldsymbol{k}\boldsymbol{\mathcal{F}} \cdot \boldsymbol{R}_g$, with $\boldsymbol{R}_g$ that is $\boldsymbol{k}$-independent. This quantity vanishes because the first Chern number has been assumed to vanish on any 2D cut of the BZ. Equation 4.33 therefore reduces to

$$\chi = s_g \det[\check{g}]\chi, \tag{4.35}$$

implying that χ transforms as a pseudoscalar that is odd under time reversal, and therefore vanishes if $s_g \det[\check{g}] = -1$ for some $g \in \mathcal{G}$.

5

BULK-BOUNDARY CORRESPONDENCE

In this chapter we derive the bulk-boundary correspondence for both the Hopf and the RTP invariants of the crystalline Hopf insulators.

We start in Sec. 5.1 with the bulk-boundary correspondence of the Hopf invariant. Contrary to some expectations [92, 93, 138], the Hopf invariant does not protect conducting surface states. In other words, all surfaces of a Hopf insulator (with or without crystalline symmetry) can be made insulating while preserving the bulk gap. What then is 'topological' about such surface states which can be spectrally disconnected from the bulk states? We demonstrate that the *faceted Chern number* – defined as the first Chern number of *all* bands localized to a single surface facet, independent of their filling – is in one-to-one correspondence with the integer-valued, bulk homotopy invariant χ.

The key notion that underlies the bulk-boundary correspondence of RTP insulators is that of an *angular-momentum anomaly* associated with a rotation-symmetric boundary – roughly speaking, the itinerant angular momenta of the surface states are non-identical to the itinerant angular momenta of the bulk-conduction or bulk-valence states. This anomaly of the surface states derives from a nontrivial RTP invariant in the bulk, as proven in Sec. 5.2.

The surface states having anomalous values of itinerant angular momenta has two implications that we explore subsequently. First, in Sec. 5.3 we show that, in the presence of an open boundary with sharply terminated hoppings, the surface-state energies necessarily interpolate across the bulk gap to connect the bulk-valence and bulk-conduction bands, ensuring that there are gapless excitations no matter where the Fermi level is positioned within the bulk energy gap.

When the boundary is not sharp, this interpolation across the bulk energy gap is not guaranteed by a nontrivial RTP invariant. Nevertheless, Sec. 5.4 shows that a more general topological feature survives that is encoded not in the energy dispersion but rather in the wave function of surface-localized states. Namely, the Berry-Zak phase of surface states along a certain symmetrically-chosen loop in the rBZ is quantized to rational multiples of 2π, and moreover these quantized values for the Berry-Zak phase are non-identical to the Berry-Zak phases of the bulk Bloch states along an equivalent loop in the bulk BZ. We call this a *Zak-phase anomaly*.

Throughout this chapter, *bulk* objects refer to the crystalline interior which has the symmetry of a 3D space group, up to exponentially-weak corrections due to a surface termination. The surface is assumed to form a *crystalline facet* that is symmetric under two out of three translational symmetries and a point group symmetries of the space group.

CHAPTER CONTENTS

5.1 FACETED CHERN NUMBER

We start this section by drawing an analogy between the Hopf invariant and the charge polarization and providing an intuitive argument why the Hopf invariant leads to a surface localized Chern number. In the geometric theory of polarization [71, 83, 139], the charge polarization is proportional to $\int_{\mathrm{BZ}} \boldsymbol{\mathcal{A}}$; analogously, one may view $\int_{\mathrm{BZ}} \boldsymbol{\mathcal{A}} \cdot \nabla \times \boldsymbol{\mathcal{A}}$ as proportional to a real-space polarization of Berry curvature [140–142]. Just as the charge polarization is revealed by the charge that accumulates at a surface termination [143], a Berry-curvature polarization of χ contributes $(-\chi/2)e^2/h$ to the geometric component (σ^s_{yx}) of the surface anomalous Hall conductance (SAHC) [144–146]. Crucially, the bulk conduction and valence bands individually and equally contribute $(-\chi/2)e^2/h$, owing to the fundamental antisymmetry of all Pauli-matrix Hamiltonians: $\sigma_y h(\boldsymbol{k})\sigma_y = -h^*(\boldsymbol{k})$. If all bands in the Hilbert space are accounted for, the net contribution to σ^s_{yx} should vanish [145], hence there should exist surface band(s) which contribute $\chi e^2/h$ to σ^s_{yx}. This argument is confirmed numerically in Fig. 5.1(c) for the MRW model (4.24) with $\chi = -1$ and will be demystified in this section.

We show that such nontrivial surface bands originate from a bulk-to-boundary flow of Berry curvature – at the critical point between the trivial and Hopf insulator. Such flow does *not* occur via the Callan-Harvey anomaly inflow mechanism [147, 148], which is understood through chiral zero modes of the Dirac equation with a mass coupling to a domain wall [149, 150]. Instead, the surface states of the Hopf insulator arise as *non*-chiral, Schrödinger-type modes on the domain wall of a generalized Weyl equation – describing a Berry dipole introduced in Chapter 3. A single surface facet of a Hopf-insulating crystal is *un*describable by a 2D lattice model of a Chern insulator, because the conjugate surface states (with opposite Chern number)

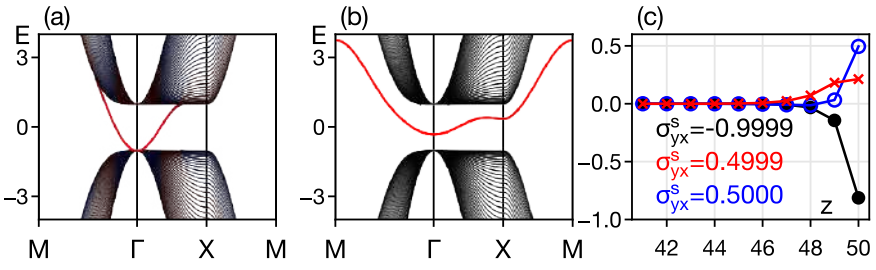

Figure 5.1: (a) Red line depicts the top-001-surface states of the Hopf insulator in the MRW tight-binding model (4.24) with $\chi = -1$ (specified by parameter $\Phi = -2$) and open boundary conditions. (b) Surface band of (a) is detached by modifying the surface Hamiltonian. (c) For a fifty-cell-tall 001 slab, we plot the layer-resolved SAHC [Eq. (12) in Ref. [140]] of the bulk valence band (blue), bulk conduction band (red), and surface band (black) illustrated in (b). Summing the layer-resolved SAHC over ten layers approximates $\sigma^s_{yx}[e^2/h]$ to exponential accuracy.

lie on the *opposite* facet of a finite slab – realizing a nonlocal 'teleportation' of Berry curvature.

5.1.1 *Faceted Chern number as a topological invariant*

We propose the faceted Chern number $\mathscr{C}_f$ as a topological invariant for any three-spatial-dimensional Hamiltonian that is a two-by-two matrix at each $\boldsymbol{k}\in$BZ, with a spectral gap (at each $\boldsymbol{k}$) separating a valence and conduction bulk band with trivial first Chern class. For such category of Hamiltonians which include the Hopf insulator, we consider a surface termination whose reduced Brillouin zone (rBZ) is a 2D cut of BZ.

The triviality of the first Chern class implies any surface-localized mode is continuously deformable to a flat-band dispersion [88, 120] and is therefore *detachable* from bulk bands. To 'detach' means to energetically separate a surface band from bulk bands while preserving all crystallographic spacetime symmetries of the surface, such that the projector to the surface-band wave function is continuous throughout rBZ, as illustrated in Fig. 5.1(a-b). (In contrast, the surface states of a 3D Chern insulator [151] are un-detachable [60].) The conceptually simplest formulation of the faceted Chern number is as a rBZ-integral of the normal to facet component of Berry curvature computed for the surface-band wave function:

$$\mathscr{C}_f := \frac{1}{2\pi}\int_{\mathrm{rBZ}} \mathrm{Tr}[\boldsymbol{\mathcal{F}}(\boldsymbol{k})\cdot\hat{\boldsymbol{n}}]d^2k, \tag{5.1}$$

with $\hat{\boldsymbol{n}}$ the outward-normal vector for a chosen facet, and Tr a trace over all surface bands, *independent* of electron filling. In Sec. 5.1.3 we present a more general formulation of $\mathscr{C}_f$ that is well-defined without need of detachment.

Let us demonstrate that $\mathscr{C}_f$ is invariant under continuous deformation of the surface-terminated Hamiltonian, so long as both bulk gap and bulk translational symmetry are maintained. Since surface bands are detachable, their wave function is exponentially localized to the surface, and therefore their net Chern number cannot change under a bulk deformation *alone*. What remains is to prove the absence of a continuous deformation between two Hamiltonians with the *same* bulk but with distinct faceted Chern numbers: $\mathscr{C}_f > \mathscr{C}'_f$. Assume to the contrary that such a deformation exists and is parametrized by $t \in [0,1]$. It is simplest to view $\mathscr{C}_f, \mathscr{C}'_f$ as applying to the top facet of a finite slab, with periodic boundary conditions in two surface-parallel directions. As t is varied, we hypothesize that $(\mathscr{C}_f - \mathscr{C}'_f)$ quanta of Berry curvature can leave the top facet and enter the bulk [141, 142]. Since the bulk Hamiltonians at $t = 0$ and $t = 1$ are indistinguishable, this Berry curvature must finally end up at the bottom facet of the slab. There must then exist an adiabatic cycle for a *bulk* Hamiltonian $h(k_x, k_y, k_z, t)$ that is periodic in t, such that $(\mathscr{C}_f - \mathscr{C}'_f)$ quanta of Berry curvature is translated by a surface-normal lattice vector over one cycle. If this translation occurs through the valence (resp. conduction) band of $h(\boldsymbol{k}, t)$, then $(\mathscr{C}_f - \mathscr{C}'_f)$ is identifiable as the second Chern number $\mathscr{C}_2$ of the valence (resp. conduction) band; $\mathscr{C}_2$ is defined [152] as the $(\boldsymbol{k}, t)$-integral of the second Chern character. The wrongness of our hypothesis becomes self-evident, because the second Chern character necessarily vanishes for a non-degenerate band of a two-band Hamiltonian, as shown in Appendix A.2.4.

The above argument relied on identifying $\mathscr{C}_2$ as the number of Berry-curvature quanta pumped by one lattice vector in an adiabatic cycle. Indeed, if $h(\boldsymbol{k}, t)$ – with trivial first Chern class and $\mathscr{C}_2 \neq 0$ – were diagonalized

with open boundary conditions in the z-direction, then the boundary theory describes (3+1)D Weyl fermions with a net chiral charge [153] equal to $\mathscr{C}_2$, in the three-dimensional, momentum-like space of (k_x, k_y, t) [142]. (These Weyl fermions may be derived in a continuum model – as chiral zero modes of the (4+1)D Dirac equation with a domain wall [147, 152].) Let us view the boundary theory as (2+1)D fermions tuned by t: over one t-cycle, $\mathscr{C}_2$ quanta of Berry curvature must be transferred at critical closings of the boundary energy gap. Since the full Hamiltonian (that operates on both boundary and bulk Hilbert spaces) is periodic in t, there must be a compensating pump of curvature through the bulk to exactly cancel the transfer of curvature at the boundary. Such a cancellation occurs between two systems of differing dimensionality, and has the same origin as the Callan-Harvey anomaly inflow [147, 148, 154]. We have proven that $\mathscr{C}_2 \neq 0$ implies a Berry-curvature pump in the bulk; the converse statement – that a pump implies $\mathscr{C}_2 \neq 0$ – has been proven by formulating the Chern-Simons magnetoelectric polarizability in terms of 'hybrid Wannier sheets' [141, 142].

Our argument for the invariance of $\mathscr{C}_f$ shows that the Callan-Harvey effect does *not* explain the Berry curvature on the Hopf-insulator surface. (In contrast, the Callan-Harvey effect is responsible for the SAHC of the 'layered Haldane model' [142].) Understanding the Hopf insulator not only reveals a new mechanism for a bulk-to-boundary flow of Berry curvature, but also leads to the bulk-boundary correspondence $\chi = \mathscr{C}_f$.

5.1.2 *Bulk-to-boundary flow of Berry curvature*

In the continuum perspective, the advertised mechanism may be understood in terms of non-chiral domain-wall modes of a generalized Weyl equation: $(i\partial_t - h)\psi = 0$ with the Hamiltonian describing the critical transition mediated by a Berry dipole. This Hamiltonian is specified by Eqs. (3.3) and (3.4) where we set $\Delta\ell = 1$ and $v = 1$, and it is invariant under rotation symmetry as given by Eq. (3.2). At the parameter value $\phi = 0$ the gap closes and the Hamiltonian describes the Berry dipole, while at $\phi \neq 0$ the phase is gapped.

As was discussed in Sec. 3.2 phase transition over such Berry dipole induces a minus unit change in the Hopf invariant $\delta\chi = -1$. We note, that away from criticality the pseudospin texture

$$\left\langle u_{v(c)}(k_x, k_y, 0) \right| \boldsymbol{\sigma} \left| u_{v(c)}(k_x, k_y, 0) \right\rangle \tag{5.2}$$

of the valence (resp. conduction) band is skyrmionic (resp. antiskyrmionic) over the (k_x, k_y) plane, as illustrated in Fig. 5.2(b). (In comparison, the meronic spin texture [20] of a $(2+1)D$ massive Dirac fermion is 'half' of a skyrmion.) To see this, we use the valence eigenstate in the gauge defined in Eq. (3.20) with $\beta(k_z) = 0$. In the limit of $\boldsymbol{k}_\perp = 0$ ($\boldsymbol{k}_\perp = \infty$) the pseudospin is pointing up (down) for the valence band and opposite for the conduction band.

To manifest the nontrivial boundary mode that develops at criticality, we solve the generalized Weyl equation with $k_z \to -i\partial_z$ and $\phi(z)$ having a domain-wall profile. It is analytically convenient to choose $\phi(z) = \phi' z$ that is linear in the interval $|z| < \Lambda$ (with $\Lambda \gg |\phi'|^{-1/2}$), with ϕ tapering off to a constant outside this interval, as depicted in Fig. 5.2(a). Then a Gaussian-localized, spin-polarized mode ψ_η exists with a Schrödinger-type dispersion E_η:

$$\psi_\eta = \kappa_\eta e^{-|\phi'|z^2/2}, \quad E_\eta = \eta(k_x^2 + k_y^2 - |\phi'|), \tag{5.3}$$

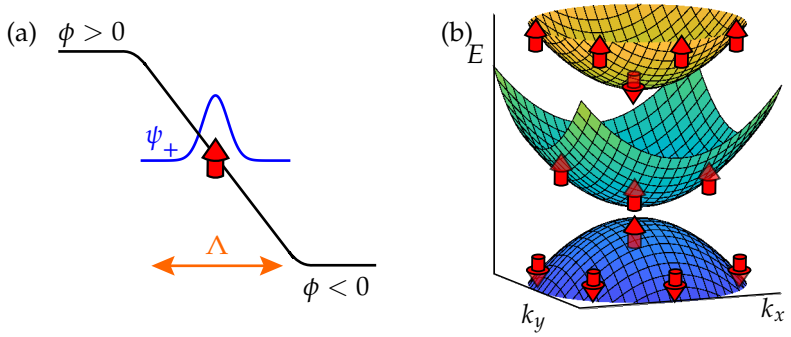

Figure 5.2: (a) The spin-polarized wave function ψ_+ localized to a domain wall of $\phi(z)$, its pseudospin is constant and denoted by a red arrow. (b) For the continuum Berry dipole Hamiltonian, the constant pseudospin texture (5.2) of the electron-like, domain-wall mode ψ_+ (middle green band) is contrasted with those of the two bulk modes (top yellow and bottom blue) which form a (anti)skyrmion structure. From this follows a unit difference in the Chern number associated with a bulk vs. domain wall mode.

with $\sigma_z \kappa_\pm = \pm\kappa_\pm$. The mass and pseudospin depend on sign$[\phi']$: $= -\eta$; we refer to modes with positive (resp. negative) mass with respect to (k_x, k_y) as electron-like (resp. hole-like).

The contrasting pseudospin textures – constant for the domain-wall mode but (anti)skyrmionic for the bulk modes – imply that the integrated Berry curvature vanishes for both electron- and hole-like domain-wall modes, but equals $+2\pi$ (resp. -2π) for the electron-like (resp. hole-like) bulk mode. We will see that the *differential* curvature – between electron-like bulk and electron-like domain-wall modes – is maintained upon regularizing our continuum model on a lattice. The Hopf insulator is a lattice regularization satisfying that all bulk modes have *trivial* first Chern number, meaning that regularization adds -2π (resp. 2π) to the Berry-curvature integral for the electron-like (resp. hole-like) band. This implies that the regularized domain-wall mode has a *nontrivial* first Chern number $= -\eta$, where $\eta = +$ (resp. $\eta = -$) corresponds to the electron-like (resp. hole-like) mode. We see that this Chern number depends on the orientation of the domain wall, like how the faceted Chern number depends on the facet orientation $\hat{\boldsymbol{n}}$ [cf. Eq. (5.1)].

Since $\phi = 0$ describes a Berry dipole and not a monopole, a regularization can be found without any fermion doubling [153], meaning that the energy gap of the lattice model closes at a single isolated wavevector (the BZ center) when $\phi = 0$. A lattice regularization satisfying the above-stated properties is given by the Moore-Ran-Wen tight-binding model [55] given in Eq. (4.24).

If $\chi = \mathscr{C}_f$ is proven for the Moore-Ran-Wen model, the correspondence would extend to the entire homotopy class of translation-invariant, two-by-two Hamiltonians. This is because χ and $\mathscr{C}_f$ are individually invariant under any continuous, bulk-gap-preserving deformations that preserve the bulk-translational symmetry; this fact is well-known for χ [55, 97] and has been proven above for $\mathscr{C}_f$. As we showed in Sec. 4.5, Hamiltonians with nonzero χ may have any non-translational symmetry that does *not* invert the pseudoscalar: $\chi \to -\chi$. Particularly, the Moore-Ran-Wen regularization retains an order-four rotational symmetry [cf. Sec. 4.4.2], which allows us to utilize our rotation-symmetric domain-wall analysis.

Considering the top surface of the MRW model as a domain wall with $\eta = +$ we conclude that the surface band carries a Chern number $\mathscr{C}_f = -1$. At the same time, the domain wall separates two phases that can be transformed into each other across a Berry dipole with $\Delta\ell = 1$ and $\nu = 1$ and hence their Hopf invariants differ by $\delta\chi = -1$. Assuming that the domain wall separates the MRW model from the vacuum with $\chi = 0$, the bulk of the MRW model carries a Hopf invariant $\chi = -1$. Thus we arrive at $\mathscr{C}_f = \chi = -1$ for the top surface. Bearing in mind that the surface-normal vector $\hat{\boldsymbol{n}}$ flips between top and bottom surface [cf. Eq. (5.1)] and so does the orientation of the domain wall, we conclude that the equality $\mathscr{C}_f = \chi = -1$ works for *both* surfaces. The generalization to $\mathscr{C}_f = \chi = N$ is attained by substituting $k_z \to Nk_z$ ($N \in \mathbb{Z}$) in the Moore-Ran-Wen model, such that $\phi = 0$ marks a critical point with $|N|$ Berry dipoles. We remark that the *full* subspace of surface states (on a single facet) has a net Chern number $= \mathscr{C}_f$; in contrast, the full Hilbert space of any strictly-2D, tight-binding Hamiltonian must have vanishing net Chern number. The absence of a strictly-2D description also applies to $\mathbb{Z}_2$-topological-insulating surface states, but in the latter case it is because an odd number of gapless, chiral fermions [147] violates the fermion-doubling theorem [153, 155].

5.1.3 *Wannier cut method*

It is possible to formulate $\mathscr{C}_f$ without detaching surface bands, but defining it for all hybrid Bloch-Wannier functions [defined in Eq. (2.34)] localized near the surface. For this we define the *faceted projector* onto $\mathcal{N}_f$ hybrid Bloch-Wannier bands, closest to a chosen facet by means of the *Wannier cut* method introduced in [156]. We consider a finite in z-direction and infinite in (x, y)-plane slab, with unit cells in z-direction labeled by $R_z = 1, \ldots \mathcal{N}_0$, and in the following referred to as layers. For large enough $\mathcal{N}_0$ the top and bottom facets are separated by a large enough distance, such that the overlap between the hybrid states at the top and at the bottom facets is negligible. First, we define the projector onto $2\mathcal{N}_f < \mathcal{N}_0$ states at the top and bottom facets. In a finite slab with periodic boundary conditions, one can define bulk-like hybrid functions $\bar{\mathcal{V}}_{j,\boldsymbol{k}_\perp,R_z}(\boldsymbol{k}_\perp, \bar{R}_z, \alpha)$ by replacing an integral over momentum k_z by a finite sum in Eq. (2.34). For large enough $\mathcal{N}_0$, bulk-like hybrid functions in a finite geometry and bulk hybrid functions in an infinite geometry converge to each other. Moreover, the hybrid functions of a finite slab with open boundary conditions, computed far enough from the facets, can be described by the bulk-like hybrid functions $\bar{\mathcal{V}}_{j,\boldsymbol{k}_\perp,R_z}(\boldsymbol{k}_\perp, \bar{R}_z, \alpha)$ up to exponentially small corrections. Then the projector onto top and bottom facets at each reduced momentum $\boldsymbol{k}_\perp$ can be expressed as:

$$P_{\text{t\&b}}(\boldsymbol{k}_\perp) = \mathbb{1}_{\boldsymbol{k}_\perp} - \sum_{j=1}^{N_v+N_c} \sum_{R_z=\mathcal{N}_f+1}^{\mathcal{N}_0-\mathcal{N}_f} \left|\bar{\mathcal{V}}_{j,\boldsymbol{k}_\perp,R_z}\right\rangle\!\left\rangle\!\left\langle\!\left\langle \bar{\mathcal{V}}_{j,\boldsymbol{k}_\perp,R_z}\right| . \tag{5.4}$$

The first term on the right-hand side is the projector onto all $\mathcal{N}_0 \times (N_v + N_c)$ states of a finite slab with reduced momentum $\boldsymbol{k}_\perp$, where to keep the method general we assume that the model has N_v valence and N_c conduction bands. This projector is given by the identity matrix in the sector corresponding to the reduced vector $\boldsymbol{k}_\perp$ and is zero at $\boldsymbol{k}'_\perp \neq \boldsymbol{k}_\perp$. From this term, we subtract projectors onto a set of bulk-like hybrid states (in both the valence and conduction subspaces), that are localized to the bulk of the finite slab. Because of the exponential localization of the hybrid states in the z-direction,

we approximate $\bar{\mathcal{V}}_{j,\boldsymbol{k}_\perp,R_z}(\boldsymbol{k}_\perp,\bar{R}_z,\alpha)\approx 0$ for $|\bar{R}_z-R_z|>R_0$, which holds up to exponentially small corrections for a large enough cut-off scale R_0. Then for large enough $\mathcal{N}_f>R_0$ and $\mathcal{N}_0-2\mathcal{N}_f>R_0$, $P_{\text{t\&b}}(\boldsymbol{k}_\perp)$ has finite support on two regions, located respectively near the bottom and the top facet. Note $P_{\text{t\&b}}(\boldsymbol{k}_\perp)$, being the difference between two projection matrices, is itself a projector.

To define the projector onto the bottom facet we additionally 'sandwich' Eq. (5.4) by a projector onto the bottom half of the slab:

$$P_{\text{b}}(\boldsymbol{k}_\perp)=P_\downarrow P_{\text{t\&b}}(\boldsymbol{k}_\perp)P_\downarrow \tag{5.5}$$

$$\text{where at each } \boldsymbol{k}_\perp\text{-sector}\quad P_\downarrow(\boldsymbol{k}_\perp)=\begin{pmatrix}\mathbb{1} & \mathbb{0}\\ \mathbb{0} & \mathbb{0}\end{pmatrix}, \tag{5.6}$$

and $\mathbb{1}$ and $\mathbb{0}$ respectively denote the identity and the zero matrices of the size $\mathcal{N}_0/2\times(N_v+N_c)$, where for simplicity we assumed that $\mathcal{N}_0$ is even. Then $P_\downarrow$ defines the projector onto first $\mathcal{N}_0/2$ layers of the slab.

We define $\mathscr{C}_f[\mathcal{N}_f]$ as the first Chern number of the $\mathcal{N}_f$ Bloch-Wannier bands whose eigenvalues lie closest to $z=0$. Viewed as a sequence in $\mathcal{N}_f$, $\mathscr{C}_f[\mathcal{N}_f]$ has a unique accumulation point ($:=\mathscr{C}_f$) because all bulk eigenbands have trivial first Chern class. This formulation manifests the unique definition of $\mathscr{C}_f$; in particular, $\mathscr{C}_f$ is invariant if a Chern-insulating layer is adsorbed onto the surface.

What does $\chi=\mathscr{C}_f$ imply for the magnetoelectric response of the Hopf insulator? It is known that the geometric contribution to the frozen-lattice, orbital magnetoelectric polarizability [60, 140, 144, 146, 152, 157] equals $(\theta/2\pi \bmod 1)e^2/h$, with the 'axion angle' [158] θ equal to an integrated Chern-Simons three-form of the Berry connection [140, 152]. For the considered class of Hamiltonians, θ is gauge-invariant and simplifies to $\pi\chi$, thus the Hopf insulator exemplifies the simplest axion insulator [24, 60, 110, 115, 140, 152] with only a Pauli-matrix Hamiltonian. The possibilities for SAHC on different facets of a Hopf-insulator crystallite are rich, and depend on the energy dispersion of surface bands as well as the electrochemical potential; the latter is tunable by differential doping or gating. Partially-filled surface bands on any facet behaves like a 2D anomalous Hall metal [159]. The detachability of surface bands allows also for complete filling and depletion, e.g., if the topologically nontrivial surface band is completely filled on the 001 facets and completely depleted on the 010 and 100, then $|\mathscr{C}_f|$ number of chiral 'hinge' modes [149, 160–162] will run around the edges of the 001 facet – a manifestation of higher-order topology.

5.2 ANGULAR-MOMENTUM ANOMALY

Here, we formulate the angular-momentum anomaly for a two-band, Pn-symmetric, insulating Hamiltonian with trivial Chern class and a non-zero RTP invariant. Firstly in Sec. 5.2.1, a sketchy formulation is given to quickly convey the essence of the anomaly. The admitted vagueness in Sec. 5.2.1 will be dispelled Sec. 5.2.2 by a detailed exposition of the projected position operator, conjoined with a case study of the P4-symmetric Moore-Ran-Wen model. Much of this subsection will rely on model-dependent, pictorial illustrations; a more formal, model-independent proof is presented in Sec. 5.2.3.

5.2.1 *Angular-momentum anomaly: sketchy introduction*

By assumption, there exists a pair of rotation-invariant reduced momenta, labeled Λ and Ξ, where both mutually-disjoint and iso-orbital conditions are fulfilled [cf. Eq. (4.18)]. This implies that the difference in polarization between Λ and Ξ is quantized to integer values. For convenience, the labels for the reduced momenta are chosen such that the RTP invariant $\Delta\mathscr{P}_{\Lambda\Xi}$ [defined in Eq. (4.17)] is positive.

Our goal is to elucidate what implications this bulk invariant has for a pn*-symmetric facet*, with the pn plane group being a subgroup (of the 3D space group Pn) that is generated by C_n rotation as well as translations in the directions perpendicular to the rotation axis. For concreteness, we consider a RTP insulator on a semi-infinite geometry defined for $z > 0$, with the z-axis coinciding with the rotation axis; the boundary at $z = 0$ forms a 'bottom' pn-symmetric facet.

The angular-momentum anomaly is a property of the itinerant angular momenta of the Hilbert space associated with this semi-infinite geometry. Roughly speaking, a nontrivial RTP invariant guarantees that certain minimal number of bands of states localized to the surface have itinerant angular momenta that are distinct from those of the bulk bands; this minimal number of 'anomalous' bands is nothing more than the absolute value of the RTP invariant itself.

To characterize what exactly makes an 'anomalous' band distinct from a bulk band, we will need to define four numbers that count Bloch states with certain itinerant angular momenta. Firstly, let us define $\sharp_{f(\mathrm{b})}\widetilde{\mathcal{L}}_v(\Lambda)$ as the number of (linearly independent) rotation-invariant Bloch states[1] in our Hilbert space that (*i*) have reduced momentum Λ, (*ii*) has support in the proximity of the bottom facet [hence the subscript (b)], and (*iii*) have itinerant angular momentum coinciding with that of the bulk-valence band $[\widetilde{\mathcal{L}}_v(\Lambda)]$. We take a 'state' localized near a surface to mean an eigenstate of the projected position operator in a semi-infinite geometry, with an eigenvalue that is close to the spatial coordinate of the surface; this will be formalized below in Sec. 5.2.2. Such a state is thus not necessarily an eigenstate of the Hamiltonian. We define $\sharp_{f(\mathrm{b})}\widetilde{\mathcal{L}}_c(\Lambda)$ almost identically as $\sharp_{f(\mathrm{b})}\widetilde{\mathcal{L}}_v(\Lambda)$, except in (*iii*) we replace 'bulk-valence' with 'bulk-conduction', and $\widetilde{\mathcal{L}}_v \to \widetilde{\mathcal{L}}_c$. Lastly, we define two other numbers $\sharp_{f(\mathrm{b})}\widetilde{\mathcal{L}}_{c,v}(\Xi)$ for states satisfying (*i*–*iii*) with $\Lambda \to \Xi$.

We propose that these counting numbers are related to the bulk RTP invariant as

$$-\sharp_{f(\mathrm{b})}\widetilde{\mathcal{L}}_v(\Lambda) + \sharp_{f(\mathrm{b})}\widetilde{\mathcal{L}}_v(\Xi) = \sharp_{f(\mathrm{b})}\widetilde{\mathcal{L}}_c(\Lambda) - \sharp_{f(\mathrm{b})}\widetilde{\mathcal{L}}_c(\Xi) = \Delta\mathscr{P}_{\Lambda\Xi}. \tag{5.7}$$

We call this relation an *angular-momentum anomaly*. Our emphasis on the 'bottom facet' is merely to fix a sign convention; if we had chosen instead a pn-symmetric facet at the 'top' of a semi-infinite bulk, then Eq. (5.7) holds with replaced subscript $(\mathrm{b}) \to (\mathrm{t})$ on the left-hand side and $\Delta\mathscr{P}_{\Lambda\Xi} \to -\Delta\mathscr{P}_{\Lambda\Xi}$ on the right-hand side.

The condition $\Delta\mathscr{P}_{\Lambda\Xi} > 0$ implies there are at least $|\Delta\mathscr{P}_{\Lambda\Xi}|$-number of 'anomalous' surface-localized bands (*a*) whose itinerant angular momentum at Λ is identical to that of the bulk-conduction band, but distinct from that of the bulk-valence band, and (*b*) whose itinerant angular momentum at Ξ

1 Whenever we discuss a 3D Hamiltonian in semi-infinite geometry ($z > 0$) or slab geometry ($z_1 < z < z_2$), we use the term *Bloch state* to describe any state with a well-defined in-plane (reduced) momentum $\boldsymbol{k}_\perp = (k_x, k_y)$.

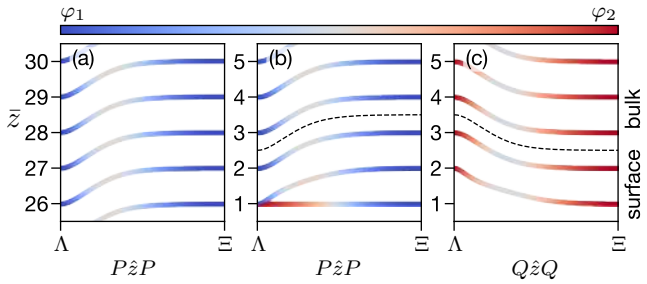

Figure 5.3: For a P4-symmetric Hamiltonian with the RTP invariant $\Delta\mathscr{P}_{\Lambda\Xi} = \mathscr{P}_\Xi - \mathscr{P}_\Lambda = +1$, we plot the spectrum of the projected position operators $P\hat{z}P$ and $Q\hat{z}Q$, along a straight-line path $\Lambda\Xi$ in rBZ. In panel (a) we focus only on the bulk-like polarization bands; whereas in (b) and (c) we recognize both bulk-like and surface-like polarization bands. The color indicates the orbital decomposition of the wave function into the basis orbitals, with blue and red tones indicating the wave function overlap with φ_1 resp. φ_2. In this particular model, a rotation-invariant Bloch-Wannier state that overlaps with φ_1 (resp. φ_2) has a bulk-valence-like (resp. bulk-conduction-like) itinerant angular momentum, thus it is possible to infer the four numbers $(\sharp_{f(\mathrm{b})}\widetilde{\mathcal{L}}_{c,v}(\Xi), \sharp_{f(\mathrm{b})}\widetilde{\mathcal{L}}_{c,v}(\Lambda))$ from the above plots. The dashed black line in panels (b) and (c) indicates (an arbitrary) partitioning of the polarization bands into bulk-like vs. surface-like, and serves an argument presented in the text of Sec. 5.2.2.

is identical to that of the bulk-valence band but distinct from that of the bulk-conduction band. The sense in which the angular-momentum values of surface-localized bands are anomalous is that they could neither derive from bulk conduction states alone, nor could they derive from bulk valence states alone.

5.2.2 *Angular-momentum anomaly: precise formulation and case study*

Let us elaborate on the meaning of 'states localized near a surface' as eigenstates of the projected position operator in a semi-infinite geometry. We have already shown in Sec. 2.1.5 that the eigenstates of the projected position operators in an infinite geometry are the hybrid Bloch-Wannier functions. The corresponding eigenvalues $\{\bar{z}_j(\boldsymbol{k}_\perp)\}$ define the charge centers of the hybrid bands in the direction of localization z that depend on $\boldsymbol{k}_\perp$; they form a ladder structure in z-direction due to the discrete translation symmetry as illustrated in Fig. 5.3(a). In the context of two-band, insulating Hamiltonians, there is only a single Bloch-Wannier state with a given $\boldsymbol{k}_\perp$ in any unit-length interval of the z-axis, and the dispersive function $\bar{z}_j(\boldsymbol{k}_\perp)$ can be identified, modulo one, with the polarization function $\mathscr{P}(\boldsymbol{k}_\perp)$ [83], as discussed in Sec. 2.1.4.2. We describe all Bloch-Wannier eigenstates corresponding to $\bar{z}_j(\boldsymbol{k}_\perp)$ as belonging to the j-th *polarization band*, in analogy with how eigenstates of a discrete-translation-invariant Hamiltonian can be sorted into energy bands. The positive value $\Delta\mathscr{P}_{\Lambda\Xi} = \mathscr{P}_\Xi - \mathscr{P}_\Lambda > 0$ implies that the ladder-rung function $\bar{z}_j(\boldsymbol{k}_\perp)$ is displaced at $\boldsymbol{k}_\perp = \Xi$ relative to Λ by a positive number $\Delta\mathscr{P}_{\Lambda\Xi} \in \mathbb{Z}^+$ of unit cells, as illustrated for $\Delta\mathscr{P}_{\Lambda\Xi} = 1$ in Fig. 5.3(a).

What implications does this bulk displacement have for surface-localized states in our semi-infinite slab geometry? Let us assume the Hamiltonian matrix elements are terminated near the surface at $z = 0$ such that a Fermi level exists within the bulk energy gap and does not intersect any surface-localized energy eigenstates; the specific values of these matrix elements are not essential to our argument. Then one can define a projector P to all

occupied states, with the restriction of $P|_{\boldsymbol{k}_\perp}$ (to a reduced-momentum sector) being a smooth function of $\boldsymbol{k}_\perp$; likewise, Q projects to all unoccupied states. The 'smooth-in-$\boldsymbol{k}_\perp$' condition would fail if the Fermi level crossed a surface state – in such a scenario the surface state would discontinuously move from projector P to Q as the state's energy passes through the Fermi level. We show in Fig. 5.3(b) and (c) the spectrum of $P\hat{z}P$ and $Q\hat{z}Q$ respectively, with each curved line associated with a polarization band.[2]

Let us sort polarization bands into two categories: *bulk-like* vs. *surface-like*. Being 'bulk-like' means to be indistinguishable from bulk polarization bands up to corrections that are exponentially small for large $z > 0$. Let us then pick a polarization band of $P\hat{z}P$ that lies sufficiently far away from the surface to be bulk-like. (Which particular band is picked is not essential.) This chosen band serves as a cutoff: every polarization band lying above the chosen band (on the z-axis) is also categorized as bulk-like; every polarization band lying below the chosen band is then surface-like. We repeat this sorting for the polarization bands of $Q\hat{z}Q$. The net result is illustrated in Fig. 5.3(b,c), with bulk-like and surface-like bands separated by a dashed line.

To reveal the angular-momentum anomaly, we first count how many bulk-like Bloch-Wannier states (coming from both projectors P and Q) exist with reduced momentum $\boldsymbol{k}_\perp = \Lambda$ and *bulk-valence-like* itinerant angular momentum $\widetilde{\mathcal{L}}_v(\Lambda)$.[3] We denote this number as $\sharp_b \widetilde{\mathcal{L}}_v(\Lambda)$; likewise, we define the number $\sharp_b \widetilde{\mathcal{L}}_v(\Xi)$ at reduced momentum $\boldsymbol{k}_\perp = \Xi$. In fact, both numbers $\sharp_b \widetilde{\mathcal{L}}_v(\Lambda)$ and $\sharp_b \widetilde{\mathcal{L}}_v(\Xi)$ are formally infinite, and only their difference is well-defined. Numbers $\sharp_b \widetilde{\mathcal{L}}_c(\Lambda)$ and $\sharp_b \widetilde{\mathcal{L}}_c(\Xi)$ are defined similarly using the *bulk-conduction-like* itinerant angular momentum.[4] Note that in our terminology, every Bloch-Wannier state at each Λ and Ξ [whether surface-like or bulk like in the partitioning via the black dashed line in Fig. 5.3(b,c)] can be characterized as having either bulk-valance like or bulk-conduction-like itinerant angular momentum.

In Fig. 5.3(b,c), any blue data-point at $\Pi = \Xi$ or Λ corresponds to a Bloch-Wannier state with itinerant angular momentum $\widetilde{\mathcal{L}}_v(\Pi)$. Since there are no blue data in panel (c), Fig. 5.3(b) should convince the reader that the difference of $\sharp_b \widetilde{\mathcal{L}}_v(\Pi)$ between the two high-symmetry points equals the polarization difference between the two choices of Π, i.e.,

$$\sharp_b \widetilde{\mathcal{L}}_v(\Lambda) - \sharp_b \widetilde{\mathcal{L}}_v(\Xi) = \Delta \mathscr{P}_{\Lambda\Xi}. \tag{5.8a}$$

Similarly, for Bloch-Wannier states with bulk-conduction-like angular momentum we find [by inspecting red data in Fig. 5.3(b,c)] that

$$\sharp_b \widetilde{\mathcal{L}}_c(\Lambda) - \sharp_b \widetilde{\mathcal{L}}_c(\Xi) = -\Delta \mathscr{P}_{\Lambda\Xi}. \tag{5.8b}$$

The minus sign on the right-hand side of Eq. (5.8b) reflects that the RTP invariant of the bulk conduction band is opposite in sign to the RTP invariant of the bulk valence band.

2 We continue to call the eigenstates of $P\hat{z}P$ and of $Q\hat{z}Q$ in the semi-infinite geometry (and also in the slab geometry) as Bloch-Wannier states (and their $\boldsymbol{k}_\perp$-dependent eigenvalues as polarization bands), just as we did for the case of bulk states in infinite geometry, even though the eigenvalues $\bar{z}_j(\boldsymbol{k}_\perp)$ (especially for the eigenstates localized near the surface) are now *not* identified with the bulk polarization as in Ref. [83].

3 Since $\widetilde{\mathcal{L}}_v(\Lambda)$ is the itinerant angular momentum of bulk valence Bloch states with reduced momentum Λ, we call this value of itinarant angular momentum in the following discussion as *bulk-valence-like* at Λ (and similarly for $\boldsymbol{k}_\perp = \Xi$).

4 The notion of *bulk-conduction-like* itinerant angular momentum at Λ is defined similarly to footnote 3 with using the bulk conduction Bloch states with replaced $\widetilde{\mathcal{L}}_v(\Lambda) \to \widetilde{\mathcal{L}}_c(\Lambda)$.

Observe that the total number of polarization bands (both bulk-like and surface-like) with angular momentum $\widetilde{\mathcal{L}}_v(\Pi)$ cannot depend on the choice between $\Pi = \Lambda$ and $\Pi = \Xi$ [cf. Dets. 5.1 for a rigorous argument]:

$$\sharp_b \widetilde{\mathcal{L}}_v(\Lambda) + \sharp_f \widetilde{\mathcal{L}}_v(\Lambda) = \sharp_b \widetilde{\mathcal{L}}_v(\Xi) + \sharp_f \widetilde{\mathcal{L}}_v(\Xi). \tag{5.9}$$

Combining Eq. (5.9) with Eqs. (5.8) gives the angular-momentum anomaly (5.7).

The mismatch between the number of surface-like Bloch-Wannier bands with bulk-valence-like itinerant angular momentum at Λ vs. at Ξ implies an anomaly, where some of these bands must change their character between Λ and Ξ. For instance, assuming $\Delta\mathscr{P}_{\Lambda\Xi} = 1$, Eq. (5.7) implies the existence of *at least* one anomalous surface-like polarization band whose itinerant angular momentum is bulk-conduction-like at Λ and bulk-valence-like at Ξ. In our model, the anomalous surface-like band lies at the bottom of Fig. 5.3(b) and exhibits the largest color range. (That there exists only one, and that it lies in the P subspace, are model-dependent details.) A non-pictorial, model-independent proof of the angular-momentum anomaly is presented in Sec. 5.2.3.

Importantly, the angular-momentum anomaly has implications beyond polarization bands. This is because the surface-like polarization band(s) are continuously deformable to surface-localized *energy* band(s) of a Hamiltonian with open boundary conditions, modulo addition or subtraction of bands whose itinerant angular momenta are bulk-valence-like at all Π, or bulk-conduction-like at all Π. (Examples of analogous deformations were discussed in Ref. [88] and Ref. [163].) As a case in point, the anomalous surface-like polarization band in Fig. 5.3(b) is continuously deformable to the surface-localized energy band in Fig. 5.5(c). Henceforth, any statement that applies equally well to surface-localized energy bands and surface-like polarization bands is said to apply to *faceted bands*, e.g., the angular-momentum anomaly holds for faceted bands. The states that make up a faceted band will be referred to as *faceted states*.

Details 5.1 The set of *all* polarization bands (both bulk-like and surface-like, coming from both projects P and Q) form basis vectors of the Hilbert space $\mathscr{H}_{\text{semi-}\infty}$ in the semi-infinite geometry. Defining $\mathscr{H}_{\text{semi-}\infty}(\boldsymbol{k}_\perp)$ as the restriction of the Hilbert space to a reduced-momentum sector, continuity over the rBZ demands that the dimension of $\mathscr{H}_{\text{semi-}\infty}(\boldsymbol{k}_\perp)$ cannot depend on $\boldsymbol{k}_\perp$. (Strictly speaking, the dimension is infinite, and what we mean is that $\dim[\mathscr{H}_{\text{semi-}\infty}(\boldsymbol{k}_\perp)] - \dim[\mathscr{H}_{\text{semi-}\infty}(\boldsymbol{k}'_\perp)] = 0$ for any $\boldsymbol{k}_\perp$ and $\boldsymbol{k}'_\perp$.) Under our mutually-disjoint assumption, $\mathscr{H}_{\text{semi-}\infty}(\Pi)$, with $\Pi \in \{\Lambda, \Xi\}$, can be decomposed into two itinerant-angular-momentum sectors:

$$\mathscr{H}_{\text{semi-}\infty}(\Pi) = \mathscr{H}_{\text{semi-}\infty}(\Pi; \widetilde{\mathcal{L}}_v) \oplus \mathscr{H}_{\text{semi-}\infty}(\Pi; \widetilde{\mathcal{L}}_c). \tag{5.10}$$

Now the dimensions of both Hilbert spaces on the right-hand side are equal by construction. This fact, combined with the constancy of $\dim[\mathscr{H}_{\text{semi-}\infty}(\boldsymbol{k}_\perp)]$ over the rBZ, implies Eq. (5.9).

5.2.3 *Proof of the angular-momentum anomaly of insulators with RTP invariant*

To increase the generality of the proven statement, in this section we consider the generic case of multi-band models with N_v valence and N_c conduction bulk bands, assuming that the former are enumerated by the index $j \in \{1, \dots N_v\}$ and the latter by the index $j \in \{N_v + 1, \dots N_v + N_c\}$. For the RTP invariant $\Delta\mathscr{P}_{\Lambda\Xi}$ to be well-defined, we assume that (*i*) bulk states along rotation-invariant lines γ_Λ and γ_Ξ fulfill the mutually-disjoint condition, meaning that the sets of itinerant angular momenta of all valence bands and of all conduction bands are disjoint: $\{\widetilde{\mathcal{L}}_j(\Pi)\}_{j=1}^{N_v} \cap \{\widetilde{\mathcal{L}}_j(\Pi)\}_{j=N_v+1}^{N_v+N_c} = \varnothing$, for $\Pi \in \{\Lambda, \Xi\}$, and (*ii*) there exist a composite band representation CBR

such that the valence band representation, restricted to reduced momenta Λ and Ξ equals to the restriction of CBR to these momenta. This multi-band generalization of the RTP will be discussed in more details in Chapter 7 of Part II, while the particular case of a two-band model corresponds to $N_v = N_c = 1$; in this case the mutually-disjoint condition is fulfilled when $\widetilde{\mathcal{L}}_v(\Pi) \neq \widetilde{\mathcal{L}}_c(\Pi)$ for $\Pi \in \Lambda, \Xi$ and the composite band representation reduces to a basis band representation induced from one of the basis orbitals $\mathrm{BBR}[\varphi_\alpha]$. If the valence subspace comprises of multiple bands, the electric polarization at a reduced momentum $\boldsymbol{k}_\perp$ is given by a sum of electric polarization of all valence bands [as was shown in Sec. 2.1.4.2):

$$\mathscr{P}(\boldsymbol{k}_\perp) = \sum_{j=1}^{N_v} \frac{i}{2\pi} \int_{-\pi}^{\pi} dk_z \left\langle u_j(\boldsymbol{k}) \middle| \partial_{k_z} u_j(\boldsymbol{k}) \right\rangle, \tag{5.11}$$

where $\left|u_j(\boldsymbol{k})\right\rangle$, $j = 1, \dots N_v$ is a set of differentiable intra-cell functions that span the valence subspace of a tight-binding Hamiltonian at each $\boldsymbol{k}$. The RTP invariant is a difference in electric polarization given by Eq. (5.11) between reduced momenta Λ and Ξ. The angular momentum anomaly (5.7) is valid for the multi-band RTP when the number of faceted bands with valence-like angular momentum at Π $\sharp_{f(\mathrm{b})}\widetilde{\mathcal{L}}_v(\Pi)$ is equal to the number of states whose itinerant angular momentum belongs to the valence set $\{\widetilde{\mathcal{L}}_j(\Pi)\}_{j=1}^{N_v}$; we prove this in the following.

First, using the notations introduced in Sec. 2.1.4.1, we express the RTP invariant in terms of the hybrid Bloch-Wannier functions. For this, we express the intra-cell function $u_j(\boldsymbol{k})$ in terms of hybrid functions

$$u_j^\alpha(\boldsymbol{k}_\perp, k_z) = \sum_{q=1}^{N_v} [U^\dagger(\boldsymbol{k}_\perp, k_z)]_{jq} \sum_{R_z=-\infty}^{\infty} e^{-ik_z(R_z+z_\alpha)} \mathcal{V}_{q\boldsymbol{k}_\perp 0}(\boldsymbol{k}_\perp, R_z, \alpha), \tag{5.12}$$

by inverting Eq. (2.34) and additionally assuming a gauge transformation $U_{jq}(\boldsymbol{k})$ that mixes bands within the valence subspace. Unitarity of the gauge transformation implies that $\sum_{q=1}^{N_v} [U^\dagger(\boldsymbol{k})]_{jq} [U(\boldsymbol{k})]_{qp} = \delta_{jp}$. After plugging Eq. (5.12) into the definition of the electric polarization (5.11) and performing some algebraic transformations, we get the following expression for the polarization:

$$\begin{aligned}
\mathscr{P}(\boldsymbol{k}_\perp) = &\sum_{j,q=1}^{N_v} \int_{-\pi}^{\pi} \frac{dk_z}{2\pi} [U(\boldsymbol{k}_\perp, k_z)]_{jq} \partial_{k_z} [U^\dagger(\boldsymbol{k}_\perp, k_z)]_{qj} \\
&+ \sum_{j=1}^{N_v} \sum_{R_z=-\infty}^{\infty} \sum_{\alpha=1}^{N_v+N_c} \left| \mathcal{V}_{j\boldsymbol{k}_\perp 0}(\boldsymbol{k}_\perp, R_z, \alpha) \right|^2 R_z \\
&+ \sum_{j=1}^{N_v} \sum_{\alpha=1}^{N_v+N_c} \int_{-\pi}^{\pi} \frac{dk_z}{2\pi} \left| u_j^\alpha(\boldsymbol{k}_\perp, k_z) \right|^2 z_\alpha,
\end{aligned} \tag{5.13}$$

where the first term, responsible for the gauge freedom, is quantized to integers. Moreover, the requirement of a global smooth gauge ensures that

this integer is independent of $\boldsymbol{k}_\perp$, and therefore, this term drops in the difference in polarization between two reduced momenta:

$$\Delta\mathscr{P}_{\Lambda\Xi} = \sum_{j=1}^{N_v}\sum_{\alpha=1}^{N_v+N_c}\left[\sum_{R_z=-R_0}^{R_0}\left|\mathcal{V}_{j\boldsymbol{k}_\perp 0}(\boldsymbol{k}_\perp, R_z, \alpha)\right|^2 R_z + \int_{-\pi}^{\pi}\frac{dk_z}{2\pi}\left|u_j^\alpha(\boldsymbol{k}_\perp, k_z)\right|^2 z_\alpha\right]\Bigg|_\Lambda^\Xi, \tag{5.14}$$

where we set the hybrid functions in unit cells $|R_z| > R_0$ to zero; since the hybrid functions are exponentially localized in z-direction, for large enough R_0 this does not modify the results up to exponentially small corrections. In the following, we show that the second term in this expression vanishes. Note, that its dependence on the basis orbitals positions z_α encodes the dependence of the electric polarization on the position of the spatial origin and on the choice of the unit cell. We can rewrite the summation over all valence states in terms of a projector onto valence subspace:

$$\begin{aligned}
&\sum_{j=1}^{N_v}\sum_{\alpha=1}^{N_v+N_c}\int_{-\pi}^{\pi}\frac{dk_z}{2\pi}\left|u_j^\alpha(\Pi, k_z)\right|^2 z_\alpha \\
&= \int_{-\pi}^{\pi}\frac{dk_z}{2\pi}\,\mathrm{Tr}_\alpha\left[\hat{z}_{\mathrm{cell}}\sum_{j=1}^{N_v}\left|u_j(\Pi,k_z)\right\rangle\left\langle u_j(\Pi,k_z)\right|\right] \\
&= \int_{-\pi}^{\pi}\frac{dk_z}{2\pi}\,\mathrm{Tr}_\alpha\left[\hat{z}_{\mathrm{cell}}P_v^{\mathrm{cell}}(\Pi,k_z)\right] = \sum_{\alpha=1}^{N_v} z_\alpha,
\end{aligned} \tag{5.15}$$

where $\hat{z}_{\mathrm{cell}} = \sum_\alpha |\alpha\rangle\, z_\alpha\, \langle\alpha|$ and in the last row we denoted the projector onto the valence subspace in the intra-cell Hilbert space as P_v^{cell}. In the last step, we used the fact that at reduced momenta $\Pi \in \{\Lambda, \Xi\}$ with fulfilled mutually-disjoint condition the valence bands form a basis of the valence subspace. Hence, the projector is k_z-independent and is equal to

$$P_v^{\mathrm{cell}} = \begin{pmatrix} \mathbb{1}_{N_v} & \mathbb{0} \\ \mathbb{0} & \mathbb{0} \end{pmatrix}, \tag{5.16}$$

where $\mathbb{1}_{N_v}$ is an identity matrix of the size N_v and $\mathbb{0}$ denote zero matrices of complementary sizes, such that the whole projector has the size $N_v + N_c$. We see that the origin-dependent term (5.15) does not depend on the concrete value of Π, and hence it vanishes in the Eq. (5.14). Then the RTP invariant expressed in terms of hybrid functions is

$$\Delta\mathscr{P}_{\Lambda\Xi} = \sum_{j=1}^{N_v}\sum_{\alpha=1}^{N_v+N_c}\sum_{R_z=-R_0}^{R_0} R_z\left[\left|\mathcal{V}_{j\Xi 0}(\Xi, R_z, \alpha)\right|^2 - \left|\mathcal{V}_{j\Lambda 0}(\Lambda, R_z, \alpha)\right|^2\right]. \tag{5.17}$$

As the second step of the proof, we express the number of states, localized on the bottom facet, with valence-like itinerant angular momentum at a given reduced momentum Π, in terms of the hybrid Bloch-Wannier functions. In the previous sections we formulated the angular-momentum anomaly for a semi-infinite geometry. However, here, for convenience, we consider a finite in z-direction and infinite in (x, y)-plane slab. For large enough systems, angular-momentum anomaly derived for the bottom facet of a finite geometry holds as well on the bottom facet of a semi-infinite geometry. In a finite

slab, the hybrid Bloch-Wannier functions are replaced by bulk-like hybrid functions $\bar{\mathcal{V}}_{j,\boldsymbol{k}_\perp,R_z}(\boldsymbol{k}_\perp,\bar{R}_z,\alpha)$ defined in Sec. 5.1.3 in the presence of periodic boundary conditions. The hybrid functions in a finite and infinite geometry converge to each other for large enough systems. Given the projector onto the bottom facet (5.5),

$$\sharp_{f(\mathrm{b})}\widetilde{\mathcal{L}}_v(\Pi) = \mathrm{Tr}\left[P_v(\Pi)P_{\mathrm{b}}(\Pi)\right], \tag{5.18}$$

where

$$P_v(\boldsymbol{k}_\perp) = \sum_{j=1}^{N_v}\sum_{R_z=-\infty}^{\infty} |\bar{\mathcal{V}}_{j\boldsymbol{k}_\perp R_z}\rangle\rangle\langle\langle\bar{\mathcal{V}}_{j\boldsymbol{k}_\perp R_z}| \tag{5.19}$$

is the projector onto the valence subspace of the Hilbert space. Taking the difference between two rotation-invariant momenta and substituting the projector onto the bottom-facet-localized states as defined using the Wannier cut in Eqs. (5.4) and (5.5), we find

$$\begin{aligned}&\sharp_{f(\mathrm{b})}\widetilde{\mathcal{L}}_v(\Xi) - \sharp_{f(\mathrm{b})}\widetilde{\mathcal{L}}_v(\Lambda)\\ &= \mathrm{Tr}\left[P_\downarrow \sum_{j=1}^{N_v}\sum_{R_z=\mathcal{N}_f+1}^{\mathcal{N}_0-\mathcal{N}_f} |\bar{\mathcal{V}}_{j,\boldsymbol{k}_\perp,R_z}\rangle\rangle\langle\langle\bar{\mathcal{V}}_{j,\boldsymbol{k}_\perp,R_z}|\right]\Big|_\Xi^\Lambda\end{aligned} \tag{5.20}$$

where in the second line we used that the identity operators computed for Λ and Ξ cancel each other and the projector on the valence subspace P_v sets the sum over conduction hybrid states to zero. In the last step of the derivation we use the explicit form of the projector $P_\downarrow$ which sets to zero the values of the hybrid function at layers $z > \mathcal{N}_0/2$. We compute the trace in Eq. (5.20) and get:

$$\begin{aligned}&\sharp_{f(\mathrm{b})}\widetilde{\mathcal{L}}_v(\Xi) - \sharp_{f(\mathrm{b})}\widetilde{\mathcal{L}}_v(\Lambda)\\ &= \sum_{j=1}^{N_v}\sum_{\alpha=1}^{N_v+N_c}\sum_{R_z=\mathcal{N}_f+1}^{\mathcal{N}_0-\mathcal{N}_f}\sum_{R_z'=0}^{\mathcal{N}_0/2} \left|\bar{\mathcal{V}}_{j\boldsymbol{k}_\perp R_z}(\boldsymbol{k}_\perp,R_z',\alpha)\right|^2\Big|_\Xi^\Lambda\\ &= \sum_{j=1}^{N_v}\sum_{\alpha=1}^{N_v+N_c}\sum_{R_z=\mathcal{N}_f+1}^{\mathcal{N}_0-\mathcal{N}_f}\sum_{R_z'=R_z-R_0}^{\min(\mathcal{N}_0/2,R_z+R_0)} \left|\bar{\mathcal{V}}_{j\boldsymbol{k}_\perp R_z}(\boldsymbol{k}_\perp,R_z',\alpha)\right|^2\Big|_\Xi^\Lambda\\ &= \sum_{j=1}^{N_v}\sum_{\alpha=1}^{N_v+N_c}\sum_{R_z=\mathcal{N}_f+1}^{\mathcal{N}_0-\mathcal{N}_f}\sum_{\bar{R}_z=-R_0}^{\min(\mathcal{N}_0/2-R_z,R_0)} \left|\bar{\mathcal{V}}_{j\boldsymbol{k}_\perp 0}(\boldsymbol{k}_\perp,\bar{R}_z,\alpha)\right|^2\Big|_\Xi^\Lambda.\end{aligned} \tag{5.21}$$

The summation over R_z in Eq. (5.21) can be split into three contributions. (*i*) For $R_z > \mathcal{N}_0/2 + R_0$ the sum over $\bar{R}_z$ has no elements as the upper limit of the sum is lower than the lower limit. (*ii*) For $R_z \leq \mathcal{N}_0/2 - R_0$ the sum over $\bar{R}_z$ runs from $-R_0$ to R_0 and together with sum over orbital index α results in the normalization of the hybrid functions which is equal to one. These terms are equal at both rotation-invariant momenta Λ and Ξ and therefore are canceled after subtraction. (*iii*) For intermediate $\mathcal{N}_0/2 - R_0 < R_z \leq \mathcal{N}_0/2 + R_0$ the sum is truncated at $\mathcal{N}_0/2 - R_z$ and since the hybrid functions depend only on $\bar{R}_z$ we can rewrite summations over R_z and $\bar{R}_z$ as

$$\begin{aligned}&\sum_{R_z=\mathcal{N}_0/2-R_0+1}^{\mathcal{N}_0/2+R_0}\sum_{\bar{R}_z=-R_0}^{\mathcal{N}_0/2-R_z} \left|\bar{\mathcal{V}}_{j\boldsymbol{k}_\perp 0}(\boldsymbol{k}_\perp,\bar{R}_z,\alpha)\right|^2\\ &\qquad = \sum_{\bar{R}_z=-R_0}^{R_0}(R_0-\bar{R}_z)\left|\bar{\mathcal{V}}_{j\boldsymbol{k}_\perp 0}(\boldsymbol{k}_\perp,\bar{R}_z,\alpha)\right|^2.\end{aligned} \tag{5.22}$$

The term proportional to R_0 in this sum, when summed over the orbital index α, is constant for the same reason as described above, and therefore it vanishes when taking the difference between rotation-invariant momenta Λ and Ξ. We arrive to the following expression for the angular momentum difference:

$$\begin{aligned}&\sharp_{f(\mathrm{b})}\widetilde{\mathcal{L}}_v(\Xi) - \sharp_{f(\mathrm{b})}\widetilde{\mathcal{L}}_v(\Lambda)\\ &= \sum_{j=1}^{N_v}\sum_{\alpha=1}^{N_v+N_c}\sum_{\bar{R}_z=-R_0}^{R_0} \bar{R}_z\left[\left|\bar{\mathcal{V}}_{j\Xi 0}(\Xi,\bar{R}_z,\alpha)\right|^2 - \left|\bar{\mathcal{V}}_{j\Lambda 0}(\Lambda,\bar{R}_z,\alpha)\right|^2\right]. \qquad (5.23)\end{aligned}$$

Finally, recall that for large enough slabs the bulk-like hybrid functions $\bar{\mathcal{V}}_{j\Pi 0}(\Pi,\bar{R}_z,\alpha)$ converge to the bulk hybrid functions of infinite geometry $\mathcal{V}_{j\Pi 0}(\Pi,\bar{R}_z,\alpha)$. In the large-size limit, the right-side of Eq. (5.23) becomes identical to the expression for the RTP invariant (5.17). This concludes the proof of the nagular momentum anomaly (5.7).

Further implications of the anomaly are discussed in the subsequent two subsections.

5.3 CONDITIONALLY-ROBUST SURFACE STATES AT SHARP BOUNDARIES

The RTP implies *conditionally-robust* surface states; namely, the interpolation of surface-state energies across the bulk energy gap is robust against gap- and rotation-symmetry-preserving deformations of the *bulk* Hamiltonian, assuming that the surface Hamiltonian is rotation-symmetric and satisfies the *sharp boundary condition*. 'Sharpness' of a boundary means that all Hamiltonian elements are exactly as they would be in the bulk, except for hopping matrix elements crossing a surface; these latter elements are set to zero. Examples of such conditionally-robust surface states were numerically observed for the rotation-symmetric Hopf-insulating models in Refs. [55, 92], but have thus far lacked explanation.

Here, we explain the relation of these conditionally-robust surface states to the RTP invariants. First, in Sec. 5.3.1 we use spectral properties of Toeplitz and circulant matrices to derive a bulk-boundary correspondence for surface states along lines connecting high-symmetry momenta in rBZ. In Sec. 5.3.2 we discus how much information the RTP invariants convey about the actual shape-topology of the Fermi lines formed by the surface states inside rBZ. Finally, in Sec. 5.3.3 we compare our theoretical discussion against concrete numerical calculations performed for the MRW model.

5.3.1 *Bulk-boundary correspondence at sharp boundaries*

To prove this conditional robustness, we first focus on rotation-invariant lines (denoted γ_Π) that project onto reduced momentum $\Pi \in \{\Lambda,\Xi\}$. By restricting the bulk Hamiltonian $h(\boldsymbol{k})$ to any of these lines, we obtain a Hamiltonian $h_\Pi(k_z)$ that depends continuously on one parameter k_z. Because of the mutually-disjoint condition (4.10) at Π, $h_\Pi(k_z)$ is a diagonal two-by-two matrix (for all k_z), in the basis that simultaneously diagonalizes the rotation matrix. Thus, $h_\Pi(k_z) = h^v_\Pi(k_z) \oplus h^c_\Pi(k_z)$ can be interpreted as a direct sum of Hamiltonians for two non-hybridizing chains, with each chain having one orbital per primitive unit cell.

Generally, the Hamiltonian of a one-orbital-per-cell chain with sharp boundaries is equal to a Hermitian Toeplitz matrix.[5] As was shown in Ref. [164] for a sufficiently long chain, the spectrum of a Toeplitz matrix is asymptotically equal to the spectrum of a corresponding circulant matrix[6] which describes the same tight-binding model with *periodic* (instead of open) boundary conditions. It is known that a Hamiltonian defined on a periodic chain of length L, with one orbital per unit cell, gives a continuous energy band in the limit $L \to \infty$. In particular, there are no isolated states outside of the (single) energy band for both $h^v_\Pi(k_z)$ and $h^c_\Pi(k_z)$. Crucially, per the result of Ref. [164], it follows that the continuity of the spectra of h^v_Π and h^c_Π persists in the presence of open boundary conditions on the chain, meaning that the two-orbital-per-cell chain h_Π has no in-gap states at sharp boundaries.

Here, the angular-momentum anomaly enters the stage. As argued in Sec. 5.2, Eq. (5.7) with $\Delta\mathscr{P}_{\Lambda\Xi} > 0$ implies the existence of $|\Delta\mathscr{P}_{\Lambda\Xi}|$-number of 'anomalous' bottom-surface-localized energy band(s) whose itinerant angular momentum is bulk-conduction-like at Λ and bulk-valence-like at Ξ. Moreover, the absence of any discrete energy eigenvalues within the bulk energy gap at both Λ and Ξ (explained in the previous paragraph) ensures that each of the anomalous surface-localized energy bands is energetically attached to the bulk valence band at Ξ, and also energetically attached to the bulk conduction band at Λ. Thus, if we associate one $E(\boldsymbol{k}_\perp)$ (i.e., energy vs. reduced-momentum) dispersion to each linearly-independent, surface-localized Bloch state, it is guaranteed that at least $|\Delta\mathscr{P}_{\Lambda\Xi}|$-number of surface-state dispersions interpolate across the bulk gap as the reduced momentum is varied along *any* (possibly curved) line connecting Λ and Ξ. We note in passing that the conditionally robust surface states are also present for multi-band RTP invariants, as discussed in more details in Chapter 7 of Part II and proved in Appendix C.2.

To be more precise, let us parametrize any such a line as $\boldsymbol{k}_\perp(t)$ with $t \in [0,1]$ [where $\boldsymbol{k}_\perp(0) = \Lambda$ and $\boldsymbol{k}_\perp(1) = \Xi$]. Then for any fixed reference energy $\bar{E}$ within the bulk energy gap, one can associate to each linearly-independent Bloch state (at energy $\bar{E}$) a scalar velocity dE_j/dt, with j an index to distinguish between multiple Bloch states crossing $\bar{E}$ [with possibly several such states along a given band, cf. Fig. 5.4(a)]. These velocities are related to the RTP invariant as

$$\Delta\mathscr{P}_{\Lambda\Xi} = -\sum_j \operatorname{sgn}\left[\frac{dE_j}{dt}\right], \tag{5.25}$$

where $\sum_j$ sums over all states at the reference energy [denoted by green dots in Fig. 5.4(a)]. Thus, there are minimally $|\Delta\mathscr{P}_{\Lambda\Xi}|$-number of Bloch states at the reference energy, all with the same sign for the velocity. In principle, however, this number can be increased by any even number, so long as each added pair of Bloch states comes with opposite signs for dE_j/dt. Such possible additions are attributed to (*i*) non-anomalous surface-localized energy bands whose itinerant angular momenta are either bulk-conduction-like at both Λ and Ξ, or bulk-valence-like at both Λ and Ξ or to (*ii*) additional

5 Elements of a Toeplitz matrix $\mathcal{T}$ are constant along each diagonal, i.e., $\mathcal{T}_{i,j} = \mathcal{T}_{i-j}$. Hermiticity further implies $\mathcal{T}_{i-j} = \mathcal{T}^*_{j-i}$.

6 Circulant matrices form a special class of Toeplitz matrices with $c_{i-j} = c_{-n+i-j}$ for matrices of size $n \times n$. Given a Toeplitz matrix $A_{i,j} = a_{i-j}$ we define the corresponding circulant matrix as

$$c_{i-j} = \begin{cases} a_0 & \text{for } i = j, \\ a_{-i+j} + a_{n-i+j} & \text{otherwise.} \end{cases} \tag{5.24}$$

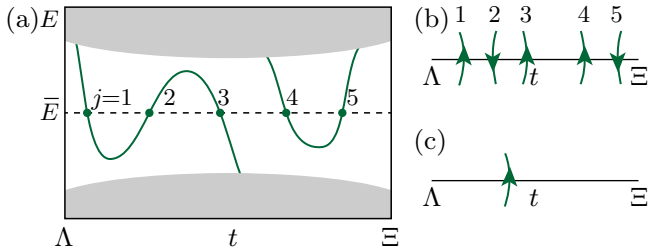

Figure 5.4: (a) Spectrum of a semi-infinite RTP insulator with an RTP invariant $\Delta\mathscr{P}_{\Lambda\Xi} = 1$ along a path in rBZ, that starts at Λ, ends at Ξ and is parametrized by a real parameter t. Given any reference energy $\bar{E}$ inside the bulk energy gap, the value of the RTP invariant is equal, up to a sign, to the sum of $\mathrm{sgn}[dE_j/dt]$ (signs of scalar velocities) over all surface-localized states (j) that cross $\bar{E}$ (green dots), cf. Eq. (5.25). (b) The surface-localized states form Fermi lines (green lines) at the Fermi energy with an orientation defined by green arrows. (c) There is an ambiguity in the exact number and position of the Fermi lines which is assigned to (*i*) the possibility to add or remove pairs of Fermi states with opposite signs of scalar velocity, and (*ii*) the possibility to shift a Fermi state along the $\Lambda\Xi$ line without removing it. In this sense panels (b) and (c) are topologically equivalent, and can both arise for $\Delta\mathscr{P}_{\Lambda\Xi} = 1$.

crossings of $\bar{E}$ by the anomalous band when parameter t swipes the interval $[0, 1]$.

Figure 5.4(a) illustrates how the counting in Eq. (5.25) is done for a schematic energy spectrum representing the case of $\Delta\mathscr{P}_{\Lambda\Xi} = 1$: there are five surface-localized Bloch states at the reference energy $\bar{E}$, of which four have pairwise opposite signs for their scalar velocity. One pair [denoted by $j = 4, 5$ in Fig. 5.4(a)] can be associated with a non-anomalous surface-localized energy band 'peeled' off from the bulk-conduction valence band. Another pair [denoted by $j = 2, 3$ in Fig. 5.4(a)] is attributed to additional crossings of energy $\bar{E}$ by the anomalous band. Contribution from these pairs vanishes in Eq. (5.25) leading to a correct prediction of the RTP invariant.

5.3.2 *Fermi-line topology*

The above argument holds for any $\bar{E}$ within the bulk energy gap, and holds in particular for $\bar{E}$ being the Fermi energy of the bulk insulating Hamiltonian for an electronic system. This has further implications for the topology of 'Fermi surfaces' at sharp boundaries. Since Fermi surfaces contributed by surface states form lines in the rBZ, we henceforth call them *Fermi lines*.

It is useful to equip each Fermi line with an orientation: for this we define a right-handed (possibly non-orthogonal) system of the following three vectors: (*i*) the first vector equals to $\hat{\boldsymbol{t}}(dE/dt)$ (with $\hat{\boldsymbol{t}}$ a unit two-vector that is locally parallel to the rBZ-line $\Lambda\Xi$, and points in the direction of increasing t), (*ii*) the second vector points in the paper-to-sky direction, and (*iii*) the third vector is locally tangential to the Fermi line. The orientation of the third vector is fixed by the handedness of the frame, thus defining the orientation of the Fermi line. For illustration, Fig. 5.4(b) presents five segments of the Fermi lines crossing the rBZ-line $\Lambda\Xi$, with orientations determined by applying the right-hand rule to Fig. 5.4(a). Because the right-hand-rule mapping is bijective, one can also start from the oriented Fermi-line segments in Fig. 5.4(b) to deduce the signs of dE_j/dt and therefore the RTP invariant via the rule in Eq. (5.25).

Let us now consider the inverse problem of determining Fermi lines from the RTP invariant(s): knowing all the RTP invariants in the rBZ, can one

infer the topology of the shape of Fermi lines, as well as their orientations? We argue that the answer is 'no', i.e., that the Fermi-line topology remains ambiguous, which can be understood as follows. For each RTP invariant between reduced momenta Π_1 and Π_2, one can infer that the sum of all Fermi-level states on a possibly-curved rBZ-line (connecting Π_1 and Π_2) must satisfy the velocity-RTP rule in Eq. (5.25). There are two potential sources of ambiguity. First, the oriented segments of Fermi lines crossing the rBZ-line $\Pi_1\Pi_2$ are determined modulo an ambiguity in the exact positioning of segments along $\Pi_1\Pi_2$; however, such smooth changes cannot induce changes in the topology. On the other hand, the Fermi lines crossing the rBZ-line $\Pi_1\Pi_2$ are fixed modulo addition/subtraction of pairs of Fermi-line segments with opposite orientations [as illustrated in Fig. 5.4(b,c)]; as this is a discontinuous change that alters the number of summands in Eq. (5.25), it should be expected that it implies a change in the Fermi line topology.

The oriented Fermi-line segments, which are in the described sense ambiguously defined over all rBZ-lines $\{\Pi_1\Pi_2\}$ on which an RTP invariant is well-defined, can be continued and connected to form closed Fermi loops that preserve orientation. We illustrate in Fig. 5.6(b,c) two topologically reconstructed Fermi lines obtained in this way for the same choice of RTP invariants, with the Fermi lines being topologically distinct from one another because of the ambiguity explained here. The ambiguity due to addition/subtraction of paired Fermi-line segments translates to an ambiguity due to addition/subtraction of 'trivial' Fermi loops; if a Fermi loop intersects any rBZ-line for which an RTP invariant is well-defined, the condition of 'triviality' means that the intersection does not modify $\sum_j \mathrm{sgn}[dE_j/dt]$.[7]

5.3.3 *Sharp-boundary states and Fermi-line topology in* P4*-symmetric model*

To illustrate the findings of this section, we focus on the same P4-symmetric tight-binding Hilbert space that formed the basis for the Moore-Ran-Wen model, presented in Sec. 4.4.2. To remind the reader, the mutually-disjoint condition holds at all rotation-invariant reduced momenta $\{\Gamma, X, M\}$, and the iso-orbital condition holds also for any pair in this set, implying an RTP invariant is well-defined for any pair in this set. There are however only two independent RTP invariants.

We start by looking at a semi-infinite Moore-Ran-Wen model Hamiltonian [given in the bulk by Eq. (4.24)] with $\Phi = -2$, for which the polarization protrudes in the negative z-direction at C_4-invariant momentum Γ [orange line in Fig. 4.2(d)]. In Fig. 5.5, we present the energy spectrum of the model, with colors (blue vs. red) indicating the contribution of basis orbitals (with on-site angular momentum $\mathcal{L} = 0$ vs. $\mathcal{L} = 1$) to the eigenstates. At rotation-invariant reduced momenta, each valence (resp. conduction) bulk state has itinerant angular momentum $\widetilde{\mathcal{L}}_v = 0$ (resp. $\widetilde{\mathcal{L}}_c = 1$). The itinerant angular momentum of the anomalous surface-localized energy band is bulk-valence-like at X and M, and bulk-conduction-like at Γ. At a sharp boundary [cf. Fig. 5.5(a)] we indeed see that, in accordance with the above argument, the surface-state energies interpolate from the bulk-conduction band at Γ to the bulk-valence band at X; likewise, a similar interpolation occurs between Γ and M.

Now let us illustrate for the present RTP invariants [shown for the studied model in Fig. 5.6(a) with the arrows denoting the direction in which the polar-

7 An example of a nontrivial loop is any that encircles only one rotation-invariant reduced momentum Π, assuming Π is mutually-disjoint and belongs to an iso-orbital subset. An example of a trivial loop is any that encircles no such Π.

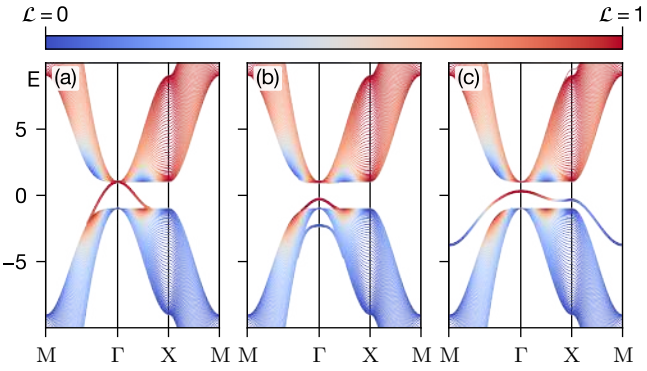

Figure 5.5: Spectrum of a semi-infinite MRW model with parameter $\Phi = -2$ [Eq. (4.24)] defined for $z > 0$. The shades of blue vs. red denote contributions to the eigenstates from the basis orbitals with angular momentum $\mathcal{L} = 0$ vs. $\mathcal{L} = 1$. At rotation-invariant reduced momenta the states are purely represented by orbitals with $\mathcal{L} = 0$ or 1. (a) Sharp boundary possessing a gapless surface state. (b) A surface-localized potential $V = -1.3$ added to both orbitals in the bottom layer of the semi-infinite system opens a gap in the surface spectrum. (c) There exist a Hamiltonian perturbation that detaches the surface state from the rest of the spectrum.

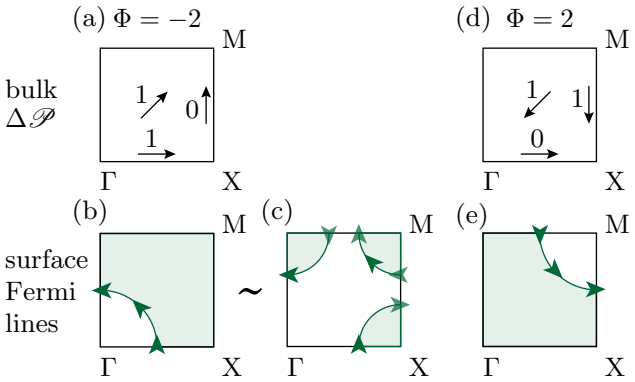

Figure 5.6: (a), (d) RTP invariants in the top right quadrant of the rBZ for the MRW model with parameter values (a) $\Phi = -2$ and (d) $\Phi = 2$. Arrows denote the direction along which the polarization is changing by the shown values. (b), (c), (e) Fermi lines are denoted by green lines and their orientations by green arrows. Green shaded areas correspond to momenta in rBZ at which the surface-localized states are occupied. In panel (b) we show the minimal number of Fermi lines that is compatible with the RTP invariants for the MRW model with $\Phi = -2$. Another possible topology of Fermi lines is shown in panel (c), which differs from panel (b) by the addition/subtraction of Fermi loops that intersect the XM rBZ lines twice and with opposite orientations. In both (b) and (c), the surface-band state at Γ (at X and M) is empty (occupied). (e) The areas of occupied surface states enclose different high-symmetry momenta in rBZ when the model parameter is changed to $\Phi = 2$ and the RTP invariants acquire different values.

ization difference is calculated and the values equal to $\Delta\mathscr{P}$ in this direction] the possible topology of Fermi lines. In Fig. 5.6(b), we draw the minimal number of (oriented) Fermi lines compatible with the RTP invariants $\Delta\mathscr{P}_{\Pi_1\Pi_2}$, $\Pi_1, \Pi_2 \in \{\Gamma, X, M\}$, $\Pi_1 \neq \Pi_2$, within one quadrant of rBZ (denoted by green arrows). The Fermi lines at other quadrants can be obtained by a four-fold rotation of the displayed pattern around Γ. The area where the surface states are occupied with electrons is denoted by a green shade. Importantly, the RTP invariant defines only the minimal amount of Fermi lines that cross a given line connecting two rotation-invariant reduced momenta. As we show in Fig. 5.6(c), the connectivity of the Fermi lines can change, for instance, due to the addition of trivial Fermi loops located between X and M, which do not enclose any rotation-invariant reduced momentum and which contribute to the summation in Eq. (5.25) with a pair of states of opposite scalar velocity. However, the ambiguity in connecting the Fermi lines does not change the fact that for the given RTP invariants, the reduced momenta X and M are surrounded by areas with one more occupied surface state than in the area around the reduced momentum Γ.

Reduced momenta around which the surface states are occupied can change when the values of the RTP invariant change. To see this, consider the MRW model with the parameter value $\Phi = 2$. The corresponding values of the topological invariants can be read from Fig. 5.6(d); in particular, note that the Hopf invariant coincides with the one for the previously considered parameter, i.e., $\chi[\Phi = -2] = \chi[\Phi = 2] = -1$. We see in Fig. 5.6(e) that with the new parameter value the areas with occupied surface states surround reduced momenta Γ and X, instead of M and X.

We emphasize that the assumption of a sharp boundary is essential for the robust surface states as it allows to use certain spectral properties of Toeplitz matrices. For non-sharp boundaries, the anomalous surface bands can be detached from the bulk bands. Because the energy eigenvalues of each anomalous surface band form a sheet over the rBZ, it is in principle possible that none of the sheets intersect the Fermi level, implying the existence of an energy gap to surface-state excitations.[8] To illustrate this point for the MRW model, we added to the bottom layer of the sharply-terminated tight-binding Hamiltonian an on-site potential that does not discriminate between s and p_+ orbitals. This leads to an energetic detachment of the anomalous surface-localized energy bands from the bulk-conduction band in Fig. 5.5(b), thus confirming that surface states are not robust for an arbitrary surface termination.[9] Finally, we show in Fig. 5.5(c) that the anomalous surface-localized energy band can be energetically detached from *both* bulk-conduction and bulk-valence bands for a particular, rotation-invariant surface termination. However, despite the complete detachment, the itinerant angular momenta of the surface energy bands remain anomalous. This has non-trivial implications for their Zak phase, which we explore in the next subsection.

5.4 ZAK-PHASE ANOMALY

The angular-momentum anomaly at two rotation-invariant momenta Λ and Ξ implies the existence of 'anomalous' faceted band(s) whose itinerant angular momentum is bulk-valence-like at one rotation-invariant, reduced

8 This however does not rule out the existence of 'gapless' excitations due to higher-order topology [115, 165] – a concept explored for delicate topological insulators in Ref. [166].

9 This is how we actually constructed the projectors P and Q with smooth-in-$\boldsymbol{k}_\perp$ restrictions $P|_{\boldsymbol{k}_\perp}$ and $Q|_{\boldsymbol{k}_\perp}$ when generating the data in Fig. 5.3.

momentum, say Λ, and bulk-conduction-like at another, say Ξ. This implies that there exists a symmetrically-chosen loop (to be specified below) in the reduced Brillouin zone which passes through both momenta, such that the Zak phase of the faceted band(s) (henceforth called the *faceted Zak phase*) is topologically distinct from both the bulk-conduction Zak phase and the bulk-valence Zak phase on the corresponding BZ loop. We call this distinction of Zak phases the *Zak-phase anomaly*.

Our discussion is structured as follows. First, in Sec. 5.4.1, we define the faceted Zak phase. Then we proceed with Sec. 5.4.2 to define the bulk-Zak phases. Having all the definitions at hand, in Sec. 5.4.3 we exemplify the Zak-phase anomaly through the P4-symmetric Moore-Ran-Wen model. Finally, in Sec. 5.4.4, we precisely formulate the Zak-phase anomaly for all Pn space groups. We clarify what we mean by two Zak phases being 'distinct', and we summarize in Table 5.2 all the 'symmetrically-chosen rBZ loop' for which the Zak-phase anomaly exists.

5.4.1 *Faceted Zak phase*

The faceted Zak phase is simplest to conceptualize in the case where the faceted band is a single surface-localized energy band that is completely detached from both the bulk-conduction and the bulk-valence bands, as illustrated in Fig. 5.5(c) for the P4-symmetric MRW model under non-sharp boundary conditions. Letting $|v(\boldsymbol{k}_\perp)\rangle$ denote the intra-cell[10] wave function of the detached band, we define the *faceted Zak phase* as a line integral of the associated Berry connection over a symmetrically-chosen loop $\mathcal{S}$ in the rBZ ($d\boldsymbol{k}_\perp$ denotes a line element along this loop):

$$\begin{aligned} \mathscr{Z}_f &= \int_{\mathcal{S}} d\boldsymbol{k}_\perp \cdot \boldsymbol{\mathcal{A}}_\perp, \\ \boldsymbol{\mathcal{A}}_\perp &= (\mathcal{A}_x, \mathcal{A}_y), \quad \mathcal{A}_\mu[v(\boldsymbol{k}_\perp)] = i \left\langle v(\boldsymbol{k}_\perp) \middle| \partial_\mu v(\boldsymbol{k}_\perp) \right\rangle . \end{aligned} \tag{5.26}$$

The path $\mathcal{S}$ is chosen so that the faceted Zak phase is quantized to integer multiples of $2\pi/n$ owing to the Pn symmetry. A few representative examples of symmetrically-chosen loops are illustrated in Fig. 5.7, but a full disclosure on the general form of the loops for any Pn symmetry is deferred to Sec. 5.4.4. We emphasize that the faceted Zak phase inputs the wave functions of surface states independent of whether the states are occupied by fermions.

More generally, one may deal with any number of surface-localized energy bands (as long as they are detached from the bulk energy bands), or any number of surface-like polarization bands. Then the faceted Zak phases are obtained as the phases of the eigenvalues of a *Wilson-loop matrix*; this matrix is a path-ordered exponential of the non-Abelian Berry connection:

$$\begin{aligned} \mathcal{W}_f &= \hat{\mathrm{T}} \exp \left[i \int_{\mathcal{S}} d\boldsymbol{k}_\perp \cdot \boldsymbol{\mathcal{A}}_\perp[v(\boldsymbol{k}_\perp)] \right], \\ \mathcal{A}_\mu^{jj'} &= i \left\langle v_j(\boldsymbol{k}_\perp) \middle| \partial_\mu v_{j'}(\boldsymbol{k}_\perp) \right\rangle, \end{aligned} \tag{5.27}$$

where $\hat{\mathrm{T}}$ is the path-ordering operator, and j, j' are band indices of the surface bands. An algorithm to extract the intra-cell wave functions $|v_j(\boldsymbol{k}_\perp)\rangle$ for surface-like polarization bands was introduced in Ref. [167] and was reviewed pedagogically in Sec. 5.1.3.

10 For the semi-infinite geometry, the 'cell' is infinite in the z-direction.

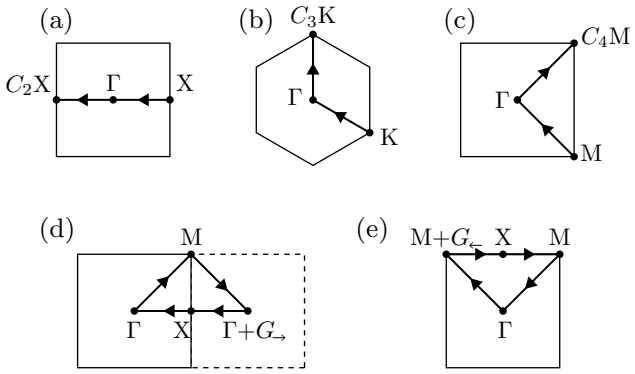

Figure 5.7: An (incomplete) list of symmetrically-chosen rBZ-loops for which a Zak-phase anomaly may exist. (a) C_2-related-, (b) C_3-related- and (c) C_4-related-two-segment loops. (d) and (e) Two exceptional four-segment loops, described in Sec. 5.4.4.

5.4.2 *Zak phase of the bulk bands*

The Zak-phase anomaly states that the faceted Zak phase is topologically distinct from the *bulk-conduction Zak phase* as well as from the *bulk-valence Zak phase*, which inputs the wave function of the bulk-conduction resp. the bulk-valence band:

$$\mathscr{Z}_j = \int_{\mathcal{S}(k_z)} d\boldsymbol{k}_\perp \cdot \boldsymbol{\mathcal{A}}_\perp[u_j(\boldsymbol{k}_\perp, k_z)], \quad j = v, c. \tag{5.28}$$

The line integral is over a loop $\mathcal{S}(k_z)$ contained within a plane of fixed k_z; if projected in the k_z direction, $\mathcal{S}(k_z)$ coincides with $\mathcal{S}$ defined for the faceted Zak phase. Note that $\mathscr{Z}_{v(c)}$ can depend on k_z through $\mathcal{S}(k_z)$ for a *general* two-band Hamiltonian. However, the C_n symmetry [in combination with the fact that $\mathcal{S}(k_z)$ is a symmetrically chosen path] imply that the admissible values of $\mathscr{Z}_j$ are quantized to integer multiples of $2\pi/n$, which reduces the prospective k_z-dependence to discontinuous jumps. But such discontinuities are forbidden under the assumption that the two-band Hamiltonian is insulating, hence the bulk Zak phase ultimately has no k_z dependence.

5.4.3 *Case study:* P4*-symmetric Moore-Ran-Wen model*

Let us illustrate the Zak-phase anomaly with the P4-symmetric MRW model Hamiltonian given in Eq. (4.24). We focus on the parameter range $-3 < \Phi < -1$ where the polarization protrudes (in the negative z-direction) at Γ, as illustrated in Fig. 4.2(d); this implies RTP invariants $\Delta\mathscr{P}_{\Gamma X} = 1$ and $\Delta\mathscr{P}_{\Gamma M} = 1$. The corresponding energetically detached anomalous surface band is illustrated in Fig. 5.5(c) for a suitable choice of a non-sharp boundary.

According to our formulation of the Zak-phase anomaly, we expect that the faceted Zak phase, computed for the anomalous surface band in Fig. 5.5(c), is distinct from the bulk Zak phases. Based on the just-mentioned RTP invariants, we further expect this mismatch of Zak phases for an rBZ-loop $\mathcal{S}_2$ passing through momenta Γ and X, as well as an rBZ-loop $\mathcal{S}_4$ passing through Γ and M. For this mismatch to be quantized to integer multiples of $2\pi/4$, the rBZ-loops must be chosen symmetrically: we choose $\mathcal{S}_2$ (resp. $\mathcal{S}_4$) such that half the loop is mapped to the other half by a two-fold (resp. four-fold) rotation in the rBZ, as illustrated in Fig. 5.7(a, c). While $\mathcal{S}_2 = X\Gamma(C_2X)$

can be chosen as a straight loop, $\mathcal{S}_4 = \mathrm{M}\Gamma(C_4\mathrm{M})$ necessarily has kinks at the four-fold-invariant momenta.[11] The advantage of these *C_m-related loops* ($m = 2, 4$) is that the Zak phase for a nondegenerate energy band is quantized to rational multiples of 2π and fully determined by the itinerant angular momenta at Γ, X and M, according to a theorem in Ref. [134] (cf. Sec. IV D 1 therein):

$$\frac{\mathscr{Z}_{\mathrm{X}\Gamma(C_2\mathrm{X}),j}}{2\pi} =_1 \frac{\widetilde{\mathcal{L}}_j(\mathrm{X}) - \widetilde{\mathcal{L}}_j(\Gamma)}{2}, \tag{5.29a}$$

$$\frac{\mathscr{Z}_{\mathrm{M}\Gamma(C_4\mathrm{M}),j}}{2\pi} =_1 \frac{\widetilde{\mathcal{L}}_j(\mathrm{M}) - \widetilde{\mathcal{L}}_j(\Gamma)}{4}, \tag{5.29b}$$

where $j \in \{v, c, f\}$ respectively denotes the bulk-valence, the bulk-conduction, and the faceted Zak phase.

Let us offer a hand-waving argument that captures the essential intuition of the above results. The Zak phase for $\mathrm{M}\Gamma(C_4\mathrm{M})$ can be expressed as a sum of two contributions: $\mathscr{Z}_{\mathrm{M}\Gamma(C_4\mathrm{M})} = \omega_{\mathrm{M}\Gamma} + \omega_{\Gamma(C_4\mathrm{M})}$, with $\omega_{\mathrm{M}\Gamma}$ [resp. $\omega_{\Gamma(C_4\mathrm{M})}$] the contribution from the oriented line $\mathrm{M}\Gamma$ [resp. $\Gamma(C_4\mathrm{M})$]. Note that $\omega_{\Gamma(C_4\mathrm{M})}$ receives as input the wave function along $\Gamma(C_4\mathrm{M})$, which is related by four-fold symmetry to the wave function along $\mathrm{M}\Gamma$. However, $\mathrm{M}\Gamma$ is mapped by four-fold rotation to the inverse of $\Gamma(C_4\mathrm{M})$, i.e., $\Gamma(C_4\mathrm{M})$ with opposite orientation. It follows that the contribution to $\mathscr{Z}_{\mathrm{M}\Gamma(C_4\mathrm{M})}$ from an infinitesimal line element along $\mathrm{M}\Gamma$ cancels the contribution from a rotation-related line element along $\Gamma(C_4\mathrm{M})$; the only nontrivial contributions to $\mathscr{Z}_{\mathrm{M}\Gamma(C_4\mathrm{M})}$ arise from applying four-fold rotation to the Bloch states at rotation-invariant momenta, thus giving Eq. (5.29b). This sketchy explanation is formalized in Appendix C.1.1.

Equations (5.29) can be applied to calculate the bulk-conduction Zak phase, the bulk-valence Zak phase, as well as the faceted Zak phase. For the bulk Zak phases, we input into the formula the values of itinerant angular momenta in the second row of the P4 segment of Table 4.1. To compute the faceted Zak phase, we apply that the itinerant angular momentum of the anomalous surface band is bulk-valence-like at X and M and bulk-conduction-like at Γ according to the angular-momentum anomaly [cf. Sec. 5.2]. The final result of these computations confirms a mismatch between the bulk and faceted Zak phases, namely:

$$\begin{aligned} \text{for } \mathrm{X}\Gamma(C_2\mathrm{X}): \ \mathscr{Z}_v = 0, \ \ \mathscr{Z}_c = 0, \ \ \mathscr{Z}_f = \pi, \\ \text{for } \mathrm{M}\Gamma(C_4\mathrm{M}): \ \mathscr{Z}_v = 0, \ \ \mathscr{Z}_c = 0, \ \ \mathscr{Z}_f = 3\pi/2, \end{aligned} \tag{5.30}$$

with all equalities understood to hold modulo 2π. Similar computations can be performed for different choices of the parameter Φ in the MRW model, with the resultant values of the Zak phases summarized in the second row and last column of Table 5.2.

5.4.4 *Zak-phase anomaly: main result*

Having obtained some intuition about the Zak-phase anomaly in specific models, we now prove it in a more general setting. Let us first specify the symmetrically-chosen loops for which a Zak-phase anomaly exists in correspondence with a nontrivial RTP invariant in general Pn symmetric

11 Compare also to similar consideration of Berry phases on C_3-related paths by Ref. [43] within the context of fragile topology.

Table 5.1: Summary of the phase diagram and the Hopf-RTP relation [cf. Eq. (6.5)] for the tight-binding models presented in Table 4.2. The MRW model corresponds to the second listed model. The column 'Phase diagram' specifies the values of the Hopf and RTP invariants in each phase of the given tight-binding models, specified by the values of the model parameter Φ.

Model symmetry			Hopf-RTP relation	
SG	$\Delta\mathcal{L}$	$\Delta \boldsymbol{r}_\perp$	Hopf-RTP relation	Phase diagram
P4	0	$(\frac{1}{2},\frac{1}{2})$	$\chi =_4 2\Delta\mathscr{P}_{\mathrm{XM}}$	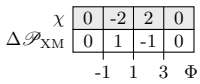
	1	$(0,0)$	$\chi =_4 \Delta\mathscr{P}_{\Gamma\mathrm{M}} + 2\Delta\mathscr{P}_{\Gamma\mathrm{X}}$	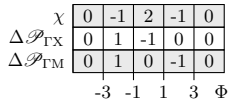
		$(\frac{1}{2},\frac{1}{2})$	$\chi =_4 \Delta\mathscr{P}_{\mathrm{M}\Gamma}$	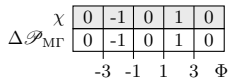
	2	$(0,0)$	$\chi =_4 2\Delta\mathscr{P}_{\mathrm{M}\Gamma}$	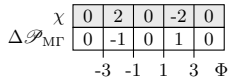
P3	0	$(\frac{1}{3},\frac{1}{3})$	$\chi =_3 \Delta\mathscr{P}_{\mathrm{K}'\mathrm{K}}$	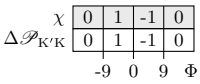
	1	$(0,0)$	$\chi =_3 \Delta\mathscr{P}_{\Gamma\mathrm{K}} + \Delta\mathscr{P}_{\Gamma\mathrm{K}'}$	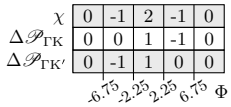
P6	1	$(0,0)$	$\chi =_6 2\Delta\mathscr{P}_{\Gamma\mathrm{K}} + 3\Delta\mathscr{P}_{\Gamma\mathrm{M}}$	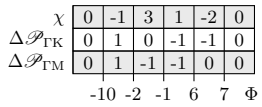
	2	$(0,0)$	$\chi =_6 2\Delta\mathscr{P}_{\mathrm{K}\Gamma}$	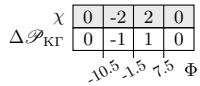
	3	$(0,0)$	$\chi =_6 3\Delta\mathscr{P}_{\mathrm{M}\Gamma}$	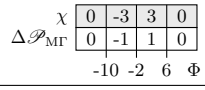

Table 5.2: Summary of the bulk-boundary correspondence [cf. Eqs. (5.32), (5.34) and (5.36)] for the tight-binding models presented in Table 4.2. The MRW model corresponds to the second listed model. The column 'Loop' lists all $\boldsymbol{k}$-loops going through at least one pair of rotation-invariant momenta for which the RTP invariant is nontrivial and a Zak-phase anomaly exists. The bulk Zak phases are given in columns '$\mathscr{Z}_v$' and '$\mathscr{Z}_c$'; the faceted Zak phase is given in the column '$\mathscr{Z}_f(\Phi)$' as a function of the parameter Φ. $\boldsymbol{G}_1 = (2\pi, 0)$ is one of the reciprocal lattice vectors in the reduced BZ.

Model symmetry			Bulk-boundary correspondence			
SG	$\Delta\mathcal{L}$	$\Delta\boldsymbol{r}_\perp$	Loop	$\mathscr{Z}_v$	$\mathscr{Z}_c$	$\mathscr{Z}_f(\Phi)$
P4	0	$(\frac{1}{2}, \frac{1}{2})$	$\Gamma\mathrm{M}(\Gamma + \boldsymbol{G}_1)\mathrm{X}\Gamma$	0	0	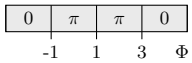
	1	$(0,0)$	$\mathrm{X}\Gamma(C_2\mathrm{X})$	0	0	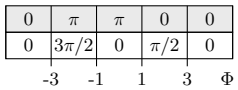
			$\mathrm{M}\Gamma(C_4\mathrm{M})$	0	0	
		$(\frac{1}{2}, \frac{1}{2})$	$\mathrm{M}\Gamma(C_4\mathrm{M})$	0	π	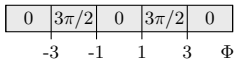
	2	$(0,0)$	$\mathrm{M}\Gamma(C_4\mathrm{M})$	0	0	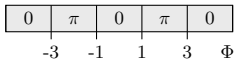
P3	0	$(\frac{1}{3}, \frac{1}{3})$	$\mathrm{K}'\mathrm{K}(C_3^{-1}\mathrm{K}')$	0	$\frac{2\pi}{3}$	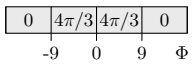
	1	$(0,0)$	$\mathrm{K}\Gamma(C_3\mathrm{K})$	0	0	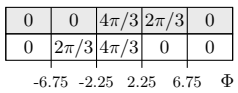
			$\mathrm{K}'\Gamma(C_3\mathrm{K}')$	0	0	
P6	1	$(0,0)$	$\mathrm{K}\Gamma(C_3\mathrm{K})$	0	0	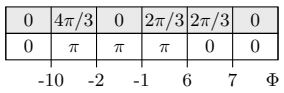
			$\mathrm{M}\Gamma(C_2\mathrm{M})$	0	0	
	2	$(0,0)$	$\mathrm{K}\Gamma(C_3\mathrm{K})$	0	0	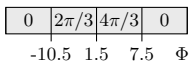
	3	$(0,0)$	$\mathrm{M}\Gamma(C_2\mathrm{M})$	0	0	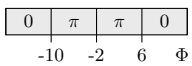

models. We assume that the RTP invariant $\Delta\mathscr{P}_{\Lambda\Xi} > 0$ for two rotation-invariant reduced momenta Λ and Ξ. The associated little groups are denoted by $\mathcal{G}_\Lambda$ and $\mathcal{G}_\Xi$, with both groups being subgroups of the cyclic, order-n group C_n, which is isomorphic to the point group of Pn.

Suppose there is an integer m that satisfies the following two properties:

(*i*) $m > 1$ and divides the order of $\mathcal{G}_\Pi$, for both $\Pi \in \{\Lambda, \Xi\}$.

(*ii*) The itinerant angular momenta of bulk-conduction and bulk-valence bands are distinct modulo m:

$$\widetilde{\mathcal{L}}_c(\Pi) \neq_m \widetilde{\mathcal{L}}_v(\Pi), \tag{5.31}$$

for both $\Pi \in \{\Lambda, \Xi\}$.

If there are multiple values of m satisfying (*i*–*ii*), for concreteness we choose the largest such value for m. Then the Zak-phase anomaly exists for a suitably chosen oriented loop in rBZ. This loop is defined as a (possibly bent) path that concatenates two segments, $\Xi\Lambda$ and $\Lambda(\Xi + \boldsymbol{G})$, such that one segment is, up to a translation by a reciprocal lattice vector and with reversed orientation, equal to the C_m rotation of the other segment: $\Lambda(\Xi + \boldsymbol{G}) = C_m(\Lambda\Xi) + \boldsymbol{G}'$. For brevity, we call such path as a *C_m-related-two-segment loop*. In Fig. 5.7(a–c), we illustrate a representative C_m-related-two-segment loop for all $m = 2, 3, 4$.[12]

Let us formulate the Zak-phase anomaly for these two-segment loops, supposing that the faceted-band subspace consists of $\mathcal{N}$ linearly-independent Bloch states that are smoothly defined over the rBZ. We emphasize that this discussion equally applies to a set of surface-localized energy bands detached from the rest of the spectrum or of surface-like polarization bands defined by the partitioning illustrated in Fig. 5.3(b,c).

Parallel transport (within the faceted-band subspace, along a rBZ loop) is encoded in $\mathcal{N}$ faceted Zak phases $\{\mathscr{Z}_f^i\}_{i=1}^{\mathcal{N}}$, which are computed by diagonalizing the $\mathcal{N}$-by-$\mathcal{N}$ Wilson-loop matrix in Eq. (5.27). For a generically chosen rBZ-loop, the $\mathcal{N}$ phases take generic values without preference for rational multiples of 2π. However, for the C_m-related-two-segment rBZ-loops, we propose that $\Delta\mathscr{P}_{\Lambda\Xi}$-number of the faceted Zak phases (denoted $\{\mathscr{Z}_f^i\}_{i=1,\ldots,\Delta\mathscr{P}_{\Lambda\Xi}}$) are symmetry-fixed to a rational multiple of $2\pi/n$ that depends on the itinerant angular momenta of the bulk-valence and bulk-conduction bands:

$$\frac{\mathscr{Z}_f^i}{2\pi} =_1 \frac{\widetilde{\mathcal{L}}_v(\Xi) - \widetilde{\mathcal{L}}_c(\Lambda)}{m}. \tag{5.32}$$

This result derives ultimately from the angular-momentum anomaly, which guarantees the existence of at least $\Delta\mathscr{P}_{\Lambda\Xi}$-number of anomalous faceted bands with itinerant angular momenta that are bulk-conduction-like at Λ and bulk-valence-like at Ξ:

$$\widetilde{\mathcal{L}}_f(\Lambda) = \widetilde{\mathcal{L}}_c(\Lambda); \quad \widetilde{\mathcal{L}}_f(\Xi) = \widetilde{\mathcal{L}}_v(\Xi). \tag{5.33}$$

Application of a theorem from Sec. IVD1 in Ref. [134] (which relates itinerant angular momenta to Zak phases) gives us Eq. (5.32), as elaborated in

12 A C_6-related-two-segment loop does not exist because there is only a single C_6-invariant reduced momentum – the rBZ center. For Hamiltonians with six-fold symmetry, a nontrivial RTP can arise solely from a subgroup (e.g., P2 or P3) of the full space group.

Appendix C.1.1. Equation (5.32) should be contrasted with the Zak phases of the bulk-valence and bulk-conduction bands:

$$\begin{aligned}\frac{\mathscr{Z}_v}{2\pi} &=_1 \frac{\widetilde{\mathcal{L}}_v(\Xi)-\widetilde{\mathcal{L}}_v(\Lambda)}{m},\\ \frac{\mathscr{Z}_c}{2\pi} &=_1 \frac{\widetilde{\mathcal{L}}_c(\Xi)-\widetilde{\mathcal{L}}_c(\Lambda)}{m},\end{aligned} \tag{5.34}$$

which also follow directly from applying the just-stated theorem to the itinerant angular momenta of each individual bulk band. Both bulk Zak phases are distinct from each of the anomalous faceted Zak phase, as can be proven by the method of contradiction. Indeed, assuming that $\mathscr{Z}_f =_{2\pi} \mathscr{Z}_v$, Eq. (5.34) implies that $\widetilde{\mathcal{L}}_v(\Lambda) =_m \widetilde{\mathcal{L}}_c(\Lambda)$ which contradicts the initial assumption (5.31). Similarly we can prove that $\mathscr{Z}_f =_{2\pi} \mathscr{Z}_v$ leads to a contradiction.

By going through all possible RTP invariants in all possible Pn-symmetric two-band Hamiltonians, we find only two exceptions to the rule that an integer m exists satisfying (*i*–*ii*). In both these exceptions (to be elaborated below), we propose that the Zak-phase anomaly exists for a *four-segment* loop going through four rotation-invariant reduced momenta $\{\Omega, \Lambda, \Omega+\boldsymbol{G}, \Xi\}$, with Ω and $\boldsymbol{G}$ specified below.

Exception 1: A P4-symmetric tight-binding Hilbert space that is a sum of two basis band representations, induced from two orbitals with onsite angular momentum difference $\Delta\mathcal{L}=0$ and centered at C_4-invariant Wyckoff positions with relative distance $\Delta\boldsymbol{r}_\perp = (1/2, 1/2)$ [for example at positions 1*a* and 1*b* defined in Fig. 4.1(a)]. According to Table 4.1, the mutually-disjoint condition in this case is fulfilled only at reduced momenta X and M, hence there is only one independent RTP invariant $\Delta\mathscr{P}_{\mathrm{XM}}$. In the first row of Table 4.2, we present a model Hamiltonian that realizes Exception 1, with a one-parameter phase diagram summarized in the first row of Table 5.1. The itinerant angular momenta of the bulk bands satisfy

$$\begin{aligned}\widetilde{\mathcal{L}}_v(\mathrm{X}) &\neq_2 \widetilde{\mathcal{L}}_c(\mathrm{X}),\\ \widetilde{\mathcal{L}}_v(\mathrm{M}) &\neq_4 \widetilde{\mathcal{L}}_c(\mathrm{M}),\\ \text{but } \widetilde{\mathcal{L}}_v(\mathrm{M}) &=_2 \widetilde{\mathcal{L}}_c(\mathrm{M}),\end{aligned} \tag{5.35}$$

implying that the choice $m=4$ violates the property (*i*) at X, while the choice $m=2$ violates the property (*ii*) at M. One may verify that a Zak-phase anomaly does not exist for a C_2-related-two-segment loop MX(M + $\boldsymbol{G}$), but it exists for four-segment loop going through $\{\Omega=\Gamma, \Lambda=\mathrm{M}, \Omega+\boldsymbol{G}=\Gamma+(2\pi,0), \Xi=\mathrm{X}\}$, as illustrated in Fig. 5.7(d).

Exception 2: A P4-symmetric tight-binding Hilbert space that is identical to Exception 1, except the onsite angular momenta difference is $\Delta\mathcal{L}=2$. In analogy with the first exception, we find the appropriate four-segment rBZ-loop that goes through $\{\Omega=\mathrm{M}, \Lambda=\Gamma, \Omega+\boldsymbol{G}=\mathrm{M}+(-2\pi,0), \Xi=\mathrm{X}\}$, as illustrated in Fig. 5.7(e).

In both Exceptions, the mutually-disjoint condition holds at Λ and Ξ, but not at Ω. [As a reminder, the last statement means that the itinerant angular momentum at Ω is identical for both bulk-valence and bulk-conduction states: $\widetilde{\mathcal{L}}_v(\Omega)=\widetilde{\mathcal{L}}_c(\Omega)\equiv\widetilde{\mathcal{L}}(\Omega)$.]

By generalizing techniques developed in Ref. [134], we derive in App. C.1.2 a relation between the Zak phases (for these four-segment rBZ-loops) and the

itinerant angular momenta of the bulk bands. We find that $\Delta\mathscr{P}_{\Lambda\Xi}$-number of the faceted Zak phases (denoted $\{\mathscr{Z}_f^i\}_{i=1,\ldots,\Delta\mathscr{P}_{\Lambda\Xi}}$) are symmetry-fixed to a rational multiple of $2\pi/n$ that depends on the bulk itinerant angular momenta as:

$$\frac{\mathscr{Z}_f^i}{2\pi} =_1 \frac{\widetilde{\mathcal{L}}(\Omega) - \widetilde{\mathcal{L}}_c(\Lambda)}{m_\Lambda} + \frac{\widetilde{\mathcal{L}}(\Omega) - \widetilde{\mathcal{L}}_v(\Xi)}{m_\Xi}, \tag{5.36a}$$

where $m_{\Lambda(\Xi)}$ denotes the maximal order of rotation symmetry of the little group $\mathcal{G}_{\Lambda(\Xi)}$. This rational value is distinct (mod 2π) from the symmetry-fixed values of the bulk-valence and bulk-conduction Zak phases:

$$\begin{aligned}\frac{\mathscr{Z}_v}{2\pi} &=_1 \frac{\widetilde{\mathcal{L}}(\Omega) - \widetilde{\mathcal{L}}_v(\Lambda)}{m_\Lambda} + \frac{\widetilde{\mathcal{L}}(\Omega) - \widetilde{\mathcal{L}}_v(\Xi)}{m_\Xi},\\ \frac{\mathscr{Z}_c}{2\pi} &=_1 \frac{\widetilde{\mathcal{L}}(\Omega) - \widetilde{\mathcal{L}}_c(\Lambda)}{m_\Lambda} + \frac{\widetilde{\mathcal{L}}(\Omega) - \widetilde{\mathcal{L}}_c(\Xi)}{m_\Xi}.\end{aligned} \tag{5.36b}$$

Once again, we can show by contradiction that the faceted Zak phase is always distinct from the bulk-valence and bulk-conduction Zak phases.

To illustrate the Zak-phase anomaly for a four-segment loop, we employ a model Hamiltonian presented in the first row of Table 4.2, and substitute the bulk values of itinerant angular momenta into Eqs. (5.36), to derive the faceted and bulk Zak phases detailed in the first row of Table 5.2. The remaining entries in Table 5.2 summarize the Zak-phase anomaly for various two-segment loops, and for all remaining tight-binding models in Table 4.2 whose phase diagrams are listed in Table 5.1.

6

RELATING THE RTP AND HOPF INVARIANTS

By considering the $\boldsymbol{k}\cdot\boldsymbol{p}$ description near Berry-dipolar band-touching points, we have previously argued in Sec. 4.3 that the RTP and Hopf invariants are not completely independent; a specific relation [cf. Eq. (4.25)] between the two invariants was extracted heuristically for a class of Hamiltonians with P4 symmetry. In this chapter, we derive this P4 result more systematically, and further generalize the Hopf-RTP relation to all Pn space groups, with the main result encapsulated in Eqs. (6.3–6.5) of Sec. 6.1. Representative case studies from all Pn space groups are presented in Sec. 6.2 to corroborate the Hopf-RTP relation.

We prove the Hopf-RTP relation in three different ways, with each offering distinct insights:

(*i*) In Sec. 6.3, we prove the relation assuming that all phase transitions are mediated by Berry dipoles (by generalizing the arguments in Sec. 4.3).

(*ii*) In Sec. 6.4, we relax the just-mentioned assumption, and prove the Hopf-RTP relation more generally by relating the angular-momentum anomaly of RTP invariants to the bulk-boundary correspondence of Hopf insulators (formulated in Chapter 5).

(*iii*) In Sec. 6.5, we prove the relation purely from a bulk perspective, by utilizing the Hopf-Chern relation from Ref. [168].

CHAPTER CONTENTS

6.1 MAIN RESULT: HOPF-RTP RELATION

Let us first formulate the RTP invariants in the most general context of a two-band, Pn-symmetric, insulating Hamiltonian with trivial first Chern class.

Consider a subset of rotation-invariant reduced momenta $\{\Pi_j\}_{j=1,\ldots,J_\alpha}$ in the rBZ. For the polarization difference between any pair j, j' in this subset

to be quantized to integer values, it is necessary that:

(*i*) The itinerant angular momenta of both bulk-conduction and bulk-valence bands satisfy the mutually-disjoint condition for all j:

$$\Delta\widetilde{\mathcal{L}}(\Pi_j) = \widetilde{\mathcal{L}}_c(\Pi_j) - \widetilde{\mathcal{L}}_v(\Pi_j) \bmod m_{\Pi_j} \neq 0. \tag{6.1}$$

(*ii*) For all j, the restriction of the valence band representation (VBR) to γ_{Π_j} is identical to the restriction of a basis band representation to γ_{Π_j}:

$$\exists\, \alpha \in \{1,2\} \text{ s.t. } \forall j \in \{1,\ldots,J_\alpha\},\ \text{VBR}\Big|_{\gamma_{\Pi_j}} = \text{BBR}[\varphi_\alpha]\Big|_{\gamma_{\Pi_j}}. \tag{6.2}$$

Here, $\text{BBR}[\varphi_\alpha]$ denotes the basis band representation induced from tight-binding-basis orbital φ_α with positional center $\boldsymbol{r}_\alpha = (\boldsymbol{r}_{\alpha,\perp}, z_\alpha)$. Note the equality in Eq. (6.2) holds with the same basis band representation (specified by $\alpha = 1,2$) for all j.

One may view condition (*ii*) as a generalization of the iso-orbital condition in Eq. (4.16) for any number of rotation-invariant reduced momenta. Conditions (*i*–*ii*) jointly imply that the polarizations at all Π_j are symmetry-fixed, modulo integers, to z_α.

We take the order (J_α) of the subset to be maximal, in the sense that every rotation-invariant reduced momentum satisfying the iso-orbital condition for $\text{BBR}[\varphi_\alpha]$ and the mutually-disjoint condition should be included in the subset. Consequently, if the subset contains a C_m-invariant reduced momentum Π_j, it also contains all momenta from the corresponding n/m-plet obtained from Π_j by a C_n rotation. Because there are only two basis band representations in a two-band Hamiltonian, all 'mutually-disjoint' rotation-invariant reduced momenta in the rBZ are sortable into at most two maximal 'iso-orbital' subsets.

6.1.1 P*n*-symmetric Hopf-RTP relation for $n = 3,4,6$

For space groups Pn ($n = 3,4,6$), a combination of symmetry (Pn), topology (triviality of Chern class) and Hilbert-space constraint (two-band Hamiltonian) ensures that all reduced momenta in the rBZ satisfying the mutually-disjoint condition belong to a *single* iso-orbital subset $\{\Pi_j\}_{j=1\ldots J}$, as shown in Appendix B.3. Then the RTP invariants relate to the Hopf invariant and the itinerant-angular-momenta differences through

$$\text{For P}n\ (n = 3,4,6), \quad \chi =_n \sum_{j=2}^{J} \Delta\widetilde{\mathcal{L}}(\Pi_j)\ \Delta\mathscr{P}_{\Pi_1\Pi_j}. \tag{6.3}$$

Within the momenta subset, the choice of Π_1 can be made arbitrarily without affecting the above relation modulo n.

6.1.2 P2-*symmetric Hopf-RTP relation*

For space group P2, depending on the equivalence class[1] of the Hamiltonian, either

1 Two Hamiltonians are equivalent if they can be continuously deformed into one another while preserving gap and P2 symmetry.

(P2-I) the rBZ contains only a single maximal momentum subset satisfying (*i–ii*), in which case one may also apply the formula (6.3) with $n = 2$, or

(P2-II) the four rotation-inequivalent rotation-invariant momenta of the rBZ can be divided into two maximal subsets, with one subset $\{\Pi^1_{j_1}\}_{j_1=1,\ldots,J_1}$ satisfying (*i–ii*) for BBR$[\varphi_1]$, and the other $\{\Pi^2_{j_2}\}_{j_2=1,\ldots,J_2}$ satisfying (*i–ii*) for BBR$[\varphi_2]$. It is shown in Appendix B.3 that neither J_1 nor J_2 can be odd, lest the first Chern invariant in the (k_x, k_y)-plane is also odd. Focusing on Hamiltonians with trivial first Chern class restricts our consideration then to $J_1 = J_2 = 2$, with the following, modified Hopf-RTP relation:

$$\text{For P2-II,} \quad \chi =_2 \sum_{\alpha=1}^{2} \Delta\mathscr{P}_{\Pi^\alpha_1 \Pi^\alpha_2}. \tag{6.4}$$

Within any maximal iso-orbital momenta subset indexed by α, the choice of Π^α_1 can be made arbitrarily without affecting the above relation modulo 2. A representative P2-symmetric model of class P2-I can be obtained by lowering the symmetry of either of the P4-symmetric models presented in the second and third rows of Tab. 4.2, while an example realization of a class P2-II Hamiltonian is presented in Sec. 6.2.2.

6.1.3 *Summarizing Hopf-RTP relation for all Pn space groups*

The previously-presented Hopf-RTP relations can be viewed as particular instances of a summarizing Hopf-RTP relation:

$$\text{For any P}n, \quad \chi =_n \sum_{\alpha=1}^{2} \sum_{j_\alpha=2}^{J_\alpha} \Delta\widetilde{\mathcal{L}}(\Pi^\alpha_{j_\alpha})\, \Delta\mathscr{P}_{\Pi^\alpha_1 \Pi^\alpha_{j_\alpha}}, \tag{6.5}$$

with one of $\{J_1, J_2\}$ possibly being zero.

6.2 MODEL HAMILTONIANS EXEMPLIFYING THE HOPF-RTP RELATION

6.2.1 *Examples for* Pn *(*$n = 3, 4, 6$*) models*

For each Pn-symmetric ($n = 3, 4, 6$) model Hamiltonian presented in Tab. 4.2, we display in Table 5.1 the particular forms of the Hopf-RTP relation, derived from Eq. (6.3) by inputting the model-dependent itinerant angular momenta listed in Table 4.1. Additionally, Table 5.1 provides a phase diagram with the values of the Hopf and RTP invariants for each phase, corroborating the relation between the invariants.

While the Tables only explicitly describe models whose tight-binding-basis orbitals differ in on-site angular momenta by $0 \leq \Delta\mathcal{L} \leq n/2$, models with $\Delta\mathcal{L} < 0$ can be obtained from the tabulated models by time reversal. One may verify that if the Hopf-RTP relation [Eq. (6.3)] holds for a model $h_{\Delta\mathcal{L}}(\boldsymbol{k})$, it holds consistently for the time-reversed model $h_{-\Delta\mathcal{L}}(\boldsymbol{k})$ [related by time reversal to $h^*_{\Delta\mathcal{L}}(-\boldsymbol{k})$ via Eq. (4.28)].

Details 6.1 For this consistency check, we utilize that the Hopf invariant and the polarization transform under time reversal as in Eq. (4.29), while the difference in itinerant angular momentum changes as

$$\Delta\widetilde{\mathcal{L}}(-\Pi; h_{-\Delta\mathcal{L}}) = m - \Delta\widetilde{\mathcal{L}}(\Pi; h_{\Delta\mathcal{L}}) \tag{6.6}$$

for a C_m-invariant momentum Π. This equality can be derived from Eq. (4.7) with the observation that $\boldsymbol{G}_{-\Pi} = C_m(-\Pi) + \Pi = -\boldsymbol{G}_\Pi$, and that time reversal inverts on-site angular momenta

while preserving Wyckoff positions. Combining these time-reversal relations into the statements of the Hopf-RTP relation [Eq. (6.3)], we get

$$\begin{aligned}
-\chi[h_{\Delta\mathcal{L}}] &\overset{\text{Eq. (6.3)}}{=_n} -\sum_{j=2}^{J} \Delta\widetilde{\mathcal{L}}(\Pi_j; h_{\Delta\mathcal{L}})\, \Delta\mathscr{P}_{\Pi_1\Pi_j}[h_{\Delta\mathcal{L}}] \\
&\overset{\text{Eqs. (6.6,4.29)}}{=_n} -\sum_{j=2}^{J} \left[m_j - \Delta\widetilde{\mathcal{L}}(-\Pi_j; h_{-\Delta\mathcal{L}})\right]\, \Delta\mathscr{P}_{-\Pi_1,-\Pi_j}[h_{-\Delta\mathcal{L}}] \\
&=_n \sum_{j=2}^{J} \Delta\widetilde{\mathcal{L}}(-\Pi_j; h_{-\Delta\mathcal{L}})\, \Delta\mathscr{P}_{-\Pi_1,-\Pi_j}[h_{-\Delta\mathcal{L}}] \\
&=_n \sum_{i=2}^{J} \Delta\widetilde{\mathcal{L}}(\Pi_i; h_{-\Delta\mathcal{L}})\, \Delta\mathscr{P}_{\Pi_1,\Pi_i}[h_{-\Delta\mathcal{L}}] \overset{\text{Eq. (4.29)}}{=_n} \chi[h_{-\Delta\mathcal{L}}].
\end{aligned} \tag{6.7}$$

To derive the third row, we used that C_m-invariant momenta always appear in n/m-plets with equal values of polarization, and therefore we deduced, that the term $\sum m_j \Delta\mathscr{P}_{-\Pi_1,-\Pi_j}$ will contribute multiples of n to the sum. To derive the fourth row, we used that a maximal subset $\{\Pi_j\}_{j=1\ldots J}$ satisfying mutually disjoint and iso-orbital conditions in a $h[\Delta\mathcal{L}]$ model is in one-to-one correspondence with a maximal iso-orbital subset $\{-\Pi_j\}_{j=1\ldots J}$ in a $h[-\Delta\mathcal{L}]$ model. Therefore one may relabel reduced momenta in the sum and arrive at the fourth row of Eq. (6.7). Using the fact that the Hopf invariant changes sign under time reversal (4.29), we conclude that if the Hopf-RTP relation holds for $h_{\Delta\mathcal{L}}$ then it must also hold for $h_{-\Delta\mathcal{L}}$.

6.2.2 *Model Hamiltonian in class* P2−II

To exemplify the Hopf-RTP relation in Eq. (6.4), we construct an explicit model with a valence band representation that is not symmetry-equivalent to a basis band representation. To do so, we start with the P4-symmetric MRW model [Eq. (4.24)] and add a term that reduces the symmetry to P2:

$$h^{\text{inv.}} = f(1-\cos k_x)\sigma_z, \tag{6.8}$$

which closes the bulk energy gap along two out of the four rotation-invariant lines (γ_X and γ_M) for $0.5 \leq f \leq 12.5$. After the gap reopens, the valence band representation satisfies

$$\begin{aligned}
\text{VBR}\Big|_{\gamma_\Gamma \cup \gamma_\text{Y}} &= \text{BBR}[\varphi_1]\Big|_{\gamma_\Gamma \cup \gamma_\text{Y}}, \\
\text{VBR}\Big|_{\gamma_\text{M} \cup \gamma_\text{X}} &= \text{BBR}[\varphi_2]\Big|_{\gamma_\text{M} \cup \gamma_\text{X}},
\end{aligned} \tag{6.9}$$

while the triviality of the Chern class is preserved. Since the mutually-disjoint condition is fulfilled at all rotation-invariant momenta, the complete set of RTP invariants is $\Delta\mathscr{P}_{\Gamma\text{Y}}, \Delta\mathscr{P}_{\text{XM}} \in \mathbb{Z}$. For the presented model, the Hopf-RTP relation reads

$$\chi =_2 \Delta\mathscr{P}_{\Gamma\text{Y}} + \Delta\mathscr{P}_{\text{MX}}. \tag{6.10}$$

6.3 HOPF-RTP RELATION FROM BERRY DIPOLES

6.3.1 *Berry-dipole transitions lead to Eq. (6.3)*

Our goal here is to prove the Hopf-RTP relation in Eq. (6.3), assuming that one begins from a canonical trivial phase and that all subsequent band touchings are Berry-dipolar. By 'canonical trivial', we mean a phase with only on-site energies and zero 'hopping' matrix elements of the real-space tight-binding Hamiltonian. In such a phase, the Hopf and RTP invariants vanish, and both bulk-valence and bulk-conduction bands are basis band representations. In the following proof we assume the valence band representation to be

induced from basis orbital φ_1, and the conduction band representation from φ_2. Then the itinerant angular momenta of the valence and conduction bands are compatible with the Berry dipole $\boldsymbol{k}\cdot\boldsymbol{p}$ Hamiltonian of the form given by Eqs. (3.3) and (3.4). We comment on the opposite choice of the orbitals inducing valence and conduction bands at the end of this section.

Let us modify the Hamiltonian and transit to a distinct gapped phase via a Berry-dipole critical point. We assume that a Berry-dipole band touching occurs at an (n/m)-multiplet of C_m-invariant momenta $\{\boldsymbol{k}^{\mathrm{t}} = (\Pi^{\mathrm{t}}, k_z^{\mathrm{t}})\}_{\mathrm{t}=1,\ldots,n/m}$. As explained in Sec. 4.3 [Eq. (4.20)], the Hopf invariant changes by an integer value:

$$\delta\chi = -\sum_{\mathrm{t}=1}^{n/m} v(\boldsymbol{k}^{\mathrm{t}})\Delta\ell(\boldsymbol{k}^{\mathrm{t}}) = -\frac{n}{m}v(\boldsymbol{k}^1)\Delta\ell(\boldsymbol{k}^1), \tag{6.11a}$$

with helicity $v(\boldsymbol{k}^{\mathrm{t}}) = \pm 1$ and spin $\Delta\ell(\boldsymbol{k}^{\mathrm{t}}) \in \mathbb{Z}$ being parameters of the Berry-dipole $\boldsymbol{k}\cdot\boldsymbol{p}$ Hamiltonian [cf. Eq. (3.3)] and $\boldsymbol{k}^1$ being a representative momentum of the n/m-multiplet. At the same time, according to Eq. (3.18), the Zak phase at reduced momentum Π_t must change by $-2\pi v(\boldsymbol{k}^{\mathrm{t}})$, implying (by the geometric theory of polarization) that the polarization at Π^{t} changes by $\delta\mathscr{P}(\Pi^{\mathrm{t}}) = -v(\boldsymbol{k}^{\mathrm{t}})$. Combining the last two equalities relates the change in the Hopf invariant to the change in polarization:

$$\delta\chi = \frac{n}{m}\Delta\ell(\boldsymbol{k}^1)\ \delta\mathscr{P}(\Pi^1). \tag{6.11b}$$

The integer-valued $\Delta\ell(\boldsymbol{k}^1)$ defined through the continuous-rotation-invariant, Berry-dipole Hamiltonian can be identified, modulo m, as the difference in itinerant angular momenta between conduction and valence states at $\boldsymbol{k}^1$ [cf. Eq. (4.19)].

One may therefore substitute $\Delta\ell \to \Delta\widetilde{\mathcal{L}}$ in Eq. (6.11b) if we relax the equality to an equivalence modulo n:

$$\delta\chi =_n \frac{n}{m}\Delta\widetilde{\mathcal{L}}(\Pi^1)\ \delta\mathscr{P}(\Pi^1) = \sum_{\Pi}\Delta\widetilde{\mathcal{L}}(\Pi)\ \delta\mathscr{P}(\Pi). \tag{6.11c}$$

In the last equality, we extended the expression to sum over all C_{m_Π}-invariant ($m_\Pi > 1$) momenta Π, with the understanding that values of Π not belonging to the (n/m)-multiplet do not contribute to the sum, as the change in polarization $\delta\mathscr{P}(\Pi)$ is zero for these non-belongers.

Next, we apply that differences $\delta\mathscr{P}$ in polarization are unaffected by the choice of spatial origin, hence one may as well redefine the polarization $\mathscr{P} \to \mathscr{P}' = \mathscr{P} - z_1$, with z_1 the z-coordinate of the positional center of basis orbital φ_1:

$$\delta\chi =_n \sum_{\Pi}\Delta\widetilde{\mathcal{L}}(\Pi)\,\delta[\mathscr{P}(\Pi) - z_1]. \tag{6.11d}$$

Beginning from the canonical trivial phase and tuning a Hamiltonian parameter, the net change of the Hopf/RTP invariants after a series of band touchings is simply a sum of changes attributed to each band touching, and moreover $\delta\chi$ is linearly related to $\delta[\mathscr{P}(\Pi) - z_1]$ [cf. Eq. (6.11d)]. This implies the Hopf invariant is related to the polarization as

$$\chi =_n \sum_{\Pi}\Delta\widetilde{\mathcal{L}}(\Pi)[\mathscr{P}(\Pi) - z_1]. \tag{6.11e}$$

By our assumption that the Hamiltonian has a RTP, there exists at least one rotation-invariant momentum (call it Π') where the mutually-disjoint

condition is satisfied: $\Delta\widetilde{\mathcal{L}}(\Pi') \neq 0$; the polarization $\mathscr{P}(\Pi')$ must then equal z_1 modulo integer, according to an argument presented below Eq. (4.9). By replacing z_1 in Eq. (6.11e) by $\mathscr{P}(\Pi')$ (mod 1), one arrives at

$$\chi =_n \sum_{\Pi} \Delta\widetilde{\mathcal{L}}(\Pi)[\mathscr{P}(\Pi) - \mathscr{P}(\Pi')] + (\text{integer}) \sum_{\Pi} \Delta\widetilde{\mathcal{L}}(\Pi). \tag{6.11f}$$

The sum $\sum_{\Pi} \Delta\widetilde{\mathcal{L}}(\Pi)$ in the last term may be recognized, modulo n, as the first Chern invariant over a 2D subtorus (of the BZ) parametrized by k_x and k_y [cf. Appendix B.1 for details]. But this Chern invariant vanishes by our assumption that the first Chern class is trivial. Therefore, we can simply drop the last term in Eq. (6.11f) under the equivalence modulo n:

$$\chi =_n \sum_{\Pi} \Delta\widetilde{\mathcal{L}}(\Pi)\Delta\mathscr{P}_{\Pi'\Pi}; \quad \Delta\mathscr{P}_{\Pi'\Pi} = \mathscr{P}(\Pi) - \mathscr{P}(\Pi'). \tag{6.11g}$$

Assuming that there is only one maximal iso-orbital subset $\{\Pi_j\}_{j=1\ldots J}$, the above equation is equivalent to Eq. (6.3). To recognize this equivalence, note in the summation over all rotation-invariant reduced momenta, that $\Delta\widetilde{\mathcal{L}}(\Pi) \neq 0$ only when Π belongs to the subset $\{\Pi_j\}_{j=1\ldots J}$, and one may as well choose $\Pi' = \Pi_1$ (a representative member of this subset) without changing the relation modulo n.

Let us finally show, that the derived result does not depend on the choice of the orbital inducing the valence band representation. Indeed, if instead of φ_1 we choose it to be φ_2, the spinor of a Berry dipole $\boldsymbol{k}\cdot\boldsymbol{p}$ Hamiltonian compatible with the itinerant angular momenta of the valence and conduction bands is given by Eq. (3.5). As was discussed in Sec. 3.2, the change in the Hopf invariant in this case is of an opposite sign than in Eq. (6.11a). Simultaneously, the differences in itinerant angular momenta between the basis Bloch functions and between conduction and valence bands are related with an extra minus sign $\Delta\widetilde{\mathcal{L}}(\Pi) =_{m_\Pi} -\left(\widetilde{\mathcal{L}_2}(\Pi) - \widetilde{\mathcal{L}_1}(\Pi)\right)$. Therefore, for a $\boldsymbol{k}\cdot\boldsymbol{p}$ expansion around Π, $\Delta\ell =_{m_\Pi} -\Delta\widetilde{\mathcal{L}}(\Pi)$, and Eq. (6.11c) holds without modifications.

Note that so far we did not reproduce Eq. (6.4) which applies for the exceptional P2-symmetric case, which leads us to raise the following question: could there have been two maximal iso-orbital subsets within the described construction? The answer is that *not under our assumption that all band touchings are Berry-dipolar*, as we proceed to clarify.

6.3.2 *Beyond the Berry-dipole assumption*

We have just derived the Hopf-RTP relation Eq. (6.3) based on an assumption that the only band touchings are Berry dipoles. What Hamiltonian phases are missed under this assumption? Could it be that the Hopf-RTP relation takes a different form in these 'missed phases'? The short answer is that there are no 'missed phases' for space groups P($n = 3, 4, 6$); however, there exists 'missed phases' for P2, for which a more general Hopf-RTP relation in Eq. (6.5) holds.

What exactly distinguishes the 'missed phases' from the phases that are not missed? To pin this down, one needs to appreciate that a Berry-dipole band touching does not transform the band representation of the bulk-valence subspace into a distinct band representation. In more detail, if one begins from the canonical trivial phase with the bulk-valence band being a basis band representation BBR$[\varphi_j]$, with φ_j a basis orbital with on-site angular momentum $\mathcal{L}_j$ and Wyckoff position $\boldsymbol{r}_j$, then any subsequent Berry-dipole

band touchings will not change the fact that the bulk-valence band is a band representation induced from an $(\mathcal{L}_j, \boldsymbol{r}_{j,\perp})$-orbital; the z-coordinate of the Wyckoff position will, however, generically differ. This follows from three facts:

(*i*) Recall that the Berry dipole is, by definition, a dipolar source of Berry curvature with zero monopole charge. Hence *Fact 1 (topological formulation): a Berry dipole cannot change the first Chern class of the bulk-valence band.* A theorem proven in Ref. [120] tells that a unit-rank Pn-symmetric band with trivial first Chern class is simply a band representation of Pn. By 'unit-rank', we mean that the band is given by a single linearly-independent Bloch function $\psi_{\boldsymbol{k}}$ over the Brillouin torus, as is certainly true for the bulk-valence band of a two-band Hamiltonian. Thus an equivalent statement is *Fact 1 (crystallographic formulation): a Berry-dipole transition preserves the band-representability of a unit-rank bulk-valence band.*

(*ii*) Because a Berry-dipole band touching occurs at an isolated $\boldsymbol{k}$-point, while the itinerant angular momentum is a property of a $\boldsymbol{k}$-line, a Berry-dipole touching cannot change the itinerant angular momenta of the bulk-valence band. Hence *Fact 2: the bulk valence band has exactly the same itinerant angular momenta as a basis band representation induced from* φ_1.

(*iii*) *Fact 3 (crystallographic formulation): two unit-rank band representations of* Pn *are equivalent as band representations if and only if they have exactly the same itinerant angular momenta.* To be equivalent as unit-rank band representations of Pn means that their corresponding representative Wannier orbitals have identical on-site angular momenta $\mathcal{L}$ and xy-projected Wyckoff positions $\boldsymbol{r}_\perp$; we have been denoting equivalence classes of band representations by $\mathrm{BR}(\mathcal{L}, \boldsymbol{r}_\perp)$. Applying the same theorem in Ref. [120], an equivalent restatement is *Fact 3 (topological formulation): given a* Pn*-symmetric, unit-rank band with trivial Chern class, its itinerant angular momenta are in a one-to-one correspondence with an equivalence class of band representations.* Fact 3 is proven in App. B.2, and contrasts with the other known fact that if the Chern class is nontrivial, the Chern invariants are *not* in one-to-one correspondence with the itinerant angular momenta [56].

Synthesizing these three facts, we find that in any Hamiltonian phase connected to the canonical trivial phase via Berry-dipole transitions, the valence band is a band representation in the same equivalence class $\mathrm{BR}(\mathcal{L}_j, \boldsymbol{r}_{j,\perp})$ as for $\mathrm{BBR}[\varphi_j]$. Thus we must admit the possibility of 'missed phases' where the bulk-valence band is a band representation but is not symmetry-equivalent to either of $\mathrm{BBR}[\varphi_j]$.

Actually, for two-band Hamiltonians with space groups Pn ($n = 3, 4, 6$), the triviality of the first Chern class and the Hilbert-space constraint of a two-band Hamiltonian altogether imply that the valence band representation is symmetry-equivalent to one of $\mathrm{BBR}[\varphi_j]$, as proven in Appendix B.3. This suggests that Eq. (6.3) holds without exceptions for the Pn ($n = 3, 4, 6$) space groups. This is true, and the most direct way to prove this is by the methods of Sec. 6.4 or Sec. 6.5. On the other hand, a trivial Chern class in the P2 space group does *not* imply the bulk-valence band is symmetry-equivalent to one of $\mathrm{BBR}[\varphi_j]$. Thus the more general Hopf-RTP relation in Eq. (6.5) is only needed for the P2 space group. For models in class P2-I this general relation coincides with Eq. (6.3), as for Pn ($n = 3, 4, 6$), while for models in class

P2-II it takes the form in Eq. (6.4). This latter relation is proven separately in Sec. 6.4.3.

6.4 HOPF-RTP RELATION FROM BULK-BOUNDARY CORRESPONDENCE

Having discussed the bulk-boundary correspondence of the crystalline Hopf insulator, we employ the faceted Chern number [introduced in Sec. 5.1] and the angular-momentum anomaly [introduced in Sec. 5.2] to prove the general, mod-n Hopf-RTP relation in Eq. (6.5). To make the proof self-contained, we recapitulate in Sec. 6.4.1 a few salient features of the bulk-boundary correspondence. Subsequently, in Secs. 6.4.2 and 6.4.3, we relate the surface signatures of both Hopf and RTP invariants, and then derive the relation between their bulk counterparts. Throughout this section, we consider a semi-infinite geometry where the insulator occupies a space with $z > 0$; our boundary will be the bottom ($z = 0$) facet.

6.4.1 *Recapitulation: Bulk-boundary correspondence of the crystalline Hopf insulator*

In the presence of a non-zero Hopf invariant, the totality of all surface-localized states (occupied and unoccupied) possesses a faceted Chern number that is equal to the bulk Hopf invariant

$$\mathscr{C}_f = \chi. \tag{6.12}$$

We note that this equality holds in the convention of the surface normal vector $\hat{\boldsymbol{n}}$ pointing outside of the sample. For the bottom facet this means that the normal vector is oriented opposite to the unit vector along the z-axis: $\hat{\boldsymbol{n}} = -\hat{\boldsymbol{e}}_z$.

There exists at most two maximal subsets of rotation-invariant reduced momenta in the rBZ satisfying the mutually-disjoint (6.1) and iso-orbital (6.2) conditions. We denote them as $\{\Pi^\alpha_{j_\alpha}\}_{j_\alpha=1,\ldots,J_\alpha}$, with α=1,2 a subset index. Picking Π^α_1 as a representative member in each subset, a complete set of independent RTP invariants is given by $\{\Delta\mathscr{P}_{\Pi^1_1\Pi^1_{j_1}}\}_{j_1=2\ldots J_1} \bigcup \{\Delta\mathscr{P}_{\Pi^2_1\Pi^2_{j_2}}\}_{j_2=2\ldots J_2}$.[2]

An angular-momentum anomaly is associated with each of the independent RTP invariants $\Delta\mathscr{P}_{\Pi^\alpha_1\Pi^\alpha_{j_\alpha}}$ [cf. Sec. 5.2]. To recapitulate what this means: defining $\mathcal{N}_c(\Pi)$ [resp. $\mathcal{N}_v(\Pi)$] as the total number of faceted states whose itinerant angular momenta are bulk-conduction-like (resp. bulk-valence-like) at Π, then

$$\begin{aligned} \mathcal{N}_v(\Pi^\alpha_{j_\alpha}) &= \mathcal{N}_v(\Pi^\alpha_1) + \Delta\mathscr{P}_{\Pi^\alpha_1\Pi^\alpha_{j_\alpha}}, \\ \mathcal{N}_c(\Pi^\alpha_{j_\alpha}) &= \mathcal{N}_c(\Pi^\alpha_1) - \Delta\mathscr{P}_{\Pi^\alpha_1\Pi^\alpha_{j_\alpha}}, \end{aligned} \tag{6.13}$$

with the total number of faceted bands being independent of Π:

$$\mathcal{N}_{\text{tot}} = \mathcal{N}_v(\Pi) + \mathcal{N}_c(\Pi). \tag{6.14}$$

2 According to Appendix B.3, a maximal subset containing only one element (i.e., one reduced momentum) is incompatible with the Hamiltonian having trivial Chern class, therefore there is at least one well-defined RTP invariant for each non-empty maximal subset.

6.4.2 *Hopf-RTP relation for a valence band that is symmetry-equivalent to a basis band representation*

Assuming that the valence band is symmetry-equivalent to a basis band representation, there is only one maximal subset of reduced momenta $\{\Pi_j\}_{j=1\ldots J}$ fulfilling the mutually-disjoint and iso-orbital conditions, and therefore a complete set of independent RTP invariants is given by $\{\Delta\mathscr{P}_{\Pi_1\Pi_j}\}_{j=2\ldots J}$.

Our next step is to relate the surface signatures of the RTP and Hopf invariants, by utilizing a relation between Chern numbers and rotation eigenvalues derived in Ref. [56] for pn-symmetric Hamiltonians and reviewed in Sec. 2.2.2.2. A simple manipulation of their relation (detailed in Appendix B.1) allows to express the faceted Chern number, modulo n, as the sum of itinerant angular momenta of all faceted states at *all* rotation-invariant reduced momenta:

$$\mathscr{C}_f =_n -\sum_{i=1}^{\mathcal{N}_{\text{tot}}}\sum_{\Pi\in\text{all}}\widetilde{\mathcal{L}}_i(\Pi),\quad \widetilde{\mathcal{L}}_i(\Pi)\in\{0,1,\ldots,m_\Pi-1\}. \tag{6.15a}$$

By 'all rotation-invariant reduced momenta', we mean not just C_n-invariant momenta, but also any C_{m_Π}-invariant momentum with $1<m_\Pi<n$, where m_Π is the order of the little group of Π. Note that each C_{m_Π}-invariant momentum appears as a member of an n/m_Π-plet of symmetry-related momenta; in Eq. (6.15a) we include all members of each multiplet. Each of $\widetilde{\mathcal{L}}_i(\Pi)$ should be understood as mod-m_Π variables taking values in $\{0,1,\ldots,m_\Pi-1\}$. The minus sign in Eq. (6.15a) [which is absent in Eq. (B.1) in the appendix] reflects the fact that the facet normal is oriented opposite to the rotation axis $\hat{\boldsymbol{z}}$. One may then apply Eq. (6.14) to separate faceted states into two categories, namely with bulk-valence-like vs. bulk-conduction-like itinerant angular momenta:

$$\mathscr{C}_f =_n -\sum_{\Pi\in\text{all}}\left[\mathcal{N}_v(\Pi)\widetilde{\mathcal{L}}_v(\Pi)+\mathcal{N}_c(\Pi)\widetilde{\mathcal{L}}_c(\Pi)\right]. \tag{6.15b}$$

For Π not belonging to the maximal subset $\widetilde{\mathcal{L}}_v(\Pi)=\widetilde{\mathcal{L}}_c(\Pi)$, meaning that partitioning of $\mathcal{N}_{\text{tot}}$ into $\mathcal{N}_v(\Pi)$ and $\mathcal{N}_c(\Pi)$ is not unique. However, the equality of itinerant angular momenta ensures that the derivation goes through *irrespective* of the chosen partitioning. A convenient choice which helps to derive the subsequent Eq. (6.15c) is to set $\mathcal{N}_{v(c)}(\Pi)=\mathcal{N}_{v(c)}(\Pi_1)$ for all Π not belonging to the maximal subset and Π_1 being the chosen representative number of the maximal subset. Inserting the angular-momentum-anomaly [Eq. (6.13)] in Eq. (6.15b), we obtain

$$\begin{aligned}\mathscr{C}_f =_n -\Bigg[&\mathcal{N}_v(\Pi_1)\left(\sum_{\Pi\in\text{all}}\widetilde{\mathcal{L}}_v(\Pi)\right)+\mathcal{N}_c(\Pi_1)\left(\sum_{\Pi\in\text{all}}\widetilde{\mathcal{L}}_c(\Pi)\right)\\&+\sum_{j=2}^{J}\Delta\mathscr{P}_{\Pi_1\Pi_j}\left(\widetilde{\mathcal{L}}_v(\Pi_j)-\widetilde{\mathcal{L}}_c(\Pi_j)\right)\Bigg].\end{aligned} \tag{6.15c}$$

The first two sums on the right-hand side are $n\mathbb{Z}$ multiples of the Chern numbers of the bulk-valence resp. bulk-conduction bands. Indeed, $(-)\sum_{\Pi\in\text{all}}\widetilde{\mathcal{L}}_v(\Pi)$ [resp. $(-)\sum_{\Pi\in\text{all}}\widetilde{\mathcal{L}}_c(\Pi)$] equals (modulo n) the Chern number in the (k_x,k_y)-plane of the bulk-valence [resp. bulk-conduction] band, as derived in App. B.1. Our assumption that the Hamiltonian has trivial Chern class implies that the first two sums in Eq. (6.15c) are zero modulo n. The third and only remaining term on the right-hand side of

Eq. (6.15c) represents the effect of the anomaly in replacing angular momenta which are bulk-conduction-like with those that are bulk-valence-like, or vice versa (depending on the sign of the RTP invariant.) A simple rewriting gives:

$$\mathscr{C}_f =_n \sum_{j=2}^{J} \Delta\mathscr{P}_{\Pi_1\Pi_j}\Delta\widetilde{\mathcal{L}}(\Pi_j), \tag{6.15d}$$

with $\Delta\widetilde{\mathcal{L}}(\Pi) = \widetilde{\mathcal{L}}_c(\Pi) - \widetilde{\mathcal{L}}_v(\Pi) \pmod{m_\Pi}$. The fact that all C_{m_Π}-invariant momenta from an n/m_Π-plet are present in the sum ensures that a possible multiples-of-m_Π difference between $\Delta\widetilde{\mathcal{L}}(\Pi)$ and $\widetilde{\mathcal{L}}_c(\Pi) - \widetilde{\mathcal{L}}_v(\Pi)$ does not modify Eq. (6.15d) modulo n.

Using the equality between the faceted Chern number and the bulk Hopf invariant $\chi = \mathscr{C}_f$ [cf. Eq. (6.12)], we arrive at the mod-n Hopf-RTP relation in Eq. (6.3). We also emphasize that, in contrast to Sec. 6.3, the present derivation made no assumption whatsoever concerning the phase transitions encountered when reaching the final Hamiltonian from the 'canonical trivial' phase.

6.4.3 *Hopf-RTP relation for a valence band that is not symmetry-equivalent to a basis band representation*

We show in Appendix B.3 that of the Pn groups, it is only the P2 group that allows for crystalline Hopf insulators whose valence band representation is not symmetry-equivalent to a basis band representation. This case arises only when the mutually-disjoint condition is satisfied for all rotation-invariant momenta:

$$\forall\Pi_j, \quad \Delta\widetilde{\mathcal{L}}(\Pi_j) = 1, \tag{6.16}$$

and when the two maximal subsets of reduced momenta (fulfilling the iso-orbital condition) each have exactly two elements, which we denote as $\{\Pi_1^\alpha, \Pi_2^\alpha\}_{\alpha=1,2}$; there are then only two RTP invariants $\{\Delta\mathscr{P}_{\Pi_1^\alpha\Pi_2^\alpha}\}_{\alpha=1,2}$.

To prove the Hopf-RTP relation (6.4), we again express the faceted Chern number in terms of the itinerant angular momenta of the faceted states, i.e., we utilize Eq. (6.15a) with $n = m_\Pi = 2$ for all Π. Because each term is integer-valued, one may freely alter plus and minus signs [in Eq. (6.15a)] without modifying the equality modulo 2. Next we insert into Eq. (6.15a) the angular-momentum-anomaly [Eqs. 6.13], obtaining:

$$\begin{aligned}\mathscr{C}_f =_2 &\sum_{\alpha=1}^{2}\left[\mathcal{N}_v(\Pi_1^\alpha)\sum_{j=1}^{2}\widetilde{\mathcal{L}}_v(\Pi_j^\alpha) + (v\to c)\right] \\ &+ \sum_{\alpha=1}^{2}\Delta\mathscr{P}_{\Pi_1^\alpha\Pi_2^\alpha}\Delta\widetilde{\mathcal{L}}(\Pi_2^\alpha).\end{aligned} \tag{6.17}$$

As elaborated in Dets. 6.2, the square-bracketed terms in the first line of Eq. (6.17) sum to an even integer and therefore can be dropped from the modulo 2 equality. Then, bearing in mind that $\chi = \mathscr{C}_f$ and $\Delta\widetilde{\mathcal{L}} = 1$ [cf. Eq. (6.16)], the desired Hopf-RTP relation (6.4) follows from Eq. (6.17).

Details 6.2 To reveal that the square-bracketed sum in Eq. (6.17) is indeed even, we rewrite the bracketed terms as

$$\sum_{\alpha=1}^{2}\sum_{j=1}^{2}\left\{\mathcal{N}_v(\Pi_1^1)\widetilde{\mathcal{L}}_v(\Pi_j^\alpha) + \left[\mathcal{N}_v(\Pi_1^\alpha) - \mathcal{N}_v(\Pi_1^1)\right]\widetilde{\mathcal{L}}_v(\Pi_j^\alpha) + (v\to c)\right\}. \tag{6.18a}$$

The first term is proportional to $\sum_{\Pi\in\text{all}}\widetilde{\mathcal{L}}_v(\Pi)$, which has the same parity as the first Chern number of the bulk-valence band; hence this term vanishes (modulo 2) under our assumption

that the Hamiltonian has trivial first Chern class. Likewise, the analogous term with $[v \to c]$ vanishes modulo 2, and we are left with

$$\begin{aligned}&\sum_{j=1}^{2}\left[\left\{\mathcal{N}_v(\Pi_1^2)-\mathcal{N}_v(\Pi_1^1)\right\}\widetilde{\mathcal{L}}_v(\Pi_j^2)+\left\{\mathcal{N}_c(\Pi_1^2)-\mathcal{N}_c(\Pi_1^1)\right\}\widetilde{\mathcal{L}}_c(\Pi_j^2)\right]\\ =_2&\sum_{j=1}^{2}\left[\left\{\mathcal{N}_v(\Pi_1^2)-\mathcal{N}_v(\Pi_1^1)\right\}\widetilde{\mathcal{L}}_v(\Pi_j^2)+\left\{-\mathcal{N}_v(\Pi_1^2)+\mathcal{N}_v(\Pi_1^1)\right\}\widetilde{\mathcal{L}}_c(\Pi_j^2)\right].\end{aligned} \tag{6.18b}$$

In obtaining the last row, we used that $\mathcal{N}_c(\Pi)=\mathcal{N}_{\text{tot}}-\mathcal{N}_v(\Pi)$ and that $\mathcal{N}_{\text{tot}}$ appearing twice and with opposite signs in the second curly-bracketed term is canceled out in the expression. Combining both terms in Eq. (6.18b), we get

$$\sum_{j=1}^{2}\left\{\mathcal{N}_v(\Pi_1^1)-\mathcal{N}_v(\Pi_1^2)\right\}\Delta\widetilde{\mathcal{L}}(\Pi_j^2)=_2\left\{\mathcal{N}_v(\Pi_1^1)-\mathcal{N}_v(\Pi_1^2)\right\}\sum_{j=1}^{2}1=_2 0. \tag{6.18c}$$

6.5 HOPF-RTP RELATION FROM HOPF-CHERN RELATION

An alternative proof of the Hopf-RTP relation derives solely from the bulk properties of the crystalline Hopf insulator and employ the Hopf-Chern relation that was originally introduced for the Hopf map by Whitehead in Ref. [168]. For simplicity, here we only focus on the case of the valence band representation being symmetry-equivalent to a basis band representation, as detailed in Sec. 6.1 and prove the relation (6.3). We structure this section as follows. We first review the original Hopf-Chern relation in Sec. 6.5.1. We then extend its applicability to $\boldsymbol{k}$-periodic tight-binding Hamiltonians in Sec. 6.5.2 and to $\boldsymbol{k}$-nonperiodic Hamiltonians in Sec. 6.5.3, then finally we apply the Hopf-Chern relation to derive the Hopf-RTP relation (6.3) in Sec. 6.5.4.

6.5.1 *Hopf-Chern relation for the Hopf map*

Let us review Whitehead's equivalent formulation [168] of the Hopf invariant of the Hopf map. It says that the Hopf invariant of a map

$$\eta:\begin{cases}S^3\to S^2,\\ \gamma(b)\mapsto b\end{cases} \tag{6.19}$$

is given by the Chern number $\mathscr{C}_\Sigma$ computed on the oriented surface Σ stretched over an inverse image ($\partial\Sigma=\gamma$) of a given base point b on the 2-sphere

$$\chi=\mathscr{C}_{\Sigma(b)},\quad \partial\Sigma(b)=\gamma(b). \tag{6.20}$$

We call this relation between the invariants the *Hopf-Chern relation*. As the boundary $\partial[\Sigma(b)]$ is mapped to the fixed base point b on the 2-sphere, it can be treated as a closed surface with a well-defined Chern number.

6.5.2 *Hopf-Chern relation for $\boldsymbol{k}$-periodic Hamiltonians*

The Hopf-Chern relation can be directly applied to compute the Hopf invariant of a two-band Hamiltonian $\tilde{h}(\boldsymbol{k})$ defined over the Brillouin torus (meaning $\tilde{h}(\boldsymbol{k})=\tilde{h}(\boldsymbol{k}+\boldsymbol{G})$ for any reciprocal lattice vector $\boldsymbol{G}$), assuming that $\tilde{h}(\boldsymbol{k})$ is in the trivial first Chern class.

To see this, consider a flattened Hamiltonian $\tilde{h}_{\text{flat}}(\boldsymbol{k})=\tilde{h}(\boldsymbol{k})/E_+(\boldsymbol{k})=\tilde{\boldsymbol{h}}_{\text{flat}}(\boldsymbol{k})\cdot\boldsymbol{\sigma}$ which defines a map $\tilde{\boldsymbol{h}}_{\text{flat}}:T^3\to S^2$ with the 3-torus given by

momenta in the first BZ and the 2-sphere given by a normalized vector of the coefficients in a Pauli matrix decomposition of a flattened Hamiltonian (as discussed in Sec. 2.1.6). Given the vanishing Chern numbers $\mathscr{C}_i = 0$ on the three BZ subtori, there exists a continuous deformation that deforms $\tilde{\boldsymbol{h}}_{\text{flat}}(\boldsymbol{k})$ on the boundary of the first BZ to a constant. From the topological perspective, this allows us to identify the whole boundary as a single point [94], turning the first BZ into a 3-sphere. Such a deformation does not modify neither the Hopf invariant, nor the Chern number computed over the surface bounded by a preimage. Therefore, the Hopf-Chern relation, that is valid for a map from a 3-sphere is also valid for a map from a 3-torus, given by the Hopf insulator Hamiltonian.

To understand how the Hopf-Chern relation (6.20) can be applied to the Hopf insulator, consider some base point on a 2-sphere $b \in S^2$ [green point in Fig. 6.1(b)]. The inverse image $\tilde{\boldsymbol{h}}_{\text{flat}}^{-1}(b) \subset T^3$ [green path in Fig. 6.1(a)] is not necessarily path-connected, but it can be decomposed into path-connected components, $\tilde{\boldsymbol{h}}_{\text{flat}}^{-1}(b) = \bigcup_i \gamma_i$, where γ_i are generically one-dimensional (possibly non-contractible) closed loops [93]. Generically, each loop γ_i can be uniquely assigned an *orientation* by the following procedure. Consider an arbitrary reference point $\boldsymbol{k}_0 \in \gamma_i$ and define a plane passing through this point and normal to γ_i at $\boldsymbol{k}_0$. Choose two orthogonal basis vectors in this plane, labeled $\hat{\boldsymbol{e}}_1$ and $\hat{\boldsymbol{e}}_2$. Then, in this plane, a circle infinitesimally close to γ_i [blue line in Fig. 6.1(a)] is parametrized by $\boldsymbol{k}(\theta) = \boldsymbol{k}_0 + \varepsilon[\hat{\boldsymbol{e}}_1 \cos(\theta) + \hat{\boldsymbol{e}}_2 \sin(\theta)]$ with $\theta \in [0, 2\pi]$ and $\varepsilon \to 0$. By considering the generic linear-order expansion of $\tilde{\boldsymbol{h}}_{\text{flat}}(\boldsymbol{k})$ around the reference point, it follows that the image of $\boldsymbol{k}(\theta)$ under the Hamiltonian map $\tilde{\boldsymbol{h}}_{\text{flat}}$ is necessarily a closed loop that winds around the base point b [blue line in Fig. 6.1(b)]. The orientation of γ_i at $\boldsymbol{k}_0$ is defined as $\boldsymbol{\tau}(\boldsymbol{k}_0) = +(-)\hat{\boldsymbol{e}}_1 \times \hat{\boldsymbol{e}}_2$ for a clockwise (counterclockwise) winding of $\tilde{\boldsymbol{h}}_{\text{flat}}[\boldsymbol{k}(\theta)]$. Note that this definition does not depend on the choice of the basis vectors $\hat{\boldsymbol{e}}_1$ and $\hat{\boldsymbol{e}}_2$. Indeed, let us assume that we have picked another pair of basis vectors $\hat{\boldsymbol{e}}_1' = \hat{\boldsymbol{e}}_1$ and $\hat{\boldsymbol{e}}_2' = -\hat{\boldsymbol{e}}_2$. Then for the same θ parametrization, momentum $\boldsymbol{k}(\theta)$ will rotate in the opposite direction, and therefore the image $\tilde{\boldsymbol{h}}_{\text{flat}}[\boldsymbol{k}(\theta)]$ will also rotate in the opposite direction. At the same time the cross product $\hat{\boldsymbol{e}}_1' \times \hat{\boldsymbol{e}}_2' = -\hat{\boldsymbol{e}}_1 \times \hat{\boldsymbol{e}}_2$. Overall, the value of the preimage orientation will not change. In Fig. 6.1(a) the orientations of γ_i are shown by green arrows.

Let us make three remarks on the presented definition of the orientation of the inverse images γ_i:

(*a*) The orientation cannot discontinuously flip along γ_i, as that would require $\tilde{\boldsymbol{h}}_{\text{flat}}[\boldsymbol{k}(\theta)]$ to pass through b while adjusting the reference point $\boldsymbol{k}_0$. However, this cannot happen because the circle $\boldsymbol{k}(\theta)$ never crosses γ_i (the inverse image of b).

(*b*) Recall that a solid angle enclosed by a path on the Bloch sphere is equal to twice the Berry phase picked by the corresponding state [70]. In the present situation, the clockwise (counterclockwise) winding of $\tilde{\boldsymbol{h}}_{\text{flat}}[\boldsymbol{k}(\theta)]$ implies a negative (positive) Berry phase on path $\boldsymbol{k}(\theta)$. Therefore, the orientation $\boldsymbol{\tau}$ indicates the direction in which the component of Berry curvature $\boldsymbol{\mathcal{F}}$ parallel with γ_i is negative.

(*c*) Finally, while the connected component γ_i might form a non-contractible loop in the BZ along one momentum direction, the number of lines that are oriented along this $\boldsymbol{k}$-direction minus the number of lines oriented in the opposite direction is equal to the Chern number of the corresponding

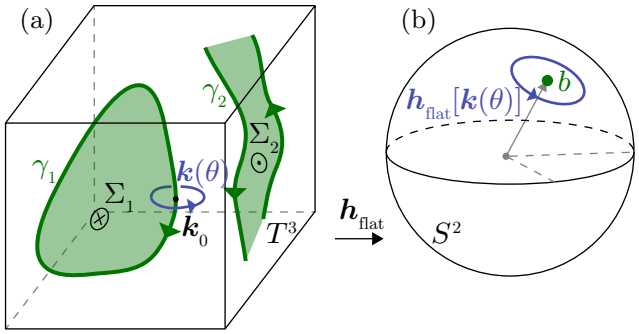

Figure 6.1: Characterizing a continuous map (the Hamiltonian) $\boldsymbol{h}_{\text{flat}}$ from the (Brillouin zone) torus T^3 to the (Bloch) sphere S^2. For a chosen base point $b \in S^2$ [green dot in (b)], the inverse image $\boldsymbol{h}_{\text{flat}}^{-1}(b)$ is a collection of closed loops γ_i [green lines in (a)] with orientation $\boldsymbol{\tau}$ defined by the arrows. The orientation is defined by considering an infinitesimal circle $\boldsymbol{k}(\theta)$ around a reference point $\boldsymbol{k}_0 \in \gamma_i$, and by checking whether the image $\boldsymbol{h}_{\text{flat}}[\boldsymbol{k}(\theta)]$ winds (counter)clockwise around b [blue line in (b)]. The paths γ_i can be inscribed a (Seifert) surface Σ_i [light green sheet in (a)] with an orientation [$\odot$ vs. $\otimes$ in (a)] inherited from the orientation of the corresponding boundary loop via the right-hand rule.

perpendicular sheet. Since we assume Hopf insulators with $C_i = 0$, each non-contractible path γ_i that is oriented along one of $\boldsymbol{k}$-axes can be paired with another path(s) oriented in the opposite direction, as illustrated in Fig. 6.1(a). This rule is rigorously proved in Dets. 6.3.

Having fixed the orientation of γ_i, we can define an oriented surface Σ_i (the *Seifert surface*) that has the oriented loop γ_i as a boundary [light green area in Fig. 6.1(a)]. The surface Σ_i always exists for contractible paths [169], while for non-contractible paths it exists if one considers a collections of several paths with opposite orientation [cf. remark (*c*) above]. The orientation of the Seifert surface Σ_i is inherited from the orientation $\boldsymbol{\tau}(\boldsymbol{k}_0)$ at $\boldsymbol{k}_0 \in \gamma_i$ by applying the right-hand rule near the boundary. Conveniently, for the *union* of the inscribed surfaces, $\bigcup_i \Sigma_i \equiv \Sigma(b)$, the boundary fulfills $\partial[\Sigma(b)] = \tilde{\boldsymbol{h}}_{\text{flat}}^{-1}(b)$ with matching orientation. The orientation of the surface fixes the overall sign of the Chern number in Eq. (6.20).

There is one additional subtlety in Hopf-Chern relation when one accounts for the crystallographic point group of a $\boldsymbol{k}$-periodic Hamiltonian. For generic Hamiltonians without point-group symmetry, the preimage lines typically avoid crossing each other, as illustrated in Fig. 6.1(a). In other words, Hamiltonians where preimage lines cross or overlap require fine-tuning of Hamiltonian parameters. On the other hand, with point-group symmetry, it is possible for two or more preimage lines to cross and even overlap/merge completely, without fine-tuning of Hamiltonian parameters. In such 'degenerate' cases, multiple Seifert surfaces become path-connected. The Hopf-Chern relation still holds by summing Chern numbers over all Seifert surfaces. To distinguish a completely-degenerate preimage line from a nondegenerate one, we characterize each line by a positive-integer-valued *multiplicity*, which is given by the (unoriented) winding number of the map $\tilde{\boldsymbol{h}}_{\text{flat}}[\boldsymbol{k}(\theta)]$. Explicit examples of nontrivial multiplicity in rotation-symmetric Hamiltonians will be discussed in Sec. 6.5.4.

Details 6.3 We prove the remark (*c*) for preimages winding along k_z direction of the torus. The proof is the same for winding in other two directions. By assumption, the first Chern

number vanishes on the T^2 subtorus of the BZ, parametrized by (k_x, k_y); k_z is defined by the right-hand rule. The Chern number is given by the following integral of the Berry curvature: $\mathscr{C} = (2\pi)^{-1} \int_{T^2} \boldsymbol{\mathcal{F}}_z dk_x dk_y$. Recall that the first Chern number $\mathscr{C}$ of a pseudospinor Hamiltonian defined on T^2 tells how many times this manifold wraps around the Bloch sphere under the Hamiltonian map $h : T^2 \to S^2$ [cf. Sec. 2.1.3.1]. If $\mathscr{C} = 0$, then any point x_0 on the Bloch sphere must be visited an even number of times as one sweeps through T^2, i.e., the preimage of x_0 consists of an even number of points $\{\boldsymbol{k}_1, \ldots, \boldsymbol{k}_{2N}\}$ in T^2. Let us define $d_{x_0} \in S^2$ as an infinitesimal outward (i.e., positively) oriented disk centered at x_0, and $\delta\Omega_{x_0} > 0$ as the solid angle subtended by d_{x_0}. The preimage of d_{x_0} comprises $2N$ disks $\{D_1, \ldots, D_{2N}\}$ encircling $\{\boldsymbol{k}_1, \ldots, \boldsymbol{k}_{2N}\}$, respectively, with orientations inherited from T^2. We now assign each D_j an index, $\mathrm{ind}[D_j] = \pm 1$, by checking whether $h(\partial D_j)$ (with the orientation of the boundary determined by right-hand rule) is parallel or antiparallel to the oriented boundary $(\partial d_{x_0}) \subset S^2$ [i.e., whether it winds (counter-)clockwise around x_0]. Applying the solid-angle interpretation of the Berry phase for pseudospinor Hamiltonians [70], the Berry curvature integrated over the oriented disk D_j equals $\mathrm{ind}[D_j]\delta\Omega_{x_0}/2$. (This equality also manifests that $-\mathrm{ind}[D_j] = -\,\mathrm{sgn}[\mathcal{F}_z(\boldsymbol{k}_j)]$, which is the preimage orientation as elaborated in the remark (*b*) above.) Because d_{x_0} is covered by the map $(h : T^2 \to S^2)$ a number of times equal to the Chern number (assumed zero), the net Berry curvature integrated over $\{D_1, \ldots, D_{2N}\}$ must vanish, implying that N of the disks $\{D_1, \ldots, D_{2N}\}$ have index opposite to the remaining N disks.

6.5.3 *Hopf-Chern relation for $\boldsymbol{k}$-nonperiodic Hamiltonians*

So far we showed that the Hopf-Chern relation can be used to compute the Hopf invariant of a $\boldsymbol{k}$-periodic Hamiltonian $\tilde{h}$. Here we extend our discussion to $\boldsymbol{k}$-nonperiodic Hamiltonians $h(\boldsymbol{k})$ which relate to $\tilde{h}(\boldsymbol{k})$

$$\tilde{h}(\boldsymbol{k}) = V(\boldsymbol{k}) h(\boldsymbol{k}) V(\boldsymbol{k})^{-1} \tag{6.21}$$

by conjugation with a diagonal unitary matrix with diagonal elements: $V_{\alpha\beta}(\boldsymbol{k}) = e^{i\boldsymbol{k}\boldsymbol{r}_\alpha}\delta_{\alpha\beta}$ encoding the spatial positioning of basis orbitals within each primitive unit cell [cf. Sec. 2.1.1 for more details on the two formalisms].

In Sec. 2.1.6.2 we demonstrated that a generalization of the Hopf invariant exists for the $\boldsymbol{k}$-nonperiodic Hamiltonian, and can be computed by integrating the Chern-Simons three-form of the Berry gauge field [cf. Eq. (4.8)]. Here we show that it can equivalently be computed via a restricted form of the Hopf-Chern relation, where we consider only the preimages of the poles of the Bloch 2-sphere.

To show this, consider a continuous interpolation between the periodic and non-periodic Hamiltonians (that was already introduced in Eq. (2.50)) $h_t(\boldsymbol{k}) = V(t\boldsymbol{k})^{-1}\tilde{h}(\boldsymbol{k})V(t\boldsymbol{k})$ which at $t = 0$ gives $h_0(\boldsymbol{k}) = \tilde{h}(\boldsymbol{k})$ and at $t = 1$ gives $h_1(\boldsymbol{k}) = h(\boldsymbol{k})$. Translational symmetry and the energy gap persist throughout this interpolation.

If $h_t(\boldsymbol{k})$ were diagonal at a particular $\boldsymbol{k}$ and t, it would remain diagonal at that $\boldsymbol{k}$ and for any $t \in [0, 1]$, since the matrix $V(t\boldsymbol{k})$ is also diagonal. Conversely, if $h_t(\boldsymbol{k})$ had off-diagonal elements at a particular $\boldsymbol{k}$ and t, its off-diagonal elements can never vanish at that $\boldsymbol{k}$ and for any t. (The reason is that the off-diagonal component of the Hamiltonian is of the form $d_x\sigma_x + d_y\sigma_y$ with (d_x, d_y) a real two-vector, and conjugation by $V = e^{i\theta\sigma_3/2}$ merely rotates the two-vector by the angle θ.) Restriction of the base point in the Hopf-Chern relation to the north and south pole, ensures that the corresponding Hamiltonian is diagonal. Thus the inverse image of either pole remains the same for all t. This and the fact that the Berry curvature is a periodic quantity in any convention, $\boldsymbol{\mathcal{F}}(\boldsymbol{k} + \boldsymbol{G}) = \boldsymbol{\mathcal{F}}(\boldsymbol{k})$, leads to a well defined and t-independent Chern number computed on the corresponding Seifert surface, meaning that $\tilde{C}_{\Sigma(b)} = C_{\Sigma(b)}$ when b is the north or the south pole of the 2-sphere. From this we conclude that the Hopf-Chern relation can be applied to compute the Hopf invariant in both conventions.

6.5.4 *Proving the Hopf-RTP relation*

6.5.4.1 *Symmetry defines preimage lines of the south pole*

Now let us apply the Hopf-Chern relation to a Hopf insulator with rotation symmetry. We assume that the model has space group symmetry Pn and the valence (conduction) band is symmetry-equivalent to a basis band representation induced from a basis orbital φ_1 (φ_2) centered at position $\boldsymbol{r}_1$ ($\boldsymbol{r}_2$) with on-site angular momentum $\mathcal{L}_1$ ($\mathcal{L}_2$). In this discussion we assume that the valence band representation is symmetry-equivalent to a basis band representation. On the one hand, lifting this assumption complicates the discussion without bringing further insights. On the other hand, the Hopf-RTP relation in the case of valence band representation non-symmetry-equivalent to a basis band representation was already proven using the boundary properties in Sec. 6.4.3.

Our choice of the valence (conduction) band representation determines the itinerant angular momentum of the valence (conduction) band at a C_m-invariant momentum Π to be $\widetilde{\mathcal{L}}_{v(c)}(\Pi) = \mathcal{L}_{1(2)} + \frac{m}{2\pi}\left(\boldsymbol{r}_{1(2),\perp}\cdot\boldsymbol{G}_\Pi\right) \mod m$, where $\boldsymbol{G}_\Pi = C_m\Pi - \Pi$. Then the Hamiltonian is diagonal at the rotation-invariant lines γ_Π at which the mutually-disjoint condition is fulfilled $\Delta\widetilde{\mathcal{L}}(\Pi) = \widetilde{\mathcal{L}}_c(\Pi) - \widetilde{\mathcal{L}}_v(\Pi) \pmod m \neq 0$. For the Hamiltonian with flattened spectrum this means that it is $h_{\text{flat}}(\Pi, k_z) = \pm\sigma_z$ which corresponds to a mapping to a north or south pole of a 2-sphere $\boldsymbol{h}_{\text{flat}}(\Pi, k_z) = (0, 0, \pm 1)$. The fact that the valence band representation is symmetry-equivalent to a basis band representation guarantees that all γ_Π lines with fulfilled mutually-disjoint condition are mapped to the same point on the 2-sphere, despite the fact that $\Delta\widetilde{\mathcal{L}}(\Pi)$ need not be identical for all Π. This one image point is the south pole $h_{\text{flat}}(\Pi, k_z) = -\sigma_z$ for our choice of valence band representation. From this we conclude that if we choose the south pole (S) to be the base point for the Hopf-Chern relation, all lines γ_Π with $\Delta\widetilde{\mathcal{L}}(\Pi) \neq 0$ belong to the inverse image of S. In Fig. 6.2(a) we illustrate this for a P4 symmetric model with basis orbitals having on-site angular momenta $\mathcal{L}_1 = 0$, $\mathcal{L}_2 = 0$ positioned at $\boldsymbol{r}_{1,\perp} = (0, 0)$, $\boldsymbol{r}_{2,\perp} = (1/2, 1/2)$. The corresponding itinerant angular momenta differences are $\Delta\widetilde{\mathcal{L}}(\Gamma) = 0$, $\Delta\widetilde{\mathcal{L}}(\mathrm{M}) = 2$, $\Delta\widetilde{\mathcal{L}}(\mathrm{X}) = 1$, which forces the lines γ_X and γ_M to map to the south pole.

6.5.4.2 *Orientation and multiplicity of γ_Π preimages*

Before discussing other possible preimage lines of the south pole, let us determine the orientation of the γ_Π lines. According to the comment (*b*) of Sec. 6.5.2, this can be done by computing the tangential-to-γ_Π component of the Berry-curvature vector. As all γ_Π lines are vertical, their orientation is $\boldsymbol{\tau}(\Pi) = -\operatorname{sgn}(\mathcal{F}_z(\Pi, k_z))\hat{\boldsymbol{e}}_z$ where $\hat{\boldsymbol{e}}_z$ denotes the unit vector in the z direction of momentum space and the Berry curvature can be computed at any k_z momentum component. In the presence of rotation symmetry, as opposed to the generic case, the rotation-invariant preimage lines are characterized not only by orientation but also by a multiplicity introduced in Sec. 6.5.2. The latter is defined as a number of times an image of a small loop around the rotation-invariant line winds around the south pole on the 2-sphere. Consider a $\boldsymbol{k}$-loop around γ_Π line parametrized as $\boldsymbol{k}(\theta) = (\Pi, k_z) + \varepsilon[\hat{\boldsymbol{e}}_1\cos(\theta) + \hat{\boldsymbol{e}}_2\sin(\theta)]$, $\theta \in [0, 2\pi]$; if the Hamiltonian in this parametrization obeys the condition $h(\theta + 2\pi/\mu) = h(\theta)$ for the largest possible integer μ, we conclude that the image of a $\boldsymbol{k}$-loop winds around the south pole μ times and the multiplicity of the inverse image is $\mu(\Pi)$. The γ_Π line can be viewed

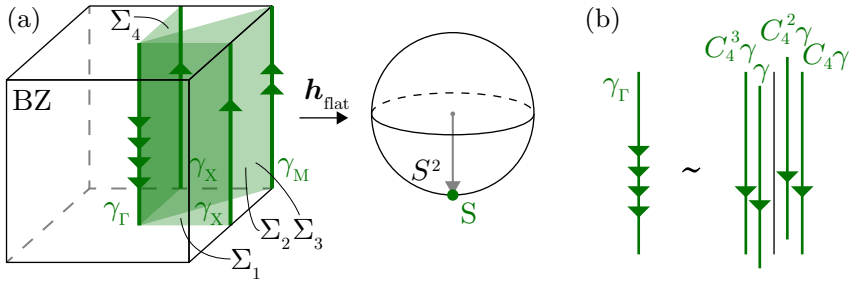

Figure 6.2: (a) Illustration of a Hopf-Chern relation in the case of a model with P4 space group and itinerant angular momenta differences $\Delta\widetilde{\mathcal{L}}(\Gamma) = 0$, $\Delta\widetilde{\mathcal{L}}(\text{M}) = 2$, $\Delta\widetilde{\mathcal{L}}(\text{X}) = 1$. The base point is chosen to be the south pole S $\sim -\sigma_z$. The symmetry forces the lines γ_{X} and γ_{M} (denoted with green) to be mapped onto S. In addition there can be other non-contractible preimages of S that appear in 4 C_4 related copies. In the presented example these four lines are degenerate along γ_Γ (shown in green). The green arrows show possible orientation of the lines that is compatible with symmetries and the no-net-winding rule. Multiple arrows show the multiplicity of the line. The oriented preimage lines are paired up to bound 4 Seifert surfaces Σ_j, $j = 1, 2, 3, 4$ (denoted by green shades). The lines with multiplicity μ form a boundary of μ distinct Seifert surfaces. (b) The four degenerate preimage lines at γ_Γ are not fixed to the rotation-invariant line by symmetry and can be split into 4 C_4-related copies by a small perturbation of the Hamiltonian.

as a degenerate set of $\mu(\Pi)$ lines, with each line having unit multiplicity and carrying the same orientation $\boldsymbol{\tau}(\Pi)$. The degeneracy is protected by the rotation symmetry.

Let us relate, as best as we can, the orientations and multiplicities of the preimage lines γ_Π to the itinerant angular-momentum difference at Π. For this purpose, we consider a Taylor expansion of the Hamiltonian around $\boldsymbol{k}_0 \in \gamma_\Pi$ up to the lowest order in $\boldsymbol{\kappa} = \boldsymbol{k} - \boldsymbol{k}_0$ in the presence of rotational symmetry. As shown in Appendix A.1.4, the expanded Hamiltonian must fulfill

$$\widetilde{R}_{C_m}(\Pi) h^{\boldsymbol{k}\cdot\boldsymbol{p}}(\boldsymbol{\kappa}) \widetilde{R}^{-1}_{C_m}(\Pi) = h^{\boldsymbol{k}\cdot\boldsymbol{p}}(C_m\boldsymbol{\kappa}), \tag{6.22}$$

with the itinerant rotation matrix $\widetilde{R}_{C_m}(\Pi)$ given in Eq. (A.31). For our choice of valence (conduction) band representation we can replace $\widetilde{\mathcal{L}}_2(\Pi) - \widetilde{\mathcal{L}}_1(\Pi)$ by $\Delta\widetilde{\mathcal{L}}(\Pi) = \widetilde{\mathcal{L}}_c(\Pi) - \widetilde{\mathcal{L}}_v(\Pi) \pmod m$ in the expression for $\widetilde{R}_{C_m}(\Pi)$. For all possible rotation symmetries C_m and differences in itinerant angular momenta $\Delta\widetilde{\mathcal{L}}(\Pi)$ the symmetry-allowed form of a flatted Hamiltonian $h_{\text{flat}}(\boldsymbol{\kappa})$ is presented in the third column of Table 6.1 with introduced notations $\kappa_\pm = \kappa_x \pm i\kappa_y$ and $\sigma_\pm = \sigma_x \pm i\sigma_y$. The corresponding vector of Hamiltonian coefficients is normalized as the corrections to the vector $\boldsymbol{h}_{\text{flat}}(\boldsymbol{\kappa} = 0) = (0, 0, -1)$ are linear in $\boldsymbol{\kappa}$ and therefore can be neglected in the norm $|\boldsymbol{h}_{\text{flat}}(\boldsymbol{\kappa})| = 1 + O(\boldsymbol{\kappa})$. The z-component of the Berry curvature in a 2-band Hamiltonian can be computed as

$$\mathcal{F}_z = \frac{1}{2}\epsilon_{abc} h_{\text{flat},a}\, \partial_x h_{\text{flat},b}\, \partial_y h_{\text{flat},c}, \tag{6.23}$$

which can be simplified to

$$\mathcal{F}_z = -2h_{\text{flat},z}(\partial_+ h_{\text{flat},+}\, \partial_- h_{\text{flat},-} - \partial_+ h_{\text{flat},-}\, \partial_- h_{\text{flat},+}), \tag{6.24}$$

as the symmetry constraints the $h_{\text{flat},z}$ component to not depend on κ_x, κ_y; the introduced notations are $\partial_\pm = (\partial_x \mp i\partial_y)/2$ and $h_{\text{flat},\pm} = (h_{\text{flat},x} \mp$

Table 6.1: For all differences between itinerant angular momenta of conduction and valence bands at a given reduced momentum Π $\Delta\widetilde{\mathcal{L}}(\Pi) = \widetilde{\mathcal{L}}_c(\Pi) - \widetilde{\mathcal{L}}_v(\Pi) \pmod m$, we present a form of flattened Hamiltonian in the vicinity of $\boldsymbol{k}_0$ point allowed by the symmetry. For this Hamiltonian we compute the $\mathcal{F}_z$ component of the Berry curvature, and deduce the resulting orientation $\boldsymbol{\tau} = \tau_z \hat{\boldsymbol{e}}_z$ and multiplicity μ of a corresponding inverse image γ_Π. In some cases (denoted with question mark) the orientation can not be determined solely from the itinerant angular momentum, however, as we will see, this does not impair the proof of the Hopf-RTP relation.

m	$\Delta\widetilde{\mathcal{L}}$	$h_{\text{flat}}(\boldsymbol{\kappa}) + \sigma_z$	$\mathcal{F}_z/2$	τ_z	μ
2	1	$(a\kappa_+ + b\kappa_-)\sigma_+ + h.c.$	$\lvert a\rvert^2 - \lvert b\rvert^2$	?	1
3	$\pm 1 \mod 3$	$a\kappa_\mp\sigma_+ + h.c.$	$\mp\lvert a\rvert^2$	± 1	1
4	$\pm 1 \mod 4$	$a\kappa_\mp\sigma_+ + h.c.$	$\mp\lvert a\rvert^2$	± 1	1
	2	$(a\kappa_+^2 + b\kappa_-^2)\sigma_+ + h.c.$	$4\left[\lvert a\kappa_+\rvert^2 - \lvert b\kappa_+\rvert^2\right]$	?	2
6	$\pm 1 \mod 6$	$a\kappa_\mp\sigma_+ + h.c.$	$\mp\lvert a\rvert^2$	± 1	1
	$\pm 2 \mod 6$	$a\kappa_\mp^2\sigma_+ + h.c.$	$\mp 4\lvert a\kappa_+\rvert^2$	± 1	2
	3	$(a\kappa_+^3 + b\kappa_-^3)\sigma_+ + h.c.$	$9\left[\lvert a\kappa_+^2\rvert^2 - \lvert b\kappa_+^2\rvert^2\right]$	?	3

$ih_{\text{flat},y})/2$. Analyzing the results of Table 6.1 we see that whenever $\Delta\widetilde{\mathcal{L}} \neq m/2$ a coefficient in front of σ_+ depends only on one of $\kappa_\pm$ and the sign of $\mathcal{F}_z$ is determined by symmetry representation alone, it is presented in the second to last column in Table 6.1. At the same time the power of a coefficient in front of σ_+ gives the multiplicity of the preimage line. Assume $h_{\text{flat},0} = -\sigma_z + (a\kappa_+^\mu + b\kappa_-^\mu)\sigma_+ + h.c.$ The loop around $\boldsymbol{k}_0$ can be parametrized with $\kappa_\pm = \varepsilon e^{\pm i\theta}$, $\theta \in [0, 2\pi]$. We see that in this parametrization $h_{\text{flat},0}(\theta + 2\pi/\mu) = h_{\text{flat},0}(\theta)$ and hence the multiplicity of γ_Π line is μ, which is listed in the last column of Table 6.1. For the example case (outlined in the previous subsection) one choice of preimage line orientations is shown in Fig. 6.2(b) with green arrows, while the number of arrows denote the multiplicities of the lines.

6.5.4.3 *Other non-contractible preimage lines γ_i*

Importantly, the BZ can contain other than γ_Π lines that are preimages of the south pole. At this stage of the proof we focus only on the preimages that form non-contractible loops along the k_z direction in the BZ and discuss how other preimages affect the result later in this section. In addition to γ_Π lines with fulfilled mutually-disjoint condition, the preimage of the south pole can contain two types of non-contractible lines: (*i*) lines that appear at generic positions in the BZ and (*ii*) lines that appear at rotation-invariant momenta $\gamma_{\Pi'}$ with violated mutually-disjoint condition, $\Delta\widetilde{\mathcal{L}}(\Pi') = 0$.

For both types of preimage lines we show, that the C_n rotation symmetry forces them to appear in n rotation-related copies. (*i*) For the preimage lines at generic positions, this follows from the symmetry condition on the Hamiltonian $R_{C_n} h(\boldsymbol{k}) R_{C_n}^{-1} = h(C_n\boldsymbol{k})$, which equates the Hamiltonians at $\boldsymbol{k}$ and at $C_n\boldsymbol{k}$ when the Hamiltonian is diagonal. (*ii*) If a preimage line happened to coincide with a C_m-invariant $\gamma_{\Pi'}$ line with violated mutually-disjoint condition, first there will be a n/m-multiplet of preimage lines at

all C_n-related $\gamma_{\Pi'}$ lines. Second, without the mutually-disjoint condition, the south pole preimage is not forced to lie at a C_m-invariant line by symmetry. Therefore, a small perturbation of the Hamiltonian can shift this preimage line away from the rotation-invariant line. But as we already argued in the case (*i*), the preimage lines at generic positions must appear in n C_n-related copies. This means that the initial preimage line, at each C_m-invariant line of a n/m-multiplet, forms m degenerate copies [cf. Fig. 6.2(b)].

We denote these additional preimage lines as γ_i and all n copies as $C_n^j\gamma_i$, $j = 0, \dots n-1$. We remark, that the preimages of the north pole ($h_{\text{flat}} = \sigma_z$) also appear as n rotation-related copies for the same reason as for the south pole; this property will be used at the end of this section.

6.5.4.4 *Orientation of non-contractible preimage lines*

Having specified all non-contractible preimages of S, we proceed by defining their orientations. First, let us introduce a scalar orientation along k_z-axis as

$$\tau_z(\boldsymbol{k}_0) = \operatorname{sgn}(\boldsymbol{\tau}(\boldsymbol{k}_0) \cdot \hat{\boldsymbol{e}}_z) \in \{-1, 1\}, \tag{6.25}$$

where $\boldsymbol{k}_0$ is a point on a considered line, and for simplicity we assume that the line crosses each plane at fixed k_z only once. Then τ_z does not depend on the specific point $\boldsymbol{k}_0$. The definition can be straightforwardly generalized if this assumption is relaxed. We proceed to define the k_z-orientations of non-contractible lines.

In addition to the symmetry constraints defined in Sec. 6.5.4.2, the orientations of the non-contractible lines are restricted by two more rules:

(*i*) Any two inverse images (γ_1 and $\gamma_2 = C_n\gamma_1$) that are related by rotation have the same k_z-orientation $\tau_z(\gamma_1) = \tau_z(\gamma_2)$, because the Berry curvature transforms as a vector under rotation.

(*ii*) As discussed in the comment (*c*) in Sec. 6.5.1 the number of upwards oriented lines must be equal to the number of downwards oriented lines, meaning that

$$\sum_{\gamma,\ \text{non-contractible along } \hat{\boldsymbol{e}}_z} \mu(\gamma)\tau_z(\gamma) = 0. \tag{6.26}$$

Crucially, each non-contractible preimage contributes to the sum number of times, equal to its multiplicity. We refer to this constraint as the *balanced orientation rule*.

For a set of all non-contractible preimage lines, γ_Π and $C_n^j\gamma_i$, the symmetry conditions and the balanced orientation rule restrict possible orientations to a limited number of options. For several concrete examples of the preimage orientations, see Table 6.2 and Fig. 6.2(a). Although in some cases, the outlined conditions are not enough to uniquely determine the orientations from the symmetry representations alone, we will see that the obtained information about orientations is enough to prove the Hopf-RTP relation.

6.5.4.5 *Seifert surface and Hopf-Chern relation for $h_{\text{flat}} = -\sigma_z$*

After determining the orientations and multiplicities of the non-contractible preimage lines, we proceed by defining the Seifert surface stretched over these lines. For this we arbitrarily pair up the preimage lines such that each pair contain upwards $\gamma_{\uparrow i}$ and downwards $\gamma_{\downarrow i}$ oriented lines. This is possible

Table 6.2: Possible preimage orientations for some crystalline Hopf models given by the space group and the symmetry $\Delta\mathcal{L} = \mathcal{L}_2 - \mathcal{L}_1$ and spatial positions $\Delta\boldsymbol{r}_\perp = \boldsymbol{r}_{2,\perp} - \boldsymbol{r}_{1,\perp}$ of the basis orbitals. Arrows $\uparrow$ and $\downarrow$ denote positive and negative orientations along k_z axis and the number of arrows [$\uparrow\uparrow$] denote multiplicity. Value in brackets [(2)] specifies how many rotation-related lines of this type constitutes the south pole preimage.

SG	$\Delta\mathcal{L}$	$\Delta\boldsymbol{r}_\perp$	$\Delta\widetilde{\mathcal{L}}(\Pi)$	orientations from symmetry	possible final orientations
P4	1	$(0,0)$	$\Delta\widetilde{\mathcal{L}}(\Gamma) = 1$ $\Delta\widetilde{\mathcal{L}}(\mathrm{X}) = 1$ $\Delta\widetilde{\mathcal{L}}(\mathrm{M}) = 1$	$\Gamma\uparrow$, $\mathrm{M}\uparrow$	$\Gamma\uparrow$, $\mathrm{M}\uparrow$, $(2)\mathrm{X}\downarrow$ or $\Gamma\uparrow$, $\mathrm{M}\uparrow$, $(2)\mathrm{X}\uparrow$, $(4)\gamma_1\downarrow$
P4	0	$(\frac{1}{2},\frac{1}{2})$	$\Delta\widetilde{\mathcal{L}}(\Gamma) = 0$ $\Delta\widetilde{\mathcal{L}}(\mathrm{X}) = 1$ $\Delta\widetilde{\mathcal{L}}(\mathrm{M}) = 2$		$(2)\mathrm{X}\uparrow$, $\mathrm{M}\downarrow\downarrow$ or $(2)\mathrm{X}\uparrow$, $\mathrm{M}\uparrow\uparrow$, $(4)\gamma_1\downarrow$
P4	1	$(\frac{1}{2},\frac{1}{2})$	$\Delta\widetilde{\mathcal{L}}(\Gamma) = 1$ $\Delta\widetilde{\mathcal{L}}(\mathrm{X}) = 0$ $\Delta\widetilde{\mathcal{L}}(\mathrm{M}) = 3$	$\Gamma\uparrow$, $\mathrm{M}\downarrow$	$\Gamma\uparrow$, $\mathrm{M}\downarrow$
P3	1	$(0,0)$	$\Delta\widetilde{\mathcal{L}}(\Gamma) = 1$ $\Delta\widetilde{\mathcal{L}}(\mathrm{X}) = 1$ $\Delta\widetilde{\mathcal{L}}(\mathrm{M}) = 1$	$\Gamma\uparrow$, $\mathrm{K}\uparrow$, $\mathrm{K}'\uparrow$	$\Gamma\uparrow$, $\mathrm{K}\uparrow$, $\mathrm{K}'\uparrow$, $(3)\gamma_1\downarrow$

due to validity of the balanced orientation rule. Note, that a preimage line with multiplicity μ forms a boundary of μ distinct Seifert surfaces. Denoting each distinct Seifert surface bounded by $\gamma_{\downarrow i}$ and $\gamma_{\uparrow i}$ as Σ_i, we express the Hopf invariant as a sum of Chern numbers C_{Σ_i} over all Seifert surfaces:

$$\chi = \sum_i C_{\Sigma_i}. \tag{6.27}$$

(A nontrivial Chern number over a Seifert surface is consistent with the triviality of the first Chern class, meaning the Chern number on any 2D sub-torus of the Brillouin zone vanishes.) The Chern number of each Seifert surface can be computed as the difference in the Berry-Zak phases computed along the paths

$$C_{\Sigma_i} = (\mathscr{Z}_{\gamma_{\uparrow i}} - \mathscr{Z}_{\gamma_{\downarrow i}})/2\pi. \tag{6.28}$$

Though $\gamma_{\uparrow i}$ and $\gamma_{\downarrow i}$ have opposite orientations, the corresponding two Zak phases are computed over paths of the same orientation, hence the minus sign in the above equation. By itself, $\mathscr{Z}_{\gamma_\uparrow}$ is a phase defined modulo 2π; however, given any global, differential gauge whose existence is guaranteed by the trivial first Chern class, the difference $(\mathscr{Z}_{\gamma_\uparrow} - \mathscr{Z}_{\gamma_\downarrow})$ is uniquely defined. Plugging Eq. (6.28) into Eq. (6.27) and taking into account the orientation along k_z-axis τ_z of each line γ we get

$$\chi = \sum_i \sum_{\gamma \in \{\gamma_{\uparrow i}, \gamma_{\downarrow i}\}} \tau_z(\gamma)\mathscr{Z}_\gamma/2\pi. \tag{6.29}$$

From this sum, we isolate the contribution from rotation-invariant lines γ_Π with fulfilled mutually-disjoint condition $\Delta\widetilde{\mathcal{L}}(\Pi) \neq 0$. For each γ_Π, we replace $\mathscr{Z}/2\pi \to \mathscr{P}$ to remind ourselves that the normalized Zak phase can be interpreted as the dimensionless polarization for a one-k-parameter Hamiltonian (4.9):

$$\chi = \sum_{\gamma_\Pi \in \boldsymbol{h}_{\text{flat}}^{-1}(\mathrm{S}); \Delta\widetilde{\mathcal{L}}(\Pi)\neq 0} \mu(\Pi)\tau_z(\Pi)\mathscr{P}(\Pi) + \sum_{\text{all other } \gamma \in \boldsymbol{h}_{\text{flat}}^{-1}(\mathrm{S})} \tau_z(\gamma)\mathscr{Z}_\gamma/2\pi. \tag{6.30}$$

The meaning of $\sum_{\gamma_\Pi}$ is to sum over all components of $\boldsymbol{h}_{\text{flat}}^{-1}(\mathrm{S})$ with the restriction: $\Delta\widetilde{\mathcal{L}}(\Pi) \neq 0$; note each term appearing once in $\sum_{\gamma_\Pi \in \boldsymbol{h}_{\text{flat}}^{-1}(\mathrm{S})}$ appears $\mu(\Pi)$ times in the double summation of Eq. (6.29). The second term in Eq. (6.30) sums over all other preimage lines, not already included in the first sum. Because γ is not necessarily vertical, it does not necessarily have the interpretation of a polarization. However, since along these lines the Hamiltonian is diagonal, the valence band does not hybridize with the conduction band and hence, $\mathscr{Z}_\gamma/2\pi =_1 z_1$. Using Eq. (6.26), we can subtract zero which is the sum over all k_z-orientations (weighted with multiplicities) of the preimage lines, multiplied by the value of z_1 and get

$$\begin{aligned}\chi = &\sum_{\gamma_\Pi \in \boldsymbol{h}_{\text{flat}}^{-1}(\mathrm{S}); \Delta\widetilde{\mathcal{L}}(\Pi)\neq 0} \mu(\Pi)\tau_z(\Pi)(\mathscr{P}(\Pi) - z_1) \\ &+ \sum_{\text{all other } \gamma \in \boldsymbol{h}_{\text{flat}}^{-1}(\mathrm{S})} \tau_z(\gamma)(\mathscr{Z}_\gamma/2\pi - z_1).\end{aligned} \tag{6.31}$$

The sum in the second row vanishes modulo n, because the preimage lines γ, that do not coincide with rotation-invariant lines with mutually-disjoint condition, necessarily come in n copies with identical k_z-orientations. n copies of an integer-valued expression $(\mathscr{Z}_\gamma/2\pi - z_1) \in \mathbb{Z}$ sum up to a multiple of n. Let us further reorganize the first term in the sum by substituting the

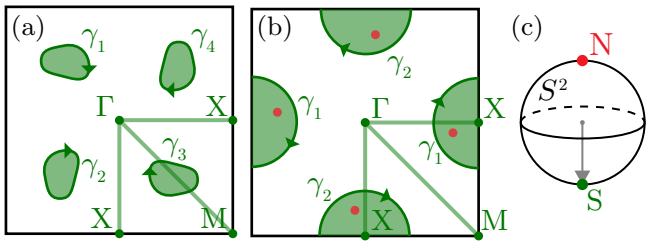

Figure 6.3: Illustration of contractible south pole preimages in a 2D horizontal cut of the BZ. (a) Closed loops at generic positions that form 4 C_4-related copies. Each of them carries an integer Chern number, therefore their contribution to the Hopf invariant is $4\mathbb{Z}$. (b) Closed loops that encircle a C_2-invariant line γ_X form 2 C_4-related copies γ_1 and γ_2. The linking number of these preimage lines with the preimages of the north pole is forced to be a multiple of 4 by rotation symmetry. (c) A 2-sphere with the north and south pole, whose preimage lines are shown in panels (a) and (b).

product of orientation and multiplicity of the rotation-invariant preimage lines $\mu(\Pi)\tau_z(\Pi)$ by the itinerant angular momentum difference $\Delta\widetilde{\mathcal{L}}(\Pi)$.

$$\chi =_n \sum_{\gamma_\Pi \in h_{\text{flat}}^{-1}(S);\Delta\widetilde{\mathcal{L}}(\Pi)\neq 0} \Delta\widetilde{\mathcal{L}}(\Pi)(\mathscr{P}(\Pi) - z_1). \tag{6.32}$$

This transformation is allowed for the following reason. According to Table 6.1, $\Delta\widetilde{\mathcal{L}} = \tau_z\,\mu \mod m$. We also know that the BZ contains n/m C_n-related copies of a C_m-invariant line, which are all part of the preimage of S. This means that in the sum over all preimages, $n/m \times \tau_z\,\mu =_n n/m \times \Delta\widetilde{\mathcal{L}}$, with $\Delta\widetilde{\mathcal{L}} \in \{0, 1, \ldots, m-1\}$. In the obtained relation (6.32), the sum over preimage lines can be replaced by the sum over a maximal set of reduced momenta $\{\Pi_j\}_{j=1\ldots J}$ with fulfilled mutually-disjoint and iso-orbital conditions. In the last step of the derivation we replace $\sum_{j=1}^{J}\Delta\widetilde{\mathcal{L}}(\Pi_j)z_1 =_n \sum_{j=1}^{J}\Delta\widetilde{\mathcal{L}}(\Pi_j)\mathscr{P}(\Pi_1)$, as for any arbitrarily chosen $\Pi_1 \in \{\Pi_j\}_{j=1\ldots J}$, $\mathscr{P}(\Pi_1) =_1 z_1$ and $\sum_{j=1}^{J}\Delta\widetilde{\mathcal{L}}(\Pi_j) \in n\mathbb{Z}$ because of a trivial Chern class of the model [cf. Appendix B.1]. With this we obtain the desired relation (6.3).

6.5.4.6 *Contractible south pole preimages do not modify relation modulo n*

To finish the proof of the Hopf-RTP relation we need to take into account other possible preimages of the south pole, that form contractible loops. There are two types of such preimages:
(*i*) A closed loop at a generic position in the BZ that is repeated n times due to C_n symmetry [cf. Fig. 6.3(a) for a P4 illustration].
(*ii*) A closed loop that encircles a C_m-invariant line in the BZ. This loop must appear in n/m copies and has a C_m-symmetric shape [cf. Fig. 6.3(b) for a P4 illustration].

Both types of preimages modify the Hopf-RTP relation only by multiples of n:
(*i*) Assume that a closed loop carries a Chern number C'. Since the loops appear as n copies in the BZ, each copy carries the same Chern number C' and together they contribute to the Hopf invariant nC', which does not modify the relation modulo n.
(*ii*) To determine the contribution to the Hopf invariant from each of the n/m copies of loops we consider preimages of the north pole of the 2-sphere [cf. Fig 6.3(c)]. These preimages also come in n C_n-related copies and if one

of them happens to be linked with a component of the preimage of the south pole, the m C_m-related copies of it will also be linked with the same component [cf. Fig. 6.3(b)]. Since the Hopf invariant can alternatively be calculated as the number of links between preimages of two points on the 2-sphere [as discussed in Sec. 2.1.6], we can conclude that each of n/m loops contributes $m\mathbb{Z}$ value to the Hopf invariant. Therefore, all loops in total contribute $n\mathbb{Z}$ and do not modify the relation modulo n.

We conclude that we considered contributions of all possible preimages of the south pole to the Hopf invariant and it is given by Eq. (6.3) up to multiples of n.

Part II

DELICATE TOPOLOGY

Two themes have indelibly shaped the paradigm of topological insulators, and couched how topological properties are discussed, modelled, and measured. The first is the notion of stability of topological insulators, and the second involves the various obstructions to forming a real-space Wannier-function (WF) representation of the valence band [72, 77, 78, 81, 134, 170–172]. In this part of the thesis we describe an extension and fine-graining of both themes, and show that the crystalline Hopf insulators, discussed in Part I, realize the notions introduced here. At the same time the crystalline Hopf insulators would be considered unstable and unobstructed according to the presently-held paradigm.

The strongest form of stability is the notion of stable equivalence introduced by K-theory [22, 30, 172–174], where the bulk/surface topological invariant of a valence subspace is immune to addition of trivial bands. The intermediate notion of fragility (reviewed in Sec. 2.2.4) means that the topological property can be nullified by adding trivial bands to the valence subspace, but not to the conduction subspace [41–43, 45, 47, 52, 175] [Fig. 2.9(a)]. A distinct notion that we introduce here is *delicate topology*, where the topological property can be nullified by adding trivial bands to either valence or conduction subspace [Fig. 2.9(b)]. For symmetry-protected delicate topology, nullification occurs only by adding trivial bands of certain symmetry representations.

As we discussed in Sec. 2.2.3, many authors have proposed a useful definition of a trivial band to be its possession of an exponentially-localized WF representation respecting the crystallographic spacetime symmetries [29–31, 47, 120, 174, 176]. By this definition, all stably-equivalent and fragile topological insulators present an obstruction to a WF representation. It has been further argued through equivariant vector bundle theory that such Wannier obstructions represent a robust property of a valence subspace summed with an *arbitrary* conduction subspace [47], and therefore such obstruction cannot exist for delicate topological insulators. Here, we introduce a distinct class of obstructions that prevents WFs from being completely localized to a single, primitive unit cell – we call this *multicellular topology*. Conversely, we adopt a distinct notion of triviality, namely that symmetry-respecting WFs exist and can be confined to a single cell by a continuous, adiabatic deformation of the Hamiltonian – *unicellularity*.

The notions of delicate and multicellular topology are distinct and a priori need not come together in any specific realization of a topological insulator. In Chapter 7 of this part we argue that both the Hopf and RTP invariants are the manifestations of delicate topology. We additionally show that the RTP invariant realizes *symmetry-protected delicate topology*, in a sense that it remains well-defined and quantized upon addition of trivial bands with certain angular momenta. This additionally provides a way to define the RTP invariant beyond the Hopf insulators in more-than-two-band Hamiltonians. Next, in Chapter 8 we discuss the multicellularity of delicate topological insulators. We show that Wannier orbitals of Hopf and RTP insulators are exponentially localized but multicellular. For given values of delicate topological invariants one can define a *grade*: a lower bound on the number of unit cells that host the multicellular Wannier orbital. Additionally, in Appendix D.3 we argue more generally that multicellularity of Wannier functions is a delicate property.

PART CONTENTS

7

DELICACY OF THE HOPF AND RTP INVARIANTS

In this chapter, we discuss the following question: what happens to the classification by the Hopf and RTP invariants when the Hilbert space is expanded by including more trivial bands? Our analysis of the postulated question is organized as follows. Firstly, in Sec. 7.1, we introduce the procedure by which we expand a topologically-nontrivial two-band Hamiltonian to a (>2)-band Hamiltonian. The implications of the Hopf invariant being delicate-topological are explored in Sec. 7.2. The implications of the RTP invariant being symmetry-protected delicate-topological as well as existence of multi-band generalization of the RTP are explored in Sec. 7.3. Finally, in Sec. 7.4, we show that the mirror-symmetric nodal-line semimetallic phase explored in Sec. 3.4.2 realizes the first-known example of a symmetry-protected delicate topological semimetal.

CHAPTER CONTENTS

7.1 (>2)-BAND HAMILTONIANS FROM TWO-BAND HAMILTONIANS

We consider a specific algorithm to produce a (>2)-band Hamiltonian from a two-band Hamiltonian: we expand the two-band Hilbert space by adding to it a basis band representation (of Pn) induced from a third, representative tight-binding-basis orbital φ_3. If φ_3 is centered at a C_n-invariant Wyckoff position $\boldsymbol{r}_3$ and forms a certain one-dimensional representation of the site-stabilizer group $\mathrm{P}n_{\boldsymbol{r}_3}$, then the Hilbert space is expanded to three bands. (The expansion is to four or more bands if $\boldsymbol{r}_3$ is not C_n-invariant.)

By construction, a basis band representation is a *tightly-bound band representation* – a band representation in which each Wannier orbital is localized to a single site, or *one-site-localized*. (A 'site' is a notion existing only in the tight-binding formalism, and represents the physical location of a tight-binding-basis orbital. If $\boldsymbol{r}_3$ is C_n-invariant, the allowed sites are $\boldsymbol{r}_3$ plus any Bravais-lattice vector.)

A choice is made whether to add this tightly-bound band representation to the conduction or valence subspace; in either case, we preserve the notion of the bulk energy gap inherited from the two-band Hamiltonian. (The choice

between conduction vs. valence is made by tuning the on-site energies of the tightly-bound band representation as desired.) After this addition procedure, we allow any continuous, Pn-symmetric deformation of the (>2)-band Hamiltonian that preserves the bulk gap. This procedure can be repeated to produce a Hamiltonian with any number of conduction and valence bands.

Given that a two-band Hamiltonian is characterized by a nontrivial Hopf or RTP invariant, one may ask if this special topological property of the conduction and valence subspace is lost under the expansion procedure detailed above. At this point, the notion of delicate topology emerges. The Hopf and RTP invariants, defined respectively by Eqs. (4.8) and (4.17), are examples of delicate topological invariants. This means their status as topological invariants is lost under the addition of certain 'trivial' bands to either the conduction or to the valence subspace. In the classification of stable/fragile crystalline topological insulators, being 'trivial' means being a band representation. In contrast, in the more refined classification of delicate crystalline topological insulators, being 'trivial' means being a *tightly-bound band representation*.

However, the Hopf and RTP invariants differ in that the Hopf invariant becomes ill-defined under the addition of *any* tightly-bound band representation (as elaborated in Sec. 7.2), while the RTP invariant loses its invariant status only under the addition of *particular* tightly-bound band representations (cf. Sec. 7.3). This difference, and its implications, are elaborated subsequently.

7.2 DELICACY OF THE HOPF INSULATORS

For two-band Hamiltonians with trivial first Chern class, a bulk-boundary correspondence equates the bulk Hopf invariant with the faceted Chern number. We will separately address whether the bulk or boundary invariant has a natural extension to (>2)-band Hamiltonians.

7.2.1 *Bulk Hopf invariant*

As originally formulated [95], the Hopf invariant classifies maps from a three-sphere (S^3) to a two-sphere (S^2). In our context, the two-sphere is the Bloch sphere – the space of two-band Hamiltonians. Our assumption that the Chern class is trivial allows to continuously deform the map such that its restriction to a 2D subtorus (of the Brillouin torus) is a constant map. In particular, it is possible to have the entire boundary of the (first) BZ map to the same point on the Bloch sphere. This allows one to compactify the boundary to a single point, $\partial\mathrm{BZ} \sim \mathrm{pt.}$, which deforms the BZ into a three-sphere, $\mathrm{BZ}/\!\sim \simeq S^3$ (where '$/\!\sim$' indicates a quotient modulo the equivalence relation [177]). It follows that maps from the Brillouin three-torus to the Bloch sphere, under the constraint of a trivial first Chern class, are topologically equivalent to maps from a three-sphere to a two-sphere and are classified by the Hopf invariant. By this definition, any enlargement of the two-band Hamiltonian renders the Hopf invariant to be ill-defined.

It was shown in Ref. [55] that for two-band Hamiltonians, the Hopf invariant has an equivalent expression as an integral of the Chern-Simons three-form of the Abelian Berry gauge field [cf. Eq. (4.8)]. Unlike the Hopf invariant, the Chern-Simons formula remains well-defined and gauge-invariant for higher-than-two-band Hamiltonians with trivial Chern class, assuming we limit ourselves to expanding only the conduction subspace. (The Chern-

Simons formula is not directly applicable to the case where the valence subspace is expanded due to the Abelian nature of the Berry gauge field in the formula.)

One may then ask if the Chern-Simons formula remains quantized to integers for (N_c+1)-band Hamiltonians with a $(N_c>1)$-band conduction subspace and trivial first Chern class. The negative answer can be rationalized from algebraic-topological considerations: the space of (N_c+1)-band Hamiltonians with a $(N_c>1)$-band conduction subspace is the complex Grassmannian $Gr_{\mathbb{C}}(N_c,1)=U(N_c+1)/[U(N_c)\times U(1)]$ [22], where $U(N_c)$ is the group of unitary matrices of dimension N_c, and it is known [99] that the first Chern class gives the complete classification of maps from the BZ three-torus to $Gr_{\mathbb{C}}(N_c,1)$ for $N_c>1$.

A different extension of the Hopf insulator to multi-band Hamiltonians was proposed in Ref. [167] for the *N-band Hopf insulators*, where N non-degenerate bands are separated by $N-1$ energy gaps; then a $\mathbb{Z}$-valued topological invariant corresponding to the third homotopy group of the *complex flag manifold* [45, 178] $Fl_{\mathbb{C}}=U(N)/U(1)^{\times N}$ is computed as the quantized sum of the non-quantized integrals of the Chern-Simons 3-form over the N individual bands. This quantity remains invariant as long as no band degeneracy is formed between any pair of bands. In this thesis, we instead focus on the 'conventional' scenario where topological invariants change only if one closes the energy gap separating the valence bands from the conduction bands. In this case the Hopf invariant can not be defined in more-than-two-band Hamiltonians and is delicate.

7.2.2 *Faceted Chern number*

We just showed that the Hopf invariant becomes ill-defined after enlargement of the two-band Hamiltonian. Can we say something about the faceted Chern number (5.1) when the rank of either the valence or the conduction subspace is larger than one? As was shown in Ref. [166] [cf. Sec. II.A.1 and Fig. 3(b) therein], in the absence of any crystalline symmetry except the lattice translation, the presence of multiple bands in a given subspace allows to modify the value of the faceted Chern number by an arbitrary integer number, depending on the number of considered faceted bands $\mathcal{N}_f$. This is due to the fact that the bulk bands can *individually* carry non-zero Chern numbers even when the total Chern number of the corresponding subspace is zero. Now, if we enlarge the set of surface-like polarization bands by including one polarization band with a bulk-like non-zero Chern number, the value of the faceted Chern number will be modified by this bulk Chern number.

While both the Hopf invariant and the faceted Chern number lose their invariance for (>2)-band Hamiltonians, there is a special case of Pn-symmetric Hamiltonians for which "$\mathscr{C}_f$ mod-n" remains a topological invariant. For this to be true, the valence band representation (and also the conduction band representation) must be symmetry-equivalent to a composite band representation that is decomposable into N_v (N_c) identical band representations $\mathrm{BR}(\mathcal{L}_v,\boldsymbol{r}_{v,\perp})$ [$\mathrm{BR}(\mathcal{L}_c,\boldsymbol{r}_{c,\perp})$]. In this case the rotation symmetry guarantees that the Chern number of each individual bulk band is a multiple of n and therefore it can modify the faceted Chern number by multiples of n which keeps the value of $\mathscr{C}_f \mod n$. In Sec. 7.3 we define this invariant in terms of the angular-momentum anomaly.

7.3 SYMMETRY-PROTECTED DELICACY OF THE RTP INSULATORS

For two-band Hamiltonians, the bulk-boundary correspondence of RTP insulators equates the bulk RTP invariant with an anomaly associated with the angular momentum of faceted states. We will separately address whether the bulk invariant or the boundary anomaly has a natural extension to (>2)-band Hamiltonians.

7.3.1 *Bulk RTP invariant*

The RTP invariant $\Delta\mathscr{P}_{\Pi\Pi'}$ has been defined as an integer-valued polarization difference of the valence band between two rotation-invariant reduced momenta Π and Π'. A natural way to extend the RTP invariant to higher-than-two-band Hamiltonians is to ask whether the valence-subspace polarization difference is fixed by symmetry to integer values if the valence/conduction subspace contains more than one band. We find that the polarization difference remains quantized if the enlarged Hamiltonian obeys two conditions which are generalizations of Eq. (6.1) and Eq. (6.2).

(*i*) The enlarged Hamiltonian satisfies the *mutually-disjoint condition* at Π and Π': collecting the itinerant angular momenta of bulk-valence and bulk-conduction states (at Π) into the respective sets $\{\widetilde{\mathcal{L}}_{v,j}(\Pi)\}_{j=1}^{N_v}$ and $\{\widetilde{\mathcal{L}}_{c,j}(\Pi)\}_{j=1}^{N_c}$, we require that the two sets are disjoint:

$$\text{mutually-disjoint condition at } \Pi\text{:}\qquad \left\{\widetilde{\mathcal{L}}_{v,j}(\Pi)\right\}_{j=1}^{N_v} \cap \left\{\widetilde{\mathcal{L}}_{c,j}(\Pi)\right\}_{j=1}^{N_c} = \varnothing. \tag{7.1}$$

This condition is required to hold for both Π and Π'.

(*ii*) There exists a composite basis band representation CBR, such that the restriction of the valence band representation VBR to Π equals the restriction of CBR to Π, and likewise $\mathrm{VBR}|_{\Pi'} = \mathrm{CBR}|_{\Pi'}$. A composite basis band representation is defined as a Whitney sum of elementary basis band representations: $\mathrm{CBR} = \mathrm{EBR}_1 \oplus \mathrm{EBR}_2 \oplus \ldots \oplus \mathrm{EBR}_{N_v}$. Each of EBR_α is induced from a basis orbital with a certain site-stabilizer symmetry representation and a certain positional center $(\boldsymbol{r}_{\alpha,\perp}, z_\alpha)$.

In general, along the rotation-invariant $\boldsymbol{k}$-line specified by Π, the tight-binding Hamiltonian $h(\Pi, k_z)$ is block-diagonal in the basis where the itinerant rotation matrix is diagonal; what the mutually-disjoint condition (*i*) gives additionally is that each block (corresponding to one angular-momentum sector) belongs either to the conduction or to the valence subspace. This implies that the Hilbert space spanned by the valence eigenstates of $h(\Pi, k_z)$ is independent of k_z. (*i*–*ii*) jointly imply that the multi-band polarization of the valence subspace of $h(\Pi, k_z)$ is equal, modulo integers, to the multi-band polarization of the just-mentioned composite band representation as detailed in Dets. 7.1. Since this statement holds also for $\Pi \leftrightarrow \Pi'$ with the *same* composite basis band representation, we deduce that the valence polarization of $h(\Pi, k_z)$ is equal, modulo integers, to the valence polarization of $h(\Pi', k_z)$. Thus one concludes the polarization difference between Π and Π' is quantized to integer values. This holds true whether or not the composite basis

band representation is identical to the valence band at rotation-invariant $\boldsymbol{k}$-lines other than Π or Π'.

Details 7.1 The multi-band polarization can be computed via the non-Abelian Wilson loop as $\mathscr{P}(\Pi) =_1 \frac{1}{2\pi} \operatorname{Im} \log \det \mathcal{W}$ (cf. Secs. 2.1.3.3 and 2.1.4.2). The multi-band polarization of the composite band representation simply equals $\sum_{\alpha=1}^{N_v} z_\alpha$, with z_α being the positional centers of the basis orbitals which are used to construct the composite band representation. The mod-one equality of $\mathscr{P}(\Pi)$ and $\sum_{j=\alpha}^{N_v} z_\alpha$ is proven similar to the proof in Dets. 4.1 of Sec. 4.2 presented for a single band. One can apply an equivalent expression of the Wilson loop in terms of the z_α and the projector $p(\Pi, k_z)$ to the valence subspace of $h(\Pi, k_z)$, as shown in Appendix C of Ref. [91]; the mutually-disjoint condition gives that $p(\Pi, k_z) = \operatorname{diag}(\mathbb{1}, \mathbb{0})$ is a k_z-independent diagonal matrix, with $\mathbb{1}$ a $N_v \times N_v$ identity matrix and $\mathbb{0}$ a $N_c \times N_c$ zero matrix.

Working within the symmetry constraints of (*i–ii*), one can generalize the RTP invariant to Hamiltonians of arbitrary number of bands. The stability of the RTP invariant under symmetry-constrained Hilbert-space enlargements is the defining property of *symmetry-protected delicate topology*.

To illustrate how the RTP invariant can be nullified, one can add to the Hilbert space any basis band representation $\mathrm{BBR}[\varphi_3]$ of Pn with a C_m-invariant Wyckoff position $\boldsymbol{r}_3$ that is *not* C_n-invariant, in other words $1 < m < n$, and with φ_3 forming a one-dimensional representation of P$n_{\boldsymbol{r}_3}$. Such a band representation necessarily has rank r greater than one, meaning that the Hilbert space is spanned by r independent Bloch states at each $\boldsymbol{k}$. However, $\mathrm{BBR}[\varphi_3]$ cannot be split/decomposed into multiple band representation of smaller rank. For such band representations, one may verify (e.g., from the Bilbao crystallographic server [179]) that for every pair of a rank-1 elementary band representation $\mathrm{BBR}[\varphi_1]$ and a rank-$(r>1)$ elementary band representation $\mathrm{BBR}[\varphi_3]$

$$\exists \text{ at most one } \Pi, \text{ s.t. } \quad \forall j = 1 \dots r, \quad \widetilde{\mathcal{L}}_1(\Pi) \neq \widetilde{\mathcal{L}}_3^j(\Pi), \tag{7.2}$$

where $\widetilde{\mathcal{L}}_1(\Pi)$ is itinerant angular momentum of $\mathrm{BBR}[\varphi_1]$ and $\widetilde{\mathcal{L}}_3^j(\Pi)$, $j = 1 \dots r$ are itinerant angular momenta of $\mathrm{BBR}[\varphi_3]$. This implies that the addition of $\mathrm{BBR}[\varphi_3]$, whether it is to the conduction or valence subspace, makes the mutually-disjoint condition unfulfillable at (at least) two rotation-invariant reduced momenta, and hence, nullifies all RTP invariants. This possibility shows that the RTP invariants are delicate.

7.3.2 *Angular-momentum anomaly*

For (>2)-band Hamiltonians with an RTP invariant $\Delta\mathscr{P}_{\Pi_1\Pi_2}$ that is well-defined and greater than zero, the angular-momentum anomaly [encapsulated by Eq. (5.7) and derived in Sec. 5.2.3] holds just as well as for two-band Hamiltonians, implying the existence of at least $\Delta\mathscr{P}_{\Pi_1\Pi_2}$-number of anomalous faceted bands whose itinerant angular momenta are bulk-conduction-like at Π_1 and bulk-valence-like at Π_2.

We remind the reader that for *two*-band Hamiltonians, an itinerant angular momentum is bulk-valence-like at Π if it is identical to the itinerant angular momentum of the bulk-valence band at Π. By assumption of a two-band Hamiltonian, the bulk-valence subspace comprises a single band, hence the itinerant angular momentum at Π is uniquely defined.

In contrast, for an N_v-band bulk-valence subspace, there is not a unique angular momentum, but a set $\{\widetilde{\mathcal{L}}_v^j(\Pi)\}_{j=1,\dots,N_v}$ of possibly non-identical angular momenta. An itinerant angular momentum that is *bulk-valence-like* is then equal to any of the N_v values in this set (which potentially contains repetitions). Likewise, one may generalize the notion of *bulk-conduction-like*

to an N_c-band bulk-conduction subspace. It is with these generalized notions that the angular-momentum anomaly [encapsulated by Eq. (5.7)] holds for $(N_c + N_v)$-band Hamiltonians.

We see that specifying $\Delta\mathscr{P}_{\Pi_1\Pi_2}$ does not uniquely specify the subspace of faceted bands, owing to the non-uniqueness in itinerant-angular-momentum values implicit in (the generalized notions of) 'bulk-conduction-like' and 'bulk-valence-like'. In other words, there are multiple, topologically-distinct faceted subspaces consistent with a single value of $\Delta\mathscr{P}_{\Pi_1\Pi_2}$. This suggests there exists a finer topological classification [of P$(n{>}2)$-symmetric $(N_c + N_v)$-band Hamiltonians] than is afforded by the RTP invariant $\Delta\mathscr{P}_{\Pi_1\Pi_2}$ alone. We believe this to be a promising research direction.

Why did we restrict the above conjecture to Pn with $n > 2$? The P2 space group is special in that there are only two irreducible representations of the C_2 point group, thus being bulk-valence-like (or bulk-conduction-like) uniquely specifies an itinerant angular momentum. This is because the mutually-disjoint condition at Π holds only if (*i*) all members of the bulk-valence-like set $\{\widetilde{\mathcal{L}}_v^j(\Pi)\}_{j=1,\ldots,N_v}$ of itinerant angular momenta are equal, (*ii*) all members of the bulk-conduction-like set $\{\widetilde{\mathcal{L}}_c^j(\Pi)\}_{j=1,\ldots,N_c}$ of itinerant angular momenta are also equal, and (*iii*) $\widetilde{\mathcal{L}}_v^1(\Pi) \neq \widetilde{\mathcal{L}}_c^1(\Pi)$. It follows that the full set of RTP invariants uniquely determines the itinerant angular momenta of the faceted subspace.

In the general setting of $(N_v + N_c)$-band Pn-symmetric Hamiltonians the angular-momentum anomaly manifests in conditionally-robust surface states that interpolate between valence and conduction band in the same way as for the 2-band Hamiltonians. Our proof of the conditional-robustness of the surface states, presented in Appendix C.2, uses certain spectral properties of block-Toeplitz matrices and generalizes the 2-band proof presented in Sec. 5.3.

For another physical manifestation of the angular-momentum anomaly – the Zak-phase anomaly – to hold, the sufficient (but not necessary) condition is to have identical itinerant angular momenta of all valence bands at Π_1, and also at Π_2; the same must be true for the conduction itinerant angular momenta. In this case, the Zak-phase anomaly tells that $\mathcal{N}$ faceted bands have a set of $\mathcal{N}$ Zak phases, with $|\Delta\mathscr{P}_{\Pi_1\Pi_2}|$ of them being symmetry-fixed to a rational multiple of $2\pi/n$, and that these symmetry-fixed Zak phases are distinct from the bulk-valence and also from the bulk-conduction Zak phase. This can be shown by applying the theorem from Sec. IV D 1 in Ref. [134] in the same way as it was done for the two-band case in Sec. 5.4.4 and Appendix C.1.

Let us finally consider the faceted Chern number of the (>2)-band RTP insulators. As we already mentioned in Sec. 7.2.2, in the special case of identical itinerant angular momenta of the valence bands $\widetilde{\mathcal{L}}_{v,j}(\Pi) = \widetilde{\mathcal{L}}_v(\Pi)$ for all $j = 1 \ldots N_v$ at each Π [and same for the conduction bands $\widetilde{\mathcal{L}}_{c,j}(\Pi) = \widetilde{\mathcal{L}}_c(\Pi)$ for all $j = 1 \ldots N_c$], the angular-momentum anomaly leads to a faceted Chern number defined modulo n. Given the itinerant angular momenta of the $\mathcal{N}_f$ faceted bands, the mod-n-Chern number is given by

$$\begin{aligned}\mathscr{C}_f &=_n -\sum_{i=1}^{\mathcal{N}_f}\sum_{\Pi}\widetilde{\mathcal{L}}_i(\Pi)\\ &=_n \sum_{\alpha=1}^{2}\sum_{j_\alpha=2}^{J_\alpha}\Delta\widetilde{\mathcal{L}}(\Pi_{j_\alpha}^\alpha)\,\Delta\mathscr{P}_{\Pi_1^\alpha\Pi_{j_\alpha}^\alpha},\end{aligned} \tag{7.3}$$

where $\{\Pi^{\alpha}_{j_\alpha}\}_{j_\alpha=1\ldots J_\alpha}$, $\alpha = 1,2$, are two maximal subsets of rotation-invariant reduced momenta satisfying conditions (6.1) and (6.2). By 'maximal' we mean that each set contains all reduced momenta, satisfying these conditions, and the size of each subset is given by an integer J_α. This relation is proven in exactly the same way as the Hopf-RTP relation in Sec. 6.4. This similarity with the Hopf-RTP relation [cf. Eq. (6.5)] of two-band Hamiltonians is not accidental. For two-band Hamiltonians with trivial Chern class, the bulk-boundary correspondence of Hopf insulators equates the Hopf invariant with the faceted Chern number: $\chi = \mathscr{C}_f$. For (>2)-band Hamiltonians with identical valence (conduction) itinerant angular momenta, the Hopf invariant loses its invariant meaning, yet the faceted Chern number remains well-defined modulo n due to the anomalous values of itinerant angular momenta.

7.4 DELICACY OF THE NODAL-LINE SEMIMETAL

In Sec. 3.4, we studied semimetallic phases in the vicinity of the Berry-dipole band touching and particularly focused on the mirror-symmetric model

$$h(\boldsymbol{k};\mathbb{m}) = 2k_z\left(k_x\sigma_x - k_y\sigma_y\right) + \left(k_x^2 + k_y^2 - k_z^2 - \mathbb{m}\right)\sigma_z, \tag{7.4}$$

which forms a Weyl semimetal for $\mathbb{m} < 0$ [with Weyl points illustrated in Fig. 7.1(a)] and transitions via a Berry dipole at $\mathbb{m} = 0$ to a nodal-line semimetal at $\mathbb{m} > 0$ [with a nodal ring illustrated in Fig. 7.1(b)].

With few exceptions [126, 180], previous analyses of the robustness of Weyl points has been based on topological invariants which are stable topological, i.e., characteristic of equivalence classes defined in K theory [181]. One may therefore expect that the two Weyl points (with opposite chirality) in our model Hamiltonian (7.4) with $\mathbb{m} < 0$ pairwise annihilate upon collision at $\mathbb{m} = 0$; after all, the stable-topological invariant associated with the union of the two Weyl points, which one may view as the Chern number of a Gaussian surface enclosing both Weyl points, vanishes.

In spite of this vanishing Chern number, the two Weyl points do not annihilate but instead 'convert' into a nodal-line ring for $\mathbb{m} > 0$. This is suggestive that the two Weyl points/nodal loop are associated with a *non-stable* topology which prevents bands from untouching. A priori, logic permits this topology to be either fragile or delicate; we confirm here that the topology is delicate. Our discussion has some overlap with Ref. [126], where the model Hamiltonian in Eq. (7.4) was first investigated in detail. The novelty of the following exposition lies in our embedding of a known model into the unifying framework of delicate topological semimetals, while also demonstrating that the returning Thouless pump, angular-momentum anomaly, conditionally-robust surface states, and Zak-phase anomaly are generalizable concepts with a wider applicability beyond rotation-symmetric Hamiltonians.

7.4.1 *Mirror-protected delicate topological invariant in the bulk*

To identify the delicate-topological invariant associated with the band touching of Eq. (7.4), it is worth recognizing that both the conduction and the valence band carry opposite eigenvalues of the z-mirror symmetry (represented by $R_{M_z} = \sigma_z$) at the reflection-invariant plane ($k_z = 0$) – this may be viewed as the reflection-symmetric analog of the mutually-disjoint condition [Eq. (4.10)], which we previously formulated for rotation-invariant $\boldsymbol{k}$-lines. One can then consider a 2-sphere (S^2) that encloses the nodes and is symmetric under M_z [illustrated with a union of red and blue hemispheres in

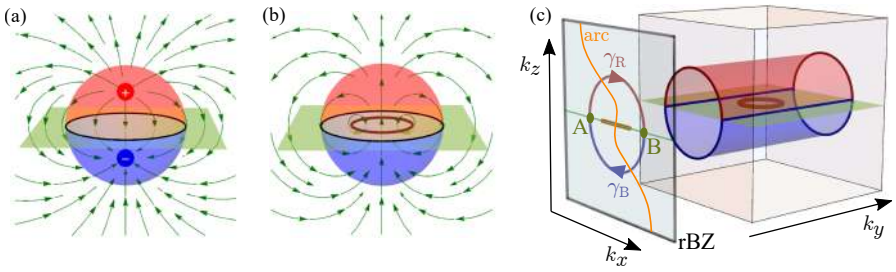

Figure 7.1: (a,b) The band degeneracy of the model in Eq. (7.4) for (a) $\mathbb{m} < 0$, and (b) $\mathbb{m} > 0$. The red/blue dots indicate a Weyl node with positive/negative chirality, and the brown loop represents a nodal-line ring. The green arrows display the Berry curvature field, whereas the bright green sheet indicates the z-mirror-invariant plane. The colored hemispheres each exhibit a non-trivial and quantized value of the Chern number. This Chern number is a symmetry-protected delicate topological invariant, which obstructs the annihilation of the Weyl points when they collide for $\mathbb{m} = 0$. (c) For $\mathbb{m} > 0$ (when nodal-line ring is present), we enclose the band degeneracy with a z-mirror-symmetric cylinder that projects onto a circular path $\gamma_R \cup \gamma_B$ in the reduced Brillouin zone (rBZ). The valence band has the same orbital character at both points A and B; however the polarization increases by 1 along the red path γ_R (projection of the semi-cylinder with positive Chern number) and drops by 1 along γ_B, thus exhibiting a returning Thouless pump (RTP). The mirror-eigenvalue anomaly on the circular path $\gamma_R \cup \gamma_B$ (with mirror-invariant points A and B) in the presence of sharp boundary condition enforces the existence of two surface Fermi arcs (orange lines) which both terminate at the rBZ projection of the nodal-line ring (brown segment located between points A and B. The Fermi arcs terminate at projections of band nodes elsewhere in rBZ (of which only a part in the (k_x, k_z)-plane is shown).

Fig. 7.1(a,b)], and argue as follows: (1) because of the mirror symmetry, the information about the continuous Hamiltonian on S^2 is fully encoded on one [e.g., the upper ($k_z > 0$)] hemisphere, and (2) due to the mutually-disjoint condition, the spectrally-flattened Hamiltonian [cf. Eq. (3.8)] over the sphere's equator [a circle in the $k_z = 0$ plane illustrated with black line in Fig. 7.1(a,b)] is simply σ_z; this implies that the equator maps to a single point on the Bloch sphere and allows to treat the hemisphere as if it were a closed 2-sphere for the purpose of topological classification. The Hamiltonian on this abstract 2-sphere exhibits an integer 'wrapping' number around the Bloch sphere, which translates into an integer-valued Chern number on the upper hemisphere. One easily verifies that for the situation with a pair of M_z-related Weyl points, this wrapping number simply equals the net Berry-monopole charge of Weyl points in the upper hemisphere [cf. Fig. 1(a) in Ref. [126]]. As a consequence, the colliding Weyl points cannot annihilate: opening of an energy gap inside the 2-sphere would contradict the existence of a non-trivial topological invariant on the 2-sphere.

It was further proven in the Supplemental material of Ref. [126], using relative homotopy groups [94], that the quantization of the Chern number persists in (>2)-band Hamiltonians – if and only if the conduction/valence bands obey the mutually-disjoint condition of M_z eigenvalues.[1] In the language we have formulated here, the Chern number on the upper hemisphere, which enforces the conversion of the Weyl-point pair into a nodal-line ring, is a symmetry-protected delicate topological invariant. One can thus interpret such (>2)-band gapless models as a (symmetry-protected) *delicate topological semimetal*. The bulk Chern number over the hemisphere is equivalent to a

1 The term 'mutually-disjoint' was not used in the previous work [126].

reflection-symmetric analog of the returning Thouless pump, as we now demonstrate. For this purpose, instead of enclosing the band degeneracy with an M_z-symmetric 2-sphere, here we enclose it with an M_z-symmetric cylinder with the cylindrical axis in a direction (say, y) orthogonal to z. One may view the cylinder as an M_z-symmetric 'inflation' of the 2-sphere, as illustrated in Fig. 7.1(c). Because of the mutually-disjoint condition, the bulk valence band (restricted to the mirror-invariant $\boldsymbol{k}$-plane) has overlap with one and only one basis orbital. This implies that an analog of the iso-orbital condition [Eq. (4.16)] is satisfied for pair of mirror-invariant $\boldsymbol{k}$-lines within this mirror-invariant $\boldsymbol{k}$-plane – including those two $\boldsymbol{k}$-lines that lie at the intersection of the cylinder with the $(k_z = 0)$-plane, and project onto mirror-invariant points [A and B in Fig. 7.1(c)] in the 2D rBZ. The projection of the cylinder forms a circular path $\gamma_R \cup \gamma_B$ in rBZ, which we decompose into two z-mirror-related semicircular segments: γ_R and γ_B.

Because of the non-trivial first Chern number on the red semi-cylinder (equalling the net Berry-monopole charge of all Weyl points in the upper hemisphere), the $\boldsymbol{k}_\perp$-dependent polarization grows by one primitive lattice period (in the direction parallel to the surface normal) as $\boldsymbol{k}_\perp \in$ rBZ is continuously advanced along γ_R. The polarization subsequently reverts to the original value after further moving along γ_B – manifesting a returning Thouless pump (RTP) along the closed path $\gamma_R \cup \gamma_B$.

7.4.2 *Bulk-boundary correspondence of mirror-protected returning Thouless pump*

Let us explain the boundary correspondents of the bulk delicate topological invariant associated with these band degeneracies. For this purpose, it is convenient to interpret the cylinder as the Brillouin zone (BZ′) of a 2D-translation-invariant, mirror-symmetric Hamiltonian h'; h' is obtained by restricting the flattened 3D Hamiltonian [Eq. (3.8)] to the cylinder, and interpreting the azimuthal coordinate of the cylinder as a linear momentum coordinate of BZ′; BZ′ projects in the y-direction to a 1D reduced Brillouin zone denoted rBZ′. Much like how the angular-momentum anomaly [Eq. (5.7)] is the boundary correspondent of the bulk rotation-protected RTP, we claim that the restricted Hamiltonian h' exhibits an analogous *mirror-eigenvalue anomaly* as the boundary correspondent to the mirror-protected RTP, under open boundary conditions that are z-mirror-symmetric.

For concreteness, we assume a half-infinite geometry with facet normal in the y-direction – which is also the direction of the cylindrical axis. What the mirror-eigenvalue anomaly means is that for at least one faceted band, the mirror eigenvalues at mirror-invariant points of rBZ′ [A and B in Fig. 7.1(c)] are opposite in sign; this can be proven with essentially the same techniques as those in Sec. 5.2.3. This alternation of mirror eigenvalues guarantees the Zak phase anomaly along a path that passes through the mirror-invariant points A and B and consists of two mirror-related sectors. One example of such path is $\gamma_R \cup \gamma_B$ illustrated in Fig. 7.1(c). The Zak-phase theorem proven in Ref. [91] guarantees the existence of at least one symmetry-quantized π Berry-Zak phase in the spectrum of the (possibly non-Abelian) Wilson loop computed along $\gamma_R \cup \gamma_B$, for the (possibly multi-band) faceted subspace – contrasting to the vanishing Berry-Zak phase of the bulk conduction and bulk valence band computed along any path in 3D BZ which projects onto $\gamma_R \cup \gamma_B$ in rBZ. This is the mirror-symmetric analog of the Zak-phase anomaly [Eqs. (5.32) and (5.34)] that we have previously formulated for rotation symmetry.

A further implication of the mirror-eigenvalue anomaly is the existence of conditionally-robust edge states over rBZ′; this means that edge-state energies of h' necessarily interpolate across the bulk energy gap of h' under sharp boundary conditions; a proof of this would utilize spectral properties of Toeplitz matrices [cf. Appendix C.2], in close analogy with the demonstration of rotation-symmetric conditionally-robust surface states presented in Sec. 5.3.

Conditionally-robust edge states of h' imply conditionally-robust *surface Fermi arcs* [orange lines in Fig. 7.1(c)] of the 3D Hamiltonian subject to sharp boundary conditions, with one arc crossing each of the semicircles γ_R and γ_B in the 2D rBZ; this holds for both the Weyl semimetal and the nodal-ring semimetal phase of the Hamiltonian in Eq. (7.4). This clarifies the origin of Fermi arcs that were observed numerically (but remained unexplained) in Fig. 2 of Ref. [126] under sharp boundary conditions. It is worth emphasizing that the surface Fermi arcs are not topologically guaranteed under non-sharp boundary conditions – a point not articulated in Ref. [126].

8

MULTICELLULARITY OF DELICATE TOPOLOGICAL INSULATORS

Stable and fragile topology enforce an obstruction to find an exponentially localized and locally-symmetric Wannier representation. As was already argued, such Wannier obstruction is absent for delicate topology. In this chapter we show that both the Hopf and the RTP invariants, studied in the previous chapters, obstruct the valence subspace (and also the conduction subspace) of the crystalline Hopf insulator from being continuously deformable to a tightly-bound band representation. The obstruction against being tightly-bound holds despite both the conduction as well as the valence bands being band representations. A different way to state this is that despite the Wannier orbitals being exponentially-localized and locally-symmetric, some of the Wannier orbitals necessarily have support across multiple primitive unit cells. Such obstructed band representations are described as *multicellular*.

Our exposition of multicellularity is organized in the present chapter as follows. First, in Sec. 8.1 we elaborate on the definition of the trivial band which is induced from a unicellular Wannier orbital. We also comment on the allowed continuous deformations of the Hamiltonian. Next, in Sec. 8.2, we show that each of the studied delicate topological invariants (Hopf and RTP) individually leads to multicellular Wannier functions. Then in Sec. 8.3 we introduce a grading of multicellularity, defined to be the smallest number of primitive unit cells that a representative Wannier orbital can be confined to, if allowing for any continuous deformation of the Hamiltonian that preserves the energy gap and symmetry. We emphasize that the set of insulators with multicellular Wannier orbitals is distinct from the set of obstructed atomic limits, whose orbitals are tightly localized but centered away from the tight-binding basis sites. We elaborate on this in Appendix D.1, where we show an example of an obstructed atomic limit that is unicellular and of a multicellular insulator that is not an obstructed atomic limit.

CHAPTER CONTENTS

8.1 AN ELABORATION ON THE DEFINITION OF UNICELLULARITY

At the onset, let us state the definition of a unicellular band, which is a set of symmetry-respecting, exponentially-localized Wannier orbitals that

span the band's Hilbert space, and each Wannier orbital can be confined to a single primitive unit cell by a continuous, adiabatic deformation of the Hamiltonian.

For a given Hamiltonian acting on the Hilbert space specified by the basis orbitals $|\boldsymbol{R},\alpha\rangle\rangle$ [cf. Sec. 2.1.1] a collection of N_v occupied bands, labeled by $j \in \{1,2,\ldots,N_v\}$, has the following Wannier representation [cf. Sec. 2.1.4.1 for the definitions]

$$W_{j,\bar{\boldsymbol{R}}}(\boldsymbol{R},\alpha) = \left\langle\!\left\langle \boldsymbol{R},\alpha \middle| W_{j,\bar{\boldsymbol{R}}} \right\rangle\!\right\rangle. \tag{8.1}$$

We call a collection of Wannier orbitals $\left\{ \left| W_{j,\bar{\boldsymbol{R}}} \right\rangle\!\right\rangle \Big\}_{j=1}^{N_v}$ *unicellular* if only $\bar{\boldsymbol{R}} = \boldsymbol{R}$ components are non-zero in the Wannier orbital, i.e., they acquire the form

$$W_{j\bar{\boldsymbol{R}}}(\boldsymbol{R},\alpha) = \delta_{\bar{\boldsymbol{R}}\boldsymbol{R}} w_j(\alpha). \tag{8.2}$$

A few clarifying remarks are in order:

(a) Recall that a primitive unit cell is a finite region of space that, when translated by the Bravais-lattice vectors, covers all space ($\mathbb{R}^d$) without overlapping. While the volume of this finite region is uniquely defined by the Bravais lattice, its boundary is not. In the definition of unicellularity, we assume that we can find a unit cell such that *all* V representative, valence-band Wannier orbitals are strictly localized within it. [A representative set of valence-band Wannier orbitals are a minimal set of Wannier orbitals which generate an infinite set of Wannier orbitals (under Bravais-lattice translations) that span the valence band.]

(b) One could adopt a generalized (i.e., less restrictive) definition of unicellularity, namely that Wannier orbitals can be constructed such that each one of them can be confined to an appropriately chosen unit cell, while not requiring these choices of unit cells to be equal to each other. We emphasize that (unless explicitly stated otherwise, see e.g. Dets. D.1 in Appendix D.2) we adopt the "strict" definition of unicellularity from (a) throughout this chapter.

(c) With regard to 'continuous, adiabatic deformation of the Hamiltonian', in addition to deformations of the matrix elements for a fixed tight-binding basis, we also allow for deformations of the tight-binding Hilbert space that maintains a pre-specified crystallographic space group $\mathcal{G}$. To clarify what this means, note that the basis states $|\boldsymbol{R},\alpha\rangle\rangle$ are themselves band representations of $\mathcal{G}$. We allow to deform the tight-binding Hilbert space in two ways.

(c-i) Firstly, consider the set of all basis vectors lying on the same position $\boldsymbol{R}+\boldsymbol{r}_\alpha$, which span a finite-dimensional Hilbert space $\mathscr{H}_{\boldsymbol{R}+\boldsymbol{r}_\alpha}$; because the tight-binding Hilbert space is a band representation of $\mathcal{G}$, $\mathscr{H}_{\boldsymbol{R}+\boldsymbol{r}_\alpha}$ must form a representation of the site stabilizer $\mathcal{G}_{\boldsymbol{R}+\boldsymbol{r}_\alpha}$. We allow for any unitary transformation within $\mathscr{H}_{\boldsymbol{R}+\boldsymbol{r}_\alpha}$.

(c-ii) Secondly, we allow to continuously displace the basis Wannier centers as $\boldsymbol{r}_\alpha \to \boldsymbol{r}_\alpha + \Delta\boldsymbol{r}_\alpha$. Its effect on the momentum-dependent Hamiltonian is a unitary transformation:

$$h(\boldsymbol{k}) \to e^{-i\boldsymbol{k}\cdot\Delta\hat{\boldsymbol{r}}} h(\boldsymbol{k}) e^{i\boldsymbol{k}\cdot\Delta\hat{\boldsymbol{r}}}, \tag{8.3}$$

with $[\Delta\hat{\boldsymbol{r}}]_{\alpha\beta} = \delta_{\alpha\beta}\Delta\boldsymbol{r}_\alpha$. Being unitary, such a deformation will not affect energies, and is automatically adiabatic. We only allow displacements that preserve the band-representability of the tight-binding Hilbert space.

Example of a deformation of the type (c-ii).— Let us consider the uniaxial tight-binding models [one example of such model is the P4 symmetric MRW model introduced in Eq. (4.24) of Sec. 4.4.2], where all of $\{\boldsymbol{R} + \boldsymbol{r}_\alpha\}$ lie on rotation-invariant axes. In the MRW model, $\boldsymbol{r}_\alpha = 0$ for all α, hence $h(\boldsymbol{k})$ is periodic, and the polarization $\mathscr{P}(\Pi)$ at C_n-invariant reduced momenta are quantized to integers, as verifiable in Fig. 4.2(d). An allowed deformation that maintains rotational symmetry is to move a basis orbital along a rotational axis; to maintain translational symmetry, all basis orbitals related by a Bravais-lattice translation must simultaneously be moved. It would follow that $\mathscr{P}(\Pi) \equiv_1 \sum_\alpha [\boldsymbol{r}_\alpha]_z$ is not generally integer-valued, with $[\boldsymbol{r}_\alpha]_z$ here referring to the coordinate on the rotational axis. Yet, differences in $\mathscr{P}(\Pi)$ over distinct C_n-invariant wavevectors remain quantized, and hence the returning Thouless pump (RTP) remains well-defined.

8.2 MULTICELLULARITY OF THE RTP AND HOPF INVARIANTS

Let us argue that the RTP invariant guarantees multicellular Wannier orbitals. In two-band models, interpreting the polarization $\mathscr{P}(\boldsymbol{k}_\perp)$ as the charge center of a hybrid Bloch-Wannier function [cf. Sec. 2.1.4.2], we conclude that a non-zero RTP invariant $\Delta\mathscr{P}_{\Pi_1\Pi_2} \neq 0$ ensures that the center of the hybrid function at Π_1 and Π_2 are positioned in different unit cells. Taking into account that the Wannier orbitals are related to the hybrid functions by a Fourier transform over the rBZ, a non-zero weight of the hybrid function at two unit cells ensures a non-zero weight of the corresponding Wannier orbital at these unit cells; therefore, the Wannier orbital is multicellular. This pictorial argument is generalized for the multi-band RTP invariant in Appendix D.2, where it is shown that a non-zero value of the RTP invariant is incompatible with a unicellular Wannier function.

Now we prove that a non-zero Hopf invariant $\chi \neq 0$ implies multicellularity independently from the RTP invariant. Note, that this is true in the absence of crystalline symmetries (except of translations which are necessary to ensure the restriction to two-band Hamitlonians). We prove multicellularity of the Hopf insulators by contradiction. Assume that the valence-band Wannier orbital is localizable to one unit cell, i.e., $W_{v\boldsymbol{0}}(\boldsymbol{R}, \alpha) = \delta_{\boldsymbol{R},\boldsymbol{0}}\kappa_v(\alpha)$, with $|\kappa_v\rangle$ a pseudo-spinor wave function that corresponds to a single point on the Bloch sphere S^2. The Fourier transform of $W_{v\boldsymbol{0}}(\boldsymbol{R}, \alpha)$ is then $\boldsymbol{k}$-independent, namely $|u_v(\boldsymbol{k})\rangle = |\kappa_v\rangle$. It is an eigenvector of a Hamiltonian that represents the trivial, constant map from the BZ to S^2, in contradiction with the assumed non-trivial Hopf invariant.

From the discussion in Chapter 7, we see that the specific forms of multicellularity – associated with the Hopf and RTP invariants – are delicate-topological. In fact, a stronger statement holds true, namely that *any* form of multicellularity existing in principle is a delicate property. In other words, for any fixed-band, insulating Hamiltonian (inclusive of, but going beyond, crystalline Hopf insulators) whose valence subspace is a band representation with a topological obstruction to being tightly-bound, this obstruction is removable by adding a certain tightly-bound band representation to either the conduction or the valence subspace. An argument based on the vector bundle theory that substantiates this statement is outlined in Appendix D.3.

8.3 GRADED MULTICELLULARITY

The RTP invariant suggests a refinement of multicellularity through the introduction of *grading*. In Sec. 8.3.1, we will first define graded multicellularity in the simplified case of an insulator whose valence subspace is composed of a single band with trivial first Chern class (i.e., a single, analytic Bloch function over the Brillouin torus). Such grading can meaningfully distinguish between different crystalline Hopf insulators, as we exemplify in Sec. 8.3.2. Finally, we extend the notion of multicellularity beyond two-band Hamiltonians in Sec. 8.3.3.

8.3.1 *Graded multicellularity in two-band Hamiltonians*

The *grade* $\mathfrak{g} \in \mathbb{Z}^+ \cup \{\infty\}$ is the lower bound on the number of primitive unit cells that make up a non-primitive cell,[1] which is able to contain a representative Wannier orbital; the lower bound is defined given that one is allowed to continuously deform a tight-binding Hamiltonian $h(\boldsymbol{k})$ of fixed matrix dimension while preserving the energy gap and crystalline symmetry. Note, that we allow to continuously and symmetrically deform the Wyckoff positions of the tight-binding-basis orbitals, as detailed in Sec. 8.1. At the same time for crystalline topological insulators in Wigner-Dyson classes A, AI and AII, the notion of grading is typically more useful when one imposes a local-symmetry condition [47, 120] on the Wannier orbitals. With this definition of grading, an insulator with $\mathfrak{g} = 1$ is referred to as *unicellular*, while all $\mathfrak{g} \geq 2$ (including $\mathfrak{g} = \infty$, in principle) correspond to different grades of multicellularity.

The notion of grading depends on whether the Wannier orbitals form an orthonormal basis for the valence band. To formalize this discussion, it is useful to distinguish between three kinds of Wannier orbitals: (1) the conventional *orthonormal ('on-') Wannier orbitals*, (2) the generalized *linear independent ('li-') Wannier orbitals*, and (3) the further relaxed *Wannier-type orbitals*.

As is well-known in the conventional case, assuming that the Chern class is trivial, *on*-Wannier orbitals are obtained by inverse Fourier transform of Bloch states [cf. Eq. (2.33)], with the (*i*) Bloch states depending smoothly on $\boldsymbol{k}$, and with (*ii*) the intra-cell components of the Bloch states being orthonormal at each $\boldsymbol{k}$:

$$\left\langle u_j^{on}(\boldsymbol{k}) \middle| u_{j'}^{on}(\boldsymbol{k}) \right\rangle = \delta_{jj'}, \quad j, j' = 1, \ldots, N_v + N_c. \tag{8.4a}$$

As respective consequences of (*i*–*ii*), the *on*-Wannier orbitals are (*i*) exponentially localized, and (*ii*) obey the orthonormality relation

$$\left\langle\!\left\langle W_{j,\boldsymbol{R}}^{on} \middle| W_{j',\boldsymbol{R}'}^{on} \right\rangle\!\right\rangle = \delta_{jj'}\delta_{\boldsymbol{R},\boldsymbol{R}'}, \tag{8.4b}$$

where $\boldsymbol{R}, \boldsymbol{R}'$ are Bravais-lattice vectors. In contrast, one may drop the normalization of the intra-cell components of the Bloch states but retain the weaker condition of orthogonality and completeness at each $\boldsymbol{k}$, resulting in *linear independent* $\left\{ \left| u_j^{li}(\boldsymbol{k}) \right\rangle \right\}_{j=1}^{N_v+N_c}$. Then the inverse Fourier transform generates *li*-Wannier orbitals, which loose their normalization and orthogonality but

1 A non-primitive cell is a path-connected volume of space that, when translated through all vectors of a Bravais lattice, does *not* cover all of space without either overlapping itself or leaving voids [10].

form a *complete* and *linear independent* basis of the Hilbert space. Similar to the *on*- case, the number of *li*-Wannier orbitals matches the dimensions of the valence resp. conduction subspace. Finally, the Wannier-*type* orbitals $\left\{\left|W_{j,\boldsymbol{R}}^{type}\right\rangle\right\rangle\Big\}_{j=1}^{N}$ considered by Ref. [172] constitute a potentially *overdetermined* basis with $N \geq N_v + N_c$, i.e., either the valence subspace or the conduction subspace (or both) are potentially represented by more Bloch states (and consequently, after applying the inverse Fourier transform, by more Wannier orbitals) than is the actual dimension of the respective band subspace. In this case, the only retained property is the *completeness* of the intra-cell components $\left\{\left|u_j^{type}(\boldsymbol{k})\right\rangle\right\}_{j=1}^{N}$ of the Bloch states at each $\boldsymbol{k}$.

Either kind of the Wannier representations is often required to be *exponentially-localized*, meaning that the amplitudes of the Wannier orbital can be bounded by $e^{-\|\boldsymbol{R}\|/r_w}$ with some width $r_w > 0$. A more stringent requirement is for the Wannier representation to be *compactly supported*, meaning that each Wannier orbital $\left|W_{j,\boldsymbol{R}}\right\rangle\rangle$ has non-vanishing amplitude on a finite number of sites that appear within a bounded region in space. Clearly, the grade $\mathfrak{g}$ could only be finite for the compactly supported Wannier orbitals.

One may ask if the graded multicellularity is more fruitfully defined in terms of the *on*-Wannier orbitals, the *li*-Wannier orbitals, or the Wannier-*type* orbitals. To place this question in a wider context, let us first review several basic relations between the existence of the various kinds of Wannier orbitals. In subsequent paragraphs, we review non-trivial results of three works [172, 182, 183] that have explored related themes.

First, note that having an exponentially-localized *on*-Wannier representation is a more stringent condition than having an exponentially-localized *li*-Wannier representation, and having either of them is more stringent than having an exponentially-localized Wannier-*type* representation. The analogous relations between the existence of *on*-Wannier/*li*-Wannier/Wannier-*type* representations also hold if we replace in the previous sentence 'exponentially-localized' by 'compactly supported'. More interestingly, if the valence subspace of a $\boldsymbol{k}$-periodic tight-binding Hamiltonian is diagonalized by (unnormalized) intra-cell functions $\left\{\left|u_j^{li}(\boldsymbol{k})\right\rangle\right\}_{j=1,\ldots,N_v}$ that are vector-valued polynomial functions of $\{e^{ik_\xi}\}_{\xi=x,y,z}$ with no zeros, the inverse Fourier transform of the intra-cell functions constitute representative compactly-supported *li*-Wannier orbitals. Since the normalization $\left\|\left|u_j^{li}(\boldsymbol{k})\right\rangle\right\|$ of a vector-valued polynomial is also guaranteed to be analytic with no zeros, the inverse Fourier transform of $\left|u_j^{li}(\boldsymbol{k})\right\rangle / \left\|\left|u_j^{li}(\boldsymbol{k})\right\rangle\right\| = \left|u_j^{on}(\boldsymbol{k})\right\rangle$ is an exponentially-localized *on*-Wannier orbital. Conversely, the non-existence of an exponentially-localized *on*-Wannier representation implies the non-existence of a compactly supported *li*-Wannier representation.

Let us next summarize the non-trivial results found by Refs. [172, 182, 183]. Assuming that the valence bands support an exponentially-localized Wannier-*type* (resp. exponentially-localized *on*-Wannier) representation, Ref. [172] (Ref. [183]) analyzed within the context of topological band theory whether the representation is *compactly supported*. In both cases, a non-trivial value of a topological invariant was found to obstruct the existence of a compactly supported Wannier representation (of the respective kind).

Namely, N. Read (generalizing an earlier work with J. Dubail [182]) showed in Ref. [172] that stable topological bands (i.e., bands belonging to a non-

trivial stable equivalence class in algebraic K-theory) in all Altland-Zirnbauer symmetry classes and in real-spatial dimensions $d \geq 2$ [22, 23] do not admit a (symmetric) compactly-supported Wannier-*type* representation, unless the nontriviality of the topological band is due solely to weak topological invariants existing already for $d = 1$. This obstruction is equivalent to saying that not all representative Wannier-*type* orbitals (respecting an Altland-Zirnbauer symmetry) can have finite extent, i.e., the 'grading' is infinite, if the notion of grade were generalized to apply to any band subspace (not just band representations), and if the lower bound on the number of primitive cells is defined in the stable-equivalence class (as opposed to an equivalence class of $h(\boldsymbol{k})$ with fixed matrix dimension).

More recently, Schindler and Bernevig in Ref. [183] showed that certain obstructed atomic insulators [31] (whose valence subspaces are band representations but whose conduction subspaces are fragile) do not admit a compactly-supported *on*-Wannier representation. This statement holds (in this case for the conventional *on*-Wannier orbitals) even if one allows for the matrix dimension of $h(\boldsymbol{k})$ to increase, so long as the conduction subspace remains fragile.

We thus find that in all the previous studies, the categorization into compact vs. non-compact has been used as a real-space-centric diagnostic for trivial vs. nontrivial band structures in the stable or fragile topological classification. (Here we view the Schindler-Bernevig model as a generalized example of fragile topology.)

Here, we opt for the 'middle ground' with respect to the three kinds of Wannier orbitals, by adopting the *fi*- case. Namely, what we propose is that:

(*a*) delicate topological insulators can have compactly-supported *fi*-Wannier orbitals, and that

(*b*) the grade $\mathfrak{g}$, as defined for *fi*-Wannier orbitals, offers a finer-grained notion of compactness, with different finite values of $\mathfrak{g}$ distinguishing different categories of delicate topological insulators.

Presently, we do not know if the analog of $\mathfrak{g}$, defined for conventional *on*-Wannier orbitals, can take finite values for delicate topological insulators. For the models presented here, the *on*-Wannier orbitals are infinite in extent.

8.3.2 *Graded multicellularity: case studies*

To exemplify Proposals (*a*–*b*) formulated in the last paragraph of Sec. 8.3.1, we proceed to briefly investigate bounds on the grade $\mathfrak{g}_{\text{Hopf}}$ of the Hopf insulator if we allow for continuous Hamiltonian deformation that may break any point group symmetry, and on the grade $\mathfrak{g}_{\text{RTP}}$ of an RTP insulator in the presence of rotation symmetry.

We begin with the case of the Hopf insulator. On one hand, based on the homotopic inequivalence of the Hopf-insulating Hamiltonian map to a constant map, it was shown in Sec. 8.2 that the Hopf insulator is not unicellular, implying a lower bound on the grade: $\mathfrak{g}_{\text{Hopf}} \geq 2$. On the other hand, one may consider the concrete MRW model of the Hopf insulator [55] [corresponding to the entry "P4, $\Delta\mathcal{L} = 1$, $\Delta\boldsymbol{r}_\perp = (0,0)$" in Table 4.2 and the Hopf invariant $\chi = -1$ or 2] with non-normalized valence intra-cell function:

$$\left|u_v^{fi}(\boldsymbol{k})\right\rangle = i\sigma_y \begin{pmatrix} \sin k_x + i \sin k_y \\ \sin k_z - i \left(\sum\limits_{\xi=x,y,z} \cos k_\xi + \Phi \right) \end{pmatrix}. \tag{8.5}$$

Its inverse Fourier transform yields an *li*-Wannier orbital supported over seven primitive unit cells: a 'central' cell, together with six 'adjacent' cells that are attributable to the appearance of $e^{\pm ik_{x,y,z}}$ in Eq. (8.5). Combining both results, we get that the grade for all Hamiltonians with the Hopf invariant $\chi = -1$ (and also $\chi = 2$) is bounded by

$$2 \leq \mathfrak{g}_{\text{Hopf}} \leq 7. \tag{8.6a}$$

The second example that we use to illustrate these ideas is the crystalline Hopf insulator characterized by RTP invariants $\Delta\mathscr{P}_{\Pi\Pi'}$ and by Hopf invariant χ [recall that the invariants are constrained through Eq. (6.5)]. For simplicity, let us assume that all rotation-invariant reduced momenta are encompassed in a single iso-orbital subset – which per Table 4.1 implies that $\Delta\boldsymbol{r}_\perp = (0,0)$, i.e., both basis orbitals lie along the same rotation axis. Because the polarization $\mathscr{P}_z(k_x, k_y)$ extends over at least $[1+\max_{\Pi,\Pi'}\{|\Delta\mathscr{P}_{\Pi\Pi'}|\}]$ rotation-invariant primitive unit layers, the *li*-Wannier orbital extends over at least the same number of primitive unit cells, giving the (rather generous) lower bound

$$\mathfrak{g}_{\text{RTP}} \geq 1 + \max_{\Pi,\Pi'}\{|\Delta\mathscr{P}_{\Pi\Pi'}|\} \tag{8.6b}$$

for the grade of RTP insulators.

In fact, a more restrictive lower bound than Eq. (8.6b) can be deduced by further considering the spread of the *li*-Wannier orbital in directions *perpendicular* to the rotation axis. Let us allude to the fact that, owing to the non-trivial value of any RTP invariant, (1) the valence band representation (VBR) of an RTP insulator *is not continuously deformable into* a basis band representation (BBR). However, it follows from the rotation eigenvalues of the valence band (under the stated assumption of a single all-encompassing iso-orbital subset) that (2) the VBR *is symmetry-equivalent to* a BBR spanned by one of the basis orbitals (let's say BBR$[\varphi_1]$).

We now argue as follows. First, the fact (1) implies that VBR must contain some contribution from orbital φ_2 in some unit cells. However, the symmetry equivalence of VBR to BBR$[\varphi_1]$, stated by fact (2), implies that the *li*-Wannier orbital transforms under C_n with the angular momentum $\mathcal{L}_1$ of orbital φ_1. This transformation rule precludes the φ_2 contribution from orbitals along the rotation axis. It can then be seen that the minimal way for the *li*-Wannier orbital to acquire a contribution from φ_2 orbitals while exhibiting the angular momentum $\mathcal{L}_1$ is due to an n-plet of sites that transform cyclically into each other under C_n in at least one of the $[1+\max_{\Pi,\Pi'}\{|\Delta\mathscr{P}_{\Pi\Pi'}|\}]$ rotation-invariant primitive unit layers. Therefore, under the stated assumptions (namely: space group Pn, an all-encompassing iso-orbital subset, and at least one RTP invariant with non-zero value), we find

$$\mathfrak{g}_{\text{RTP}} \geq n + \max_{\Pi,\Pi'}\{|\Delta\mathscr{P}_{\Pi\Pi'}|\}. \tag{8.6c}$$

In particular, for the non-trivial phases of the MRW model (which fulfill the stated assumption with $n = 4$ and $\max_{\Pi,\Pi'}\{|\Delta\mathscr{P}_{\Pi\Pi'}|\} = 1$), in combination with the argument presented before Eq. (8.6a), we obtain that

$$5 \leq \mathfrak{g}_{\text{MRW}} \leq 7. \tag{8.6d}$$

8.3.3 *Grading of models with* >2 *bands*

We finally generalize the definition of graded multicellularity to delicate topological insulators with an N_v-band valence subspace, i.e., the valence

subspace is spanned by $N_v > 1$ linearly independent Bloch states at each $\boldsymbol{k}$. For this purpose, it is convenient to adopt in the present subsection certain bundle-theoretic language: we view the valence subspace as a rank-N_v vector bundle, with an N_v-(complex)-dimensional vector space associated with each $\boldsymbol{k}$ of the base space (our Brillouin torus). In constructing the $\mathcal{fi}$-Wannier orbitals, we must first decompose the rank-N_v bundle into N_v unit-rank bundles (i.e., line bundles); this decomposition amounts to choosing N_v orthogonal (but not necessarily normalized) intra-cell functions $\left\{\left|u_j^{\mathcal{fi}}(\boldsymbol{k})\right\rangle\right\}_{j=1,\ldots,N_v}$ which span the N_v-dimensional vector space at each $\boldsymbol{k}$.

The inverse Fourier transform of $\left|u_j^{\mathcal{fi}}(\boldsymbol{k})\right\rangle$ defines representative (i.e., translation-inequivalent) $\mathcal{fi}$-Wannier orbitals $\left|W_{j,\boldsymbol{R}}^{\mathcal{fi}}\right\rangle\rangle$, and we define the *partial grade* $\mathfrak{g}_j$ of the j-th line bundle to be the number of primitive unit cells in which $\left|W_{j,\boldsymbol{R}}^{\mathcal{fi}}\right\rangle\rangle$ has a finite support. The *total grade* $\mathfrak{g}$ is then defined as the lower bound of the *sum* of the partial grades of all representative $\mathcal{fi}$-Wannier orbitals,

$$\mathfrak{g} - 1 = \min \sum_{j=1}^{N_v} \left(\mathfrak{g}_j - 1\right), \tag{8.7}$$

given that one is allowed to continuously deform the tight-binding Hamiltonian $h(\boldsymbol{k})$ of fixed matrix dimension while preserving the energy gap and crystalline symmetry.

For a concrete example, consider the case of an RTP insulator with an N_v-rank valence subspace and $\max_{\Pi,\Pi'}\{|\Delta\mathscr{P}_{\Pi\Pi'}|\} = M$, thereby generalizing the discussion of a crystalline Hopf insulator in Sec. 8.3.2. For simplicity, we also assume that all basis orbitals whose band representations coincide with the valence band representation at rotation invariant momenta Π are centered at the same position z_v along the rotation axis. We argue that the total grade $\mathfrak{g}$ obeys again the inequality (8.6b). Indeed, when one constructs the $\mathcal{fi}$-Wannier orbitals, the decomposition of the rank-N_v bundle into N_v line bundles leaves us a choice as to how to distribute the M quanta of 2π Zak phases among the N_v line bundles; effectively, we must choose an integer decomposition $M = \mathrm{n}_1 + \mathrm{n}_2 + \ldots + \mathrm{n}_{N_v}$.[2] This limits each partial grade to $\mathfrak{g}_j \geq 1 + \left|\mathrm{n}_j\right|$, and the total grade to $\mathfrak{g} \geq 1 + \sum_{j=1}^{N_v} \left|\mathrm{n}_j\right| \geq 1 + M$, irrespective of the rank of the valence subspace. We see that no matter how one performs the distribution, the inequality (8.6b) holds.

In addition, by adopting similar assumptions and arguments that led to Eq. (8.6c), we anticipate that each bundle with $\mathrm{n}_j \neq 0$ must have support on at least n unit cells within some rotation-invariant primitive unit layer. Optimally, one can imagine these n unit cells to be the same ones for each bundle (alternatively, one could imagine assigning all the M quanta of 2π Zak phase into a single bundle), allowing us to generalize to the (>2)-band case also the *stricter* bound in Eq. (8.6c).

Determining the exact value of the grade for Hopf and RTP insulators in space groups Pn, as well as of other multicellular topological insulators, constitutes an interesting question that we leave open for future studies. We further anticipate the grade as defined by Eq. (8.7) to be invariant under the addition of unicellular band representations that do not trivialize the delicate topological invariants, but further research is needed to firmly establish such a property of graded multicellularity.

2 Under the simplifying assumption of equal z centers of basis orbitals, each integer n_j corresponds to a charge center jump between two rotation-invariant momenta of a corresponding j-th band from the chosen vector bundle decomposition. These jumps are integer valued as all relevant basis orbitals are centered at the same z position in the BZ.

9

CONCLUSION AND OUTLOOK

In this thesis we introduced two new concepts in topological band theory. First, we defined delicate topology and explained its difference from fragile and stable topology. Second, we showed that delicate topological insulators can be described in terms of multicellular Wannier orbitals, and form an obstruction to localize these orbitals within one unit cell. Delicate and multicellular topological insulators would be missed by the modern classification schemes, such as K-theory [22], symmetry indicators [29] or topological quantum chemistry [31]. Here we developed novel methods, based on the notion of band representations [112, 113], to capture delicate topological invariants. Delicate topological insulators are the *simplest* topological insulators, in the sense that they are realizable by two-band Hamiltonians. In contrast, the minimal dimension of a tight-binding Hamiltonian matrix (at each momentum) that models a topological insulator with vanishing first Chern numbers is four in the case of stable topology, and three in the case of fragile topology [120].

In Chapter 4, we studied two-band delicate Hamiltonians whose n-fold rotation symmetry protects a new topological invariant – the returning Thouless pump (RTP) – in addition to the celebrated Hopf invariant that requires no point-group symmetry. Therefore we name these two-band insulators crystalline Hopf insulators. The RTP describes how the Zak phase advances by an integer multiple of 2π across half a reciprocal-lattice vector, then retracts by the same quantity over the next half of the same reciprocal-lattice vector. Such a Zak-phase evolution could conceivably be measured in interferometric experiments [184] with ultra-cold atoms or molecules [127, 185].

The RTP invariant extends Pontrjagin's seminal classification of two-band insulating Hamiltonians in three spatial dimensions [93, 97], which, in the case of trivial first Chern class, is given by the Hopf invariant. As proof of principle, we have found a tight-binding model with a trivial Hopf invariant but a nontrivial RTP invariant. In Chapter 6, we have exhaustively established mod-n relations between the Hopf and RTP invariants for all possible n-fold symmetric Hamiltonians ($n = 2, 3, 4, 6$); such relations allow to determine the Hopf invariant modulo n by a measurement of the Zak phase given the *a priori* knowledge of the itinerant angular momentum of bulk-conduction and bulk-valence bands. Presently we know of no other method, even existing in principle, to measure the Hopf invariant in condensed-matter systems.

In Chapter 5, we have proposed a bulk-boundary correspondence for Hopf and RTP invariants. A slab geometry of a Hopf insulator realizes teleportation of the Berry curvature from one slab surface to another, which leads to a surface Chern number despite the vanishing Chern numbers in the bulk. Specifically, the Chern number, computed for all occupied and unoccupied states localized on a single surface of the Hopf insulator is equal

in magnitude to the bulk Hopf invariant. Using these results, it was already shown in Ref. [166], that the Hopf insulator may exhibit quantized surface magnetism and higher-order topology. The RTP invariant in its turn reveals itself on rotation-symmetric crystal facets: the surface-localized states carry anomalous values of the itinerant angular momenta and of the Berry-Zak phase. These values are thus non-identical to the itinerant angular momenta, respectively to the Berry-Zak phase, of the bulk-conduction states, and also non-identical to corresponding quantities of the bulk-valence states. The itinerant angular momentum anomaly has further consequences: it guarantees the existence of metallic surface states, if the Hamiltonian matrix is sharply terminated at a rotation-symmetric facet. Such surface states are robust against continuous deformations of the *bulk* Hamiltonian that preserve both the bulk energy gap and Pn symmetry; however the same surface states can in principle be removed from any energy within the bulk energy gap, if the sharp boundary condition is relaxed. We expect the sharp boundary to be a good approximation to the surface termination of layered materials with weak, inter-layer, van-der-Waals coupling, such as Bi_2Se_3 [186, 187].

In Chapters 7 and 8, delicacy and multicellularity is proved for both the Hopf and the RTP invariants of the crystalline Hopf insulators. The RTP invariant is an example of symmetry-protected delicate topology, which allows generalizing it to models with more than two-bands assuming that the bulk valence and conduction bands transform differently under the symmetry. Furthermore, adopting a generalized definition of non-orthogonal Wannier orbitals, we introduced the notion of graded multicellularity, where the grade specifies the minimal number of unit cells necessary to host the multicellular Wannier function. In order to derive a lower bound, the grade is minimized over all Hamiltonians that can be continuously deformed into each other, while preserving the gap and the protecting symmetry. We derived top and bottom bounds on the value of the grade in crystalline Hopf insulators, showing that it is finite. Whether this grade remains finite for the standard choice of orthonormal Wannier orbitals or these orbitals are inevitably non-compact as in Ref. [183] (i.e. they extend over infinite number of unit cells) is an interesting question for further research.

Given the novel and unconventional theoretical properties of delicate topological insulators presented in this thesis, the biggest open question is their materialization or experimental simulation. With this goal in mind, one presently-achieved advancement (presented in Chapter 3) is an elucidation of the topological semimetallic phases that generically intermediate the transition from trivial to crystalline Hopf insulators. In particular, we have found that the crystalline-Hopf phase lies in proximity to a mirror-symmetry-protected, nodal-line semimetal previously studied in Ref. [126]; this mirror-protected semimetal is the only delicate topological semimetal that we know presently, and demonstrates that the returning Thouless pump (and its corresponding boundary anomalies) are generalizable concepts with a wider applicability beyond rotation-symmetric Hamiltonians.[1] One may then conceive the strategy of beginning from an existing Weyl or nodal-line semimetal, then inducing an energy gap by material engineering to enter the Hopf/RTP insulator phase. In this regard, we remark that a delicate-topological semimetallic Hamiltonian similar to our case study in Eq. (3.29) has been previously applied to model the ferromagnetic compound $HgCr_2Se_4$ [189]. Additionally, strain-induced conversions of mirror-related

1 While not directly applicable to metals, a three-band touching in the phonon band structure was recently argued to be delicate topological [188].

Weyl points to mirror-protected nodal loops were recently predicted [190] for a family of two-element hexagonal compounds, including ZrTe, MoC and WC, with the initial motivation of materializing band degeneracies with non-Abelian topological charges [191]; it would be interesting to revisit these materials with a focus on mirror-protected delicate topology.

A possible complication in materializing Hopf/RTP insulators is the observation that in most known tight-binding models, next-nearest-neighbor hoppings have larger magnitude than nearest-neighbor hoppings. It is interesting to analyze whether this is required by principle. If not, a theoretical development of tight-binding Hamiltonians with larger nearest-neighbor hoppings is an important step to expand the material options for an experimental realization. However, it is worth remarking that having larger next-nearest-neighbor hoppings is not physically unrealistic – one would consider materials which lie further from the tight-binding limit and closer to the nearly-free-electron regime [10]; it may also be necessary to look for basis Wannier orbitals which represent anisotropic hybridizations of multiple chemical orbitals. Beyond solid-state realizations, a recent proposal [127, 185] suggests a way to realize long-ranged hoppings in periodically driven ultra-cold dipolar molecules trapped in an optical lattice.

A second difficulty in Hopf/RTP materializations is that realistic materials often require more than a two-band description. A generalization of the Hopf invariant to arbitrarily many (say N) bands exists, assuming that all N bands are energetically detached from one another [167]. Whether or not such generalization is easier to materialize than the two-band Hopf insulator remains to be seen. Here we showed that the RTP invariant allows an alternative generalization to more-than-two-band Hamiltonians without requiring all bands to be detached from each other, and hence a multi-band RTP insulator is a more promising candidate for materialization. Symmetry protection of the RTP invariant suggests a high-throughput algorithm of searching for a material realization. First, one needs to identify all space groups that are compatible with non-zero RTP invariants. For these groups, one can search for concrete materials, invariant under elements of these groups, in material databases [192, 193]. Among the materials with available electronic structure, the relevant candidates are those, whose low energy band representations fulfill the necessary conditions for quantization of the RTP invariants (cf. Sec. 7.3.1). Computing the RTP invariants using first-principle techniques [194] for these candidates will reveal materials in delicate topological phases.

Another important direction of further research is finding examples of delicate topology beyond our assumption of rotational symmetry and a trivial Chern class. There are three possible directions of generalization. Firstly, investigating existence of delicate topology in other Altland-Zirnbauer symmetry classes (cf. Table 2.1) is important for a more complete classification of delicate topological phases. Secondly, one can study delicate topological invariants protected by other crystalline symmetries. For instance, mirror symmetry can also protect an RTP invariant (as demonstrated by our case study in Sec. 7.4), while it forces the Hopf invariant to be zero for 3D-translation-invariant Hamiltonians. However, a systematic study of mirror-protected delicate topology in all spatial dimensions is still lacking and would be desirable. Finally, the extension of the Pontrjagin classification in the presence of rotation symmetry could be generalized to models with a non-trivial first Chern class. In this case, the two-band models in the absence of point-group symmetries are classified by four invariants: three

Chern numbers computed on two-dimensional cuts of the BZ and the fourth invariant that takes integer values modulo twice the greatest common divisor of the three Chern numbers [93, 95]. It is possible that some analog of the topological invariants discussed here will likewise acquire an ambiguity depending on the Chern class.

In summary, this thesis opens the world of novel topological phases of matter – named delicate – which are defined under a relaxed stability condition. The discussed bulk and boundary properties of these insulators present yet unexplored grounds within non-interacting topological band theory and show that the classification of topological insulators is not yet complete. Going beyond non-interacting picture, one may ask whether delicate topology can be defined in interacting systems and how multicellularity of the corresponding Wannier orbitals affects the range of interactions. This is an interesting direction for future research.

Part III

APPENDIX

A

MORE ON BERRY DIPOLE

A.1 ROTATION-INVARIANT SPINOR-FORM HAMILTONIAN

In this Appendix, we derive a rotation-symmetric $\boldsymbol{k}\cdot\boldsymbol{p}$ Hamiltonian of the spinor form specified by Eq. (3.4). This is achieved in two ways.

First, we derive the $\boldsymbol{k}\cdot\boldsymbol{p}$ Hamiltonian assuming the continuous rotation symmetry, which restricts the Hamiltonian as specified in Eq. (3.2). This discussion is organized into three parts. First, in Appendix A.1.1 we translate the symmetry requirement of the Hamiltonian matrix $h^{\boldsymbol{k}\cdot\boldsymbol{p}}(\boldsymbol{k})$ to a condition on the spinor $\zeta(\boldsymbol{k})$. In Sec. A.1.2 we derive the general symmetry-compatible form of the spinor $\zeta(\boldsymbol{k})$ to the lowest order in each momentum component and in the tunable parameter ϕ. Then, in Appendix A.1.3 we show how the obtained general form can always be continuously deformed into the simple form shown in Eq. (3.3) of the main text.

Second, we derive the symmetry-allowed $\boldsymbol{k}\cdot\boldsymbol{p}$ Hamiltonian as a Taylor expansion of a lattice Hamiltonian around a rotation-invariant momentum. For this, in Appendix A.1.4, we show that the $\boldsymbol{k}\cdot\boldsymbol{p}$ Hamiltonian is symmetric under discrete rotation symmetry, specified by the itinerant rotation matrix of the lattice Hamiltonian at the considered rotation-invariant momentum. Finally, in Appendix A.1.5, we derive the general form of the spinor with discrete rotation symmetry.

A.1.1 *Equivalent symmetry condition on the spinor function*

We first show that if the symmetry condition in Eq. (3.2) is applied to spinor-form Hamiltonians [Eq. (3.4)], then this is equivalent to the following condition on the spinor function:

$$R_\theta \zeta(\boldsymbol{k}) = e^{i\beta(\boldsymbol{k})}\zeta(\theta\boldsymbol{k}), \quad R_\theta = e^{-i(\theta\Delta\ell/2)\sigma_z}, \tag{A.1}$$

where β is an arbitrary $\boldsymbol{k}$-dependent phase. To show this, recall that conjugation of a Pauli matrix σ_i with $\exp(i\omega\sigma_z)$ gives

$$\begin{aligned} &\exp(i\omega\sigma_z)\sigma_i \exp(-i\omega\sigma_z) = T(2\omega)_{ij}\sigma_j \\ &\text{with} \quad T(\omega) = \begin{pmatrix} \cos\omega & -\sin\omega & 0 \\ \sin\omega & \cos\omega & 0 \\ 0 & 0 & 1 \end{pmatrix}. \end{aligned} \tag{A.2}$$

By choosing the particular value $\omega = -\theta\Delta\ell/2$ we obtain $R_\theta \sigma_i R_\theta^{-1} = T(-\theta\Delta\ell)_{ij}\sigma_j$. The application of this relation to the spinor-form Hamiltonian in Eq. (3.4) gives

$$\begin{aligned} R_\theta h(\boldsymbol{k}) R_\theta^{-1} &= [\zeta^\dagger \sigma_i \zeta] T(-\theta\Delta\ell)_{ij}\sigma_j \\ &= [\zeta^\dagger T(\theta\Delta\ell)_{ji}\sigma_i \zeta]\sigma_j \\ &= [\zeta^\dagger R_\theta^{-1}\boldsymbol{\sigma} R_\theta \zeta]\cdot\boldsymbol{\sigma}\Big|_{\boldsymbol{k}}, \end{aligned} \tag{A.3}$$

where the last line reminds us that the function ζ (in all of the consecutive expressions) is to be evaluated at $\boldsymbol{k}$. Separately, the symmetry condition in Eq. (3.2) applied to the spinor-form Hamiltonian in Eq. (3.4) implies

$$R_\theta h(\boldsymbol{k}) R_\theta^{-1} = [\zeta^\dagger \boldsymbol{\sigma}\zeta]\cdot\boldsymbol{\sigma}\Big|_{\theta\boldsymbol{k}}, \tag{A.4}$$

i.e., evaluated at $\theta\boldsymbol{k}$. The relation in Eq. (A.1) follows from comparing Eqs. (A.3) and (A.4) after considering that

$$\zeta^\dagger\boldsymbol{\sigma}\zeta = \xi^\dagger\boldsymbol{\sigma}\xi \;\Leftrightarrow\; \zeta = \xi e^{i\beta} \tag{A.5}$$

with β an arbitrary phase factor (compare also to the first part of Dets. 3.2). The equivalence in Eq. (A.5) follows because $\zeta^\dagger\boldsymbol{\sigma}\zeta$ can be interpreted as the expectation value of spin for spinor ζ, and the expectation value of all spin components can agree for a pair of spinors only if they differ by an unobservable phase factor.

A.1.2 *General form of the spinor function*

To ensure that $h(\boldsymbol{k})$ is analytic in $\boldsymbol{k}$, we impose that $\zeta(\boldsymbol{k})$ is also analytic and hence admits convergent Taylor expansions in $\boldsymbol{k}$. Given the symmetry condition (A.1) on the spinor function $\zeta(\boldsymbol{k})$, we aim to find the most general symmetry-compatible choice of the spinor up to linear order in (k_x, k_y, k_z), with the motivation that $\boldsymbol{k} = \boldsymbol{0}$ marks a prospective band-touching point. The zeroth-order-in-$\boldsymbol{k}$ term is parametrized by an additional real parameter ϕ, such that $\zeta(\boldsymbol{k} = \boldsymbol{0}, \phi = 0) = 0$:

$$\zeta^{(0)}(\boldsymbol{k},\phi) = \begin{pmatrix} A_1 k_+ + B_1 k_- + C_1(k_z + i\phi) + D_1(k_z - i\phi) \\ A_2 k_+ + B_2 k_- + C_2(k_z + i\phi) + D_2(k_z - i\phi) \end{pmatrix}, \tag{A.6}$$

where $k_\pm = k_x \pm i k_y$, and A_j, B_j, C_j, D_j $(j = 1, 2)$ are complex coefficients. We derive constraints on these coefficients by plugging the ansatz into Eq. (A.1). Note that one side of the equation is multiplied by the phase $e^{i\beta(\boldsymbol{k})}$, which is required to be analytic such that $\zeta(\boldsymbol{k})$ is also analytic. In the following, we assume it to be $\boldsymbol{k}$-independent, $\beta(\boldsymbol{k}) = \beta$, as all $\boldsymbol{k}$-dependent terms will contribute to higher orders in $(\boldsymbol{k}, \phi)$. Since the variables $k_\pm$, $k_z \pm i\phi$ are independent of each other, we proceed by equating the coefficients that multiply them on the left vs. the right side of the equation.

We proceed in steps as follows.

(*i*) Equate the coefficients in front of $k_z + i\phi$ and $k_z - i\phi$, get:

$$C_1 e^{-i\theta\Delta\ell/2} = C_1 e^{i\beta}, \qquad C_2 e^{i\theta\Delta\ell/2} = C_2 e^{i\beta}. \tag{A.7a}$$

$$D_1 e^{-i\theta\Delta\ell/2} = D_1 e^{i\beta}, \qquad D_2 e^{i\theta\Delta\ell/2} = D_2 e^{i\beta}. \tag{A.7b}$$

If we assume that $\beta \neq \pm\theta\Delta\ell/2$, then $C_{1,2} = D_{1,2} = 0$, implying that the spinor dependence on k_z and ϕ is of higher order. We ignore such a possibility as it requires fine tuning, leaving us with the following two possibilities: either $\beta = \theta\Delta\ell/2$ or $\beta = -\theta\Delta\ell/2$. We opt for the first of the two options, and comment on the other choice at the end of this section. In that case, we find that

$$D_1 = C_1 = 0, \tag{A.8}$$

while C_2 and D_2 are arbitrary.

(*ii*) Equate the coefficients in front of k_+:

$$A_1 \left[e^{-i\theta\Delta\ell/2} - e^{i\theta\Delta\ell/2} e^{i\theta} \right] = 0, \tag{A.9a}$$

$$A_2\, e^{i\theta\Delta\ell/2} \left[1 - e^{i\theta} \right] = 0. \tag{A.9b}$$

From this we conclude that

$$\begin{aligned} &A_2 = 0, \\ &A_1 \neq 0, \quad \text{if } \Delta\ell = -1. \end{aligned} \tag{A.10}$$

Both coefficients vanish if $\Delta\ell \neq -1$, (cf. implications below).

(*iii*) Similarly equate the coefficients in front of k_- to get:

$$\begin{aligned} &B_2 = 0, \\ &B_1 \neq 0, \quad \text{if } \Delta\ell = 1. \end{aligned} \tag{A.11}$$

It follows from Eqs. (A.10) and (A.11) that if $|\Delta\ell| \neq 1$ then all linear terms in $k_\pm$ vanish. In that case, we are led to include higher-order terms in the ansatz (A.6).

The possible second-order contributions in $k_\pm$ are

$$\zeta^{(1)}(k_+, k_-) = \begin{pmatrix} L_1 k_+^2 + M_1 k_-^2 + N_1 k_+ k_- \\ L_2 k_+^2 + M_2 k_-^2 + N_2 k_+ k_- \end{pmatrix}. \tag{A.12}$$

with six complex coefficients. We deduce the coefficients in front of the quadratic terms in the same way as for the linear terms.

(*i*) First, equate coefficients in front of $k_+ k_-$:

$$N_1 e^{-i\theta\Delta\ell/2} = N_1 e^{i\theta\Delta\ell/2}, \tag{A.13a}$$

$$N_2 e^{i\theta\Delta\ell/2} = N_2 e^{i\theta\Delta\ell/2}. \tag{A.13b}$$

From this we conclude that $N_1 = 0$, while N_2 can take arbitrary values. Therefore, independent of the Berry-dipole spin $\Delta\ell$, the second component of the spinor generically depends on the quadratic form $k_+ k_- = k_x^2 + k_y^2$.

(*ii*) Equate coefficients in front of k_+^2:

$$L_1 \left[e^{-i\theta\Delta\ell/2} - e^{i\theta\Delta\ell/2} e^{i2\theta} \right] = 0, \tag{A.14a}$$

$$L_2\, e^{i\theta\Delta\ell/2} \left[1 - e^{i2\theta} \right] = 0. \tag{A.14b}$$

This gives

$$\begin{aligned} &L_2 = 0, \\ &L_1 \neq 0, \quad \text{if } \Delta\ell = -2. \end{aligned} \tag{A.15}$$

(*iii*) Similarly for coefficients in front of k_-^2 we get:

$$\begin{aligned} &M_2 = 0, \\ &M_1 \neq 0, \quad \text{if } \Delta\ell = 2. \end{aligned} \tag{A.16}$$

For $|\Delta\ell| = 2$ Eqs. (A.15) and (A.16) define quadratic dependence on $k_\pm$ in the first component of the spinor. However, for $|\Delta\ell| > 2$ these contributions vanish and we need to consider still higher orders in $k_\pm$.

In the following we derive the lowest-in-$k_\pm$ term that is allowed by a given Berry-dipole spin $\Delta\ell$ in the first component of the spinor. To achieve this, we first derive all allowed terms of the form $k_+^p k_-^q$ with p, q being non-negative integers (the set $\mathbb{N} \cup \{0\}$), and then among these terms find the one with the lowest order $p + q$.

(*i*) Equate coefficients in front of $k_+^p k_-^q$ in the first component of the spinor:

$$e^{-i\theta\Delta\ell/2} = e^{i\theta\Delta\ell/2} e^{i\theta(p-q)}. \tag{A.17}$$

This equation is fulfilled if $q - p = \Delta\ell$, and hence, the allowed terms have the form $k_+^p k_-^{p+\Delta\ell}$ with both $p, p + \Delta\ell \in \mathbb{N} \cup \{0\}$. This pair of conditions can be expressed compactly as $p \geq \max\{0, -\Delta\ell\}$.

(*ii*) To find among all allowed terms the one with the lowest order, we need to find

$$p_* = \underset{p \geq \max\{0,-\Delta\ell\}}{\arg\min} \; (2p + \Delta\ell), \tag{A.18a}$$

which, depending on the sign of $\Delta\ell$, is

$$p_* = \begin{cases} 0, & \Delta\ell > 0 \\ -\Delta\ell, & \Delta\ell < 0 \end{cases}. \tag{A.18b}$$

Therefore, given the value $\Delta\ell$, the first component of the spinor to the lowest order in $k_\pm$ is $\left(k_{-\,\mathrm{sgn}(\Delta\ell)}\right)^{|\Delta\ell|}$.

By combining all the constraints derived for a given Berry-dipole spin $\Delta\ell$, we get the general form of the rotation-symmetric spinor:

$$\zeta(\boldsymbol{k}, \phi) = \begin{pmatrix} Z_{\Delta\ell} \left(k_{-\,\mathrm{sgn}(\Delta\ell)}\right)^{|\Delta\ell|} \\ C_2(k_z + i\phi) + D_2(k_z - i\phi) + N_2 k_+ k_- \end{pmatrix}, \tag{A.19}$$

where $Z_{\Delta\ell}$, C_2, D_2 and N_2 are arbitrary complex coefficients.

Let us conclude the discussion by analyzing how the result changes if we instead adopt the second option of the phase, $\beta = -\theta\Delta\ell/2$. Then, following the steps that were described in this section, we derive that the spinor function has the form

$$\zeta(\boldsymbol{k}, \phi) = \begin{pmatrix} C_1(k_z + i\phi) + D_1(k_z - i\phi) + N_1 k_+ k_- \\ Z'_{\Delta\ell} \left(k_{\mathrm{sgn}(\Delta\ell)}\right)^{|\Delta\ell|} \end{pmatrix}. \tag{A.20}$$

To understand the difference between the two Hamiltonians, respectively defined through spinors (A.19) and (A.20), we note that the conduction

band of the spinor-form Hamiltonian [Eq. (3.4)] is proportional to the spinor $|u_c(\boldsymbol{k})\rangle \propto \zeta(\boldsymbol{k})$, while the valence band can be expressed as $|u_v(\boldsymbol{k})\rangle \propto \sigma_y \zeta^*(\boldsymbol{k})$. We can define an angular momentum $\ell_{v(c)}$ of the valence (conduction) eigenstate at the rotation axis as

$$R_\theta \left| u_{v(c)}(0,0,k_z) \right\rangle = e^{i\theta \ell_{v(c)}} \left| u_{v(c)}(0,0,k_z) \right\rangle . \tag{A.21}$$

Both the Hamiltonian $h(\boldsymbol{k})$ and the rotation matrix R_θ are expressed in a basis given by the orbitals φ_1, φ_2; since the rotation matrix is diagonal in this basis, these orbitals get a factor $e^{-i\theta\Delta\ell/2}$ resp. $e^{i\theta\Delta\ell/2}$ under rotation by an angle θ and therefore have angular momenta $\ell_{1(2)} = -(+)\Delta\ell/2$. Since valence and conduction bands at rotation axis diagonalize the rotation matrix, the set $\{\ell_v, \ell_c\}$ coincides with the set $\{\pm\Delta\ell/2\}$, meaning that at rotation axis the valence and conduction bands are of a single orbital character. Computing the valence and conduction angular momenta for the spinor (A.19), we observe that a valence (resp. conduction) band has angular momentum $\ell_v = -\Delta\ell/2$ (resp. $\ell_c = \Delta\ell/2$), meaning that it is of the φ_1 (resp. φ_2) character. For the spinor (A.20), the valence (resp. conduction) angular momentum has opposite sign and the corresponding band is of the φ_2 (resp. φ_1) character.

To relate the valence (resp. conduction) band given by spinor (A.20) to the valence (resp. conduction) band given by spinor (A.19), it is enough to flip the order of the basis orbitals and change the sign of the Berry-dipole spin in the rotation matrix written in the new basis. This deformation allows us to extend the results presented for the spinor (3.3) in Chapter 3 to the spinor (3.5), which are the simplified forms of the spinors (A.19) and (A.20), respectively.

A.1.3 *Continuous deformation of the spinor to simplified form*

Consider a Hamiltonian $h(\boldsymbol{k}, \phi)$ [cf. Eq. (3.4)] encoded by the spinor in Eq. (A.19). Let us first argue what are the allowed continuous deformations of this Hamiltonian that preserve its rotation symmetry and 'topology', in a sense that will be made increasingly precise.

Let us assume the energy bands of $h(\boldsymbol{k}, \phi)$ touch at $(\boldsymbol{k}, \phi) = (\boldsymbol{0}, 0)$ and nowhere else in the $(\boldsymbol{k}, \phi)$-space, which we take to be isomorphic to $\mathbb{R}^4$. For any constant-ϕ slice of $(\boldsymbol{k}, \phi)$-space, one can define a three-parameter Hamiltonian $h(\boldsymbol{k})$ and its associated continuum Hopf and Zak numbers [cf. Eqs. (3.15) and (3.16)]. These numbers are the $\boldsymbol{k} \cdot \boldsymbol{p}$ analogs of the Hopf and RTP-Zak invariants for tight-binding Hamiltonians. Assuming that $h(\boldsymbol{k})$ is a truncated Taylor expansion of a tight-binding Hamiltonian, changes in the continuum Hopf/Zak numbers (as ϕ is tuned through zero) equal changes in the lattice Hopf/RTP invariants (of the tight-binding Hamiltonian which regularizes the $\boldsymbol{k} \cdot \boldsymbol{p}$ Hamiltonian). In particular, this implies

$$\delta\chi^{\text{cont.}} = \chi^{\text{cont.}}(\phi = 0^+) - \chi^{\text{cont.}}(\phi = 0^-) \in \mathbb{Z}. \tag{A.22}$$

This integer quantization holds under continuous deformation of the $\boldsymbol{k} \cdot \boldsymbol{p}$ Hamiltonian $h(\boldsymbol{k}, \phi; t)$ parametrized by $t \in [0, 1]$, if we impose for all t that the energy gap closes only at $(\boldsymbol{k}, \phi) = (\boldsymbol{0}, 0)$.

This freedom given to us by the t parameter allows us to bring the spinor derived in Eq. (A.19) to a simpler form. The condition that the gap closes only at $(\boldsymbol{k}, \phi) = (\boldsymbol{0}, 0)$ can be enforced by insisting that $|Z_{\Delta\ell}| \neq 0$ and $|C_2| \neq |D_2|$. Indeed, the gap closes if and only if $\zeta = 0$. Imposing that the first component of ζ vanishes implies $k_{-\,\mathrm{sgn}(\Delta\ell)} = 0$, and hence also $N_2 k_+ k_- = 0$. Then

the second component of ζ equal to zero is equivalent to $C_2(k_z + i\phi) = -D_2(k_z - i\phi)$, which implies that $(|C_2| - |D_2|)\sqrt{k_z^2 + \phi^2} = 0$. This means that when $|C_2| \neq |D_2|$, the spinor turns to zero only at $(\boldsymbol{k}, \phi) = (\boldsymbol{0}, 0)$.

Hence, we are allowed to continuously adjust the coefficients to certain preferred values as long as we avoid $|Z_{\Delta\ell}| = 0$ (and also avoid $|C_2| = |D_2|$) throughout the interpolation. Since this constraint on our interpolation does not involve N_2, we can always set this parameter to zero. We may as well take $Z_{\Delta\ell} = 1$. The selected values of C_2 and D_2 depend on the ratio between their magnitudes. We choose $C_2 = 1$, $D_2 = 0$ if $|C_2| > |D_2|$ and $C_2 = 0$ $D_2 = -1$ if $|C_2| < |D_2|$. There exists a continuous deformation of the spinor-form Hamiltonian from arbitrary initial values of the coefficients to the specified ones without closing the energy gap and without breaking the rotation symmetry (and thus without altering the topological invariants of the corresponding Berry dipole). The final form of the spinor is

$$\zeta(\boldsymbol{k}, \phi) = \begin{pmatrix} \left(k_{-\,\mathrm{sgn}(\Delta\ell)}\right)^{|\Delta\ell|} \\ v\,k_z + i\phi \end{pmatrix}, \tag{A.23}$$

where

$$v = \mathrm{sgn}(|C_2| - |D_2|) \in \{-1, 1\}. \tag{A.24}$$

This is the form of the spinor utilized throughout the main text, beginning from Eq. (3.3). A similar deformation performed on the spinor in Eq. (A.20) leads to

$$\zeta(\boldsymbol{k}, \phi) = \begin{pmatrix} v\,k_z + i\phi \\ \left(k_{\mathrm{sgn}(\Delta\ell)}\right)^{|\Delta\ell|} \end{pmatrix}. \tag{A.25}$$

A.1.4 *Symmetry of $\boldsymbol{k}\cdot\boldsymbol{p}$-expansion of a lattice Hamiltonian*

In this Appendix we derive the rotation-symmetry constraint of a lattice Hamiltonian expanded for small $\boldsymbol{k}$ around a rotation-symmetric point in the BZ. A lattice Hamiltonian obeys the following symmetry condition:

$$R_{C_m} h(\boldsymbol{k}) R_{C_m}^{-1} = h(C_m \boldsymbol{k}). \tag{A.26}$$

We now expand the Hamiltonian around point $\boldsymbol{k}_\Pi = (\Pi, k_z)$ where the reduced momentum Π is shifted by a reciprocal lattice vector after m-fold rotation, $C_m\Pi = \Pi + \boldsymbol{G}_\Pi$. Adopting the local momentum $\boldsymbol{\kappa} = \boldsymbol{k} - \boldsymbol{k}_\Pi$, we obtain

$$\begin{aligned} R_{C_m} h(\boldsymbol{k}_\Pi + \boldsymbol{\kappa}) R_{C_m}^{-1} &= h(C_m \boldsymbol{k}_\Pi + C_m \boldsymbol{\kappa}) \\ &= h(\boldsymbol{k}_\Pi + \boldsymbol{G}_\Pi + C_m \boldsymbol{\kappa}). \end{aligned} \tag{A.27}$$

We use that the Hamiltonians at momenta shifted by a reciprocal lattice vector are related by

$$h(\boldsymbol{k} + \boldsymbol{G}) = V_{\boldsymbol{G}}^{-1} h(\boldsymbol{k}) V_{\boldsymbol{G}}\ , \tag{A.28}$$

with $[V_{\boldsymbol{G}}]_{\alpha\beta} = \exp(i\boldsymbol{r}_\alpha \cdot \boldsymbol{G})\delta_{\alpha\beta}$. Applying this relation to Eq. (A.27) we get

$$V_{\boldsymbol{G}_\Pi} R_{C_m} h(\boldsymbol{k}_\Pi + \boldsymbol{\kappa}) (V_{\boldsymbol{G}_\Pi} R_{C_m})^{-1} = h(\boldsymbol{k}_\Pi + C_m \boldsymbol{\kappa}). \tag{A.29}$$

We now expand the Hamiltonian at small $\boldsymbol{\kappa}$ around $\boldsymbol{k}_\Pi$ and denote this expansion as $h^{\boldsymbol{k}\cdot\boldsymbol{p}}(\boldsymbol{\kappa})$. Using the itinerant rotation matrix defined in Eq. (4.5), we get the symmetry condition on the $\boldsymbol{k}\cdot\boldsymbol{p}$-Hamiltonian

$$\widetilde{R}_{C_m}(\Pi) h^{\boldsymbol{k}\cdot\boldsymbol{p}}(\boldsymbol{\kappa}) \widetilde{R}_{C_m}^{-1}(\Pi) = h^{\boldsymbol{k}\cdot\boldsymbol{p}}(C_m \boldsymbol{\kappa}). \tag{A.30}$$

The itinerant rotation matrix can be written as

$$\widetilde{R}_{C_m}(\Pi) = \exp\left(-i\pi\frac{\widetilde{\mathcal{L}}_2(\Pi) - \widetilde{\mathcal{L}}_1(\Pi)}{m}\sigma_z\right). \tag{A.31}$$

Therefore, the Berry-dipole spin $\Delta\ell$ in the $\boldsymbol{k}\cdot\boldsymbol{p}$ expansion around $\boldsymbol{k}_\Pi$ is given modulo the order of rotation symmetry m by the itinerant angular momentum difference $\widetilde{\mathcal{L}}_2(\Pi) - \widetilde{\mathcal{L}}_1(\Pi)$ between the basis Bloch states.

A.1.5 *Spinor function of $\boldsymbol{k}\cdot\boldsymbol{p}$-expansion of a lattice Hamiltonian*

In this Appendix we derive a spinor in the lowest order in $(\boldsymbol{\kappa}, \phi)$ that is allowed by the discrete rotation symmetry (A.30) of a $\boldsymbol{k}\cdot\boldsymbol{p}$ Hamiltonian around momentum $\boldsymbol{k}_\Pi$ and of the spinor form (3.4). To fix the notations, we assume that at rotation-invariant line γ_Π [line projected onto Π in the (k_x, k_y) plane] the valence band coincides with a band representation induced from the first basis orbital φ_1. (We will comment on the opposite choice, when the orbital φ_2 induces the valence band representation, at the end of this Appendix.) This means that the valence (conduction) itinerant angular momentum $\widetilde{\mathcal{L}}_{v(c)}(\Pi)$ is equal to the itinerant angular momentum of the first (second) basis orbital $\widetilde{\mathcal{L}}_{1(2)}(\Pi)$, and the itinerant rotation matrix in Eq. (A.31) can be rewritten as

$$\widetilde{R}_{C_m}(\Pi) = \exp\left(-i\pi\frac{\Delta\widetilde{\mathcal{L}}(\Pi)}{m}\sigma_z\right), \tag{A.32}$$

where $\Delta\widetilde{\mathcal{L}}(\Pi) = \widetilde{\mathcal{L}}_c(\Pi) - \widetilde{\mathcal{L}}_v(\Pi) \pmod m$. The sought spinor is then continuously deformable to

$$\zeta(\boldsymbol{\kappa}, \phi) = \begin{pmatrix} A\kappa_-^{\Delta\widetilde{\mathcal{L}}(\Pi)} + B\kappa_+^{m-\Delta\widetilde{\mathcal{L}}(\Pi)} \\ v\kappa_z + i\phi \end{pmatrix}, \tag{A.33}$$

where $v \in \{-1, 1\}$ is defined as in Sec. A.1.3. Depending on the value of $\Delta\widetilde{\mathcal{L}}(\Pi)$, we can further deform the first component of the spinor (A.33) to

$$\zeta_1(\boldsymbol{\kappa}) = \begin{cases} \kappa_-^{\Delta\widetilde{\mathcal{L}}(\Pi)} & \text{if } \Delta\widetilde{\mathcal{L}}(\Pi) < m/2 \quad \text{or} \quad \begin{cases} \Delta\widetilde{\mathcal{L}}(\Pi) = m/2 \\ |A| > |B| \end{cases} \\ \kappa_+^{m-\Delta\widetilde{\mathcal{L}}(\Pi)} & \text{if } \Delta\widetilde{\mathcal{L}}(\Pi) > m/2 \quad \text{or} \quad \begin{cases} \Delta\widetilde{\mathcal{L}}(\Pi) = m/2 \\ |A| < |B| \end{cases} \end{cases}. \tag{A.34}$$

Throughout these deformations the gap does not close and therefore the value of the continuum Hopf and Zak phase numbers do not change. By identifying the power of the $\kappa_\pm$ in Eq. (A.34) with the absolute value of the Berry-dipole spin $|\Delta\ell|$ [as in Eq. (A.23)] and the sign of $\kappa_\pm$ with minus the sign of the Berry-dipole spin, we conclude that to the lowest order in $\boldsymbol{\kappa}$, the Berry-dipole spin $\Delta\ell$ obtained from a Taylor expansion of a lattice model is the lowest-in-absolute-value integer that obeys the constraint

$$\Delta\ell \mod m = \Delta\widetilde{\mathcal{L}}(\Pi). \tag{A.35}$$

In the following we proceed to prove the deformability of a symmetry-constrained spinor

$$\widetilde{R}_{C_m}(\Pi)\zeta(\boldsymbol{\kappa}, \phi) = e^{i\beta(\boldsymbol{\kappa})}\zeta(C_m\boldsymbol{\kappa}, \phi) \tag{A.36}$$

to the form given in Eqs. (A.33) and (A.34). The main difference from the proof given in Appendix A.1.2 is that the symmetry is lowered from SO(2) to C_m and as a consequence the Berry-dipole spin is changed from being an integer $\Delta\ell \in \mathbb{Z}$ to $\Delta\widetilde{\mathcal{L}}(\Pi) \in \mathbb{Z}_m$. As we show in the following, this modulo m ambiguity is a source of a modified expression for the first component of the spinor in Eq. (A.33).

(*i*) As the first step, we determine the dependence of the spinor on κ_z and ϕ. We start as in Appendix A.1.2, by assuming the linear dependence on $(\kappa_z \pm i\phi)$ and equating the coefficients in front of independent variables. We again conclude, that to have a non-constant dependence on κ_z and ϕ, the phase β must be equal to $\pm\pi\Delta\widetilde{\mathcal{L}}(\Pi)/m$. The initial assumption that the valence band of the lattice model at rotation-invariant line γ_Π is purely of the φ_1 character trivially implies that the valence (conduction) band of the $\boldsymbol{k}\cdot\boldsymbol{p}$ expansion at $\boldsymbol{\kappa} = \boldsymbol{0}$ is of a φ_1 (φ_2) character. The conduction band of a spinor-form Hamiltonian is proportional to ζ, therefore, to ensure the aforementioned orbital characters, the dependence on κ_z and ϕ must be present only in the second component of the spinor. This is true when $\beta = \pi\Delta\widetilde{\mathcal{L}}(\Pi)/m$, and then the second spinor component is $\zeta_2(\boldsymbol{\kappa},\phi) = C\cdot(\kappa_z + i\phi) + D\cdot(\kappa_z - i\phi) + f(\kappa_+,\kappa_-)$.

(*ii*) We proceed to determine the spinor dependence on $\kappa_\pm$. First, with the chosen β, the second component of the spinor must not change when the momentum is rotated,

$$\zeta_2(\boldsymbol{\kappa},\phi) = \zeta_2(C_m\boldsymbol{\kappa},\phi). \tag{A.37}$$

Therefore, to the lowest order in $\boldsymbol{\kappa}$, $\zeta_2(\boldsymbol{\kappa},\phi) = C(\kappa_z + i\phi) + D(\kappa_z - i\phi) + N\kappa_+\kappa_-$.

(*iii*) The first component of the spinor, which to the lowest order in $(\boldsymbol{\kappa},\phi)$ depends only on $\kappa_\pm$, transforms under rotation as

$$\zeta_1(\kappa_+,\kappa_-) = e^{i2\pi\Delta\widetilde{\mathcal{L}}(\Pi)/m}\zeta_1(C_m\kappa_+, C_m\kappa_-). \tag{A.38}$$

We want to find the lowest powers of κ_+^p and κ_-^q which are allowed by the symmetry to constitute ζ_1. For the former term, Eq. (A.38) has the form $\kappa_+^p = \kappa_+^p \exp\Big(i2\pi[\Delta\widetilde{\mathcal{L}}(\Pi) + p]/m\Big)$. By solving it for the lowest possible $p > 0$ we get $p = m - \Delta\widetilde{\mathcal{L}}(\Pi)$. Similarly, the lowest possible $q = \Delta\widetilde{\mathcal{L}}(\Pi)$.

From the steps (*i-iii*), we get the following spinor

$$\zeta(\boldsymbol{\kappa},\phi) = \begin{pmatrix} A\kappa_-^{\Delta\widetilde{\mathcal{L}}(\Pi)} + B\kappa_+^{m-\Delta\widetilde{\mathcal{L}}(\Pi)} \\ C(\kappa_z + i\phi) + D(\kappa_z - i\phi) + N\kappa_+\kappa_- \end{pmatrix}. \tag{A.39}$$

(*iv*) With the same argument as presented in Appendix A.1.3, we can continuously deform this spinor to the form given in Eq. (A.33), without altering the Hopf and Zak phase numbers.

(*v*) Let us finally show, that the spinor (A.33) can be further deformed to have the first component given by Eq. (A.34). We first consider $\Delta\widetilde{\mathcal{L}}(\Pi) \neq m/2$, and see that one of the terms $A\kappa_-^{\Delta\widetilde{\mathcal{L}}(\Pi)}$ and $B\kappa_+^{m-\Delta\widetilde{\mathcal{L}}(\Pi)}$ is of higher order than another, and therefore can be neglected. After that, the coefficient in front of the remaining term can be deformed to be $A = 1$ resp. to $B = 1$,

without closing the gap.

(*vi*) Alternatively, when $\Delta\widetilde{\mathcal{L}}(\Pi) = m/2$, the two just discussed terms are of the same order $m/2$ and none of them can be neglected. However, we can continuously deform these terms to a simpler form without closing the gap. Importantly, if $|A| \neq |B|$, the gap closes only at $\kappa_+ = \kappa_- = \kappa_z = \phi = 0$. Therefore, we can deform the coefficients A and B, while keeping the sign of their relative magnitude $\mathrm{sgn}(|A| - |B|)$ constant. This means that for $|A| > |B|$ we can deform the coefficients to be $A = 1$ and $B = 0$, while for $|A| < |B|$ the resulting coefficients are $A = 0$ and $B = 1$. Thus, we arrive to the first component of the spinor given in Eq. (A.34).

Let us finally discuss what happens if we choose the valence band to coincide at rotation-invariant line γ_Π with the band representation induced from the second orbital φ_2. In this case the itinerant rotation matrix can be written as

$$\widetilde{R}_{C_m}(\Pi) = \exp\left(i\pi\frac{\Delta\widetilde{\mathcal{L}}(\Pi)}{m}\sigma_z\right), \tag{A.40}$$

and the Berry-dipole spin fulfills the constraint

$$\Delta\ell \mod m = m - \Delta\widetilde{\mathcal{L}}(\Pi). \tag{A.41}$$

To ensure the correct orbital characters of the valence and conduction bands, the dependence on κ_z and ϕ must enter only the first component of the spinor, for which the phase β must again be fixed to $\pi\Delta\widetilde{\mathcal{L}}(\Pi)/m$. Similar derivation as presented above shows that the spinor which defines a $\boldsymbol{k}\cdot\boldsymbol{p}$ Hamiltonian can be deformed to $\sigma_x\zeta(\boldsymbol{\kappa},\phi)$ with $\zeta(\boldsymbol{\kappa},\phi)$ given in Eqs. (A.33) and (A.34).

A.2 ANALYTIC RESULTS FOR SPINOR-FORM BERRY DIPOLE

In this Appendix we derive and list several analytic results related to the Berry-dipole Hamiltonian specified by Eqs. (3.3) and (3.4) of the main text. Our discussion is organized into several parts as follows. First, in Appendix A.2.1 we analyze the flux through a hemisphere associated with the Berry-dipole Hamiltonian, deriving in particular the result in Eq. (3.10) of Sec. 3.1. We continue in Appendix A.2.2 with listing for the same class of Hamiltonians the expressions for the Berry connection, Berry curvature, and Chern-Simons form. This discussion is followed in Appendix A.2.3 with a derivation of the change of the continuum Hopf number across a Berry-dipole gap closing, which depends on the Berry-dipole spin as captured by Eq. (3.17) in Sec. 3.2. In the course of the latter derivation, we utilize that the second Chern character of arbitrary two-band Hamiltonians necessarily vanishes. This property, which we also used in Sec. 2.1.6.2, is finally derived in Appendix A.2.4.

A.2.1 *Berry flux associated with a Berry dipole*

In this Appendix we derive that, for a rotation-symmetric Berry dipole given by the spinor function in Eq. (3.3) with $\phi = 0$, the Berry flux Ψ through the upper hemisphere is quantized, and given by Eq. (3.10), i.e., it is negatively proportional to the Berry-dipole spin $\Delta\ell$. The discussion is organized into two parts: we first explain why the flux through the hemisphere is quantized for $\phi = 0$ at all, and afterwards we proceed with the actual integration.

To understand the quantization of the flux through the hemisphere, note that the second component of the spinor in Eq. (3.3) [which is the same as Eq. (A.23) in the previous Appendix] *vanishes* for $k_z = \phi = 0$. Setting ϕ to 0 [which is assumed throughout the present discussion], we find that the valence-band state is, up to an unimportant phase factor, constant throughout the plane $k_z = 0$ with the momentum origin $\boldsymbol{k} = \boldsymbol{0}$ removed (we refer to this plane as the *punctured equatorial plane* $\mathcal{P}$):

$$\left|u_v(k_x, k_y, 0)\right\rangle = \frac{i\sigma_y \zeta^*(k_x, k_y, 0)}{\left\|\zeta(k_x, k_y, 0)\right\|} \propto \begin{pmatrix} 0 \\ 1 \end{pmatrix}. \tag{A.42}$$

It follows that the spectrally flattened Hamiltonian

$$\begin{aligned} \frac{h(k_x, k_y, 0)}{\sqrt{-\det h(k_x, k_y, 0)}} &= \mathbb{1} - 2\left|u_v(k_x, k_y, 0)\right\rangle\left\langle u_v(k_x, k_y, 0)\right| \\ &= \sigma_z \end{aligned} \tag{A.43}$$

is constant inside $\mathcal{P}$ [126]. This implies that any two-dimensional sheet with boundary in $\mathcal{P}$ wraps around the Bloch sphere integer number of times.[1] The integer-valued 'wrapping number' around the Bloch sphere is known to be in a one-to-one correspondence with the quantized Berry-flux through the sheet [195]; it thus follows that the considered Berry-flux through the sheet with boundary in $\mathcal{P}$ must also be quantized.

We next show that the quantized flux is specifically equal to $-2\pi\Delta\ell$ if the Berry-dipole spin equals $\Delta\ell$. A particularly simple choice of a sheet with boundary at the equatorial plane, that we considered in the main text [cf. Eq. (3.1)], is the *upper hemisphere*. However, for the purpose of analytic integration, another choice is more convenient, namely the closed surface on which the spinor function $\zeta(\boldsymbol{k})$ has norm equal to 1, i.e.,

$$\mathcal{M} = \left\{ \boldsymbol{k} \;\middle|\; \left(k_x^2 + k_y^2\right)^{|\Delta\ell|} + k_z^2 = 1, k_z > 0 \right\}. \tag{A.44}$$

We choose again the gauge of the valence state $|u_v(\boldsymbol{k})\rangle$ to be governed by the left-side of the proportionality symbol in Eq. (A.42), where the norm $\|\zeta(\boldsymbol{k})\| = 1$ now drops from the expressions. We parametrize the points on the surface $\mathcal{M}$ with spherical coordinates $\theta \in [0, \pi/2]$ and $\varphi \in [0, 2\pi]$ as

$$k_x = (\sin\theta)^{\frac{1}{|\Delta\ell|}} \cos\varphi, \quad k_y = (\sin\theta)^{\frac{1}{|\Delta\ell|}} \sin\varphi, \quad k_z = \cos\theta. \tag{A.45}$$

The normalized valence state on $\mathcal{M}$ in the specified gauge is

$$|u_v(\theta, \varphi)\rangle = \begin{pmatrix} v\,\cos\theta \\ -\sin\theta e^{i\Delta\ell\varphi} \end{pmatrix}. \tag{A.46}$$

The flux through the surface $\mathcal{M}$ [which we know to be equal to the flux through the hemisphere due to the vanishing divergence $\nabla_{\boldsymbol{k}} \cdot \boldsymbol{\mathcal{F}} = 0$ for the momenta (with gapped spectrum) between $\mathcal{M}$ and the hemisphere], is computed as

$$\Psi\begin{pmatrix}\text{rotation-sym.}\\ \text{Berry dipole}\end{pmatrix} = \int_{\{\boldsymbol{k}\in\mathbb{R}^3 | k_z > 0\}} \boldsymbol{\mathcal{F}} \cdot \nabla_{\boldsymbol{k}} \varrho\, \delta(\varrho - 1) d^3\boldsymbol{k} \tag{A.47}$$

1 Mathematically, one defines an equivalence '$\sim$' that identifies all the points on the boundary of the sheet as the same point; this operation preserves the continuity of the Hamiltonian h. The quotient space "hemisphere/$\sim$" is homeomorphic to S^2. The wrapping of sphere (the compactified sheet) around another (the Bloch) sphere is known to be characterized by the homotopy group $\pi_2(S^2) = \mathbb{Z}$.

with the shorthand $\varrho = ||\zeta(\boldsymbol{k})||$, and the delta function constraining the integral to the desired surface. Transforming the integrand to the right-handed coordinate system (ϱ, θ, ϕ), then integrating over ϱ, one obtains

$$\Psi\left(\begin{smallmatrix}\text{rotation-sym.}\\ \text{Berry dipole}\end{smallmatrix}\right) = \int_{\mathcal{M}} \boldsymbol{\mathcal{F}} \cdot \nabla_{\boldsymbol{k}}\varrho \frac{d\theta d\phi}{\nabla_{\boldsymbol{k}}\varrho \cdot \nabla_{\boldsymbol{k}}\theta \times \nabla_{\boldsymbol{k}}\phi}. \tag{A.48}$$

The Berry-curvature vector is given by

$$\begin{aligned} |\nabla_{\boldsymbol{k}} u\rangle &= \nabla_{\boldsymbol{k}}\varrho \,|\partial_\varrho u\rangle + \nabla_{\boldsymbol{k}}\theta \,|\partial_\theta u\rangle + \nabla_{\boldsymbol{k}}\phi \,|\partial_\phi u\rangle\,, \\ \boldsymbol{\mathcal{F}}(\boldsymbol{k}) &= i\langle\nabla_{\boldsymbol{k}} u| \times |\nabla_{\boldsymbol{k}} u\rangle = -2\mathrm{Im}\,\langle\partial_\theta u|\partial_\phi u\rangle\, \nabla_{\boldsymbol{k}}\theta \times \nabla_{\boldsymbol{k}}\phi + \ldots \end{aligned} \tag{A.49}$$

where "…" denotes terms involving a cross product with $\nabla_{\boldsymbol{k}}\varrho$. Substituting this expression into (A.48), we find that the Jacobian determinant cancels out,

$$\begin{aligned} \Psi\left(\begin{smallmatrix}\text{rotation-sym.}\\ \text{Berry dipole}\end{smallmatrix}\right) &= \int_0^{2\pi} d\varphi \int_0^{\pi/2} d\theta \left[-2\,\mathrm{Im}\,\langle\partial_\theta u_v|\partial_\varphi u_v\rangle\right] \\ &= 2\pi \int_0^{\pi/2} d\theta \left[-\Delta\ell \sin 2\theta\right] = -2\pi\Delta\ell, \end{aligned} \tag{A.50}$$

The final results is precisely Eq. (3.10) of the main text.

A.2.2 *Expressions for Berry connection, Berry curvature, and Chern-Simons 3-form*

Without a detailed derivation, we proceed to list several analytical results for rotation-symmetric Berry dipole with spin $\Delta\ell \in \mathbb{Z}$. We assume the gauge in which the normalized eigenstate corresponding to the valence band is given by

$$\begin{aligned} u_v(\boldsymbol{k}) &= i\sigma_y \zeta^*(\boldsymbol{k}) / \|\zeta(\boldsymbol{k})\| \\ &= \frac{1}{\left[(k_x^2+k_y^2)^{|\Delta\ell|} + k_z^2 + \phi^2\right]^{\frac{1}{2}}} \begin{pmatrix} vk_z - i\phi \\ -\left[k_x + \mathrm{sgn}(\Delta\ell)\, ik_y\right]^{|\Delta\ell|} \end{pmatrix} \end{aligned} \tag{A.51}$$

Substituting this spinor function into the definition of the Berry connection $\boldsymbol{\mathcal{A}}(\boldsymbol{k}) = \langle u_v(\boldsymbol{k})|i\nabla_{\boldsymbol{k}} u_v(\boldsymbol{k})\rangle$ we get the following components:

$$\mathcal{A}_x = +\frac{(\Delta\ell)(k_x^2+k_y^2)^{|\Delta\ell|-1}}{(k_x^2+k_y^2)^{|\Delta\ell|} + k_z^2 + \phi^2} k_y, \tag{A.52a}$$

$$\mathcal{A}_y = -\frac{(\Delta\ell)(k_x^2+k_y^2)^{|\Delta\ell|-1}}{(k_x^2+k_y^2)^{|\Delta\ell|} + k_z^2 + \phi^2} k_x, \tag{A.52b}$$

$$\mathcal{A}_z = -\frac{v\phi}{(k_x^2+k_y^2)^{|\Delta\ell|} + k_z^2 + \phi^2}, \tag{A.52c}$$

where we used $\operatorname{sgn}(\Delta\ell)|\Delta\ell| = \Delta\ell$. For components of the gauge-invariant Berry curvature $\boldsymbol{\mathcal{F}}(\boldsymbol{k}) = \nabla_{\boldsymbol{k}} \times \boldsymbol{\mathcal{A}}(\boldsymbol{k})$ we find

$$\mathcal{F}_x = -\frac{2(\Delta\ell)\left[k_x k_z - v\ \operatorname{sgn}(\Delta\ell) k_y \phi\right](k_x^2 + k_y^2)^{|\Delta\ell|-1}}{\left[(k_x^2 + k_y^2)^{|\Delta\ell|} + k_z^2 + \phi^2\right]^2}, \tag{A.53a}$$

$$\mathcal{F}_y = -\frac{2(\Delta\ell)\left[k_y k_z + v\ \operatorname{sgn}(\Delta\ell) k_x \phi\right](k_x^2 + k_y^2)^{|\Delta\ell|-1}}{\left[(k_x^2 + k_y^2)^{|\Delta\ell|} + k_z^2 + \phi^2\right]^2}, \tag{A.53b}$$

$$\mathcal{F}_z = -\frac{2(\Delta\ell)|\Delta\ell|(k_z^2 + \phi^2)(k_x^2 + k_y^2)^{|\Delta\ell|-1}}{\left[(k_x^2 + k_y^2)^{|\Delta\ell|} + k_z^2 + \phi^2\right]^2}. \tag{A.53c}$$

Finally, for the Chern-Simons form we obtain

$$\boldsymbol{\mathcal{F}} \cdot \boldsymbol{\mathcal{A}} = \frac{2v\,(\Delta\ell)\,|\Delta\ell|\,\phi\,(k_x^2 + k_y^2)^{|\Delta\ell|-1}}{\left[(k_x^2 + k_y^2)^{|\Delta\ell|} + k_z^2 + \phi^2\right]^2}. \tag{A.54}$$

For the purpose of the next subsection, it is convenient to switch to the standard cylindrical coordinates $\boldsymbol{k} \sim (k_\rho, k_\varphi, k_z)$, leading to

$$\boldsymbol{\mathcal{F}} \cdot \boldsymbol{\mathcal{A}}\, d^3\boldsymbol{k} = \frac{2v\,\Delta\ell\,|\Delta\ell|\,k_\rho^{2|\Delta\ell|-1}}{\left(k_\rho^{2|\Delta\ell|} + k_z^2 + \phi^2\right)^2} \phi\, dk_\rho dk_\varphi dk_z \tag{A.55}$$

where $d^3\boldsymbol{k} = dk_x dk_y dk_z = k_\rho\, dk_\rho dk_\varphi dk_z$.

A.2.3 *Change of Hopf invariant across Berry-dipole transition*

We now derive Eq. (3.17) of the main text. We achieve this in two ways: first, we follow the analytic results of the previous subsection to carry out the integration explicitly; subsequently we present an alternative proof that does not rely on the knowledge of the complicated expressions in Eqs. (A.52–A.55). The latter derivation requires certain familiarity with the language of differential forms, in particular with the 2-form formulation of the Berry curvature.

We depart from Eq. (A.55), expressed in the cylindrical coordinates, and plug it into Eq. (3.15) which defines the Hopf number of a continuum model. Noting that the integration over dk_φ yields a factor 2π, we proceed to integrate over k_ρ to find

$$\begin{aligned}
\chi^{\text{cont.}} &= -\frac{1}{4\pi^2}\int_{\mathbb{R}^3} d^3\boldsymbol{k}\, \boldsymbol{\mathcal{F}} \cdot \boldsymbol{\mathcal{A}} \\
&= -\frac{v\phi\Delta\ell}{2\pi}\int_{-\infty}^{+\infty} dk_z \int_0^{+\infty} dk_\rho \frac{2|\Delta\ell|\,k_\rho^{2|\Delta\ell|-1}}{\left(k_\rho^{2|\Delta\ell|} + k_z^2 + \phi^2\right)^2} \\
&= \frac{v\phi\Delta\ell}{2\pi}\int_{-\infty}^{+\infty} dk_z \left.\frac{1}{k_\rho^{2|\Delta\ell|} + k_z^2 + \phi^2}\right|_{k_\rho=0}^{+\infty} \\
&= -\frac{v\Delta\ell\phi}{2\pi}\int_{-\infty}^{+\infty} dk_z \frac{1}{k_z^2 + \phi^2}.
\end{aligned} \tag{A.56}$$

The antiderivative of the integrated function is $\frac{1}{|\phi|}\arctan\left(\frac{k_z}{|\phi|}\right)$, leading to

$$\chi^{\text{cont.}} = -\frac{1}{2} v\Delta\ell\ \operatorname{sgn}(\phi). \tag{A.57}$$

We find that the change in the continuum Hopf number as ϕ changes sign from negative to positive is $\delta\chi^{\text{cont.}} = -v\Delta\ell$, as advertised in Eq. (3.17) of the main text.

Alternatively, we can derive the desired result as follows. Note that the change $\delta\chi^{\text{cont.}}$ is defined as a difference in the Chern-Simons form integrals [Eq. (3.15)] at two fixed values of the parameter $\phi > 0$ and $\phi < 0$. This change can be equivalently computed as an integral of the Chern-Simons form over the 3-sphere enclosing the Berry-dipole degeneracy in the four-dimensional $(\boldsymbol{k}, \phi)$-space, i.e.,

$$\begin{aligned}\delta\chi^{\text{cont.}} &= -\frac{1}{4\pi^2}\oint_{S^3}\mathcal{F}\wedge\mathcal{A}\\ &= -\frac{1}{4\pi^2}\oint_{S^3}\frac{3!}{2!\,1!}\mathcal{F}_{[\alpha\beta}\mathcal{A}_{\gamma]}\,dx_\alpha\,dx_\beta\,dx_\gamma,\end{aligned}\tag{A.58}$$

where $\{x_\alpha\}_{\alpha=1}^3$ are right-handed coordinates on the 3-sphere [cf. Dets. 2.2 for differential form notations]. Such deformation of the integration domain is possible without changing the invariant by virtue of the Stokes' theorem, because the differential of the Chern-Simons 3-form (this differential is proportional to the *second Chern character* [63])

$$\text{ch}_2(\mathcal{F}) \propto d(d\mathcal{A}\wedge\mathcal{A}) = \mathcal{F}\wedge\mathcal{F}\tag{A.59}$$

is *zero for two-band Hamiltonians* (the proof of this statement is postponed to Appendix A.2.4), and therefore the integral of $\mathcal{F}\wedge\mathcal{F}$ over a 4-dimensional space without singularities also vanishes.

For the same reason, to simplify the calculation, we can slightly modify the surface of integration from a 3-sphere to a diffeomorphic 3-manifold on which the spinor function $\zeta(\boldsymbol{k},\phi)$ is normalized to unity: $\|\zeta(\boldsymbol{k},\phi)\| = 1$. We use 3-spherical coordinates to parametrize this manifold as $\phi = \cos\psi$, $k_z = \sin\psi\cos\theta$, $k_y = (\sin\psi\sin\theta)^{1/|\Delta\ell|}\sin\varphi$, and $k_x = (\sin\psi\sin\theta)^{1/|\Delta\ell|}\cos\varphi$, with the 3-spherical angles running through intervals $\psi\in[0,\pi]$, $\theta\in[0,\pi]$, $\varphi\in[0,2\pi]$. The spinor function on the defined 3-manifold

$$\zeta(\psi,\theta,\varphi) = \begin{pmatrix}\sin\psi\sin\theta e^{-i\Delta\ell\varphi}\\ v\sin\psi\cos\theta + i\cos\psi\end{pmatrix},\tag{A.60}$$

is indeed normalized, $\|\zeta(\psi,\theta,\varphi)\| = 1$. We adopt the gauge choice of Eq. (A.51), in which the conduction eigenstate is $u_c(\psi,\theta,\varphi) = \zeta(\psi,\theta,\varphi)$. We opt to explicitly analyze the change in the Hopf invariant only for the conduction band, and then extend the result to the valence band, as both bands of a two-band Hamiltonian possess the same Hopf invariant, owing to a symmetry $\sigma_y h(\boldsymbol{k})\sigma_y = -h^*(\boldsymbol{k})$ of any Hamiltonian that is a sum of Pauli matrices.

The Chern-Simons 3-form on this 3-manifold is found

$$\begin{aligned}\mathcal{F}\wedge\mathcal{A} &= 3\,\mathcal{F}_{[\alpha\beta}\mathcal{A}_{\gamma]}dx_\alpha dx_\beta dx_\gamma\\ &= 3\left(i\partial_{[\alpha}\zeta^\dagger\partial_\beta\zeta\right)\left(i\zeta^\dagger\partial_{\gamma]}\zeta^\dagger\right)\,dx_\alpha\,dx_\beta\,dx_\gamma,\end{aligned}\tag{A.61}$$

where $\{x_\alpha\}_{\alpha=1}^3 = (\psi,\theta,\varphi)$ are coordinates on the 3-manifold. We find

$$\begin{aligned}i\zeta^\dagger\partial_\psi\zeta &= v\cos\theta,\\ i\zeta^\dagger\partial_\theta\zeta &= -v\sin\psi\cos\psi\sin\theta,\\ i\zeta^\dagger\partial_\varphi\zeta &= \Delta\ell\sin^2\psi\sin^2\theta\end{aligned}\tag{A.62}$$

for the components of the Berry connection, and

$$\begin{aligned} i\partial_\psi\zeta^\dagger\partial_\theta\zeta &= -i\partial_\theta\zeta^\dagger\partial_\psi\zeta = v\sin^2\psi\sin\theta, \\ i\partial_\psi\zeta^\dagger\partial_\varphi\zeta &= -i\partial_\varphi\zeta^\dagger\partial_\psi\zeta = \Delta\ell\sin\psi\cos\psi\sin^2\theta, \\ i\partial_\theta\zeta^\dagger\partial_\varphi\zeta &= -i\partial_\varphi\zeta^\dagger\partial_\theta\zeta = \Delta\ell\sin^2\psi\sin\theta\cos\theta \end{aligned} \tag{A.63}$$

for the components of the Berry curvature. After we insert these components to Eq. (A.61) and perform the antisymmetrization as in Eq. (2.56), we finally obtain the Chern-Simons 3-form

$$\mathcal{F}\wedge\mathcal{A} = 2v\Delta\ell\sin^2\psi\sin\theta\,d\psi\,d\theta\,d\varphi \tag{A.64}$$

on the considered 3-manifold. The integration over the 3-manifold is straightforward, resulting in the change of the continuum Hopf number

$$\delta\chi^{\text{cont.}} = -\frac{1}{4\pi^2}\int_0^\pi d\psi\int_0^\pi d\theta\int_0^{2\pi} d\varphi\,2v\Delta\ell\sin^2\psi\sin\theta \tag{A.65}$$

$$= -v\Delta\ell, \tag{A.66}$$

which is again the result given in Eq. (3.17).

A.2.4 *Vanishing of the second Chern character for two-band Hamiltonians*

In this part of the present Appendix, we move beyond Berry-dipole Hamiltonians, and review a particular property that applies to *arbitrary* smooth two-band Hamiltonian $h(\boldsymbol{k},\phi)$. Namely, while the second Chern class necessarily vanishes for each fibre of a line bundle [196] (i.e., for any single non-degenerate energy band), this is not generally true of the second Chern *character*.[2] Nevertheless, we show here that the second Chern character vanishes for each fibre of a line bundle (i.e., for any single non-degenerate energy band at each $\boldsymbol{k}$ point) corresponding to the valence band of a *two-band* Hamiltonian $h(\boldsymbol{k},\phi) = \boldsymbol{h}(\boldsymbol{k},\phi)\cdot\boldsymbol{\sigma}$, with $\boldsymbol{h}\neq\boldsymbol{0}$. Note that the vanishing of the second Chern character is a *local* property of the $(\boldsymbol{k},\phi)$-space Hamiltonian, and is (for the case of crystalline models) valid irrespective of whether the Hamiltonian is periodic over the Brillouin zone. We have applied this result in a proof of the quantization of the Hopf invariant in Sec 2.1.6.2 and in the analytic considerations presented in Appendix A.2.3.

To reveal this local property, we normalize $\boldsymbol{h}/\|\boldsymbol{h}\| \equiv \boldsymbol{\eta}$. It is well-known that Berry curvature plays the role of the skyrmion density [68], $\mathcal{F}_{\alpha\beta} \propto \epsilon_{ijk}\eta^i\partial_\alpha\eta^j\partial_\beta\eta^k$. Then the second Chern character $\propto \mathcal{F}\wedge\mathcal{F}$ [63] has components

$$(\mathcal{F}\wedge\mathcal{F})_{\alpha\beta\gamma\delta} \propto \sum_{\varsigma\in\mathfrak{S}_4}\operatorname{sgn}(\varsigma)\epsilon_{ijk}\epsilon_{lmn}\eta^i(\partial_{\alpha'}\eta^j)(\partial_{\beta'}\eta^k)\eta^l(\partial_{\gamma'}\eta^m)(\partial_{\delta'}\eta^n) \tag{A.67}$$

where $\mathfrak{S}_4$ is the permutation group of four elements, ς is any of the permutations of the four Greek indices, and we introduced primed notation $\alpha' = \varsigma(\alpha)$ (and similar for β,γ,δ) to achieve brevity.

2 The i'th Chern class vanishes if i is greater than the rank of the bundle [196]. However, the vanishing of the second Chern class for line bundles does not imply the vanishing of the second Chern character, since both quantities differ additively by a wedge product of the first Chern character [68].

The product of the two Levi-Civita symbols can be written [100] as a linear combination of products of three Kronecker symbols "$\pm\delta^{ad}\delta^{be}\delta^{cf}$" where $\{a,b,c\}$ (resp. $\{d,e,f\}$) is a permutation of indices $\{i,j,k\}$ (resp. $\{l,m,n\}$) used in the expression above. It is easily seen that all the resulting terms will contain at least one product of the type "$(\partial_\mu \eta^g)(\partial_\nu \eta^g)$" with μ,ν being distinct elements of $\{\alpha,\beta,\gamma,\delta\}$. Since such an expression for product of derivatives is symmetric in $\mu \leftrightarrow \nu$, while the 4-form $\mathcal{F}\wedge\mathcal{F}$ is antisymmetric in those same indices due to the antisymmetrization over the permutations in $\mathfrak{S}_4$, the corresponding term is canceled. As this argument can be repeated for *all* the terms obtained by replacing the Levi-Civita symbols by Kronecker symbols, one concludes that $\mathcal{F}\wedge\mathcal{F} = 0$ for the valence band of a strictly two-band model.

B

MORE ON ROTATION SYMMETRY

B.1 CHERN NUMBER FROM ITINERANT ANGULAR MOMENTUM

In this Appendix we show that in the presence of n-fold rotational symmetry, given itinerant angular momenta of a set of bands, $\widetilde{\mathcal{L}}_j(\Pi)$, their total Chern number on a symmetry-preserving two-dimensional cut is constrained by

$$\mathscr{C}_{xy} =_n \sum_j \sum_{\Pi} \widetilde{\mathcal{L}}_j(\Pi), \tag{B.1}$$

where Π runs over all rotation-invariant momenta in rBZ and j is an index for all occupied bands.

To see that this is true we utilize the result of Ref. [56] (reviewed in Sec. 2.2.2.2), which relates the Chern number of a rotation-symmetric model to the rotation eigenvalues at all high-symmetry momenta:

$$C_2: \quad e^{i2\pi\mathscr{C}_{xy}/2} = \prod_j \widetilde{\rho}_{2,j}(\Gamma)\, \widetilde{\rho}_{2,j}(\mathrm{X})\, \widetilde{\rho}_{2,j}(\mathrm{Y})\, \widetilde{\rho}_{2,j}(\mathrm{M}), \tag{B.2}$$

$$C_3: \quad e^{i2\pi\mathscr{C}_{xy}/3} = \prod_j \widetilde{\rho}_{3,j}(\Gamma)\, \widetilde{\rho}_{3,j}(\mathrm{K})\, \widetilde{\rho}_{3,j}(\mathrm{K}'), \tag{B.3}$$

$$C_4: \quad e^{i2\pi\mathscr{C}_{xy}/4} = \prod_j \widetilde{\rho}_{4,j}(\Gamma)\, \widetilde{\rho}_{2,j}(\mathrm{X})\, \widetilde{\rho}_{4,j}(\mathrm{M}), \tag{B.4}$$

$$C_6: \quad e^{i\pi\mathscr{C}_{xy}/3} = \prod_j \widetilde{\rho}_{6,j}(\Gamma)\, \widetilde{\rho}_{3,j}(\mathrm{K})\, \widetilde{\rho}_{2,j}(\mathrm{M}). \tag{B.5}$$

The rotation eigenvalue of a band can be expressed in terms of its itinerant angular momentum as

$$\widetilde{\rho}_{m,j}(\Pi) = \exp\Big(i2\pi\widetilde{\mathcal{L}}_j(\Pi)/m\Big). \tag{B.6}$$

Taking the logarithm on both sides of Eq. (B.2) [resp. Eq. (B.3)] gives immediately the desired result: Eq. (B.1) for $n = 2$ [resp. for $n = 3$]. The generalization to $n = 4, 6$ is less obvious because the right-hand sides of Eqs. (B.3)–(B.5) involve $\widetilde{\rho}_{m,j}$ with $m \neq n$. Here, we utilize that n/m copies of a C_m-invariant reduced momentum appear in rBZ of a C_n-symmetric model, and therefore such a momentum contributes n/m times to the sum in Eq. (B.1). In contrast, it only contributes once to the products in Eqs. (B.2)–(B.5). By combining the formulas (B.2)–(B.6) and after taking care of the multiplicity of the high-symmetry momenta, comparison of the exponents leads us to the conclusion summarized by Eq. (B.1).

Let us remark that when discussing the faceted Chern number in Sec. 6.4.2, we introduce an additional minus sign: $\mathscr{C}_f = -\mathscr{C}_{xy}$. This is because the faceted Chern number is computed with respect to the outward surface normal ($\hat{\boldsymbol{n}}$), while $\mathscr{C}_{xy}$ is computed with respect to the positive z-direction ($\hat{\boldsymbol{e}}_z$), and at the bottom facet the two are antiparallel ($\hat{\boldsymbol{n}} = -\hat{\boldsymbol{e}}_z$).

B.2 ITINERANT ANGULAR MOMENTA DEFINE THE BAND REPRESENTATION

We are here to prove a useful fact presented in Sec. 6.3.2, namely that *two rank-one band representations (BRs) of* Pn *are symmetry-equivalent as band representations if and only if they have exactly the same itinerant angular momenta.*

Without loss of generality, such an equivalence class of rank-one BRs is specified by $(\mathcal{L}, \boldsymbol{r}_\perp)$, with $\boldsymbol{r}_\perp$ the (x,y)-projection of a C_n-invariant Wyckoff position $\boldsymbol{r}$; this condition of C_n-invariance is necessary [134] for the BR to be of unit rank. What $\mathcal{L}$ specifies is that for any m-fold rotation (C_m) in the site-stabilizer group P$n_{\boldsymbol{r}}$, the corresponding operator acts on the (exponentially-localized) representative Wannier orbital localized at Wyckoff position $\boldsymbol{r}$ and translated by a Bravais-lattice vector $\boldsymbol{R}$ as

$$\hat{C}_m W_{\boldsymbol{R}} = e^{i2\pi\mathcal{L}/m} W_{C_m\boldsymbol{R}+(C_m\boldsymbol{r}-\boldsymbol{r})}. \tag{B.7}$$

The Fourier transform of $W_{\boldsymbol{R}}$ defines a Bloch function $\psi_{\boldsymbol{k}}$ that is periodic and analytic over the Brillouin torus. Equation (B.7) then implies a corresponding symmetry action on the Bloch function:

$$\hat{C}_m \psi_{\boldsymbol{k}} = \widetilde{\rho}_m(\boldsymbol{k})\psi_{C_m\boldsymbol{k}}, \quad \widetilde{\rho}_m(\boldsymbol{k}) = e^{i2\pi\mathcal{L}/m} e^{i(C_m\boldsymbol{k}-\boldsymbol{k})\cdot\boldsymbol{r}}. \tag{B.8}$$

[cf. discussion below Eq. (4.7) for the meaning of the two exponents in Eq. (B.8)] For any rotation-invariant reduced momentum Π_j with an m_j-order little group,

$$C_{m_j}\text{-invariant } \Pi_j: \quad \widetilde{\rho}_{m_j}(\Pi_j, k_z) = e^{i2\pi\widetilde{\mathcal{L}}_j/m_j} \tag{B.9}$$

defines the mod-m_j itinerant angular momentum $\widetilde{\mathcal{L}}_j$. All itinerant angular momenta may be collected as $(\Pi_1, \widetilde{\mathcal{L}}_1, \ldots, \Pi_J, \widetilde{\mathcal{L}}_J)$, with the total number (J) of rotation-invariant momenta uniquely determined by the Pn space group.

Let us then consider all possible equivalence classes of unit-rank BRs labeled by $(\mathcal{L}, \boldsymbol{r}_\perp)$, and all possible itinerant angular momenta (allowed for unit-rank BRs) labeled by $(\Pi_1, \widetilde{\mathcal{L}}_1, \ldots, \Pi_J, \widetilde{\mathcal{L}}_J)$. Proving the italicized statement above reduces to proving that (B.8–B.9) gives a bijective map between

$$(\mathcal{L}, \boldsymbol{r}_\perp) \mapsto (\Pi_1, \widetilde{\mathcal{L}}_1, \ldots, \Pi_J, \widetilde{\mathcal{L}}_J). \tag{B.10}$$

The map (B.10) is surjective, because the allowed itinerant angular momenta of a unit-rank BR of Pn are, by construction, given by (B.8–B.9) for some value of $(\mathcal{L}, \boldsymbol{r}_\perp)$.

To further show that the map (B.10) is injective, we would like to prove that $(\mathcal{L}_a, \boldsymbol{r}_{a,\perp})$ and $(\mathcal{L}_b, \boldsymbol{r}_{b,\perp})$ map to distinct itinerant angular momenta if $(\mathcal{L}_a, \boldsymbol{r}_{a,\perp}) \neq (\mathcal{L}_b, \boldsymbol{r}_{b,\perp})$. Indeed, suppose

$$\begin{aligned} (\mathcal{L}_a, \boldsymbol{r}_{a,\perp}) &\mapsto (\Pi_1^a, \widetilde{\mathcal{L}}_1^a, \ldots, \Pi_J^a, \widetilde{\mathcal{L}}_J^a), \\ (\mathcal{L}_b, \boldsymbol{r}_{b,\perp}) &\mapsto (\Pi_1^b, \widetilde{\mathcal{L}}_1^b, \ldots, \Pi_J^b, \widetilde{\mathcal{L}}_J^b). \end{aligned} \tag{B.11}$$

If $\mathcal{L}_a \neq \mathcal{L}_b$, Eq. (B.8) guarantees that $\widetilde{\mathcal{L}}^a \neq \widetilde{\mathcal{L}}^b$ for the rotation-invariant reduced momentum at the center of the rBZ. To complete the proof of injectivity, we just need to show that in the case $\mathcal{L}_a = \mathcal{L}_b$ but $\boldsymbol{r}_{a,\perp} \neq \boldsymbol{r}_{b,\perp}$, the two labels for itinerant angular momenta in Eq. (B.11) are distinct. This amounts to showing that $e^{i(C_m\boldsymbol{k}-\boldsymbol{k})\cdot\boldsymbol{r}_a} \neq e^{i(C_m\boldsymbol{k}-\boldsymbol{k})\cdot\boldsymbol{r}_b}$ for at least one C_m-invariant $\boldsymbol{k}$, according to Eq. (B.8). Equivalently, we want to find one C_m-invariant reduced momentum Π such that

$$(C_m\Pi - \Pi)\cdot(\boldsymbol{r}_{a,\perp} - \boldsymbol{r}_{b,\perp}) \neq_{2\pi} 0, \tag{B.12}$$

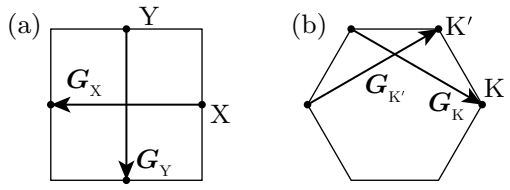

Figure B.1: C_m-invariant momenta in rBZ for (a) $m = 2$ and (b) $m = 3$. Two reciprocal lattice vectors $\boldsymbol{G}_j = C_m\Pi_j - \Pi_j$, computed for these momenta are linearly-independent.

with '$\cdot$' understood here to be a dot product of two-component vectors.

Fact 1: $(C_m\Pi - \Pi)$ is necessarily a reciprocal vector of the reduced reciprocal lattice (rRL), by our assumption that $\boldsymbol{k} = (\Pi, k_z)$ is C_m-invariant.

Fact 2: By our assumption that the Wyckoff positions are distinct, $\boldsymbol{r}_{a,\perp} - \boldsymbol{r}_{b,\perp}$ is not a vector of the reduced Bravais lattice that is dual to the rRL.

Fact 3: For any Pn space group, one can always find a nontrivial divisor m $(1 < m \leq n)$ of n together with two nonzero, C_m-invariant momenta $\{\Pi_1, \Pi_2\}$, namely

$$\begin{aligned}
&\text{P2}: \quad m = 2, \quad \Pi_1 = \text{X}, \quad \Pi_2 = \text{Y},\\
&\text{P3}: \quad m = 3, \quad \Pi_1 = \text{K}, \quad \Pi_2 = \text{K}',\\
&\text{P4}: \quad m = 2, \quad \Pi_1 = \text{X}, \quad \Pi_2 = \text{Y},\\
&\text{P6}: \quad m = 3, \quad \Pi_1 = \text{K}, \quad \Pi_2 = \text{K}',
\end{aligned} \tag{B.13}$$

[with $\{\text{X}, \text{Y}, \text{K}, \text{K}'\}$ illustrated in Fig. B.1], such that $C_m\Pi_j - \Pi_j = \boldsymbol{G}_j$ gives two linearly-independent, primitive rRL vectors $\{\boldsymbol{G}_1, \boldsymbol{G}_2\}$, with corresponding primitive vectors $\{\boldsymbol{R}_1, \boldsymbol{R}_2\}$ that satisfy the duality condition $\boldsymbol{R}_i \cdot \boldsymbol{G}_j = 2\pi\delta_{ij}$ and span the reduced Bravais lattice.

The above facts imply that one can always find Π such that Eq. (B.12) holds true. Indeed, suppose we pick $\Pi = \Pi_1$, then either Eq. (B.12) holds true, or $(C_m\Pi - \Pi) = \boldsymbol{G}_1$ is orthogonal to $(\boldsymbol{r}_{a,\perp} - \boldsymbol{r}_{b,\perp})$. The latter case means that $(\boldsymbol{r}_{a,\perp} - \boldsymbol{r}_{b,\perp})$ is proportional to $\boldsymbol{R}_2$ with a non-integer-valued proportionality constant. It would then follow that a different choice for $\Pi = \Pi_2$ would render Eq. (B.12) true. This completes the proof of injectivity, and hence also of bijectivity of the map (B.10).

B.3 TRIVIAL FIRST CHERN CLASS RESTRICTS BAND REPRESENTATIONS

In Sec. B.3.1, we prove that *for any two-band,* Pn*-symmetric* ($n = 3, 4, 6$)*, insulating Hamiltonian with trivial first Chern class, its valence band (and also its conduction band) is a band representation that is symmetry-equivalent to one of the two basis band representations.* To remind the reader, a basis band representation BBR$[\varphi_\alpha]$ is induced from one of the two tight-binding-basis orbitals φ_1 or φ_2, and to be symmetry-equivalent as band representations means there exists a space-group-equivariant isomorphism between the two corresponding vector bundles. In Sec. B.3.2, we explain why the above italicized statement does not hold for P2 symmetry.

B.3.1 Pn symmetry ($n > 2$): *Trivial Chern class implies symmetry equivalence to basis band representation*

Because two unit-rank band representations of Pn are symmetry-equivalent if and only if their itinerant angular momenta coincide at all rotation-invariant $\boldsymbol{k}$ [as proven in Appendix B.2], the above italicized statement is equivalent to: for any two-band, Pn-symmetric ($n = 3, 4, 6$), insulating Hamiltonian with trivial first Chern class, its valence band is characterized by the same set of itinerant angular momenta as one of $\{\mathrm{BBR}[\varphi_\alpha]\}_{\alpha=1,2}$. The last statement on itinerant angular momenta may be translated symbolically as[1]

$$\begin{aligned} \text{either } \forall\, \Pi:\ \widetilde{\mathcal{L}}_v(\Pi) &= \widetilde{\mathcal{L}}_1(\Pi), \\ \text{or } \forall\, \Pi:\ \widetilde{\mathcal{L}}_v(\Pi) &= \widetilde{\mathcal{L}}_2(\Pi). \end{aligned} \tag{B.14}$$

To remind the reader of the above symbolic notations: the itinerant angular momenta of the valence (conduction) band are denoted as $\widetilde{\mathcal{L}}_{v(c)}(\Pi)$, while the itinerant angular momenta of $\mathrm{BBR}[\varphi_{1(2)}]$ are denoted as $\widetilde{\mathcal{L}}_{1(2)}(\Pi)$. If Π is C_m-invariant (with m the maximal rotational order of the little group), then both $\widetilde{\mathcal{L}}_{v(c)}(\Pi)$ and $\widetilde{\mathcal{L}}_{1(2)}(\Pi)$ are mod-m quantities ($\in \{0, \ldots, m-1\}$); at each Π, $\{\widetilde{\mathcal{L}}_1(\Pi), \widetilde{\mathcal{L}}_2(\Pi)\} = \{\widetilde{\mathcal{L}}_v(\Pi), \widetilde{\mathcal{L}}_c(\Pi)\}$.

Our proof will utilize the mod-n relation (proven in Appendix B.1) between the Chern number and the itinerant angular momenta [cf. Eq. (B.1)]. We proceed to prove proposition (B.14) by contradiction, assuming on the contrary that (cf. footnote 1)

$$\begin{aligned} &\exists\, \Pi\ :\ \widetilde{\mathcal{L}}_v(\Pi) = \widetilde{\mathcal{L}}_2(\Pi) \neq \widetilde{\mathcal{L}}_1(\Pi) \\ \text{and}\quad &\exists\, \Pi'\ :\ \widetilde{\mathcal{L}}_v(\Pi') = \widetilde{\mathcal{L}}_1(\Pi') \neq \widetilde{\mathcal{L}}_2(\Pi'). \end{aligned} \tag{B.15}$$

In the rBZ of a Pn symmetric model with $n \in \{3, 4, 6\}$, one can always find three and only three rotation-inequivalent rotation-invariant reduced momenta $\{\Pi_j\}_{j=1,2,3}$, such that Π_j is C_{m_j}-invariant, and all rotation-invariant momenta in the rBZ can be obtained from $\{\Pi_j\}_{j=1,\ldots 3}$ by a C_n rotation. Momentum Π_j belongs to an (n/m_j)-multiplet of reduced momenta that is obtained by applying n-fold rotation(s) to Π_j; because the orbital inducing the valence band representation is centered at a C_n-invariant Wyckoff position, the itinerant angular momenta at all members of the multiplet are identical. Therefore, our assumption (B.15) can be rewritten, modulo trivial relabelling of numeric subscripts, as

$$\widetilde{\mathcal{L}}_v(\Pi_1) = \widetilde{\mathcal{L}}_2(\Pi_1) \neq \widetilde{\mathcal{L}}_1(\Pi_1), \tag{B.16}$$

$$\widetilde{\mathcal{L}}_v(\Pi_2) = \widetilde{\mathcal{L}}_1(\Pi_2) \neq \widetilde{\mathcal{L}}_2(\Pi_2), \tag{B.17}$$

$$\widetilde{\mathcal{L}}_v(\Pi_3) = \widetilde{\mathcal{L}}_1(\Pi_3) \quad \text{or} \quad \widetilde{\mathcal{L}}_v(\Pi_3) = \widetilde{\mathcal{L}}_2(\Pi_3). \tag{B.18}$$

First, assuming the first option in Eq. (B.18), we compute the Chern number of the valence band in the rotation-preserving 2D cut by means of Eq. (B.1),

$$\mathscr{C}^v_{xy} =_n \sum_\Pi \widetilde{\mathcal{L}}_v(\Pi) =_n \sum_\Pi \widetilde{\mathcal{L}}_1(\Pi) + \frac{n}{m_1}[\widetilde{\mathcal{L}}_2(\Pi_1) - \widetilde{\mathcal{L}}_1(\Pi_1)] \tag{B.19}$$

$$=_n \frac{n}{m_1}\left[\widetilde{\mathcal{L}}_2(\Pi_1) - \widetilde{\mathcal{L}}_1(\Pi_1)\right], \tag{B.20}$$

1 Although we have phrased (B.14) using an 'exclusive or', the fact that $\mathrm{BBR}[\varphi_1]$ and $\mathrm{BBR}[\varphi_2]$ are not symmetry-equivalent implies that the two statements combined in the proposition (B.14) can never be true simultaneously. Therefore, one can equivalently treat the proposition as involving the usual 'inclusive or', the negation of which is the proposition (B.15).

where the summation goes over all rotation-invariant momenta in the rBZ. In the first row we used that momentum Π_1 is a member of an n/m_1-plet, and in the second row we used that the basis band representation has a vanishing Chern number [120]. Because $\widetilde{\mathcal{L}}_2(\Pi_1) \neq \widetilde{\mathcal{L}}_1(\Pi_1)$ [cf. Eq. (B.16)] and $\widetilde{\mathcal{L}}_{1(2)}(\Pi_1) \in \{0, \ldots, m_1 - 1\}$, their difference is nonzero and is never a multiple of m_1; therefore, we conclude that the Chern number of the valence band is necessarily non-zero, which contradicts our initial assumption. If, instead, we opt for the second option in Eq. (B.18), similar steps as in Eq. (B.20) and the fact that $\widetilde{\mathcal{L}}_2(\Pi_2) \neq \widetilde{\mathcal{L}}_1(\Pi_2)$ [cf. Eq. (B.17)] and $\widetilde{\mathcal{L}}_{1(2)}(\Pi_2) \in \{0, \ldots, m_2 - 1\}$ lead to a Chern number

$$\mathscr{C}^v_{xy} =_n \frac{n}{m_2}\left[\widetilde{\mathcal{L}}_1(\Pi_2) - \widetilde{\mathcal{L}}_2(\Pi_2)\right] \neq_n 0, \tag{B.21}$$

which again contradicts the initial assumption. This together proves the proposition (B.14).

B.3.2 P2 *symmetry: trivial Chern class does not imply symmetry equivalence to a basis band representation*

In the case of P2-symmetric Hamiltonians, the rBZ contains *four* (rather than three, as above) rotation-inequivalent C_2-invariant reduced momenta. We remark that the presented calculation (B.20), which results in a non-zero value of the Chern number, also applies to the case of space group P2 when the valence itinerant angular momentum is given by Eqs. (B.16)–(B.18) together with $\widetilde{\mathcal{L}}_v(\Pi_4) = \widetilde{\mathcal{L}}_j(\Pi_4)$ given that $\widetilde{\mathcal{L}}_v(\Pi_3) = \widetilde{\mathcal{L}}_j(\Pi_3)$. However a *vanishing* Chern number is compatible with the following choice of the valence itinerant angular momenta

$$\widetilde{\mathcal{L}}_v(\Pi_1) = \widetilde{\mathcal{L}}_2(\Pi_1) \neq \widetilde{\mathcal{L}}_1(\Pi_1), \tag{B.22}$$
$$\widetilde{\mathcal{L}}_v(\Pi_2) = \widetilde{\mathcal{L}}_2(\Pi_2) \neq \widetilde{\mathcal{L}}_1(\Pi_2), \tag{B.23}$$
$$\widetilde{\mathcal{L}}_v(\Pi_3) = \widetilde{\mathcal{L}}_1(\Pi_3) \neq \widetilde{\mathcal{L}}_2(\Pi_3), \tag{B.24}$$
$$\widetilde{\mathcal{L}}_v(\Pi_4) = \widetilde{\mathcal{L}}_1(\Pi_4) \neq \widetilde{\mathcal{L}}_2(\Pi_4). \tag{B.25}$$

The Chern number in this case can be computed as

$$\mathscr{C}^v_{xy} =_2 \sum_{j=1}^{4} \widetilde{\mathcal{L}}_v(\Pi_j) =_2 \sum_{j=1}^{4} \widetilde{\mathcal{L}}_1(\Pi_j) + \sum_{j=1}^{2} \Delta\widetilde{\mathcal{L}}(\Pi_j) =_2 0, \tag{B.26}$$

where we used that by assumption $\Delta\widetilde{\mathcal{L}}(\Pi_j) \neq 0$, and therefore $\Delta\widetilde{\mathcal{L}}(\Pi_j) = 1$, $j = 1, 2$. This scenario (dubbed 'case P2-II') is therefore studied separately when analyzing the relation between the Hopf and the RTP invariants in Chapter 6.

C

MORE ON BULK-BOUNDARY CORRESPONDENCE

C.1 PROOF OF ZAK-PHASE ANOMALY

In this Appendix we provide necessary proofs in order to compete our discussion of the Zak-phase anomaly presented in Sec. 5.4 of the main text. As a reminder, this anomaly manifests the faceted Zak phases computed along certain symmetrically-chosen rBZ loops, which have distinct values from the bulk Zak phases (both conduction and valence). We subdivide this Appendix into two parts: in Appendix C.1.1 we prove the Zak-phase anomaly when the loop can be chosen to be two-segment, and in Appendix C.1.2 we generalize this proof to the cases when a four-segment loop is necessary to detect the Zak-phase anomaly.

C.1.1 *Zak-phase anomaly for C_m-related-two-segment loops*

We assume that the RTP invariant $\Delta\mathscr{P}_{\Lambda\Xi} > 0$ for two rotation-invariant reduced momenta Λ and Ξ and that there exists an integer $m > 1$ such that at both reduced momenta $\Pi \in \{\Lambda, \Xi\}$ the mutually-disjoint condition is fulfilled modulo m: $\widetilde{\mathcal{L}}_c(\Pi) \neq_m \widetilde{\mathcal{L}}_v(\Pi)$. Then the loop, on which one can detect the Zak-phase anomaly is $\mathcal{S} = \Xi\Lambda(\Xi + \boldsymbol{G})$ [cf. Fig. C.1(a) for an example]. This loop consists of two segments, $\Xi\Lambda$ and $\Lambda(\Xi + \boldsymbol{G})$, which are related to each other by a C_m rotation, reversal of orientation and possibly shift by a reciprocal lattice vector in rBZ, $\Lambda(\Xi + \boldsymbol{G}) = C_m\Lambda\Xi + \boldsymbol{G}'$.

The techniques to evaluate the Zak phase for a C_m-related-two-segment loop, given the itinerant angular momenta at the two C_m-invariant momenta in said loop, have been developed in Ref. [91] and Ref. [134]. We review these techniques here as a warm-up for the more complicated case of the four-segment loops, which require a generalization of the known techniques. Much of the intuition behind these techniques can be conveyed by calculating the Zak phase of a single faceted band.

C.1.1.1 *Single isolated band*

To compute the Zak phase of an isolated band we express it as a phase of a corresponding Wilson loop

$$e^{i\mathscr{Z}_j} = \mathcal{W}^j_{\mathcal{S}} = \hat{\mathrm{T}} \exp\left[i \int_{\mathcal{S}} d\boldsymbol{k}_\perp \cdot \boldsymbol{\mathcal{A}}_\perp[u_j(\boldsymbol{k}_\perp)] \right]. \tag{C.1}$$

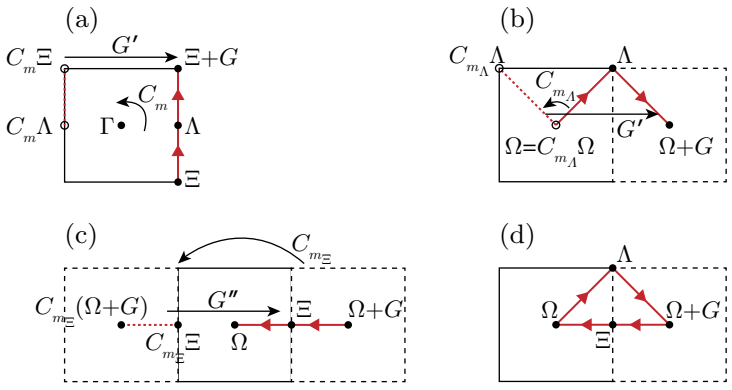

Figure C.1: Illustration of notations introduced in Appendix C.1 to compute the Zak phase over a symmetrically chosen loop in rBZ. (a) Notations for a C_m-related-two-segment loop. (b–d) Notations for a four-segment loop. In (b) we introduce notations for the first two segments, in (c) for the second two segments. The whole loop is illustrated in (d).

The Zak phase along the two-segmented loop $\Xi\Lambda(\Xi+\boldsymbol{G})$ can be written out as

$$\begin{aligned}
\mathscr{Z}_{\Xi\Lambda(\Xi+\boldsymbol{G}),j} =_{2\pi}& \operatorname{Im}\log \mathcal{W}^j_{(\Xi+\boldsymbol{G})\leftarrow\Lambda\leftarrow\Xi} \\
=_{2\pi}& \operatorname{Im}\log \mathcal{W}^j_{(\Xi+\boldsymbol{G})\leftarrow\Lambda}\mathcal{W}^j_{\Lambda\leftarrow\Xi} \\
=_{2\pi}& \operatorname{Im}\log \widetilde{\rho}_{m,j}(\Xi)\left[\mathcal{W}^j_{\Lambda\leftarrow\Xi}\right]^\dagger \widetilde{\rho}_{m,j}(\Lambda)^{-1}\mathcal{W}^j_{\Lambda\leftarrow\Xi} \\
=_{2\pi}& \frac{2\pi}{m}\left[\widetilde{\mathcal{L}}_j(\Xi)-\widetilde{\mathcal{L}}_j(\Lambda)\right]
\end{aligned} \tag{C.2}$$

where in the second row we decomposed a Wilson loop into two Wilson lines. In the third row we related two Wilson lines, computed along symmetry related paths, via eigenvalues $\widetilde{\rho}_{m,j}(\Pi)$ of the itinerant rotation matrix (4.5), and also took into account that Wilson lines computed on two paths, which are related to each other by a reciprocal lattice translation, are equal to each other. In the fourth row we applied the definition of itinerant symmetry eigenvalues in terms of itinerant angular momenta $\widetilde{\rho}_{m,j}(\Pi)=\exp\left(i2\pi\widetilde{\mathcal{L}}_j(\Pi)/m\right)$ and used that two Wilson lines computed along the same path in opposite directions canceled out. Note, that a single-band Wilson loop is a complex number and hence all terms in Eq. (C.2) commute with each other. Substituting the values of the itinerant angular momentum for the faceted, bulk-valence and bulk-conduction bands, we arrive to Eqs. (5.32) and (5.34).

C.1.1.2 *Several faceted bands*

In the case, when there are several faceted bands we need to apply the theorem, proven in Ref. [134], in order to compute the Zak phases. Applied to our setup, the theorem is formulated as follows.

Let us consider a set of $\mathcal{N}_f$ faceted bands. At each reduced momentum $\Pi\in\{\Lambda,\Xi\}$, determine the set of itinerant angular momenta of these bands $\{\widetilde{\mathcal{L}}_j(\Pi)\}_{j=1\ldots\mathcal{N}_f}$. Each of these itinerant angular momenta takes one of the two values $\widetilde{\mathcal{L}}_j(\Pi)\in\{\widetilde{\mathcal{L}}_v(\Pi),\widetilde{\mathcal{L}}_c(\Pi)\}$. Next, determine a pair $(\Pi_*,\widetilde{\mathcal{L}}^*(\Pi_*))$, such that $\#\widetilde{\mathcal{L}}^*(\Pi_*)\geq\#\widetilde{\mathcal{L}}(\Pi)$ for all $\Pi\in\{\Lambda,\Xi\}$ and $\widetilde{\mathcal{L}}\in\{0,\ldots m-1\}$. Reduced momentum, other than Π_* we denote Π_s. Then if $r=\#\widetilde{\mathcal{L}}^*(\Pi_*)+\#\widetilde{\mathcal{L}}(\Pi_s)-$

	Λ	Ξ
$\#\widetilde{\mathcal{L}}_v$	$\mathcal{N}_v^{\mathrm{na}}$	$\mathcal{N}_v^{\mathrm{na}} + \mathcal{N}^{\mathrm{a}}$
$\#\widetilde{\mathcal{L}}_c$	$\mathcal{N}_c^{\mathrm{na}} + \mathcal{N}^{\mathrm{a}}$	$\mathcal{N}_c^{\mathrm{na}}$

Table C.1: Number of bands with fixed itinerant angular momenta at a fixed rotation-invariant point for a set of surface localized bands with $\mathcal{N}_v^{\mathrm{na}}$ valence-bulk-like $\mathcal{N}_c^{\mathrm{na}}$ conduction-bulk-like and $\mathcal{N}^{\mathrm{a}}$ anomalous bands.

$\mathcal{N}_f > 0$, there exists r Zak phases computed along a two-segmented loop $\Xi\Lambda(\Xi + \boldsymbol{G})$ that are quantized to

$$\mathscr{Z} = \pm 2\pi \left[\widetilde{\mathcal{L}}(\Pi_s) - \widetilde{\mathcal{L}}^*(\Pi_*)\right]/m, \tag{C.3}$$

with the $+$ (resp. $-$) sign corresponding to $\Pi_* = \Lambda$ (resp. Ξ).

The RTP invariant ensures that there will be $\mathcal{N}^{\mathrm{a}} = |\Delta\mathscr{P}_{\Lambda\Xi}|$ anomalous bands with itinerant angular momenta that are bulk-conduction-like at Λ and bulk-valence-like at Ξ [cf. Eq. (5.33)]. The amount of non-anomalous faceted bands with bulk-valence-like (bulk-conduction-like) itinerant angular momenta at both Λ and Ξ, we denote as $\mathcal{N}_v^{\mathrm{na}}$ ($\mathcal{N}_c^{\mathrm{na}}$). Then the total number of bands with each value of itinerant angular momentum at rotation-invariant $\boldsymbol{k}_\perp$-points is summarized in Table C.1. The theorem of Ref. [134] summarized in the above paragraph, applied to these values of the itinerant angular momenta, guarantees that the given set of faceted bands will have at least $\mathcal{N}^{\mathrm{a}} = \Delta\mathscr{P}_{\Lambda\Xi}$ Zak phases with quantized values

$$\frac{\mathscr{Z}_f}{2\pi} =_1 \frac{\widetilde{\mathcal{L}}_v(\Xi) - \widetilde{\mathcal{L}}_c(\Lambda)}{m}. \tag{C.4}$$

C.1.2 *Zak-phase anomaly for four-segment loops*

In this Appendix we discuss in more details the bulk-boundary correspondence of the RTP between Λ and Ξ reduced momenta, when

$$\widetilde{\mathcal{L}}_v(\Lambda) \neq_{m_\Lambda} \widetilde{\mathcal{L}}_c(\Lambda), \tag{C.5}$$
$$\widetilde{\mathcal{L}}_v(\Xi) \neq_{m_\Xi} \widetilde{\mathcal{L}}_c(\Xi), \tag{C.6}$$
$$m_\Lambda \neq m_\Xi. \tag{C.7}$$

This happens only in two distinct P4-symmetric Hilbert spaces, that were described in the main text. In both cases, one can construct a four-segment loop which is a concatentation of two two-segment rBZ-loops: the first loop $\Omega\Lambda(\Omega + \boldsymbol{G})$ consists of two segments related by C_{m_Λ} symmetry $\Lambda(\Omega + \boldsymbol{G}) = C_{m_\Lambda}(\Lambda\Omega) + \boldsymbol{G}'$ [cf. Fig. C.1(b) for an example], and second loop $(\Omega + \boldsymbol{G})\Xi\Omega$ consists of two segments related by C_{m_Ξ} symmetry $\Xi\Omega = m_\Xi(\Xi(\Omega + \boldsymbol{G})) + \boldsymbol{G}''$ [cf. Fig. C.1(c) for an example]. An example of the entire four-segment loop $\mathcal{S}_4 = \Omega\Lambda(\Omega + \boldsymbol{G})\Xi\Omega$ is presented in Fig. C.1(d). Here we introduced another rotation-invariant momentum Ω at which the mutually-disjoint condition is violated $\widetilde{\mathcal{L}}_v(\Omega) = \widetilde{\mathcal{L}}_c(\Omega) = \widetilde{\mathcal{L}}(\Omega)$.

We again consider a set of faceted bands with $\mathcal{N}^{\mathrm{a}}$ anomalous bands and $\mathcal{N}_v^{\mathrm{na}} + \mathcal{N}_c^{\mathrm{na}}$ non-anomalous bands. Then the Zak phases of these faceted

bands are computed as phases of the Wilson loop eigenvalues. The Wilson loop along our chosen loop $\mathcal{S}_4$ is

$$\begin{aligned}
&\mathcal{W}_{\Omega\leftarrow\Xi\leftarrow(\Omega+\boldsymbol{G})\leftarrow\Lambda\leftarrow\Omega}\\
&=\mathcal{W}_{\Omega\leftarrow\Xi}\mathcal{W}_{\Xi\leftarrow(\Omega+\boldsymbol{G})}\mathcal{W}_{(\Omega+\boldsymbol{G})\leftarrow\Lambda}\mathcal{W}_{\Lambda\leftarrow\Omega}\\
&=\Big[\widetilde{R}_{C_{m_\Xi}}(\Omega)\mathcal{W}^\dagger_{\Xi\leftarrow(\Omega+\boldsymbol{G})}\widetilde{R}^{-1}_{C_{m_\Xi}}(\Xi)\mathcal{W}_{\Xi\leftarrow(\Omega+\boldsymbol{G})}\\
&\quad\times\widetilde{R}_{C_{m_\Lambda}}(\Omega)\mathcal{W}^\dagger_{\Lambda\leftarrow\Omega}\widetilde{R}^{-1}_{C_{m_\Lambda}}(\Lambda)\mathcal{W}_{\Lambda\leftarrow\Omega}\Big].
\end{aligned}\tag{C.8}$$

Here we decomposed the Wilson loop into four Wilson lines, and related every pair of Wilson lines, computed along the symmetry related paths, via the itinerant rotation matrices (4.5). Contrary to the derivation of Appendix C.1.1 the Wilson loops and the rotation matrices are square matrices of size $\mathcal{N}_f=\mathcal{N}^{\mathrm{a}}+\mathcal{N}_v^{\mathrm{na}}+\mathcal{N}_c^{\mathrm{na}}$ and therefore do not commute. To analyze the eigenvalues of this matrix, first, observe that $\widetilde{R}_{C_m}(\Omega)$ is proportional to identity matrix; this is because an eigenvalue of $\widetilde{R}_{C_m}(\Omega)$ can only take one of two values – the rotational representation of the bulk-conduction band: $e^{i2\pi\widetilde{\mathcal{L}}_c(\Omega)/m}$ or the rotational representation of the bulk-valence band: $e^{i2\pi\widetilde{\mathcal{L}}_v(\Omega)/m}$; but by assumption, the mutually-disjoint condition is violated at Ω: $\widetilde{\mathcal{L}}_c(\Omega)=\widetilde{\mathcal{L}}_v(\Omega)\equiv\widetilde{\mathcal{L}}(\Omega)$. Thus $\widetilde{R}_{C_m}(\Omega)$ can only modify the Wilson loop by a constant, multiplicative factor[1]

$$\begin{aligned}
&\mathcal{W}_{\Omega\leftarrow\Xi\leftarrow(\Omega+\boldsymbol{G})\leftarrow\Lambda\leftarrow\Omega}\\
&=\Big[\mathcal{W}^\dagger_{\Xi\leftarrow(\Omega+\boldsymbol{G})}\widetilde{R}^{-1}_{C_{m_\Xi}}(\Xi)\mathcal{W}_{\Xi\leftarrow(\Omega+\boldsymbol{G})}\mathcal{W}^\dagger_{\Omega\Lambda}\widetilde{R}^{-1}_{C_{m_\Lambda}}(\Lambda)\mathcal{W}_{\Lambda\leftarrow\Omega}\Big]\\
&\quad\times\exp\left(i2\pi\left[\widetilde{\mathcal{L}}(\Omega)/m_\Lambda+\widetilde{\mathcal{L}}(\Omega)/m_\Xi\right]\right)
\end{aligned}\tag{C.9}$$

In the following denote the Wilson lines as $Z_1=\mathcal{W}_{\Lambda\leftarrow\Omega}$ and $Z_2=\mathcal{W}_{\Xi\leftarrow(\Omega+\boldsymbol{G})}$ which are unitary matrices. Thus eigenvalues of the matrices $\widetilde{R}^{-1}_{C_{m_\Lambda}}(\Lambda)$ (resp. $\widetilde{R}^{-1}_{C_{m_\Xi}}(\Xi)$) and $Z_1^\dagger\widetilde{R}^{-1}_{C_{m_\Lambda}}(\Lambda)Z_1$ (resp. $Z_2^\dagger\widetilde{R}^{-1}_{C_{m_\Xi}}(\Xi)Z^2$) are the same. One can always find a projector $\mathscr{B}_1$ (resp. $\mathscr{B}_2$) onto the eigenspace of $Z_1^\dagger\widetilde{R}^{-1}_{C_{m_\Lambda}}(\Lambda)Z_1$ (resp. $Z_2^\dagger\widetilde{R}^{-1}_{C_{m_\Xi}}(\Xi)Z_2$) corresponding to the eigenvalue $\varrho_1=\exp\Big(-i2\pi\widetilde{\mathcal{L}}_c(\Lambda)/m_\Lambda\Big)$ (resp. $\varrho_2=\exp\Big(-i2\pi\widetilde{\mathcal{L}}_v(\Xi)/m_\Xi\Big)$). Denote projectors onto the orthogonal complements as $\mathscr{D}_j=I_{\mathcal{N}_f}-\mathscr{B}_j$, $j=1,2$. Then the Wilson loop can be rewritten as

$$\begin{aligned}
&\mathcal{W}_{\Omega\leftarrow\Xi\leftarrow(\Omega+\boldsymbol{G})\leftarrow\Lambda\leftarrow\Omega}\\
&=\Big[\mathscr{B}_2\mathscr{B}_1\varrho_2\varrho_1+\mathscr{B}_2\varrho_2\mathscr{D}_1Z_1^\dagger\widetilde{R}^{-1}_{C_{m_\Lambda}}(\Lambda)Z_1\mathscr{D}_1\\
&\quad+\mathscr{D}_2Z_2^\dagger\widetilde{R}^{-1}_{C_{m_\Xi}}(\Xi)Z_2\mathscr{D}_2\mathscr{B}_1\varrho_1\\
&\quad+\mathscr{D}_2Z_2^\dagger\widetilde{R}^{-1}_{C_{m_\Xi}}(\Xi)Z_2\mathscr{D}_2\mathscr{D}_1Z_1^\dagger\widetilde{R}^{-1}_{C_{m_\Lambda}}(\Lambda)Z_1\mathscr{D}_1\Big]\\
&\quad\times\exp\left(i2\pi\left[\widetilde{\mathcal{L}}(\Omega)/m_\Lambda+\widetilde{\mathcal{L}}(\Omega)/m_\Xi\right]\right).
\end{aligned}\tag{C.10}$$

Knowing the itinerant angular momenta of the faceted bands at rotation-invariant points Λ and Ξ [cf. Table C.1], we find the ranks of the projectors $\mathrm{rank}(\mathscr{B}_1)=\mathcal{N}_c^{\mathrm{na}}+\mathcal{N}^{\mathrm{a}}$ and $\mathrm{rank}(\mathscr{B}_2)=\mathcal{N}_v^{\mathrm{na}}+\mathcal{N}^{\mathrm{a}}$. Because the dimensions of all matrices considered are identically equal to $(\mathcal{N}_v^{\mathrm{na}}+\mathcal{N}_c^{\mathrm{na}}+\mathcal{N}^{\mathrm{a}})$, it

1 Here we disallow band representations that are not induced from the two basis orbitals φ_1 and φ_2 to be attached to the surface. The presented proof does not go through if faceted bands are augmented with a band representation with a different itinerant angular momentum at Ω.

follows from dimension counting that the two vector spaces projected by $\mathscr{B}_1$ and $\mathscr{B}_2$ have a nonzero intersection with dimension at least equal to $\mathcal{N}^{\mathrm{a}}$. In other words, any vector $|v\rangle$ in this at-least-$\mathcal{N}^{\mathrm{a}}$-dimensional subspace satisfies

$$\mathscr{B}_1 |v\rangle = \mathscr{B}_2 |v\rangle = |v\rangle , \quad \mathscr{D}_1 |v\rangle = \mathscr{D}_2 |v\rangle = 0. \tag{C.11}$$

It follows from the decomposition of the Wilson-loop matrix in Eq. (C.10) that

$$\mathcal{W} |v\rangle = \varrho_2 \varrho_1 \exp\left(i2\pi \left[\widetilde{\mathcal{L}}(\Omega)/m_\Lambda + \widetilde{\mathcal{L}}(\Omega)/m_\Xi \right] \right) |v\rangle , \tag{C.12}$$

with an eigenvalue that does not depend on Z_j. Thus we conclude that there are at least $\mathcal{N}^{\mathrm{a}}$-number of Zak phases quantized to

$$\mathscr{Z} = 2\pi \left[\frac{\widetilde{\mathcal{L}}(\Omega) - \widetilde{\mathcal{L}}_c(\Lambda)}{m_\Lambda} + \frac{\widetilde{\mathcal{L}}(\Omega) - \widetilde{\mathcal{L}}_v(\Xi)}{m_\Xi} \right] . \tag{C.13}$$

As discussed in Sec. 5.4.4 this phase is distinct from both bulk-valence and bulk-conduction Zak phases. This completes the proof of the Zak-phase anomaly.

C.2 PROOF OF CONDITIONALLY-ROBUST SURFACE STATES

In this Appendix we derive the constraint on energy eigenvalues, which we applied in Sec. 7.3.2 to infer the metallic signatures at open boundaries with sharply terminated hoppings of RTP insulators with *multiple* energy bands. The first proof we present in Sec. C.2.1 follows directly from spectral properties of finite-dimensional, block Toepliz matrices derived in Ref. [197], and here translated to the language of the Bloch band theory. An alternative proof valid in the limit of an infinite-sized lattice is provided in Sec. C.2.2 within the transfer-matrix formalism, with certain restrictions on the number of bands and the range of hopping.

C.2.1 *Spectral bounds for block Toeplitz matrices*

Theorem C.2.1. *Consider a one-dimensional N_{b}-band model with a momentum-space Bloch Hamiltonian $h(k)$. For the purpose of this Appendix we adopt the periodic convention, $h(k) = h(k + 2\pi)$. We use $E_a(k)$ to denote the eigenvalues of the Hamiltonian, where $a \in \{1, \ldots, N_{\mathrm{b}}\}$ is the band index and $k \in [-\pi, +\pi]$ is the momentum in the first Brillouin zone. We define the spectral bounds of the bulk Hamiltonian as*

$$E_{\min} = \sup \left\{ E \in \mathbb{R} \;\middle|\; \forall a, k : E_{\min} \leq E_a(k) \right\} , \tag{C.14}$$

$$E_{\max} = \inf \left\{ E \in \mathbb{R} \;\middle|\; \forall a, k : E_{\min} \geq E_a(k) \right\} . \tag{C.15}$$

Let further λ be an eigenvalue of a finite chain with open boundaries, with $\mathcal{N}$ unit cells, and with sharply terminated hopping. We claim that λ is constrained by the same bounds,

$$E_{\min} \leq \lambda \leq E_{\max}. \tag{C.16}$$

In other words, in the presence of the sharp boundary condition there cannot be an edge state lying outside the energy range set by the bulk states.

Remark: *In a physical setting, we usually assume $h(k)$ to be a smooth function that obeys the global spectral bound at every k. However, for the purpose of the proof, we only need to assume that $h(k)$ is L^1-integrable (possibly discontinuous) and that it obeys the spectral bound in Eqs. (C.14) and (C.15) at* almost *every momentum k.*

Proof. For each $r \in \mathbb{Z}$ we define the $N_\mathrm{b} \times N_\mathrm{b}$ matrix

$$\mathcal{T}_r = \frac{1}{2\pi} \int_{-\pi}^{+\pi} dk\, e^{-irk} h(k), \tag{C.17}$$

which in the physical setting encodes the hopping amplitude between each pair of orbitals separated by r unit cells. More generally, the matrices $\{\mathcal{T}_r\}_{r\in\mathbb{Z}}$ are all well-defined if $h(k)$ is L^1-integrable. The Hamiltonian of the finite chain with $\mathcal{N}$ unit cells and with the sharp boundary condition is then given by the block Toeplitz matrix

$$\mathcal{H}_\mathcal{N} = \begin{pmatrix} \mathcal{T}_0 & \mathcal{T}_1 & \cdots & \mathcal{T}_{\mathcal{N}-1} \\ \mathcal{T}_{-1} & \mathcal{T}_0 & \ddots & \vdots \\ \vdots & \ddots & \ddots & \mathcal{T}_1 \\ \mathcal{T}_{-1+\mathcal{N}} & \cdots & \mathcal{T}_{-1} & \mathcal{T}_0 \end{pmatrix}, \tag{C.18}$$

i.e., with the block structure $(\mathcal{H}_\mathcal{N})_{j,j'} = \mathcal{T}_{j'-j}$.

Let further $\psi^{(\mathcal{N})} = \left(\psi_1^{(\mathcal{N})}, \psi_2^{(\mathcal{N})}, \ldots, \psi_\mathcal{N}^{(\mathcal{N})}\right)^\top$ be an arbitrary eigenstate of the Hamiltonian in Eq. (C.18) with eigenvalue λ, i.e., $\mathcal{H}_\mathcal{N}\psi^{(\mathcal{N})} = \lambda\psi^{(\mathcal{N})}$, where each of $\left\{\psi_j^{(\mathcal{N})}\right\}_{j=1}^{\mathcal{N}}$ is an N_b-component vector of amplitudes of the eigenvector within the j^{th} unit cell. We know that eigenstates of finite Hermitian matrices, such as the Hamiltonian in Eq. (C.18), have finite L^2 norm that can be rescaled to unity, i.e.,

$$\left\|\psi^{(\mathcal{N})}\right\|^2 = \sum_{j=1}^{\mathcal{N}} \left\|\psi_j^{(\mathcal{N})}\right\|^2 = \sum_{j=1}^{\mathcal{N}} \sum_{a=1}^{N_\mathrm{b}} \left|\psi_{j,a}^{(\mathcal{N})}\right|^2 = 1, \tag{C.19}$$

where $\left\{\psi_{j,a}^{(\mathcal{N})}\right\}_{a=1}^{N_\mathrm{b}}$ are the components of the wave function within j^{th} unit cell.

We introduce the function

$$v^{(\mathcal{N})}(k) = \sum_{j=1}^{\mathcal{N}} e^{-ijk} \psi_j^{(\mathcal{N})}. \tag{C.20}$$

The function $v^{(\mathcal{N})}(k)$ at momenta $k = \frac{2\pi\alpha}{\mathcal{N}}, \alpha \in \mathbb{Z}$ can be interpreted as the Fourier transform of the wave function $\psi^{(\mathcal{N})}$. Nevertheless, we here mean to define $v^{(\mathcal{N})}(k)$ for *all* $k \in [-\pi, +\pi]$. Since the sum in Eq. (C.20) is finite and the summands are bounded by the norm in Eq. (C.19), one finds that $v^{(\mathcal{N})}(k)$ is also a bounded function, thus one does not have to worry about potential divergences. In fact, one can explicitly derive that

$$\begin{aligned} \left\|v^{(\mathcal{N})}\right\|^2 &\equiv \frac{1}{2\pi} \int_{-\pi}^{+\pi} dk\, \left[v^{(\mathcal{N})}(k)\right]^\dagger \cdot v^{(\mathcal{N})}(k) \\ &= \frac{1}{2\pi} \sum_{j,j'=1}^{\mathcal{N}} \left[\psi_j^{(\mathcal{N})}\right]^\dagger \cdot \psi_{j'}^{(\mathcal{N})} \int_{-\pi}^{+\pi} dk\, e^{i(j-j')k} \\ &= \sum_{j=1}^{\mathcal{N}} \left[\psi_j^{(\mathcal{N})}\right]^\dagger \cdot \psi_j^{(\mathcal{N})} \equiv \left\|\psi^{(\mathcal{N})}\right\|^2, \end{aligned} \tag{C.21}$$

which is similar to the Parseval's identity (a remark on this is added below the proof). We limit our attention to normalized states, $\|\psi\|^2 = \|v\|^2 = 1$.

We proceed to study the expression

$$\begin{aligned}\lambda = \left[\psi^{(\mathcal{N})}\right]^\dagger \mathcal{H}_\mathcal{N} \psi^{(\mathcal{N})} &\overset{(C.18)}{=} \sum_{j,j'=1}^{\mathcal{N}} \left[\psi_j^{(\mathcal{N})}\right]^\dagger \cdot (\mathcal{H}_\mathcal{N})_{j,j'} \cdot \psi_{j'}^{(\mathcal{N})} \\ &\overset{(C.17)}{=} \frac{1}{2\pi}\int_{-\pi}^{+\pi} dk \sum_{j,j'=1}^{\mathcal{N}} e^{i(j-j')k} \left[\psi_j^{(\mathcal{N})}\right]^\dagger \cdot h(k) \cdot \psi_{j'}^{(\mathcal{N})} \\ &\overset{(C.20)}{=} \frac{1}{2\pi}\int_{-\pi}^{+\pi} dk \left[v^{(\mathcal{N})}(k)\right]^\dagger \cdot h(k) \cdot v^{(\mathcal{N})}(k). \end{aligned} \tag{C.22}$$

Note that the last expression in Eq. (C.22) is a weighted (over k) expectation value of operator $h(k)$ for the vector $v^{(\mathcal{N})}(k)$, which we expect to be bounded by the values in Eqs. (C.14) and (C.15). To explicitly verify this, we decompose $v^{(\mathcal{N})}(k)$ into the complete basis of orthonormal eigenstates $\{u_a(k)\}_{a=1}^{N_\mathrm{b}}$ of $h(k)$ at each k, i.e.,

$$v^{(\mathcal{N})}(k) = \sum_{a=1}^{N_\mathrm{b}} c_a^{(\mathcal{N})}(k) u_a(k). \tag{C.23}$$

From Eq. (C.21) we obtain a constraint on the coefficient functions $c_a(k)$, namely

$$\begin{aligned} 1 = \left\|v^{(\mathcal{N})}\right\|^2 &= \frac{1}{2\pi}\int_{-\pi}^{+\pi} dk \sum_{a,a'=1}^{N_\mathrm{b}} [c_a^{(\mathcal{N})}(k)]^* c_{a'}^{(\mathcal{N})}(k) u_a^\dagger(k) \cdot u_{a'}(k) \\ &= \frac{1}{2\pi}\int_{-\pi}^{+\pi} \sum_{a=1}^{N_\mathrm{b}} \left|c_a^{(\mathcal{N})}(k)\right|^2, \end{aligned} \tag{C.24}$$

where * denotes complex conjugation. We therefore manipulate the last expression in Eq. (C.22) as

$$\begin{aligned} (C.22) &= \frac{1}{2\pi}\int_{-\pi}^{+\pi} dk \sum_{a,a'=1}^{N_\mathrm{b}} [c_a^{(\mathcal{N})}(k)]^* c_{a'}^{(\mathcal{N})}(k) u_a^\dagger(k) \cdot h(k) \cdot u_{a'}(k) \\ &= \frac{1}{2\pi}\int_{-\pi}^{+\pi} dk \sum_{a=1}^{N_\mathrm{b}} \left|c_a^{(\mathcal{N})}(k)\right|^2 E_a(k) \\ &\overset{(C.14)}{\geq} \frac{1}{2\pi}\int_{-\pi}^{+\pi} dk \sum_{a=1}^{N_\mathrm{b}} \left|c_a^{(\mathcal{N})}(k)\right|^2 E_\mathrm{min} \overset{(C.24)}{=} E_\mathrm{min}. \end{aligned} \tag{C.25}$$

Thus, Eqs. (C.22) and (C.25) together constitute the first inequality in Eq. (C.16). The complementary part of Eq. (C.16) follows from utilizing in the last line of Eq. (C.25) the inequality in Eq. (C.15). This completes the proof of the spectral bound for any finite (but arbitrarily large) system size $\mathcal{N}$. □

Before proceeding with alternative insights into the spectral bounds for block Toeplitz matrices, let us briefly clarify why the above proof does not generalize to a semi-infinite chain of unit cells. The crucial complication is that for infinite-dimensional Hermitian operators there are eigenstates that do not have a well-defined L^2 norm. Examples include plane waves of an infinite chain of unit cells with no boundaries, and also the bulk states of a semi-infinite chain which arise in the presently discussed context. As a consequence, the limit $\lim_{\mathcal{N}\to\infty} v^{(\mathcal{N})}(k)$ defined in Eq. (C.20) may be non-analytic, and the manipulations in Eqs. (C.21–C.25) become ill-defined. However, if one assumes that ψ_j in Eq. (C.20) exponentially decays for large

$|j|$, then one can take the limit $\mathcal{N} \to \infty$ while keeping $v(k)$ analytic, and the above proof does indeed carry forward to a semi-infinite chain. Exponential decay of wave functions in the 'forbidden' energy range is best illustrated by the transfer-matrix formalism [198], which is elaborated next.

C.2.2 *Spectral bounds from transfer matrix formalism*

The following proof applies to a semi-infinite chain of unit cells with one edge, and manifests a new principle that is not present in the previous proof. Namely, suppose an energy eigenstate satisfies (*i*) the sharp boundary condition, and (*ii*) has energy outside the energy bounds of an infinite chain without edges [cf. Eqs. (C.14) and (C.15)]; then the eigenstate amplitude grows exponentially away from the chain edge, and is therefore not L^2-normalizable. We will demonstrate this principle, and also prove the spectral bound under sharp boundary conditions, with the simplifying assumption of a one-band Hamiltonian with nearest-neighbor hopping matrix elements.

Let us denote the wave function on a chain by ψ_j, with $j = 1, 2, \ldots$ taking any positive-integer values denoting the coordinate of each 'site' on a chain. With only nearest-neighbor hoppings given by complex matrix element b, and an on-site potential with real matrix element a, the eigenproblem to solve is

$$\bar{b}\psi_{j-1} + b\psi_{j+1} = (E - a)\psi_j \tag{C.26}$$

for $j \geq 2$, with the sharp boundary condition imposed by

$$b\psi_2 = (E - a)\psi_1. \tag{C.27}$$

Without loss of generality, one can (1) redefine the origin on the energy axis to remove a from Eqs. (C.26) and (C.27), then (2) perform a j-dependent phase transformation of ψ_j such that b becomes real, and finally (3) rescale the Hamiltonian by a multiplicative constant such that $b = 1$. Then Eq. (C.26) can be transformed to

$$\begin{pmatrix} \psi_{j+1} \\ \psi_{j+2} \end{pmatrix} = \mathscr{T} \begin{pmatrix} \psi_{j-1} \\ \psi_j \end{pmatrix}, \quad \mathscr{T}(E) = \begin{pmatrix} -1 & E \\ -E & E^2 - 1 \end{pmatrix}, \tag{C.28}$$

with $\mathscr{T}$ the *transfer matrix* relating the wave functions across any four adjacent sites (not including the first two). The transfer matrix has eigenvalues

$$\lambda_\pm(E) = -1 + \frac{E^2}{2} \pm \sqrt{\frac{E^4}{4} - E^2}, \quad \lambda_+\lambda_- = 1. \tag{C.29}$$

The last equality follows from $\mathscr{T}$ having unit determinant, which is a general property of transfer matrices [198].

For $E^2 < 4$, $\lambda_\pm(E) = e^{\pm i2k(E)}$ with $k(E)$ a real number determined by $E = 2\cos(k)$. Generally, unimodular eigenvalues of the transfer matrix translate to Hamiltonian eigenstates whose wave functions (on two sites) are invariant (in amplitude) upon repeated application of the transfer matrix, meaning that these are extended, Bloch-wave states. For our model, $\lambda_\pm(E)$ is simply the phase factor acquired by translating a plane wave with wave number $k(E)$ by two sites.

For $E^2 = 4$, the transfer matrix has an eigenvalue degeneracy: $\lambda_\pm = 1$. Introducing a small parameter δ in $E = \eta 2 + \delta/4$ with $\eta = \pm 1$, one finds $\lambda_\pm = 1 \pm \sqrt{\eta\delta} + O(\delta)$. Thus tuning δ across zero (a branch point) changes

λ_+ from a unimodular phase factor to a real number that is larger than one, and λ_- into a real number less than one. In fact, since $(E^4/4 - E^2)$ is a monotone-increasing function of $|E|$ for $E^2 > 4$, it follows that λ_+ is also monotone-increasing in $|E|$ for $E^2 > 4$. Combining this fact with our constraint $\lambda_+\lambda_- = 1$, one finds λ_- is monotone-decreasing in $|E|$ but remains positive for any finite E. Thus it may be concluded for $E^2 > 4$ that $\lambda_+ > 1$ and $0 \leq \lambda_- < 1$. For what follows, it is useful to record the left eigenvectors of the transfer matrix corresponding to $\lambda_\pm$:

$$\phi^L_\pm = \left(-\frac{E^2}{2} \pm \sqrt{\frac{E^4}{4} - E^2}, E \right), \tag{C.30}$$

with the right eigenvectors $\phi^R_\pm$ satisfying the bi-orthonormality conditions: $\phi^L_\pm \cdot \phi^R_\pm = 1$ and $\phi^L_\mp \cdot \phi^R_\pm = 0$. (We use "$\cdot$" to denote the inner product of a two-element row vector with a two-element column vector.)

Let us study whether a wave function satisfying the sharp boundary condition can be normalized. The wave function on the first two sites is constrained by the sharp boundary condition of Eq. (C.27) as $\psi_2 = E\psi_1$. Let us express the wave function on the first two sites as a linear combination of right eigenvectors of the transfer matrix:

$$\begin{pmatrix} \psi_1 \\ \psi_2 \end{pmatrix} = c_+\phi^R_+ + c_-\phi^R_-. \tag{C.31}$$

The complex coefficient c_+ is determined by utilizing the bi-orthonormality condition:

$$c_+ = \phi^L_+ \cdot \begin{pmatrix} \psi_1 \\ \psi_2 \end{pmatrix} = \left(\frac{E^2}{2} + \frac{1}{2}\sqrt{E^4 - 4E^2} \right) \psi_1 \neq 0. \tag{C.32}$$

Since the bracketed term is strictly positive for $E^2 > 4$, one deduces $c_+ \neq 0$ (c_- is obtained analogously, but its value is less important for our purposes.) It follows that applying the transfer matrix r times to the wave function on the first two sites:

$$\begin{pmatrix} \psi_{1+2r} \\ \psi_{2+2r} \end{pmatrix} = \mathscr{T}^r \begin{pmatrix} \psi_1 \\ \psi_2 \end{pmatrix} = c_+(\lambda_+)^r\phi^R_+ + c_-(\lambda_-)^r\phi^R_- \tag{C.33}$$

gives a wave function that is exponentially growing as $e^{r\ln\lambda_+}$ as one moves away for the chain edge ($j = 1$). The desired conclusion, then, is that there exists no normalizable Hamiltonian eigenstate (under sharp boundary conditions) outside the energy interval $[-2, 2]$, this interval being the energy band of extended Hamiltonian eigenstates for an infinite chain without edges.

To briefly rationalize why this proof works, observe that the transfer-matrix eigenvalue $|\lambda_+|$ and coefficient $|c_+|$ [cf. Eq. C.32] being monotone-increasing functions of $|E|$ is special: it requires that there is a single dominant energy scale in the problem. We mean that the energy E (where one considers a sharp boundary state) is dominant over all other relevant energy scales in the Hamiltonian; in this model, the hopping parameter $b = 1$ gives the only other (unit) energy scale to compare with E. (The on-site energy a is irrelevant.) The existence of a single energy scale for sufficiently large $|E|$ is of course also true for Hamiltonians with more bands and longer-ranged hoppings, and for this reason we expect our transfer-matrix proof of spectral bounds will generalize. We leave this to future investigations.

Finally, it is worth remarking that with two or more energetically separated bulk bands, there are clearly multiple, competing energy scales when E lies within a bulk band gap, and our argument breaks down, admitting the possibility of surface states under sharp boundary conditions.

D

MORE ON MULTICELLULARITY

D.1 MULTICELLULARITY VS THE OBSTRUCTED ATOMIC LIMIT

Let us comment on the intersection between multicellular topological insulators and obstructed atomic insulators, and show that neither of these notions necessarily implies the other.

D.1.1 *Multicellular topological insulators are not necessarily obstructed atomic insulators*

According to the theory of topological quantum chemistry [176], the obstructed atomic insulator is a band representation whose valence band is spanned by a set of symmetric exponentially-localized Wannier orbitals $\{W_{j,\boldsymbol{R}}\}_{j=1\ldots N_v}$, whose corresponding Wannier centers do not coincide with the 'atomic positions' (to be clarified below); moreover, owing to certain crystallographic point-group symmetries that fix each Wannier center to a high-symmetry Wyckoff position, the Wannier center cannot be smoothly deformed to the atomic positions which are assumed to lie on a distinct Wyckoff position. From the perspective of tight-binding models, the 'atomic positions' are naturally identified with the positions of basis vectors, $\boldsymbol{r}_\alpha$, $\alpha = 1, \ldots, N_v + N_c$.

According to this definition, the MRW model of the crystalline Hopf insulator [cf. (4.24)] is not an obstructed atomic insulator, as its valence Wannier orbitals are centered at the same Wyckoff position $1a$ (with site stabilizer C_4) as the basis 'atomic' orbitals. A second example is the Hopf insulator without point-group symmetry. Because the Wannier center (of the valence subspace) is movable without symmetry restriction, it is (trivially) not an obstructed atomic insulator; yet, the Hopf insulator remains multicellular, based on an argument presented in Sec. 8.2.

D.1.2 *Obstructed atomic insulators are not necessarily multicellular*

The title of this subsection is exemplified by an inversion-symmetric Su-Schrieffer-Heeger- (SSH-) [12] type model, whose tight-binding basis is given in each unit cell by an inversion-even s and an inversion-odd ip orbital localized to the same inversion-invariant Wyckoff position $1a$ [cf. Fig. D.1(a)]. In this basis, the matrix representation of inversion (about center $1a$) is σ_z, while time-reversal symmetry is represented by $\sigma_z K$ with K being the complex conjugation. A representative tight-binding Hamiltonian is given by

$$h(k) = \cos k\sigma_z + \sin k\sigma_x, \quad \sigma_z h(k)\sigma_z = h(-k). \tag{D.1}$$

To obtain exponentially-localized Wannier orbitals for the energy bands, we need to find eigenvectors of $h(k)$ that are smooth and periodic over

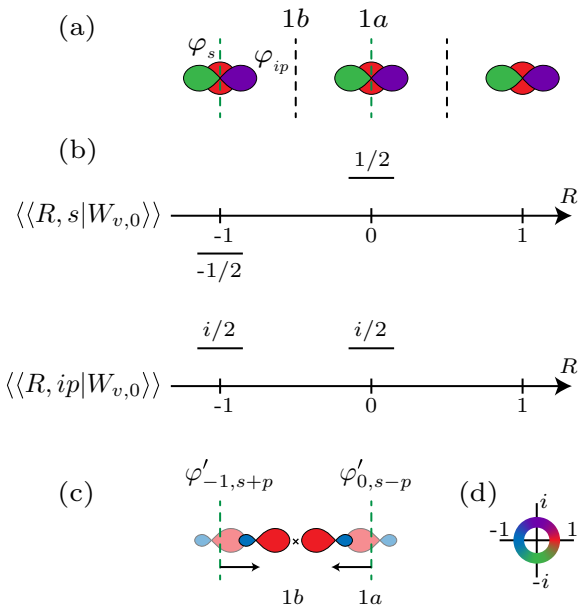

Figure D.1: (a) SSH-type model with inversion-even φ_s and inversion-odd φ_{ip} tight-binding basis orbitals localized at $1a$ Wyckoff positions. The color indicates the amplitude of the orbital's wave function according to the color scheme displayed in panel (d). The primitive unit cells centered at $1a$ resp. $1b$ Wyckoff positions are bounded by black resp. green dashed lines. (b) The valence Wannier orbital is a linear combination of basis orbitals at neighboring sites. The coefficients $\langle\langle R, \alpha|W_{v,0}\rangle\rangle$ are presented as a function of the Bravais vector R. (c) The hybridized orbitals $\varphi'_{-1,s+p}$ and $\varphi'_{0,s-p}$ that contribute to the valence Wannier orbital are formed from basis orbitals with coefficients denoted by colors from the color wheel (d). Their centers can be shifted to position $1b$ while preserving the inversion symmetry.

the Brillouin zone. In spite of our model Hamiltonian $h(k)$ being real, the requirements of smoothness and periodicity can only be fulfilled by complex-valued eigenvectors, because both valence and conduction bands of our model Hamiltonian have a nontrivial first Stiefel-Whitney class (i.e., they carry π Berry phase) [120, 199]. One choice of smooth, periodic eigenvectors is

$$|u_v(k)\rangle = -ie^{ik/2}\begin{pmatrix}\sin k/2\\ -\cos k/2\end{pmatrix}, \quad |u_c(k)\rangle = -ie^{ik/2}\begin{pmatrix}\cos k/2\\ \sin k/2\end{pmatrix}. \tag{D.2}$$

for the valence and conduction subspace respectively. The corresponding valence Wannier orbital is centered at the $1b$ 'mid-bond' Wyckoff position and is formed by an inversion-odd linear combination of atomic orbitals from two nearest-neighbor $1a$ sites [Fig. D.1(b)] as can be derived by using Eq. (2.33):

$$\begin{aligned}\langle\langle R,\alpha|W_{v,0}\rangle\rangle &= \int \frac{dk}{2\pi} e^{ikR} u_v^\alpha(k)\\ &= (\delta_{R,0}\delta_{\alpha,s} - \delta_{R,-1}\delta_{\alpha,s} + i\delta_{R,0}\delta_{\alpha,ip} + i\delta_{R,-1}\delta_{\alpha,ip})/2,\end{aligned} \tag{D.3}$$

To express this in simpler terms, we can define a new sp-hybridized basis $\{\varphi'_{R,s-p}, \varphi'_{R,s+p}\}_{R\in\mathbb{Z}}$ such that each new basis vector is a linear combination of the old basis vectors (on the same site):

$$|R,s-p\rangle\rangle = \frac{1}{\sqrt{2}}\left(|R,s\rangle\rangle + i\,|R,ip\rangle\rangle\right), \tag{D.4a}$$

$$|R,s+p\rangle\rangle = \frac{1}{\sqrt{2}}\left(|R,s\rangle\rangle - i\,|R,ip\rangle\rangle\right). \tag{D.4b}$$

such that the valence Wannier orbital is simply the sum:

$$|W_{v,0}\rangle\rangle = \frac{1}{\sqrt{2}}\left(|0,s-p\rangle\rangle - |-1,s+p\rangle\rangle\right) \tag{D.5}$$

as illustrated in Fig. D.1(c). [Note Eq. (D.4) is a basis change of the type (c-i) discussed in Sec. 8.1.]

If the unit cell is defined to be centered at the $1a$ 'atomic' position (bounded by black dashed lines in Fig. D.1(a)), then $|W_{v,0}\rangle\rangle$ would have support on two unit cells. Crucially, if the primitive unit cell is defined to be centered at the $1b$ 'midbond' position (bounded by green dashed lines in Fig. D.1(a)), then $|W_{v,0}\rangle\rangle$ can be continuously deformed to lie within said unit cell. To appreciate this, observe from Fig. D.1(c) that $|W_{v,0}\rangle\rangle$ currently has support only on the right and left edge of a $1b$-centered unit cell. Since the two orbitals on the right-hand side of Eq. (D.5) are not individually inversion-symmetric, their centers are not fixed to the $1a$ Wyckoff position. Instead the two orbitals are mutually related by inversion about the $1b$ position. By a continuous transformation of type (c-ii) discussed in Sec. 8.1, one can symmetrically displace the centers of $\{\varphi'_{R,s\pm p}\}$ to all lie at $1b$ positions; for example, Fig. D.1(c) illustrates the left-shifting of $\varphi'_{0,s-p}$ and the right-shifting of $\varphi'_{-1,s+p}$. It follows that $|W_{v,0}\rangle\rangle$ now has support only on the $1b$ position with spatial coordinate $-1/2$, demonstrating that the SSH model is unicellular.

In spite of the above examples, the notions of multicellular topological insulators and obstructed atomic limits are not necessarily disjoint, and finding an example that simultaneously manifests both notions deserves a separate investigation.

D.2 MULTICELLULARITY OF RTP MODELS

In this appendix, we substantiate the claim from Sec. 8.2 that Wannier orbitals of a non-trivial RTP phase are necessarily multicellular. The proof is by contradiction, namely we first show that unicellular Wannier orbitals pose constraints on the Berry curvature in the momentum space, whence the multicellularity of Wannier orbitals in RTP models will be seen as an immediate consequence. Our discussion is split into two parts. First, we prove in Sec. D.2.1 that Wannier orbitals in RTP models are multicellular, while remaining agnostic about the particular shape of the Wannier orbital. Then, in Sec. D.2.2 we prove a stronger statement, namely that if the RTP is protected by a rotation symmetry around the z-axis, then the RTP must necessarily extend over multiple layers in the z-direction.

D.2.1 *Flatness of Berry connection in unicellular models*

Based on the definition given in Eq. (8.2) we show that unicellular Wannier orbitals $W_{j,\bar{\boldsymbol{R}}}(\boldsymbol{R},\alpha)$ encode Bloch bands with flat Berry connection, $\mathrm{Tr}[\boldsymbol{\mathcal{F}}]=0$. To see this, first note the corresponding intra-cell functions are [cf. Eq. (2.33)]

$$\begin{aligned} u_j^\alpha(\boldsymbol{k}) &= e^{-i\boldsymbol{k}\boldsymbol{r}_\alpha}\sum_{\boldsymbol{R}} e^{i\boldsymbol{k}\cdot\boldsymbol{R}} W_{j,\boldsymbol{R}}(0,\alpha) \\ &\overset{\text{Eq. (8.2)}}{=} e^{-i\boldsymbol{k}\cdot\boldsymbol{r}_\alpha} w_j(\alpha). \end{aligned} \tag{D.6}$$

We see that the unicellular assumption imposes the derivative to be $\nabla_{\boldsymbol{k}} u_j^\alpha(\boldsymbol{k}) = -i\boldsymbol{r}_\alpha u_j^\alpha(\boldsymbol{k})$. From this we conclude for the corresponding Berry curvature

$$\begin{aligned} \mathrm{Tr}[\boldsymbol{\mathcal{F}}(\boldsymbol{k})] &= i\sum_{j=1}^{N_v}\left[\nabla_{\boldsymbol{k}} u_j(\boldsymbol{k})\right]^\dagger \times \nabla_{\boldsymbol{k}} u_j(\boldsymbol{k}) \\ &= i\sum_{j=1}^{N_v}\sum_{\alpha=1}^{N_v+N_c}\left|u_j^\alpha(\boldsymbol{k})\right|^2(\boldsymbol{r}_\alpha\times\boldsymbol{r}_\alpha) = 0, \end{aligned} \tag{D.7}$$

which vanishes due to the cross product of each position vector $\boldsymbol{r}_\alpha$ with itself.

Details D.1 We remark that this conclusion remains true if one adopts the *generalized* unicellularity [cf. remark (b) in Sec. 8.1] of the valence Wannier orbitals. In such case $W_{j\bar{\boldsymbol{R}}}(\boldsymbol{R},\alpha) = \delta_{\bar{\boldsymbol{R}}+\boldsymbol{R}_\alpha,\boldsymbol{R}} w_j(\alpha)$, where $\boldsymbol{R}_\alpha$ indicates the various choices of the unit cell for the individual Wannier orbitals, nevertheless each orbital type (α) contributes to any Wannier orbital $|W_{j,\bar{\boldsymbol{R}}}\rangle\rangle$ only through a single site (the one corresponding to Bravais vector $\bar{\boldsymbol{R}}+\boldsymbol{R}_\alpha$). Then the intra-cell function is $u_j^\alpha(\boldsymbol{k}) = e^{-i\boldsymbol{k}\cdot(\boldsymbol{R}_\alpha+\boldsymbol{r}_\alpha)} w_j(\alpha)$, and its derivative of becomes $\nabla_{\boldsymbol{k}} u_j^\alpha(\boldsymbol{k}) = -i(\boldsymbol{r}_\alpha+\boldsymbol{R}_\alpha)u_j^\alpha(\boldsymbol{k})$ and one obtains Berry curvature

$$\mathrm{Tr}[\boldsymbol{\mathcal{F}}(\boldsymbol{k})] = i\sum_{j=1}^{N_v}\sum_{\alpha=1}^{N_v+N_c}\left|u_j^\alpha(\boldsymbol{k})\right|^2[(\boldsymbol{r}_\alpha+\boldsymbol{R}_\alpha)\times(\boldsymbol{r}_\alpha+\boldsymbol{R}_\alpha)] = 0, \tag{D.8}$$

which vanishes due to the cross product of each position vector $(\boldsymbol{r}_\alpha+\boldsymbol{R}_\alpha)$ with itself. Therefore, *generalized* unicellular Wannier orbitals also lead to flat Berry connection; in other words, RTP insulators are not representable by generalized unicellular Wannier orbitals. We remark that for the proof presented in Sec. D.2.2 we did not find similar extension to generalized unicellularity – the unicellular discussion assumed therein must be the "strict" one as defined by remark (a) in Sec. 8.1.

It follows from the flatness of the Berry connection [Eq. (D.7)] that unicellular Wannier orbitals cannot exhibit RTP. To see this, recall that the RTP invariant corresponds to an integral of Berry curvature on certain half-sheet inside the Brillouin zone. As the RTP feature is invariant under continuous deformations that preserve the rotation symmetry and the bulk energy gap,

it follows from Eq. (D.7) that RTP vanishes for all models that are deformable into a representation with unicellular Wannier orbitals. Therefore, non-trivial RTP implies multicellular Wannier orbitals [i.e., ones not compatible with the ansatz in Eq. (8.2)].

Before concluding this section, we briefly remark that the same conclusion can also be reached by adapting the homotopy argument presented in Sec. 8.2 for the multicellularity of models with non-trivial Hopf invariant. To that end, note that the classifying space of Hamiltonians in the considered symmetry class at a generic momentum $\boldsymbol{k}$ is $M = U(N_c + N_v)/U(N_c) \times U(N_v)$, where $U(N)$ is the group of rank-N unitary matrices, and as usual N_c (N_v) denotes the number of conduction (valence) bands. Furthermore, for momenta along high-symmetry lines exhibiting mutually disjoint eigenvalues of the valence vs. conduction bands, the classifying space (i.e., space of spectrally normalized Hamiltonians) constitutes a single point $(-\mathbb{1}_{N_v\times N_v}) \oplus (+\mathbb{1}_{N_c\times N_c}) \equiv h_0$ in M. We now use homotopy theory to study equivalence classes of maps from a sheet bounded by two such high-symmetry lines to M, while subject to the constraint that the boundary of the sheet is mapped to h_0. It can be shown [126] that these equivalence classes are captured by the pointed homotopy group $\pi_2(M) = \mathbb{Z}$, and that non-trivial RTP corresponds to non-trivial elements of this group. Since unicellular Wannier orbitals (i.e., the atomic limits) clearly correspond to the trivial element of this classification, it follows from the homotopy theory that non-trivial elements (i.e., those exhibiting RTP) cannot be continuously deformed into the atomic limit (i.e., they are multicellular).

D.2.2 *Multi-layered Wannier orbitals in RTP models*

In this section we prove a *stronger* statement concerning the multicellularity of Wannier orbitals in rotation-symmetry-protected RTP models: the Wannier orbitals must extend over several layers along the rotation axis (without loss of generality set along the z-direction). To prove this statements, we find it useful to decompose all vectors into an in-plane (perpendicular to the rotation axis, "$\perp$") and out-of-plane (parallel with the rotation axis, "$\parallel$") components, $\boldsymbol{b} = (\boldsymbol{b}_\perp, b_\parallel) = \boldsymbol{b}_\perp + b_\parallel \hat{\boldsymbol{e}}_z$.

We depart from the following ansatz for single-layer Wannier orbitals, which generalizes the unicellular ansatz in Eq. (8.2),

$$W_{j,\bar{\boldsymbol{R}}}(\boldsymbol{R}, \alpha) = \delta_{\bar{R}_\parallel, R_\parallel} w_{j,\bar{\boldsymbol{R}}_\perp}(\boldsymbol{R}_\perp, \alpha). \tag{D.9}$$

The idea behind the ansatz in Eq. (D.9) is that the support of orbital α to all Wannier orbitals $\left\{ \left| W_{j,\bar{\boldsymbol{R}}} \right\rangle\!\!\right\rangle \right\}_{j\in\{1,\ldots,N_v\}}$ is limited to a *single layer* labeled by $\bar{R}_\parallel$ and located at position z_α within unit cell in z-direction, compatible with the intended meaning of "single-layer Wannier orbitals".

Starting with the Wannier orbitals of the form in Eq. (D.9), we show that there exists a continuous deformation of the Hamiltonian that preserves the symmetries and the energy gap such that the Berry curvature of the corresponding Bloch states *becomes* oriented along the z-direction in the entire Brillouin zone at the end of the deformation. From this we argue that this prevents the realization of RTP models by single-layer Wannier orbitals.

Proceeding in steps, we first obtain the intra-cell functions by plugging the ansatz (D.9) into the Fourier transform in Eq. (D.6)

$$u_j^\alpha(\boldsymbol{k}) = e^{-i\boldsymbol{k}\boldsymbol{r}_\alpha} \sum_{\bar{\boldsymbol{R}}_\perp} e^{i\boldsymbol{k}\bar{\boldsymbol{R}}_\perp} w_{j\bar{\boldsymbol{R}}_\perp}(0, \alpha). \tag{D.10}$$

Their derivatives in momentum space are

$$\nabla_{\boldsymbol{k}} u_j^{\alpha}(\boldsymbol{k}) = \sum_{\bar{\boldsymbol{R}}_\perp} i(\bar{\boldsymbol{R}}_\perp - \boldsymbol{r}_\alpha) e^{i\boldsymbol{k}\bar{\boldsymbol{R}}_\perp - i\boldsymbol{k}\boldsymbol{r}_\alpha} w_{j\bar{\boldsymbol{R}}_\perp}(0,\alpha). \tag{D.11}$$

We can now express the single-band Berry curvature

$$\begin{aligned}
\boldsymbol{\mathcal{F}}_j(\boldsymbol{k}) &= i\left[\nabla_{\boldsymbol{k}} u^{\nu}(\boldsymbol{k})\right]^{\dagger} \times \nabla_{\boldsymbol{k}} u^{\nu}(\boldsymbol{k}) \\
&= i \sum_{\alpha, \bar{\boldsymbol{R}}_{\perp 1}, \bar{\boldsymbol{R}}_{\perp 2}} e^{i\boldsymbol{k}\cdot(\bar{\boldsymbol{R}}_{\perp 2} - \bar{\boldsymbol{R}}_{\perp 1})} \left[w_{j\bar{\boldsymbol{R}}_{\perp 1}}(0,\alpha)\right]^{*} w_{j\bar{\boldsymbol{R}}_{\perp 2}}(0,\alpha) \\
&\qquad \cdot (\bar{\boldsymbol{R}}_{\perp 1} \times \bar{\boldsymbol{R}}_{\perp 2} - \boldsymbol{r}_\alpha \times \bar{\boldsymbol{R}}_{\perp 2} - \bar{\boldsymbol{R}}_{\perp 1} \times \boldsymbol{r}_\alpha + \boldsymbol{r}_\alpha \times \boldsymbol{r}_\alpha) \\
&= i \sum_{\alpha, \bar{\boldsymbol{R}}_{\perp 1}, \bar{\boldsymbol{R}}_{\perp 2}} e^{i\boldsymbol{k}\cdot(\bar{\boldsymbol{R}}_{\perp 2} - \bar{\boldsymbol{R}}_{\perp 1})} \left[w_{j\bar{\boldsymbol{R}}_{\perp 1}}(0,\alpha)\right]^{*} w_{j\bar{\boldsymbol{R}}_{\perp 2}}(0,\alpha) \\
&\qquad \cdot \left[\bar{\boldsymbol{R}}_{\perp 1} \times \bar{\boldsymbol{R}}_{\perp 2} - \boldsymbol{r}_{\alpha,\perp} \times \bar{\boldsymbol{R}}_{\perp 2} - \bar{\boldsymbol{R}}_{\perp 1} \times \boldsymbol{r}_{\alpha,\perp} \right. \\
&\qquad \left. - z_\alpha(\hat{\boldsymbol{e}}_z \times \bar{\boldsymbol{R}}_{\perp 2} + \bar{\boldsymbol{R}}_{\perp 1} \times \hat{\boldsymbol{e}}_z)\right]
\end{aligned} \tag{D.12}$$

where in the last equality we separated the orbital position into parallel and orthogonal to the rotation axis components $\boldsymbol{r}_\alpha = \boldsymbol{r}_{\alpha,\perp} + z_\alpha \hat{\boldsymbol{e}}_z$ and used the fact that a cross product of $\boldsymbol{r}_\alpha$ with itself is zero. In the final expression the first three terms give contribution only to the z-component of the Berry curvature $\mathcal{F}_{j,z}(\boldsymbol{k})$ as they contain cross products of pairs of *in-plane* vectors. At the same time two last terms can be made to vanish by a continuous deformation of the Hamiltonian that preserves the symmetries and the energy gap. In this deformation the centers of the basis orbitals are adiabatically shifted along z-axis until $z_\alpha = 0$ for all α. To preserve the energy gap this must be done while preserving the hoppings between every pair of basis orbitals. After such a deformation we find $\boldsymbol{\mathcal{F}}_j(\boldsymbol{k}) \parallel \hat{\boldsymbol{e}}_z$, and the same is true after we sum over all occupied bands j. Since the RTP invariant is equal to an integral of Berry curvature on a sheet *parallel* with $\hat{\boldsymbol{e}}_z$ and it does not change under continuous deformations of the Hamiltonian described above, the Berry curvature in Eq. (D.12) cannot generate RTP. It therefore follows that models with a non-trivial RTP invariant cannot be deformed to acquire the Wannier representation in Eq. (D.9), i.e., their Wannier orbitals are necessarily multi-layered in the z-direction.

D.3 MULTICELLULARITY IS DELICATE

In this appendix we outline the proof of the following statement: a multicellular obstruction, that prevents the valence/conduction bands from forming a tightly-bound band representation, is delicate. In other words, addition of trivial bands (tightly-bound BRs) to either valence or conduction subspace lifts the obstruction and allows deformation of the valence/conduction band representation to a tightly-bound BR.

This follows from a few facts in space-group-equivariant vector bundle theory that we will just state, referring the reader to Ref. [47] for the detailed argument. For a rapid initiation to the terminology (see Ref. [200] for an introductory discussion of band topology from the perspective of vector bundles): an energy band can be viewed as a vector bundle [45, 47, 173, 196] with the base space equal to the Brillouin zone and with fibres in direct correspondence with the $\boldsymbol{k}$-dependent Bloch functions; while 'space-group-equivariance' means, in our context, that applying the rotation operator to a Bloch function at $\boldsymbol{k}$ produces a Bloch function at $C_n\boldsymbol{k}$ within the same band.

The first fact we need, proven in Appendix G of Ref. [47], states that a tightly-bound band representation and a non-tightly-bound representation (with the same space group $\mathcal{G}$, Wyckoff position, and site-stabilizer representation) are isomorphic as $\mathcal{G}$-equivariant vector bundles (the standard notion of isomorphism in vector bundles is explained in Ref. [196]; the notion of a space-group-equivariant isomorphism is explained in Ref. [47]). The second fact follows from the universal space-group-equivariant vector bundle theorem,[1] which states that a $\mathcal{G}$-equivariant isomorphism between two vector bundles ($\mathfrak{E}$ and $\mathfrak{E}'$) corresponds bijectively to a $\mathcal{G}$-equivariant homotopy between $\mathfrak{E}$ and $\mathfrak{E}'$. Applied to our context, this means there exists a continuous, $\mathcal{G}$-symmetric deformation between a non-tightly-bound band representation and a tightly-bound representation (with the same data specified above). If the band representation in question is the valence band of a tight-binding Hamiltonian, the existence of this $\mathcal{G}$-equivariant isomorphism (Fact 1) is guaranteed only if the rank of the conduction subspace is unconstrained.[2] Equivalently stated (due to Fact 2), if one can arbitrarily expand the conduction subspace by adding tightly-bound band representations, a valence band representation can always be continuously deformed to a tightly-bound band representation while preserving space-group symmetry. This is equivalent to stating that multicellularity of the valence Wannier orbitals is a delicate property, exactly as advertised in the previous paragraph.

1 The universal bundle theorem in Ref. [201] applies to $\mathcal{P}$-equivariant vector bundles with finite group $\mathcal{P}$. For $\mathcal{G}$-equivariant vector bundles with $\mathcal{G}$ a space group, we observe that the translation subgroup of $\mathcal{G}$ acts trivially on the bundle, hence we may directly apply the universal bundle theorem with $\mathcal{P}$ identified as the (finite) point group of $\mathcal{G}$.

2 We note that the presence of an antisymmetry, such as chiral or PHS, relates the conduction-subspace bundle to the valence-subspace bundle. This possibly precludes the use of the (space-group-equivariant) universal bundle theorem, whose application assumes that the conduction subspace is unconstrained. Thus for chiral symmetry classes, multicellularity is not necessarily concomitant with delicate topology; it has been suggested in Ref. [202] that multicellularity is concomitant with stable topology.

NOTATIONS

$\simeq$	homeomorphism of topological spaces
$\mathbb{0}, \mathbb{1}$	zero matrix, identity matrix
$a =_n b$	equivalence modulo n: $a \,(\mathrm{mod}\ n) = b \,(\mathrm{mod}\ n)$
α	label of tight-binding basis orbital
$\mathcal{A} = \mathcal{A}_\alpha \, dk_\alpha$	Berry-connection 1-form
$\boldsymbol{\mathcal{A}} = (\mathcal{A}_x, \mathcal{A}_y, \mathcal{A}_z)$.	Berry-connection vector
$\mathcal{A}_\mu^{jj'}$	non-Abelian Berry connection
b, b'	points on the Bloch sphere
$\beta(\boldsymbol{k})$, $e^{i\beta(\boldsymbol{k})}$	phase (factor), $U(1)$ gauge transformation of a Bloch/continuum state
$\mathrm{BR}(\mathcal{L}, \boldsymbol{r}_\perp)$	band repr. induced from an $(\mathcal{L}, \boldsymbol{r}_\perp)$-orbital
$\mathrm{BBR}[\varphi_\alpha]$	basis band repr. induced from an orbital φ_α
$\lvert\mathrm{BZ}\rvert$	volume of Brillouin zone
c, v	label for conduction and valence band
C_2, C_3, C_4, C_6, C_n ...	rotation symmetry of order $2, 3, 4, 6, n$
$\mathscr{C}, \mathscr{C}_2$	(second) Chern number
$\mathscr{C}_f$	faceted Chern number
$\mathrm{ch}_2(\mathcal{F})$	second Chern character
$\mathfrak{C}$	chiral symmetry
CBR	composite band repr.
d	differential
$\mathbb{d}$	order of Berry dipole
$\delta_{\alpha\beta}, \delta_{ij}$	Kronecker symbol
$\delta(\boldsymbol{k})$	Dirac delta function (in $\boldsymbol{k}$-space)
∂	boundary operator
$\mathcal{D}$	2D domain of integration
$\mathfrak{D}$	codimension of band node formation
$\hat{\boldsymbol{e}}_j$	unit vector
E	energy
$\bar{E}$	reference energy
dE_j/dt	a scalar velocity of a j-th Bloch state
$\varepsilon > 0$	infinitesimally small real number
$\epsilon_{\alpha\beta\gamma}$	fully antisymmetric Levi-Civita symbol

$\mathcal{F} = \mathcal{F}_{\alpha\beta}\, dk_\alpha \wedge dk_\beta$.	Berry-curvature 2-form
$\boldsymbol{\mathcal{F}} = (\mathcal{F}_x, \mathcal{F}_y, \mathcal{F}_z)$ ..	Berry-curvature vector
$\varphi_{\boldsymbol{R},\alpha} = \lvert \boldsymbol{R}, \alpha \rangle\rangle$	tight-binding-basis orbitals of $\mathscr{H}$
$\varphi_\alpha = \lvert \alpha \rangle$	tight-binding-basis orbitals of $\mathscr{H}_{\text{cell}}$
γ	path, 1D domain of integration
γ_Π	rotation-invariant line in the BZ
$\Gamma, \mathrm{K}, \mathrm{K}', \mathrm{M}, \mathrm{X}$	high-symmetry points in rBZ
$\boldsymbol{G}$, $\boldsymbol{G}_\Pi = C_m \Pi - \Pi$	reciprocal lattice vector
$\mathcal{G}$	space group
$\mathcal{G}_{\boldsymbol{r}}$, ...	site-stabilizer group at $\boldsymbol{r} = (\boldsymbol{r}_\perp, z)$
$\mathcal{G}_\Pi$	little group of $\Pi \in$ rBZ
$g \in \mathcal{G}$	element of the space group
$\check{g}$	matrix repr. of g acting on spatial coordinates
$\mathfrak{g}$	grade of multicellular (*li*-)Wannier orbital
ϕ, ...	tuning parameter in continuum Hamiltonians
Φ	tuning parameter in lattice Hamiltonians
$h, h(\boldsymbol{k})$	Hamiltonian (in momentum space)
$h_{\text{flat}}(\boldsymbol{k})$	spectrally flattened Hamiltonian
$\tilde{h}, \tilde{h}(\boldsymbol{k})$	Hamiltonian in the periodic-in-$\boldsymbol{k}$ convention
$\boldsymbol{h} = (h_x, h_y, h_z)$	2-band Hamiltonian decomposed to $\sigma_{x,y,z}$
$\boldsymbol{h}_{\text{flat}} \in S^2$	2-band Hamiltonian with flattened spectrum decomposed to $\sigma_{x,y,z}$
$H \subset \mathcal{G}$	subgroup of a space group
$\mathscr{H}$	tight-binding Hilbert space
$\mathscr{H}_{\text{cell}}$	intra-cell Hilbert space
$\mathcal{H}_\mathcal{N}$	finite chain Hamiltonian with $\mathcal{N}$ unit cells
J_α	size of a maximal iso-orbital subset fulfilling conditions (6.1) and (6.2)
χ	Hopf invariant of lattice Hamiltonian
$\chi^{\text{cont.}}$	Hopf number of continuum Hamiltonian
$\boldsymbol{k} = (k_x, k_y, k_z)$	(crystal) momentum vector
$\boldsymbol{k}_\perp = (k_x, k_y)$	reduced momentum
$\boldsymbol{\kappa} = (\kappa_x, \kappa_y, \kappa_z)$	small momentum around band touching point
κ	radius of considered spheres in $\boldsymbol{k}$-space
$\Delta\ell \in \mathbb{Z}$	Berry-dipole spin
$\mathcal{L}, \Delta\mathcal{L}$	(difference of) on-site angular momentum
$\widetilde{\mathcal{L}}, \Delta\widetilde{\mathcal{L}}$	(difference of) itinerant angular momentum

$\sharp_{b(f)}\widetilde{\mathcal{L}}_{v(c)}(\Pi)$ ..... number of bulk (faceted) states at Π with val.-(cond.-)band-like itin. ang. momentum

$m \in \{2,3,4,6\}$ ..... order of little-group rotation symmetry

m_Π ..... order of little-group at red. momentum Π

M_z ..... z-mirror symmetry

$\mu(\gamma)$, $\mu(\Pi)$ ..... multiplicity of preimage γ, γ_Π

$n \in \{2,3,4,6\}$ ..... order of crystalline rotation symmetry

$\hat{\boldsymbol{n}}$ ..... unit vector normal to a surface

N_v, N_c ..... number of conduction resp. valence bands

$\mathcal{N}_v(\Pi), \mathcal{N}_c(\Pi)$ ..... number of faceted states with $\widetilde{\mathcal{L}}_f(\Pi) = \widetilde{\mathcal{L}}_v(\Pi), \widetilde{\mathcal{L}}_c(\Pi)$

$v \in \{+1,-1\}$ ..... Berry-dipole helicity

pt. ..... point (as a topological space)

$\mathfrak{P}$ ..... particle-hole symmetry

$\mathscr{P}$ ..... electric polarization

$\Delta\mathscr{P}_{\Pi_1\Pi_2}$ ..... RTP invariant, $\mathscr{P}_{\Pi_2} - \mathscr{P}_{\Pi_1}$

Pn, $n \in \{2,3,4,6\}$ .. considered space groups

P$n_{\boldsymbol{r}}$ ..... presently considered site-stabilizer groups

p$n \subset$ Pn ..... plane group generated by C_n rotation and two out of three translations

P or P_v ..... projector onto filled (valence) states

$P\hat{z}P$, $Q\hat{z}Q$ ..... projected position operators in z-direction

P_{b}, $(P_{\mathrm{t\&b}})$ ..... faceted projector onto bottom facet (onto top and bottom facets)

$P_\downarrow$ ..... projector onto lower half of a finite slab

P_v^{cell} ..... projector onto valence subspace in $\mathscr{H}_{\mathrm{cell}}$

$\Pi, \Xi, \Lambda, \Omega$ ..... rotation-invariant reduced momenta in rBZ

Ψ ..... Berry flux through a hemisphere

$\big|\psi_{j,\boldsymbol{k}}\big\rangle\big\rangle$ ..... Bloch (eigen)state

$\psi_{j,\boldsymbol{k}}(\boldsymbol{R},\alpha)$ ..... tight-binding Bloch function

$\psi^{(\mathcal{N})}$ ..... eigenstate of an $\mathcal{N}$-unit-cell Hamiltonian

(ψ,θ,φ) ..... 3-spherical coordinates

Q or P_c ..... projector onto empty (conduction) states

$\boldsymbol{r} = (x,y,z) = (\boldsymbol{r}_\perp, z)$ position vector

$R_\theta = e^{-i\theta\Delta\ell/2\cdot\sigma_z}$ .... continuous rotation operator for Berry-dipole Hamiltonian

R_{C_m} ..... discrete rot. operator of crystalline $h(\boldsymbol{k})$

$\widetilde{R}_{C_m}(\Pi)$	itinerant rot. operator of $h(\Pi+\boldsymbol{k})$
$\widetilde{\rho}_{m,\alpha}(\Pi)$	eigenvalues of $\widetilde{R}_{C_m}(\Pi)$
$\boldsymbol{R}$	Bravais vector
$\boldsymbol{\mathcal{R}}=(\hat{x},\hat{y},\hat{z})$	discrete position operator
rBZ($\ni \boldsymbol{k}_\perp$)	(momentum in) reduced Brillouin zone
rRL	reduced reciprocal lattice
RTP	returning Thouless pump
S $\sim -\sigma_z$	south pole of the Bloch sphere
S^2, S^3	2-sphere, 3-sphere
$\mathcal{S}$	momentum-loop in rBZ
$s_g=\pm 1$	reversal of time component of symmetry g
$\boldsymbol{\sigma}=(\sigma_x,\sigma_y,\sigma_z)$	vector of Pauli matrices
Σ	Seifert surface stretched over preimage line
$t\in[0,1]$	parametrization of homotopy & closed loops
$\hat{\boldsymbol{t}}$	unit vector tangent to parametrized loop
$\mathrm{t}\in\{1,...,T\}$ in $\boldsymbol{k}^{\mathrm{t}},\Pi^{\mathrm{t}}$	label of consecutive Berry-dipole transitions
$\hat{\mathrm{T}}$	path-ordering operator
T^3	3-torus
$\mathcal{T},\{\mathcal{T}_r\}_{r\in\mathbb{Z}}$	blocks within a block Toeplitz matrix
$\mathscr{T}$	transfer matrix
$\boldsymbol{\tau}(\boldsymbol{k}_0)$	orientation of a preimage path at $\boldsymbol{k}_0$
$\boldsymbol{\tau}(\Pi)$	orientation of rot.-inv. line γ_Π
τ_z	orientation along k_z-axis for non-contractible along k_z loops
Θ	time-reversal symmetry
$\lvert u(\boldsymbol{k})\rangle$, $\lvert u^{on}(\boldsymbol{k})\rangle$	(normalized) intra-cell part of Bloch state
$\lvert u^{li}(\boldsymbol{k})\rangle$	orthogonal but not orthonormal intra-cell part of Bloch state
$v^{(\mathcal{N})}(k)$	Fourier transform of $\psi^{(\mathcal{N})}$
$\mathcal{V}_{j,\boldsymbol{k}_\perp,\bar{R}_z}(\boldsymbol{k}_\perp,R_z,\alpha)$ ..	hybrid Bloch-Wannier function localized in z-direction
$[V(\boldsymbol{k})]_{\alpha\beta}=e^{i\boldsymbol{k}\boldsymbol{r}_\alpha}\delta_{\alpha\beta}$.	matrix relating periodic and non-periodic tight-binding Hamiltonians
VBR	valence band repr.
$\lvert W_{j,\boldsymbol{R}}\rangle\rangle$, $\lvert W^{on}_{j,\boldsymbol{R}}\rangle\rangle$ ...	conventional (orthonormal) Wannier orbital
$\lvert W^{li}_{j,\boldsymbol{R}}\rangle\rangle$	linear independent and complete set of (*li*-)Wannier orbitals

$\left\|W_{j,\boldsymbol{R}}^{type}\right\rangle\!\rangle$	Wannier-*type* orbital
$\mathcal{W}_{\mathcal{S}}$	Wilson loop computed along $\mathcal{S}$
WPT	Weyl point trajectory
$\mathscr{Z}$	Berry-Zak phase
$\mathscr{Z}^{\text{cont.}}, \delta\mathscr{Z}^{\text{cont.}}$	(change of) continuum Zak phase
$\bar{z}_j, \bar{z}_j(\boldsymbol{k})$	eigenvalues of projected position operator
$\zeta = (\zeta_1, \zeta_2)^\top$	two-component spinor

BIBLIOGRAPHY

1. Bhattacharya, S., Likhachev, M. & Kumar, V. Topological Constraints in Search-Based Robot Path Planning. *Auton. Robots* **33,** 273–290. doi:10.1007/s10514-012-9304-1 (2012).
2. Bhattacharya, S., Lipsky, D., Ghrist, R. & Kumar, V. Invariants for Homology Classes with Application to Optimal Search and Planning Problem in Robotics. *Ann. Math. Artif. Intell.* **67,** 251–281. doi:10.1007/s10472-013-9357-7 (2013).
3. Mirkin, S. M. in *eLS* (ed John Wiley & Sons, Ltd) First (Wiley, 2001). doi:10.1038/npg.els.0001038.
4. *Topology in Molecular Biology* (ed Monastyrskii, M. I.) (Springer, 2007).
5. Mermin, N. D. The topological theory of defects in ordered media. *Rev. Mod. Phys.* **51,** 591. doi:10.1103/RevModPhys.51.591 (1979).
6. Skyrme, T. A unified field theory of mesons and baryons. *Nucl. Phys.* **31,** 556–569. doi:https://doi.org/10.1016/0029-5582(62)90775-7 (1962).
7. Bogdanov, A. N. & Yablonskii, D. A. Thermodynamically stable "vortices" in magnetically ordered crystals. The mixed state of magnets. *J. Exp. Theor. Phys.* **68,** 101 (1989).
8. Nagaosa, N. & Tokura, Y. Topological Properties and Dynamics of Magnetic Skyrmions. *Nat. Nanotechnol.* **8,** 899–911. doi:10.1038/nnano.2013.243 (2013).
9. Hasan, M. Z. & Kane, C. L. *Colloquium* : Topological Insulators. *Rev. Mod. Phys.* **82,** 3045–3067. doi:10.1103/RevModPhys.82.3045 (2010).
10. Ashcroft, N. W. & Mermin, N. D. *Solid state physics* (Thomson Learning, 20 Channel Center Street, Boston, MA 02210, USA, 1976).
11. Bloch, F. Ueber die Quantenmechanik der Elektronen in Kristallgittern. *Z. Phys.* **52,** 555–600. doi:10.1007/BF01339455 (1929).
12. Su, W. P., Schrieffer, J. R. & Heeger, A. J. Solitons in Polyacetylene. *Phys. Rev. Lett.* **42,** 1698. doi:10.1103/PhysRevLett.42.1698 (1979).
13. C. L. Kane & E. J. Mele. Quantum Spin Hall Effect in Graphene. *Phys. Rev. Lett.* **95,** 226801. doi:10.1103/PhysRevLett.95.226801 (2005).
14. V. Klitzing, K., Dorda, G. & Pepper, M. New Method for High-Accuracy Determination of the Fine-Structure Constant Based on Quantized Hall Resistance. *Phys. Rev. Lett.* **45,** 494. doi:10.1103/PhysRevLett.45.494 (1980).
15. Halperin, B. I. Quantized Hall Conductance, Current-Carrying Edge States, and the Existence of Extended States in a Two-Dimensional Disordered Potential. *Phys. Rev. B* **25,** 2185–2190. doi:10.1103/PhysRevB.25.2185 (1982).
16. Landau, L. Diamagnetismus der Metalle. *Z. Phys.* **64,** 629–637. doi:https://doi.org/10.1007/BF01397213 (1930).
17. Thouless, D. J., Kohmoto, M., Nightingale, M. P. & den Nijs, M. Quantized Hall Conductance in a Two-Dimensional Periodic Potential. *Phys. Rev. Lett.* **49,** 405–408. doi:10.1103/PhysRevLett.49.405 (1982).

18. Haldane, F. D. M. Model for a quantum Hall effect without Landau levels: Condensed-matter realization of the "parity anomaly". *Phys. Rev. Lett.* **61,** 2015. doi:10.1103/PhysRevLett.61.2015 (1988).
19. C. L. Kane & E. J. Mele. Z_2 topological order and the quantum spin Hall effect. *Phys. Rev. Lett.* **95,** 146802. doi:10.1103/PhysRevLett.95.146802 (2005).
20. Bernevig, B. A., Hughes, T. L. & Zhang, S.-C. Quantum Spin Hall Effect and Topological Phase Transition in HgTe Quantum Wells. *Science* **314,** 1757–1761. doi:10.1126/science.1133734 (2006).
21. König, M., Wiedmann, S., Brüne, C., Roth, A., Buhmann, H., Molenkamp, L., Qi, X.-L. & Zhang, S.-C. Quantum spin Hall insulator state in HgTe quantum wells. *Science* **318,** 766–770. doi:10.1126/science.1148047 (2007).
22. Kitaev, A. Periodic table for topological insulators and superconductors. *AIP Conf. Proc.* **1134,** 22. doi:10.1063/1.3149495 (2009).
23. Ryu, S., Schnyder, A. P., Furusaki, A. & Ludwig, A. W. W. Topological insulators and superconductors: tenfold way and dimensional hierarchy. *New J. Phys.* **12,** 065010. doi:10.1088/1367-2630/12/6/065010 (2010).
24. Hughes, T. L., Prodan, E. & Bernevig, B. A. Inversion Symmetric Topological Insulators. *Phys. Rev. B* **83,** 245132. doi:10.1103/PhysRevB.83.245132 (2011).
25. Teo, J. C. Y., Fu, L. & Kane, C. L. Surface states and topological invariants in three-dimensional topological insulators: Application to $Bi_{1-x}Sb_x$. *Phys. Rev. B* **78,** 045426. doi:10.1103/PhysRevB.78.045426 (2008).
26. Kim, Y., Kane, C. L., Mele, E. J. & Rappe, A. M. Layered Topological Crystalline Insulators. *Phys. Rev. Lett.* **115,** 086802. doi:10.1103/PhysRevLett.115.086802 (2015).
27. Fu, L. Topological Crystalline Insulators. *Phys. Rev. Lett.* **106,** 106802. doi:10.1103/PhysRevLett.106.106802 (2011).
28. Varjas, D., de Juan, F. & Lu, Y.-M. Bulk invariants and topological response in insulators and superconductors with nonsymmorphic symmetries. *Phys. Rev. B* **92,** 195116. doi:10.1103/PhysRevB.92.195116 (2015).
29. Po, H. C., Vishwanath, A. & Watanabe, H. Symmetry-based indicators of band topology in the 230 space groups. *Nat. Commun.* **8,** 50. doi:10.1038/s41467-017-00133-2 (2017).
30. Kruthoff, J., de Boer, J., van Wezel, J., Kane, C. L. & Slager, R.-J. Topological Classification of Crystalline Insulators through Band Structure Combinatorics. *Phys. Rev. X* **7,** 041069. doi:10.1103/PhysRevX.7.041069 (2017).
31. Bradlyn, B., Elcoro, L., Cano, J., Vergniory, M. G., Wang, Z., Felser, C., Aroyo, M. I. & Bernevig, B. A. Topological quantum chemistry. *Nature* **547,** 298–305. http://dx.doi.org/10.1038/nature23268 (2017).
32. Elcoro, L., Wieder, B. J., Song, Z., Xu, Y., Bradlyn, B. & Bernevig, B. A. Magnetic Topological Quantum Chemistry. *Nat. Commun.* **12,** 5965. doi:10.1038/s41467-021-26241-8 (2021).

33. Po, H. C. Symmetry indicators of band topology. *J. Phys. Condens. Matter* **32,** 263001. doi:10.1088/1361-648x/ab7adb (2020).

34. Cano, J. & Bradlyn, B. Band Representations and Topological Quantum Chemistry. *Annu. Rev. Condens. Matter Phys.* **12,** 225–246. doi:10.1146/annurev-conmatphys-041720-124134 (2021).

35. Tanaka, Y. Experimental realization of a topological crystalline insulator in SnTe. *Nat. Phys.* **8,** 800. doi:10.1038/nphys2442 (2012).

36. Ma, J., Yi, C., Lv, B., Wang, Z., Nie, S., Wang, L., Kong, L., Huang, Y., Richard, P., Zhang, P., Yaji, K., Kuroda, K., Shin, S., Weng, H., Bernevig, B. A., Shi, Y., Qian, T. & Ding, H. Experimental evidence of hourglass fermion in the candidate nonsymmorphic topological insulator KHgSb. *Sci. Adv.* **3,** e1602415. doi:10.1126/sciadv.1602415 (2017).

37. Vergniory, M. G., Elcoro, L., Felser, C., Regnault, N., Bernevig, B. A. & Wang, Z. A complete catalogue of high-quality topological materials. *Nature* **566,** 480–485. doi:10.1038/s41586-019-0954-4 (2019).

38. Zhang, T., Jiang, Y., Song, Z., Huang, H., He, Y., Fang, Z., Weng, H. & Fang, C. Catalogue of topological electronic materials. *Nature* **566,** 475–479. doi:10.1038/s41586-019-0944-6 (2019).

39. Tang, F., Po, H. C., Vishwanath, A. & Wan, X. Comprehensive search for topological materials using symmetry indicators. *Nature* **566,** 486–489. doi:10.1038/s41586-019-0937-5 (2019).

40. Tang, F., Po, H. C., Vishwanath, A. & Wan, X. Efficient Topological Materials Discovery Using Symmetry Indicators. *Nat. Phys.* **15,** 470–476. doi:10.1038/s41567-019-0418-7 (2019).

41. Po, H. C., Watanabe, H. & Vishwanath, A. Fragile Topology and Wannier Obstructions. *Phys. Rev. Lett.* **121,** 126402. doi:10.1103/PhysRevLett.121.126402 (2018).

42. Bradlyn, B., Wang, Z., Cano, J. & Bernevig, B. A. Disconnected elementary band representations, fragile topology, and Wilson loops as topological indices: An example on the triangular lattice. *Phys. Rev. B* **99,** 045140. doi:10.1103/PhysRevB.99.045140 (2019).

43. Bouhon, A., Black-Schaffer, A. M. & Slager, R.-J. Wilson loop approach to fragile topology of split elementary band representations and topological crystalline insulators with time-reversal symmetry. *Phys. Rev. B* **100,** 195135. doi:10.1103/PhysRevB.100.195135 (2019).

44. Ahn, J., Park, S. & Yang, B.-J. Failure of Nielsen-Ninomiya Theorem and Fragile Topology in Two-Dimensional Systems with Space-Time Inversion Symmetry: Application to Twisted Bilayer Graphene at Magic Angle. *Phys. Rev. X* **9,** 021013. doi:10.1103/PhysRevX.9.021013 (2019).

45. Bouhon, A., Bzdušek, T. & Slager, R.-J. Geometric approach to fragile topology beyond symmetry indicators. *Phys. Rev. B* **102,** 115135. doi:10.1103/PhysRevB.102.115135 (2020).

46. Liu, S., Vishwanath, A. & Khalaf, E. Shift Insulators: Rotation-Protected Two-Dimensional Topological Crystalline Insulators. *Phys. Rev. X* **9,** 031003. doi:10.1103/PhysRevX.9.031003 (2019).

47. Alexandradinata, A., Höller, J., Wang, C., Cheng, H. & Lu, L. Crystallographic splitting theorem for band representations and fragile topological photonic crystals. *Phys. Rev. B* **102,** 115117. doi:10.1103/PhysRevB.102.115117 (2020).

48. Wieder, B. J. & Bernevig, B. A. *The Axion Insulator as a Pump of Fragile Topology* 2018. doi:10.48550/ARXIV.1810.02373.

49. de Paz, M. B., Vergniory, M. G., Bercioux, D., García-Etxarri, A. & Bradlyn, B. Engineering Fragile Topology in Photonic Crystals: Topological Quantum Chemistry of Light. *Phys. Rev. Research* **1,** 032005. doi:10.1103/PhysRevResearch.1.032005 (2019).

50. Wang, H.-X., Guo, G.-Y. & Jiang, J.-H. Band topology in classical waves: Wilson-loop approach to topological numbers and fragile topology. *New J. Phys.* **21,** 093029. doi:10.1088/1367-2630/ab3f71 (2019).

51. Peri, V., Song, Z.-D., Serra-Garcia, M., Engeler, P., Queiroz, R., Huang, X., Deng, W., Liu, Z., Bernevig, B. A. & Huber, S. D. Experimental Characterization of Fragile Topology in an Acoustic Metamaterial. *Science* **367,** 797–800. doi:10.1126/science.aaz7654 (2020).

52. Song, Z.-D., Elcoro, L., Xu, Y.-F., Regnault, N. & Bernevig, B. A. Fragile Phases as Affine Monoids: Classification and Material Examples. *Phys. Rev. X* **10,** 031001. doi:10.1103/PhysRevX.10.031001 (2020).

53. Hwang, Y., Ahn, J. & Yang, B.-J. Fragile topology protected by inversion symmetry: Diagnosis, bulk-boundary correspondence, and Wilson loop. *Phys. Rev. B* **100,** 205126. doi:10.1103/PhysRevB.100.205126 (2019).

54. Song, Z.-D., Elcoro, L. & Bernevig, B. A. Twisted Bulk-Boundary Correspondence of Fragile Topology. *Science* **367,** 794–797. doi:10.1126/science.aaz7650 (2020).

55. Moore, J. E., Ran, Y. & Wen, X.-G. Topological Surface States in Three-Dimensional Magnetic Insulators. *Phys. Rev. Lett.* **101,** 186805. doi:10.1103/PhysRevLett.101.186805 (2008).

56. Fang, C., Gilbert, M. J. & Bernevig, B. A. Bulk topological invariants in noninteracting point group symmetric insulators. *Phys. Rev. B* **86,** 115112. doi:10.1103/PhysRevB.86.115112 (2012).

57. P. Lowdin. On the NonOrthogonality Problem Connected with the Use of Atomic Wave Functions in the Theory of Molecules and Crystals. *J. Chem. Phys.* **18,** 365 (1950).

58. Slater, J. C. & Koster, G. F. Simplified LCAO Method for the Periodic Potential Problem. *Phys. Rev.* **94,** 1498–1524 (1954).

59. Goringe, C. M., Bowler, D. R. & Hernández, E. Tight-binding modelling of materials. *Rep. Prog. Phys.* **60,** 1447 (1997).

60. Vanderbilt, D. *Berry Phases in Electronic Structure Theory: Electric Polarization, Orbital Magnetization and Topological Insulators* doi:10.1017/9781316662205 (Cambridge University Press, 2018).

61. Bernevig, B. A. & Hughes, T. L. *Topological Insulators and Topological Superconductors* (Princeton University Press, 2013).

62. Dobardžić, Dimitrijević, & Milovanović, Generalized Bloch theorem and topological characterization. *Phys. Rev. B* **91,** 125424. doi:10.1103/PhysRevB.91.125424 (2015).

63. Nakahara, M. *Geometry, Topology and Physics, Second Edition* doi:10.1201/9781420056945 (Taylor & Francis, 2003).

64. Wilczek, F. & Zee, A. Appearance of Gauge Structure in Simple Dynamical Systems. *Phys. Rev. Lett.* **52,** 2111. doi:PhysRevLett.52.2111 (1984).

65. Mead, C. A. The geometric phase in molecular systems. *Rev. Mod. Phys.* **64,** 51–85. doi:10.1103/RevModPhys.64.51 (1992).

66. Kemp, C. J. D., Cooper, N. R. & Ünal, F. N. Nested-sphere description of the N-level Chern number and the generalized Bloch hypersphere. *Phys. Rev. Research* **4,** 023120. doi:10.1103/PhysRevResearch.4.023120 (2022).

67. Milnor, J. W. & Stasheff, J. D. *Characteristic Classes* (Prinston University press, Prinston, New Jersey, 1974).

68. Stone, M. & Goldbart, P. *Mathematics for Physics* (Pimander-Casaubon, Alexandria, 2008).

69. Soluyanov, A. A. & Vanderbilt, D. Smooth gauge for topological insulators. *Phys. Rev. B* **85,** 115415. doi:10.1103/PhysRevB.85.115415 (2012).

70. Berry, M. V. Quantal Phase Factors Accompanying Adiabatic Changes. *Proc. R. Soc. Lond A* **392,** 45. doi:0.1098/rspa.1984.0023 (1984).

71. Zak, J. Berry's phase for energy bands in solids. *Phys. Rev. Lett.* **62,** 2747. doi:10.1103/PhysRevLett.62.2747 (1989).

72. Brouder, C., Panati, G., Calandra, M., Mourougane, C. & Marzari, N. Exponential Localization of Wannier Functions in Insulators. *Phys. Rev. Lett.* **98,** 046402. doi:10.1103/PhysRevLett.98.046402 (2007).

73. Leone, R. The geometry of (non)-Abelian adiabatic pumping. *J. Phys. A: Math. Theor.* **44,** 295301. doi:10.1088/1751-8113/44/29/295301 (2011).

74. Wannier, G. H. The Structure of Electronic Excitation Levels in Insulating Crystals. *Phys. Rev.* **52,** 191–197. doi:10.1103/PhysRev.52.191 (1937).

75. Marzari, N. & Vanderbilt, D. Maximally localized generalized Wannier functions for composite energy bands. *Phys. Rev. B* **56,** 12847. doi:10.1103/PhysRevB.56.12847 (1997).

76. N. Marzari, A. A. Mostofi, J. R. Yates, I. Souza & D. Vanderbilt. Maximally localized Wannier functions: Theory and applications. *Rev. Mod. Phys.* **84,** 1419. doi:10.1103/RevModPhys.84.1419 (2012).

77. Thouless, D. J. Wannier functions for magnetic sub-bands. *J. Phys. Condens. Matter* **17,** L325–L327. doi:10.1088/0022-3719/17/12/003 (1984).

78. Soluyanov, A. A. & Vanderbilt, D. Wannier representation of $\mathbb{Z}_2$ topological insulators. *Phys. Rev. B* **83,** 035108. doi:10.1103/PhysRevB.83.035108 (2011).

79. Roy, R. Z_2 classification of quantum spin Hall systems: An approach using time-reversal invariance. *Phys. Rev. B* **79,** 195321. doi:10.1103/PhysRevB.79.195321 (2009).

80. Soluyanov, A. A. & Vanderbilt, D. Computing topological invariants without inversion symmetry. *Phys. Rev. B* **83,** 235401. doi:10.1103/PhysRevB.83.235401 (2011).

81. Taherinejad, M., Garrity, K. F. & Vanderbilt, D. Wannier center sheets in topological insulators. *Phys. Rev. B* **89,** 115102. doi:10.1103/PhysRevB.89.115102 (2014).

82. Resta, R. Theory of the Electric Polarization in Crystals. *Ferroelectrics* **136,** 51–55. doi:10.1080/00150199208016065 (1992).

83. King-Smith, R. D. & Vanderbilt, D. Theory of polarization of crystalline solids. *Phys. Rev. B* **47,** 1651–1654. doi:10.1103/PhysRevB.47.1651 (1993).
84. Resta, R. Macroscopic Electric Polarization as a Geometric Quantum Phase. *EPL* **22,** 133–138. doi:10.1209/0295-5075/22/2/010 (1993).
85. Resta, R. Macroscopic polarization in crystalline dielectrics: the geometric phase approach. *Rev. Mod. Phys.* **66,** 899. doi:10.1103/RevModPhys.66.899 (1994).
86. Zak, J. Band Center—A Conserved Quantity in Solids. *Phys. Rev. Lett.* **48,** 359–362. doi:10.1103/PhysRevLett.48.359 (1982).
87. Thouless, D. J. Quantization of particle transport. *Phys. Rev. B* **27,** 6083–6087. doi:10.1103/PhysRevB.27.6083 (1983).
88. Fidkowski, L., Jackson, T. S. & Klich, I. Model Characterization of Gapless Edge Modes of Topological Insulators Using Intermediate Brillouin-Zone Functions. *Phys. Rev. Lett.* **107,** 036601. doi:10.1103/PhysRevLett.107.036601 (2011).
89. Rhim, J.-W., Bardarson, J. H. & Slager, R.-J. Unified Bulk-Boundary Correspondence for Band Insulators. *Phys. Rev. B* **97,** 115143. doi:10.1103/PhysRevB.97.115143 (2018).
90. Kivelson, S. Wannier functions in one-dimensional disordered systems: Application to fractionally charged solitons. *Phys. Rev. B* **26,** 4269–4277. doi:10.1103/PhysRevB.26.4269 (1982).
91. Alexandradinata, A., Dai, X. & Bernevig, B. A. Wilson-loop characterization of inversion-symmetric topological insulators. *Phys. Rev. B* **89,** 155114. doi:10.1103/PhysRevB.89.155114 (2014).
92. Deng, D.-L., Wang, S.-T., Shen, C. & Duan, L.-M. Hopf insulators and their topologically protected surface states. *Phys. Rev. B* **88,** 201105. doi:10.1103/PhysRevB.88.201105 (2013).
93. Kennedy, R. Topological Hopf-Chern insulators and the Hopf superconductor. *Phys. Rev. B* **94,** 035137. doi:10.1103/PhysRevB.94.035137 (2016).
94. Hatcher, A. *Algebraic Topology* (Cambridge University Press, Cambridge, 2002).
95. Hopf, H. Über die Abbildungen der dreidimensionalen Sphäre auf die Kugelfläche. *Math. Ann.* **104,** 637–665. doi:10.1007%2FBF01457962 (1931).
96. Wilczek, F. & Zee, A. Linking Numbers, Spin, and Statistics of Solitons. *Phys. Rev. Lett.* **51,** 2250–2252. doi:10.1103/PhysRevLett.51.2250 (1983).
97. Pontrjagin, L. A classification of mappings of the three-dimensional complex into the two-dimensional sphere. *Mat. Sb.* **9(51),** 331. http://mi.mathnet.ru/msb6073 (1941).
98. Auckly, D. & Kapitanski, L. The Pontrjagin–Hopf invariants for Sobolev maps. *Commun. Contemp. Math.* **12,** 121–181. doi:10.1142/S0219199710003695 (2010).
99. Kennedy, R. *Homotopy Theory of Topological Insulators* PhD thesis (Universität zu Köln, 2014).
100. Fecko, M. *Differential Geometry and Lie Groups for Physicists* (Cambridge University Press, Cambridge, 2006).

101. Kramers, H. A. Théorie générale de la rotation paramagnétique dans les cristaux. *Proceedings of the Royal Netherlands Academy of Arts and Sciences* **33,** 959–972 (1930).

102. Sato, M. & Ando, Y. Topological superconductors: a review. *Rep. Prog. Phys.* **80,** 076501. doi:10.1088/1361-6633/aa6ac7 (2017).

103. Dyson, F. J. *J. Math. Phys.* **3,** 1199 (1962).

104. Altland, A. & Zirnbauer, M. R. Nonstandard symmetry classes in mesoscopic normal-superconducting hybrid structures. *Phys. Rev. B* **55,** 1142. doi:10.1103/PhysRevB.55.1142 (1997).

105. Slager, R.-J., Mesaros, A., Juricic, V. & Zaanen, J. The space group classification of topological band-insulators. *Nat. Phys.* **9.** Article, 98–102. http://dx.doi.org/10.1038/nphys2513 (2012).

106. Dong, X.-Y. & Liu, C.-X. Classification of topological crystalline insulators based on representation theory. *Phys. Rev. B* **93,** 045429. doi:10.1103/PhysRevB.93.045429 (2016).

107. Hsieh, T. H., Lin, H., Liu, J., Duan, W., Bansil, A. & Fu, L. Topological crystalline insulators in the SnTe material class. *Nat. Commun.* **3,** 982. doi:10.1038/ncomms1969 (2012).

108. Xu, S.-Y., Liu, C., Alidoust, N., Neupane, M., Qian, D., Belopolski, I., Denlinger, J. D., Wang, Y. J., Lin, H., Wray, L. A., Landolt, G., Slomski, B., Dil, J. H., Marcinkova, A., Morosan, E., Gibson, Q., Sankar, R., Chou, F. C., Cava, R. J., Bansil, A. & Hasan, M. Z. Observation of a topological crystalline insulator phase and topological phase transition in Pb1-xSnxTe. *Nat. Commun.* **3.** Article, 1192. http://dx.doi.org/10.1038/ncomms2191 (2012).

109. Fu, L. & Kane, C. L. Topological insulators with inversion symmetry. *Phys. Rev. B* **76,** 045302. doi:10.1103/PhysRevB.76.045302 (2007).

110. Turner, A. M., Zhang, Y., Mong, R. S. K. & Vishwanath, A. Quantized response and topology of magnetic insulators with inversion symmetry. *Phys. Rev. B* **85,** 165120. doi:10.1103/PhysRevB.85.165120 (2012).

111. Fu, L. & Kane, C. L. Time reversal polarization and a Z_2 adiabatic spin pump. *Phys. Rev. B* **74,** 195312. doi:10.1103/PhysRevB.74.195312 (2006).

112. Zak, J. Symmetry Specification of Bands in Solids. *Phys. Rev. Lett.* **45,** 1025–1028. doi:10.1103/PhysRevLett.45.1025 (1980).

113. Zak, J. Band representations and symmetry types of bands in solids. *Phys. Rev. B* **23,** 2824–2835. http://link.aps.org/doi/10.1103/PhysRevB.23.2824 (1981).

114. Benalcazar, W. A., Bernevig, B. A. & Hughes, T. L. Quantized electric multipole insulators. *Science* **357,** 61–66. doi:10.1126/science.aah6442 (2017).

115. Schindler, F., Cook, A. M., Vergniory, M. G., Wang, Z., Parkin, S. S. P., Bernevig, B. A. & Neupert, T. Higher-order topological insulators. *Sci. Adv.* **4.** doi:10.1126/sciadv.aat0346 (2018).

116. Song, Z., Wang, Z., Shi, W., Li, G., Fang, C. & Bernevig, B. A. All Magic Angles in Twisted Bilayer Graphene are Topological. *Phys. Rev. Lett.* **123,** 036401. doi:10.1103/PhysRevLett.123.036401 (2019).

117. Po, H. C., Zou, L., Senthil, T. & Vishwanath, A. Faithful Tight-Binding Models and Fragile Topology of Magic-Angle Bilayer Graphene. *Phys. Rev. B* **99,** 195455. doi:10.1103/PhysRevB.99.195455 (2019).

118. Shiozaki, K. & Sato, M. Topology of crystalline insulators and superconductors. *Phys. Rev. B* **90,** 165114. doi:10.1103/PhysRevB.90.165114 (2014).

119. Wang, Z., Alexandradinata, A., Cava, R. J. & Bernevig, B. A. Hourglass fermions. *Nature* **532,** 189–194. doi:10.1038/nature17410 (2016).

120. Alexandradinata, A. & Höller, J. No-go theorem for topological insulators and high-throughput identification of Chern insulators. *Phys. Rev. B* **98,** 184305. doi:10.1103/PhysRevB.98.184305 (2018).

121. Murakami, S., Iso, S., Avishai, Y., Onoda, M. & Nagaosa, N. Tuning phase transition between quantum spin Hall and ordinary insulating phases. *Phys. Rev. B* **76,** 205304. doi:10.1103/PhysRevB.76.205304 (2007).

122. Von Neumann, J. & Wigner, E. Über das Verhalten von Eigenwerten bei adiabatischen Prozessen. *Phys. Z.* **30,** 465. doi:10.1007/978-3-662-02781-3_20 (1929).

123. Bzdušek, T. & Sigrist, M. Robust doubly charged nodal lines and nodal surfaces in centrosymmetric systems. *Phys. Rev. B* **96,** 155105. doi:10.1103/PhysRevB.96.155105 (2017).

124. Wikipedia contributors. *Pauli matrices — Wikipedia, The Free Encyclopedia* [Online; accessed 7-September-2021]. 2021. https://en.wikipedia.org/w/index.php?title=Pauli_matrices&oldid=1041247224.

125. Wan, X., Turner, A., Vishwanath, A. & Savrasov, S. Y. Topological semimetal and Fermi-arc surface states in the electronic structure of pyrochlore iridates. *Phys. Rev. B* **83,** 205101. doi:https://doi.org/10.1103/PhysRevB.83.205101 (2011).

126. Sun, X.-Q., Zhang, S.-C. & Bzdušek, T. Conversion Rules for Weyl Points and Nodal Lines in Topological Media. *Phys. Rev. Lett.* **121,** 106402. doi:10.1103/PhysRevLett.121.106402 (2018).

127. Schuster, T., Flicker, F., Li, M., Kotochigova, S., Moore, J. E., Ye, J. & Yao, N. Y. Realizing Hopf Insulators in Dipolar Spin Systems. *Phys. Rev. Lett.* **127,** 015301. doi:10.1103/PhysRevLett.127.015301 (2021).

128. Panati, G. Triviality of Bloch and Bloch–Dirac Bundles. *Ann. Henri Poincaré* **8,** 995–1011. doi:10.1007/s00023-007-0326-8 (2007).

129. De Nittis, G. & Gomi, K. The FKMM-invariant in low dimension. *Lett. Math. Phys.* **108,** 1225–1277. doi:10.1007/s11005-017-1029-9 (2018).

130. Peterson, F. P. Some remarks on Chern classes. *Ann. Math.* 414–420. doi:10.2307/1970191 (1959).

131. E. I. Blount. in *Solid State Physics*, Vol. 13, edited by F. Seitz and D. Turnbull (Academic, New York). 1962.

132. Alexandradinata, A. & Glazman, L. Semiclassical theory of Landau levels and magnetic breakdown in topological metals. *Phys. Rev. B* **97,** 144422. doi:10.1103/PhysRevB.97.144422 (2018).

133. Michel, L. & Zak, J. Connectivity of energy bands in crystals. *Phys. Rev. B* **59,** 5998–6001. doi:10.1103/PhysRevB.59.5998 (1999).

134. Höller, J. & Alexandradinata, A. Topological Bloch oscillations. *Phys. Rev. B* **98,** 024310. doi:10.1103/PhysRevB.98.024310 (2018).

135. Watanabe, H., Po, H. C. & Vishwanath, A. Structure and Topology of Band Structures in the 1651 Magnetic Space Groups. *Sci. Adv.* **4,** eaat8685. doi:10.1126/sciadv.aat8685 (2018).

136. Parameswaran, S. A. Topological order and absence of band insulators at integer filling in non-symmorphic crystals. *Nat. Phys.* **9,** 299–303. doi:10.1038/nphys2600 (2013).

137. Po, H. C., Watanabe, H., Zaletel, M. P. & Vishwanath, A. Filling-enforced quantum band insulators in spin-orbit coupled crystals. *Sci. Adv.* **2,** e1501782. doi:10.1126/sciadv.1501782 (2016).

138. Liu, C., Vafa, F. & Xu, C. Symmetry-protected topological Hopf insulator and its generalizations. *Phys. Rev. B* **95,** 161116. doi:10.1103/PhysRevB.95.161116 (2017).

139. Resta, R. The insulating state of matter: a geometrical theory. *Eur. Phys. J. B* **79,** 121–137. doi:10.1140/epjb/e2010-10874-4 (2011).

140. Essin, A. M., Moore, J. E. & Vanderbilt, D. Magnetoelectric polarizability and axion electrodynamics in crystalline insulators. *Phys. Rev. Lett.* **102,** 146805. doi:10.1103/PhysRevLett.102.146805 (2009).

141. Taherinejad, M. & Vanderbilt, D. Adiabatic Pumping of Chern-Simons Axion Coupling. *Phys. Rev. Lett.* **114,** 096401. doi:10.1103/PhysRevLett.114.096401 (2015).

142. Olsen, T., Taherinejad, M., Vanderbilt, D. & Souza, I. Surface theorem for the Chern-Simons axion coupling. *Phys. Rev. B* **95,** 075137. doi:10.1103/PhysRevB.95.075137 (2017).

143. Vanderbilt, D. & King-Smith, R. D. Electric polarization as a bulk quantity and its relation to surface charge. *Phys. Rev. B* **48,** 4442–4455. doi:10.1103/PhysRevB.48.4442 (1993).

144. Essin, A. M., Turner, A. M., Moore, J. E. & Vanderbilt, D. Orbital magnetoelectric coupling in band insulators. *Phys. Rev. B* **81,** 205104. doi:10.1103/PhysRevB.81.205104 (2010).

145. Rauch, T., Olsen, T., Vanderbilt, D. & Souza, I. Geometric and nongeometric contributions to the surface anomalous Hall conductivity. *Phys. Rev. B* **98,** 115108. doi:10.1103/PhysRevB.98.115108 (2018).

146. Malashevich, A., Souza, I., Coh, S. & Vanderbilt, D. Theory of orbital magnetoelectric response. *New J. Phys.* **12,** 053032. doi:10.1088/1367-2630/12/5/053032 (2010).

147. Callan, C. & Harvey, J. Anomalies and fermion zero modes on strings and domain walls. *Nucl. Phys. B.* **250,** 427–436. doi:https://doi.org/10.1016/0550-3213(85)90489-4 (1985).

148. Golterman, M. F., Jansen, K. & Kaplan, D. B. Chern-Simons currents and chiral fermions on the lattice. *Phys. Lett. B* **301,** 219–223. doi:https://doi.org/10.1016/0370-2693(93)90692-B (1993).

149. Jackiw, R. & Rebbi, C. Solitons with fermion number 1/2. *Phys. Rev. D* **13,** 3398. doi:10.1103/PhysRevD.13.3398 (1976).

150. Creutz, M. Aspects of chiral symmetry and the lattice. *Rev. Mod. Phys.* **73,** 119–150. doi:10.1103/RevModPhys.73.119 (2001).

151. Kohmoto, M., Halperin, B. I. & Wu, Y.-S. Quantized Hall effect in 3D periodic systems. *Phys. B: Condens. Matter* **184,** 30–33. doi:https://doi.org/10.1016/0921-4526(93)90316-X (1993).

152. Qi, X.-L., Hughes, T. L. & Zhang, S.-C. Topological Field Theory of Time-Reversal Invariant Insulators. *Phys. Rev. B* **78,** 195424. doi:10.1103/PhysRevB.78.195424 (2008).

153. Nielsen, H. & Ninomiya, M. Absence of neutrinos on a lattice: (I). Proof by homotopy theory. *Nucl. Phys. B* **185,** 20–40. doi:https://doi.org/10.1016/0550-3213(81)90361-8 (1981).

154. Stone, M. Edge waves in the quantum Hall effect. *Ann. Phys.* **207,** 38–52. doi:10.1016/0003-4916(91)90177-A (1991).

155. Nielsen, H. & Ninomiya, M. Absence of neutrinos on a lattice: (II). Intuitive topological proof. *Nucl. Phys. B* **193,** 173–194. doi:https://doi.org/10.1016/0550-3213(81)90524-1 (1981).

156. Trifunovic, L. Bulk-and-edge to corner correspondence. *Phys. Rev. Research* **2,** 043012. doi:10.1103/PhysRevResearch.2.043012 (2020).

157. Essin, A. M., Moore, J. E. & Vanderbilt, D. Erratum: Magnetoelectric Polarizability and Axion Electrodynamics in Crystalline Insulators [Phys. Rev. Lett. 102, 146805 (2009)]. *Phys. Rev. Lett.* **103,** 259902(E). doi:10.1103/PhysRevLett.103.259902 (2009).

158. Wilczek, F. Two applications of axion electrodynamics. *Phys. Rev. Lett.* **58,** 1799–1802. doi:10.1103/PhysRevLett.58.1799 (1987).

159. Haldane, F. D. M. Berry Curvature on the Fermi Surface: Anomalous Hall Effect as a Topological Fermi-Liquid Property. *Phys. Rev. Lett.* **93,** 206602. doi:10.1103/PhysRevLett.93.206602 (2004).

160. Goldstone, J. & Wilczek, F. Fractional Quantum Numbers on Solitons. *Phys. Rev. Lett.* **47,** 986–989. doi:10.1103/PhysRevLett.47.986 (1981).

161. Zhang, F., Kane, C. L. & Mele, E. J. Surface State Magnetization and Chiral Edge States on Topological Insulators. *Phys. Rev. Lett.* **110,** 046404. doi:10.1103/PhysRevLett.110.046404 (2013).

162. Sitte, M., Rosch, A., Altman, E. & Fritz, L. Topological Insulators in Magnetic Fields: Quantum Hall Effect and Edge Channels with a Nonquantized θ Term. *Phys. Rev. Lett.* **108,** 126807. doi:10.1103/PhysRevLett.108.126807 (2012).

163. Alexandradinata, A., Wang, Z. & Bernevig, B. A. Topological Insulators from Group Cohomology. *Phys. Rev. X* **6,** 021008. doi:10.1103/PhysRevX.6.021008 (2016).

164. Zhu, Z. & Wakin, M. B. On the Asymptotic Equivalence of Circulant and Toeplitz Matrices. *IEEE Trans. Inf. Theory* **63,** 2975–2992. doi:10.1109/TIT.2017.2676808 (2017).

165. Song, Z., Fang, Z. & Fang, C. $(d-2)$-Dimensional Edge States of Rotation Symmetry Protected Topological States. *Phys. Rev. Lett.* **119,** 246402. doi:10.1103/PhysRevLett.119.246402 (2017).

166. Zhu, P., Hughes, T. L. & Alexandradinata, A. Quantized surface magnetism and higher-order topology: Application to the Hopf insulator. *Phys. Rev. B* **103,** 014417. doi:10.1103/PhysRevB.103.014417 (2021).

167. Lapierre, B., Neupert, T. & Trifunovic, L. N-band Hopf insulator. *Phys. Rev. Research* **3,** 033045. doi:10.1103/PhysRevResearch.3.033045 (2021).

168. Whitehead, J. H. C. An Expression of Hopf's Invariant as an Integral. *Proc. Natl. Acad. Sci.* **33,** 117–123. doi:10.1073/pnas.33.5.117 (1947).

169. Baez, J. & Muniain, J. P. *Gauge Fields, Knots and Gravity* (World Scientific, Hackensack, NJ, 1994).

170. Thonhauser, T. & Vanderbilt, D. Insulator/Chern-insulator transition in the Haldane model. *Phys. Rev. B* **74,** 235111. doi:10.1103/PhysRevB.74.235111 (2006).

171. Budich, J. C., Eisert, J., Bergholtz, E. J., Diehl, S. & Zoller, P. Search for localized Wannier functions of topological band structures via compressed sensing. *Phys. Rev. B* **90,** 115110. doi:10.1103/PhysRevB.90.115110 (2014).

172. Read, N. Compactly supported Wannier functions and algebraic *K*-theory. *Phys. Rev. B* **95,** 115309. doi:10.1103/PhysRevB.95.115309 (2017).

173. Freed, D. S. & Moore, G. W. Twisted Equivariant Matter. *Ann. Henri Poincare* **14,** 1927–2023. doi:10.1007/s00023-013-0236-x (2013).

174. Shiozaki, K., Sato, M. & Gomi, K. Topological crystalline materials: General formulation, module structure, and wallpaper groups. *Phys. Rev. B* **95,** 235425. doi:10.1103/PhysRevB.95.235425 (2017).

175. Else, D. V., Po, H. C. & Watanabe, H. Fragile topological phases in interacting systems. *Phys. Rev. B* **99,** 125122. doi:10.1103/PhysRevB.99.125122 (2019).

176. Cano, J., Bradlyn, B., Wang, Z., Elcoro, L., Vergniory, M. G., Felser, C., Aroyo, M. I. & Bernevig, B. A. Building blocks of topological quantum chemistry: Elementary band representations. *Phys. Rev. B* **97,** 035139. doi:10.1103/PhysRevB.97.035139 (2018).

177. Wikipedia contributors. *Quotient space (topology) — Wikipedia, The Free Encyclopedia* [Online; accessed 15-November-2021]. 2021. https://en.wikipedia.org/w/index.php?title=Quotient_space_(topology)&oldid=1053106154.

178. Tiwari, A. & Bzdušek, T. Non-Abelian topology of nodal-line rings in $\mathcal{PT}$-symmetric systems. *Phys. Rev. B* **101,** 195130. doi:10.1103/PhysRevB.101.195130 (2020).

179. Elcoro, L., Bradlyn, B., Wang, Z., Vergniory, M. G., Cano, J., Felser, C., Bernevig, B. A., Orobengoa, D., de la Flor, G. & Aroyo, M. I. Double crystallographic groups and their representations on the Bilbao Crystallographic Server. *J. Appl. Crystallogr.* **50,** 1457–1477. doi:10.1107/S1600576717011712 (2017).

180. Lim, L.-K. & Moessner, R. Pseudospin Vortex Ring with a Nodal Line in Three Dimensions. *Phys. Rev. Lett.* **118,** 016401. doi:10.1103/PhysRevLett.118.016401 (2017).

181. Horava, P. Stability of Fermi Surfaces and *K* Theory. *Phys. Rev. Lett.* **95,** 016405. doi:10.1103/PhysRevLett.95.016405 (2005).

182. Dubail, J. & Read, N. Tensor network trial states for chiral topological phases in two dimensions and a no-go theorem in any dimension. *Phys. Rev. B* **92,** 205307. doi:10.1103/PhysRevB.92.205307 (2015).

183. Schindler, F. & Bernevig, B. A. Noncompact atomic insulators. *Phys. Rev. B* **104,** L201114. doi:10.1103/PhysRevB.104.L201114 (2021).

184. Atala, M., Aidelsburger, M., Barreiro, J. T., Abanin, D., Kitagawa, T., Demler, E. & Bloch, I. Direct measurement of the Zak phase in topological Bloch bands. *Nat. Phys.* **9,** 795–800. doi:10.1038/nphys2790 (2013).

185. Schuster, T., Flicker, F., Li, M., Kotochigova, S., Moore, J. E., Ye, J. & Yao, N. Y. Floquet engineering ultracold polar molecules to simulate topological insulators. *Phys. Rev. A* **103,** 063322. doi:10.1103/PhysRevA.103.063322 (2021).

186. Zhang, H., Liu, C.-X., Qi, X.-L., Dai, X., Fang, Z. & Zhang, S.-C. Topological insulators in Bi_2Se_3, Bi_2Te_3 and Sb_2Te_3 with a single Dirac cone on the surface. *Nat. Phys.* **5,** 438–442. doi:10.1038/nphys1270 (2009).

187. Zhang, H., Liu, C.-X., Qi, X.-L., Deng, X.-Y., Dai, X., Zhang, S.-C. & Fang, Z. Electronic structures and surface states of topological insulator $Bi_{1-x}Sb_x$. *Phys. Rev B* **80,** 085307. doi:10.1103/PhysRevB.80.085307 (2009).

188. Park, S., Hwang, Y., Choi, H. C. & Yang, B.-J. Topological acoustic triple point. *Nat. Commun.* **12,** 6781. doi:10.1038/s41467-021-27158-y (2021).

189. Xu, G., Weng, H., Wang, Z., Dai, X. & Fang, Z. Chern Semimetal and the Quantized Anomalous Hall Effect in $HgCr_2Se_4$. *Phys. Rev. Lett.* **107,** 186806. doi:10.1103/PhysRevLett.107.186806 (2011).

190. Bouhon, A., Wu, Q., Slager, R.-J., Weng, H., Yazyev, O. V. & Bzdušek, T. Non-Abelian reciprocal braiding of Weyl nodes and its manifestation in ZrTe. *Nat. Phys.* **16,** 1137–1143. doi:10.1038/s41567-020-0967-9 (2020).

191. Wu, Q., Soluyanov, A. A. & Bzdušek, T. Non-Abelian band topology in noninteracting metals. *Science* **365,** 1273–1277. doi:10.1126/science.aau8740 (2019).

192. FIZ Karlsruhe. *Inorganic Crystal Structure Database* http://www2.fiz-karlsruhe.de/icsd_home.html.

193. Mounet, N., Gibertini, M., Schwaller, P., Campi, D., Merkys, A., Marrazzo, A., Sohier, T., Castelli, I. E., Cepellotti, A., Pizzi, G. & Marzari, N. *Two-dimensional materials from high-throughput computational exfoliation of experimentally known compounds* 2020. doi:10.24435/materialscloud:az-b2.

194. Gresch, D., Autès, G., Yazyev, O. V., Troyer, M., Vanderbilt, D., Bernevig, B. A. & Soluyanov, A. A. Z2Pack: Numerical implementation of hybrid Wannier centers for identifying topological materials. *Phys. Rev. B* **95,** 075146. doi:10.1103/PhysRevB.95.075146 (2017).

195. Xiao, D., Chang, M.-C. & Niu, Q. Berry phase effects on electronic properties. *Rev. Mod. Phys.* **82,** 1959–2007. doi:10.1103/RevModPhys.82.1959 (2010).

196. Hatcher, A. *Vector Bundles and K-Theory* https://pi.math.cornell.edu/~hatcher/VBKT/VBpage.html (Unpublished, 2003).

197. Miranda, M. & Tilli, P. Asymptotic Spectra of Hermitian Block Toeplitz Matrices and Preconditioning Results. *SIAM J. Matrix Anal. Appl.* **21,** 867–881. doi:10.1137/S0895479896313036 (2000).

198. Lee, D. H. & Joannopoulos, J. D. Simple scheme for surface-band calculations. I. *Phys. Rev. B* **23,** 4988–4996. doi:10.1103/PhysRevB.23.4988 (1981).

199. Ahn, J., Kim, D., Kim, Y. & Yang, B.-J. Band Topology and Linking Structure of Nodal Line Semimetals with Z_2 Monopole Charges. *Phys. Rev. Lett.* **121,** 106403. doi:10.1103/PhysRevLett.121.106403 (2018).

200. Fruchart, M. & Carpentier, D. An introduction to topological insulators. *C. R. Phys.* **14,** 779–815. doi:10.1016/j.crhy.2013.09.013 (2013).

201. Atiyah, M. F. *K-theory* (W. A. Benjamin, New York, Amsterdam, 1967).

202. Chen, Y.-C., Lin, Y.-P. & Kao, Y.-J. *Protected Gapless Edge States In Trivial Topology* 2022. doi:10.48550/ARXIV.2206.04858.

COLOPHON

This document was typeset using the typographical look-and-feel `classicthesis` developed by André Miede. The style was inspired by Robert Bringhurst's seminal book on typography *"The Elements of Typographic Style"*.